Geosynthetic Reinforced Retaining Walls with Limited Fill Space under Static Footing Loading

By

Jamal Ismael Kakrasul

Submitted to the graduate degree program in Civil, Environmental, and Architectural Engineering and the Graduate Faculty of the University of Kansas in partial fulfillment of the requirements for the degree of Doctor of Philosophy.

_____

Chairperson Dr. Jie Han

_____

Dr. Hongyi Cai

_____

Dr. Rongqing Hui

_____

Dr. Robert L. Parsons

_____

Dr. Steven D. Schrock

Date Defended: 01/16/2018

The Dissertation Committee for Jamal Ismael Kakrasul

certifies that this is the approved version of the following dissertation:

Geosynthetic Reinforced Retaining Walls with Limited Fill Space under Static Footing Loading

_____

Chairperson Dr. Jie Han

Date approved: 01/16/2018

Abstracts

Geosynthetic reinforced retaining (GRR) walls, which typically consist of reinforced soil mass, facing units, and retained fill, are extensively used for highways, bridge abutments, and service roads throughout the world. In recent decades, GRR walls have been increasingly built with limited fill space, which has posed challenges for designing such walls with satisfactory performance, especially under surface loading, such as bridge foundations. Since the GRR walls with limited fill space are retaining walls under special conditions, only limited information related to such walls is available in the literature and therefore their performance has not been well understood. The objective of this study was to evaluate the performance of limited fill space GRR walls subjected to static footing loading.

To fulfill the above research objective, a comprehensive experimental study and numerical analysis were conducted. The experimental study included a series of laboratory model tests to investigate the performance of GRR walls constructed with limited fill space subjected to strip footing loading. The devised experimental program consisted of 11 model tests with different retained medium distances, geosynthetic-reinforced fill widths, footing offset distances, and reinforcement layouts. The model tests were constructed and tested in a model box under a plane strain condition in the geotechnical testing laboratory at the University of Kansas. The dimensions of the model box were 2.4 m long, 0.5 m wide, and 1.1 m high. The model walls were 1.0 m high and 0.45 m wide. In each model test, a load was applied on the top of the wall through a 200 mm wide rigid plate to simulate a strip footing. Earth pressure cells, reflection targets on the sides of the wall, and fixed benchmarks on facing units, and on the loading plate

were installed to measure earth pressure distributions, wall deformations, and wall facing displacements, and footing settlements, respectively.

To interpret the reduced-scale modeling results based on the scaling ratio between the model and the prototype, a scale effect analysis was performed to find the correct scale ratio between the model and the prototype wall. The wall models were designed based on the findings of the scale effect analysis.

The experimental test results showed that limiting the size of the retained medium and the reinforced fill affected the internal stability of the wall, the lateral wall facing displacement, and the footing settlement. Reduction of the wall width from 0.5H to 0.3H (H is the wall height) resulted in excessive wall deformation and footing settlement, and even sudden failure of the model wall. On the other hand, the test results revealed that connecting geosynthetic reinforcement to the stable retained medium resulted in substantial reduction in the lateral displacement of the wall facing and the settlement of the footing. The test results also demonstrated that bending geosynthetic reinforcement upward along the back of the reinforced soil enhanced internal stability and resulted in considerable reduction in the lateral displacement of the wall facing and increase in the bearing capacity of the footing.

The experimental test results also showed that the vertical earth pressures along the depth of the model tests increased with the increase of the depth of the model and the applied footing load. Likewise, the lateral earth pressures on the wall facing along the depth of the model tests increased with the applied footing load. In addition, the vertical earth pressures and the lateral earth pressures measured from the model tests with the reinforced fill width of 0.3H were lower than those calculated by the exiting theoretical methods (i.e., 2:1 distribution method, Rankine's active earth pressure theory and Janssen's equation). However, the results of Janssen's equation

were in better agreement with the experimental results as compared to the result of Rankine's theory.

The numerical analysis was performed by using the continuum mechanics-based program FLAC 2D Version 8.0 to verify the experimental results. In the numerical analysis, backfill soil was modeled as a linearly elastic perfectly plastic material with the Mohr Coulomb (MC) failure criterion. The wall facing, the stable retained medium, and the foundation were modeled as a linearly elastic material. A strip element was utilized to simulate the reinforcement and modeled as a linearly elastic perfectly plastic material. The lateral displacement of the wall facing, the footing settlement, the vertical earth pressures, lateral earth pressures, and the maximum strains in the reinforcement were computed by the numerical analysis under the applied footing loads and compared to the results from the experimental tests. The results obtained from the numerical analysis generally agreed with those measured from the experimental tests.

In addition, a numerical parametric study was conducted to assess the factors influencing the performance of GRR walls with limited fill space subjected to static footing loading. The influence factors consisted of the reinforced fill width (reinforcement length), the reinforcement rear connection, the footing size, the footing offset distance, the stiffness of reinforcement, the friction angle of the backfill soil, and the wall height. The parametric study showed that the maximum lateral displacement of the wall facing, and the footing settlement increased with the reduction in the reinforced fill width, the friction angle of the backfill soil, and the footing offset distance. In contrast, the maximum lateral displacement of the wall facing, and the footing settlement decreased with an increase in the reinforcement stiffness, the footing offset distance, and the decrease in the footing size. The parametric study also showed that the connection of the reinforcement to the stable medium at rear, bending-upward the reinforcement around the back

of the reinforced fill and overlapped the reinforcement from the back of the reinforced fill resulted in considerable reduction in the maximum lateral displacement of the wall facing and the footing settlement. The maximum strain in the reinforcement increased with the reduction in the reinforced fill width, the friction angle of the backfill soil, and the footing offset distance. However, the maximum strain in the reinforcement decreased with the increase in the reinforcement stiffness, the decrease in the footing size and the footing offset distance. Additionally, the vertical earth pressures computed on the wall along the wall facing of the wall models were lower than those computed along the centerline of the footing under all the applied footing loads. Also, the vertical earth pressures computed on the wall along the wall facing of wall models were generally lower than those calculated by the 2:1 distribution method. However, the vertical earth pressures computed along the centerline of the footing along were generally higher than those calculated by the 2:1 distribution method. Similarly, the lateral earth pressures computed on the wall facing of wall models were lower than those calculated by the exiting methods (i.e., Rankine's active earth pressure theory and Janssen's equation with the 2:1 distribution method). However, the lateral earth pressures calculated using Janssen's equation showed better agreement with the lateral earth pressures computed by the numerical analysis as compared to those calculated using Rankine's theory.

Acknowledgements

I would like to express my sincere gratitude to my advisor, Professor. Jie Han, for his invaluable academic and personal guidance and support throughout my experience as a student. Dr. Han helped me in all the way possible to pursue my Ph.D. degree at the University of Kansa and hence I would love to thank him again.

I would love to appreciate Mr. Charles Olcese, the director of international student service at the University of Kansas, for his support and help during my study.

I also want to thank my major sponsor, The Human Capacity Development Program in Kurdistan Region-Iraq, HCDP, for providing most of the funds throughout my Ph.D. study. Also,

I would like to acknowledge Itasca group for providing two-year loan of the latest version of FLAC2D.

I would like to thank my Ph.D. committee members, Professor Robert L. Parsons, Professor, Professor Hongyi Cai, Professor Steven D. Schrock, and Professor Rongqing Hui for their guidance and help in reviewing this dissertation.

I would like to thank the members of KU geotechnical society for their support during the experimental work. Special thanks to Seyed Mustapha Rahmaninezhad, and Mehari Weldu.

Finally, I would love to appreciate my family, especially my precious wife for her countless supports and love. She went through a lot of difficulties during my study by taking care of three pretty girls patiently. I want to thank her again for her patient and being a precious mother.

Table of Contents

List of Figures

List of Tables

Chapter 1 Introduction

1.1 Introduction

Over the past decades, tremendous amount of geosynthetic-reinforced retaining (GRR) structures have been used for highways and residential areas throughout the world. The extensive use of GRR structures is for the construction of new highway infrastructures, like bridge abutments and embankments (Yasrobi et al. 2009b, Rahmaninezhad 2009, and Han 2015). GRR walls typically consist of reinforced fill, facing elements, and retained soil. Facing elements can have different materials and various shapes and sizes. Reinforced fill consists of reinforced elements (such as "geosynthetic") and soil, and retained soil is the existing or placed material next to the reinforced fill. Figure 1.1 shows a typical cross-section of a GRR wall. This type of wall acts as a composite system that can provide the same performance as a cantilever or gravity-type retaining wall for lower cost and less construction time.

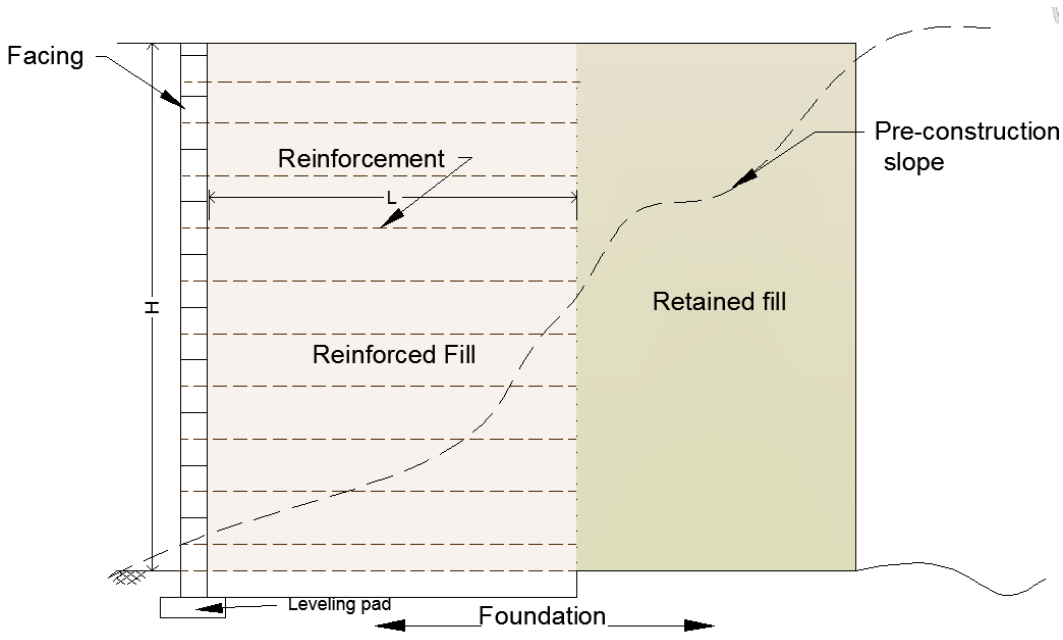

Figure 1.1 Typical cross-section of a GRR wall

Understanding and predicting the behavior of GRR walls during construction and loading stages has been the subject of many researchers all over the world (Kakrasul et al. 2016; Chen et al. 2015; Allen and Bathurst 2014a; Allen an Bathurst 2014b; Bloser et al 2012; Adam et al 2011; Han and Leshchinsky 2010; Han and Leshchinsky 2006; and Leshchinsky et al. 2004). Furthermore, the current design and construction guidelines provide decent details for GRR walls. The important parameter for design of GRR walls is the reinforced fill width (also the reinforcement length, L). For the design of reinforced retaining walls, AASHTO (2014) and Berg et al. (2009) require the minimum length of the reinforcement should not be less than seventy percent of the wall height ($L_{min} = 0.7H$).

Roadways and other engineering structures are sometimes constructed in rugged, mountainous terrain, or adjacent to bedrocks. Also widening of roads can happen adjacent to existing stabilized faces, bedrock formations, or stabilized retaining structures (e.g. soil nail walls) at a close distance. As a result, there is a confined space for backfill of a wall. this type of retaining wall is often referred to as a narrow or limited fill space wall (Greco 2013; Yang et al. 2011; Fan and Fang 2010; Kniss et al. 2007; Leshchinsky et al. 2004; Take and Valsangkar 2001).

1.2 Problem Statement

Since the confined fill space limits full mobilization of lateral earth pressures behind the wall, the lateral earth pressure distributions in limited space retaining walls are different from those with sufficient fill space and may not be predicted accurately using the Rankine and Coulomb methods (Greco 2013; Yang et al. 2011; Yang et al. 2011; Han and Leshchinsky 2010; Fan and Fang 2010; Lee et al. 2010; Kniss et al. 2007; Morrison et al. 2006; Leshchinsky et al. 2004; Take and Valsangkar 2001). In other words, the mechanics of limited space retaining walls are different

from traditional retaining walls; therefore, the earth pressures in limited space retaining walls are different from theoretical earth pressures.

Researchers (Woodruff 200; Han and Leshchinsky 2010; Lee et al. 2010; and Yang et al. 2011) pointed out that the critical failure plane within a limited space GRR wall is not as linear as the Rankine failure plane. Woodruff (2003) observed that the critical failure plane was bilinear for low (L/H) ratio walls. Han and Leshchinsky (2010), Lee et al. (2010), and Yang et al. (2011) showed from their analytical studies that for short reinforcement length the critical failure plane was bilinear, and partially passed through the reinforced fill and partially occurred along the interface between the reinforced fill and the stable retained medium. Yang et al. (2011) also pointed out that the Rankine theory overestimated the inclination angle of the critical failure plane.

In addition, due to limited fill space, reinforcement may not have sufficient anchorage length in the fill. Morrison et al. (2006) reported that soil arching existed close to the base of the limited fill space MSE wall at the shored interface. It indicates that design calculations may overestimate pullout resistance for narrowed MSE walls if the arching effect was neglected. Since the maximum tensile strength of the reinforcement may rely on the anchorage of the reinforcement at the rear, Leshchinsky et al. (2004) and Lawson and Yee (2005) provided some practical suggestions to develop the tensile strength of the reinforcement for limited fill space walls. Their suggestions were: (1) to anchor the rear end of the reinforcement by connecting the reinforcement to anchors or nails fixed into a rigid zone beyond and (2) to wrap the reinforcement around the back of the reinforced fill (i.e., hook the reinforcement to a required length). These suggestions have been investigated in this study.

Another important behavior of GRR walls is lateral wall displacement. Chew et al. (1998) observed a 50 percent increase in the wall displacement because of shortening the reinforcement

length from 0.7H to 0.5H. However, Ling and Leshchinsky (2003) indicated that based on the maximum displacement and tensile load mobilized in the reinforcement layers, a wall with a reinforcement length equal to 0.5H provided the satisfactory performance as the wall with a reinforcement length equal to 0.7H. Since wall facing displacement of GRR walls is an important factor in the design of the walls, the evaluation of the wall displacement for limited fill space GRR walls is part of the current study.

1.3 Research Objectives

The objectives of this study are to investigate the behavior of GRR walls with limited fill space and examine the effects of backfill and reinforced fill width, reinforcement configurations, and footing offset distance on the performance of GRR walls under a static footing loading condition.

1.4 Research Tasks

In this study, the following tasks has been completed:

I. reviewed the published research on the geosynthetic-reinforced retaining walls with full and limited fill space;

II. performed analyses to investigate the scale effect of the reduced test models;

III. designed and conducted laboratory model tests on geosynthetic-reinforced retaining walls to investigate the behavior of GRR walls with full and limited fill space under static footing loading;

IV. performed numerical analyses using the finite difference method-based software to simulate the GRR model tests, and

V. Performed parametric study to analyze the performance of GRR walls with limited fill space subjected to static footing loading

1.5 Dissertation organization

This dissertation consists of eight chapters. Following this chapter, a literature review of previous studies on limited fill space walls is described in Chapter Two. Chapter Three presents scale effect analyses. The material properties (soil, geogrid, and modular block facing), layout of model tests, test apparatus, and test instrumentation and measurements are described in Chapter Four. Chapter Five describes the experimental test results and discussion. Chapter Six presents the numerical simulation of the laboratory model tests. A parametric study to investigate the influence factors on the performance of the GRR wall with limited fill space is presented in Chapter Seven. Chapter Eight presents conclusions and recommendations.

Chapter 2 Literature Review

2.1 Introduction

Geosynthetic-reinforced retaining (GRR) walls, which are one type of retaining walls, consist of reinforced fill, facing elements, and retained soil and have been widely used for highways, bridge abutments and service roads throughout the world. This chapter presents a review of previous studies on basic concepts, design methods, and behavior of geosynthetic reinforced retaining walls with an emphasis on the walls with limited fill space.

2.2 Mechanics and design methods of reinforced retaining walls

Various methods (e.g., coherent gravity method, simplified method, tieback wedge method, K-stiffness method, etc..) have been proposed for design of reinforced soil retaining walls (Allen et al. (2001); Elias et al. (2001); Bathurst et al. (2008); Anderson et al (2010); and Allen et al. (2014a and 2014b)). Three major associations, the American Association of State Highway and Transportation Officials (AASHTO) (2014), the Federal Highway Administration (FHWA) (2009), and the National Concrete Masonry Association (NCMA) (2009), considered some of these methods in their guidelines. In this section, the concept of reinforced soil and the design methods of reinforced retaining walls available in the literature are briefly explained.

2.2.1 Basic mechanics of reinforced soil

McKittrick (1978) explained the concept of reinforced soil in a simple mechanics as shown in Figure 2.1. Figure 2.1(a) shows a granular soil sample subjected to an axial load, which induces lateral expansion of the sample. McKittrick (1978) stated that due to the dilation of the

sample, its lateral strain is larger than one-half of the vertical strain. When horizontal elements are included in the soil (Figure 2.1(b)), the friction between the soil and the reinforcement elements prevents lateral soil deformation. In this case, the restraining force provided by the reinforcement is equal to the thrust force due to the at-rest earth pressure. This scenario is true only when the reinforcement is inextensible (i.e. the deformation of the reinforcement at failure is much smaller than the deformation of the soil).

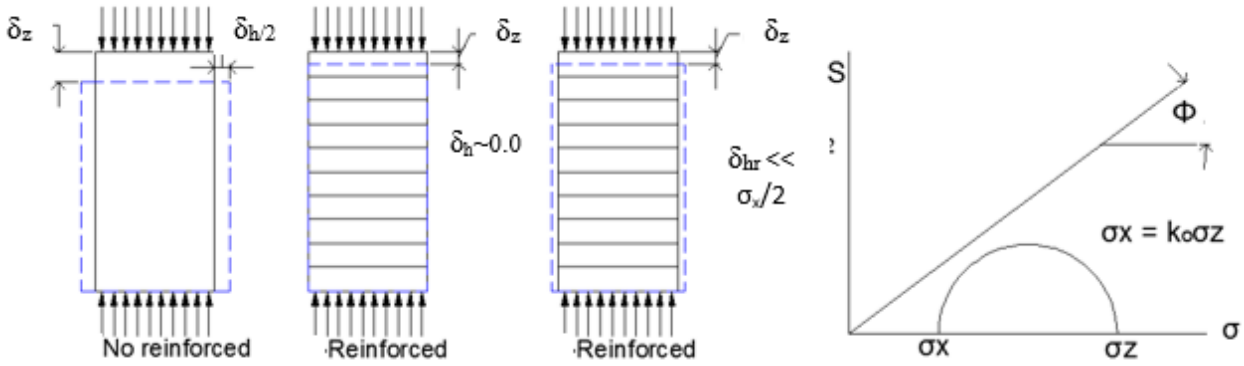

Figure 2.1 Basic mechanics of reinforced soil (after McKittrick, 1978)

However, when extensible reinforcement (i.e. the deformation of the reinforcement at failure is comparable to or even larger than the deformation of the soil), for example, when the geosynthetic is used, the sample likely has the deformation (δ_{hr}) (Figure 2(c)). However, the deformation of the sample with geosynthetic reinforcement is much smaller than that of the unreinforced sample because the reinforcement elements provide equivalent lateral confining stresses so that the lateral deformation of the sample is reduced and its internal stability for the system is maintained.

2.2.2 Stress transfer mechanism

Stability of reinforced soil depends on the mechanism of load transfer between the soil and the reinforcement, which is affected by the interface properties between the soil and the reinforcement, including frictional and passive resistance as shown in Figure 2.2. For sheet type reinforcement, such as geosynthetic, friction is the dominant mechanism, while for the reinforcement having a large number of transverse elements, such as grids and wire meshes, the dominant mechanism is passive resistance.

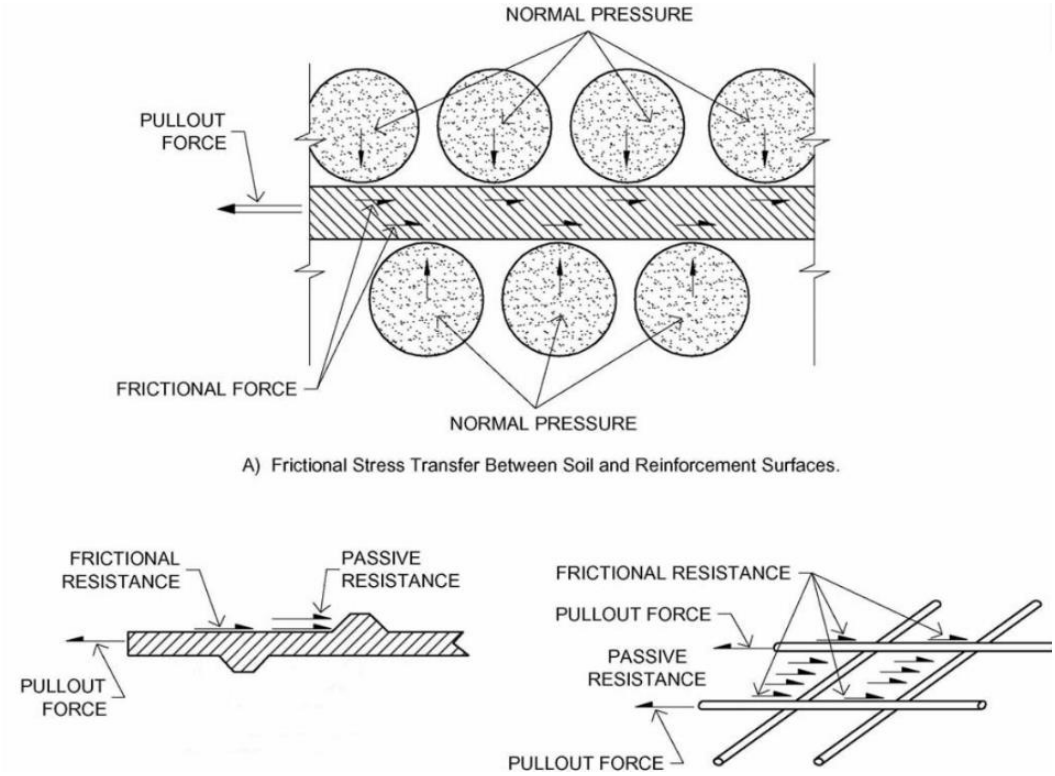

Figure 2.2 Soil-Reinforcement Stress Transfer Mechanism: (a) Friction and (b) Passive Resistance (FHWA 2002)

2.2.3 Design criteria

Design of reinforced retaining walls including GRR walls requires checking both external and internal stability. For external stability analysis, reinforced fill is treated as a rigid block and the analytical methods for gravity walls can be used. Figure 2.3 shows the three possible external failure modes that occur in the reinforced retaining walls. Deep-seated failure, also referred to as global failure, may occur in the foundation. Sliding may happen if the horizontal force behind the rigid block exceeds the factored shear resistance at the interface between the soil and the foundation. Overturning may occur if the driving moment due to the horizontal forces behind the rigid block exceeds the sum of the resisting moments in the wall system.

For internal stability, pullout capacity, reinforcement strength, and facing connection strength should be checked. Figure 2.4 shows the possible internal failure mechanisms that occur in the reinforced retaining walls. Reinforcement pullout occurs when the tensile force in the reinforcement becomes larger than the pullout resistance of the reinforcement. However, reinforcement rupture occurs when the tensile force in the reinforcement exceeds the ultimate strength of the reinforcement. The factors affecting the behavior of the reinforced fill are strain compatibility, reinforcement properties and distribution, fill properties, interaction, foundation, and construction.

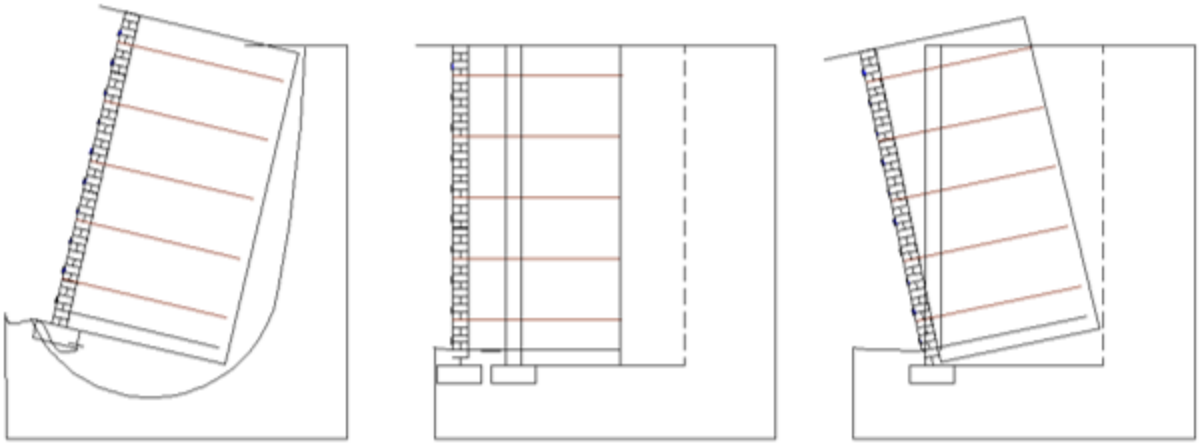

Figure 2.3 Possible external failure modes

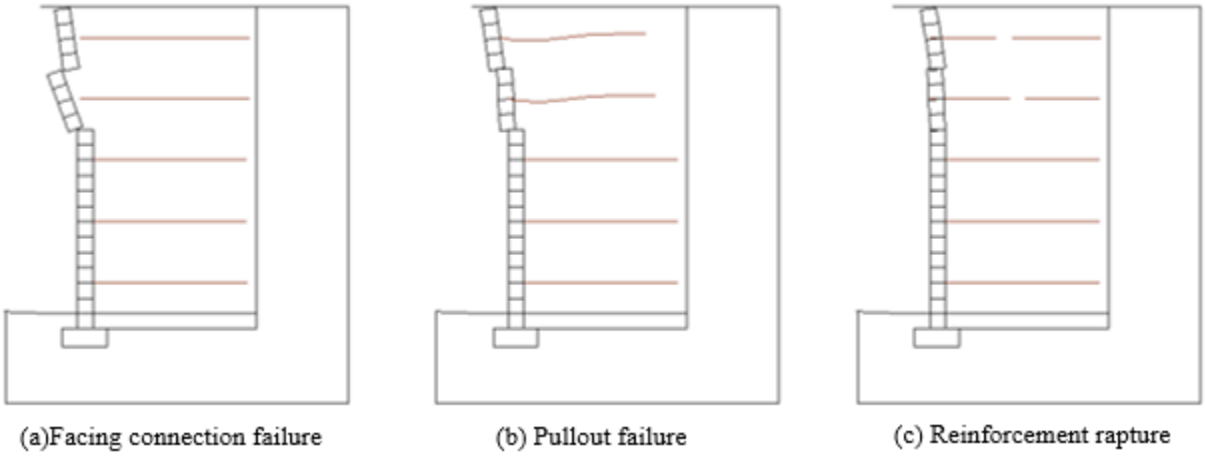

Figure 2.4 Possible internal failure modes

2.2.4 Design methods

The following section provides a brief description of the common design methods used in practice for conventional reinforced retaining walls.

Coherent gravity method

This method considers the reinforced fill as a gravity structure having a rectangular cross-section with a height, H and a reinforcement length, L (Figure 2.5). The coherent gravity method is recommended where the short-term axial tensile strain of reinforcement is less than or equal to one percent (i.e., inextensible reinforcement) (Anderson et al 2010). The Meyerhof bearing pressure distribution concept is used to estimate the vertical earth pressure at each reinforcement level (Anderson et al. 2012). In this method, the coefficient of lateral earth pressure varies from $k = k_o$ to $k = k_a$ in the 6 m of the wall height (Figure 2.5). This figure shows the reinforced fill mass is divided into two zone, the active and resistive zone by a bilinear plane that goes through the toe of the wall.

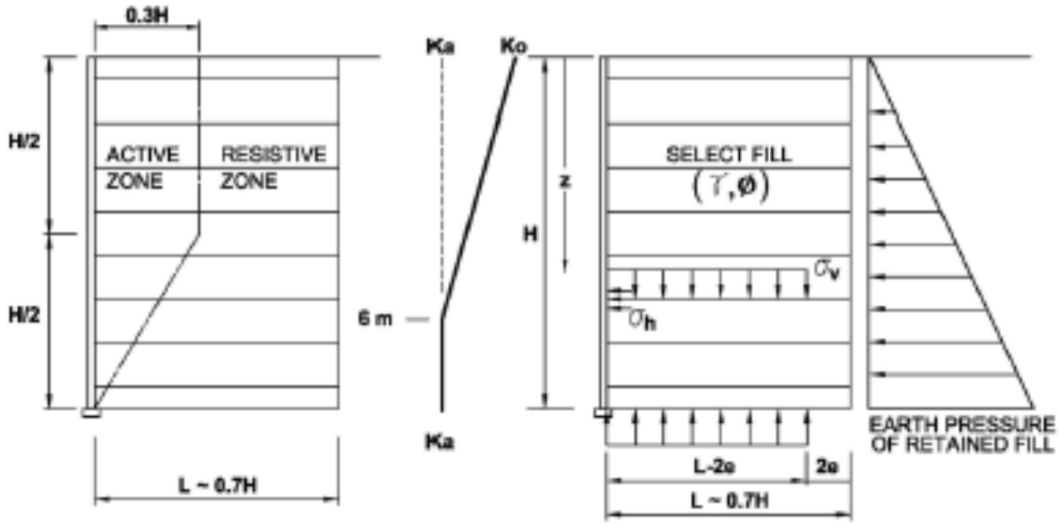

Figure 2.5 Characteristics of the coherent gravity method (Anderson et al. 2012)

Tieback wedge method

The tieback wedge method was developed as an extension of the trial wedge method (Anderson et al. 2012) and has been used for the extensible type reinforcement retaining walls

such as GRR walls. The tieback wedge method is recommended for walls where the short-term axial reinforcement tensile strain exceeds one percent (i.e., geosynthetic). Allen et al. (2001) adapted this method later for reinforced retaining walls with welded wire reinforcement. This method assumes that the active state of the lateral earth pressure is mobilized, and the Rankine or Coulomb failure plane is developed. Figure 2.6 illustrates the concept of the tieback wedge method. When the wall batter is less than 10 degrees, a failure plane that is inclined at an angle of $(45+\phi/2)$ to the horizontal and passes through the toe of the wall defines the active and resistive zone boundary. This method also assumes that the inclusion of the reinforcement does not change the Rankine failure plane, and hence the reinforcement strain allows the failure wedge to develop. In this method the reinforcement acts as a tieback and restrains the active wedge from failing.

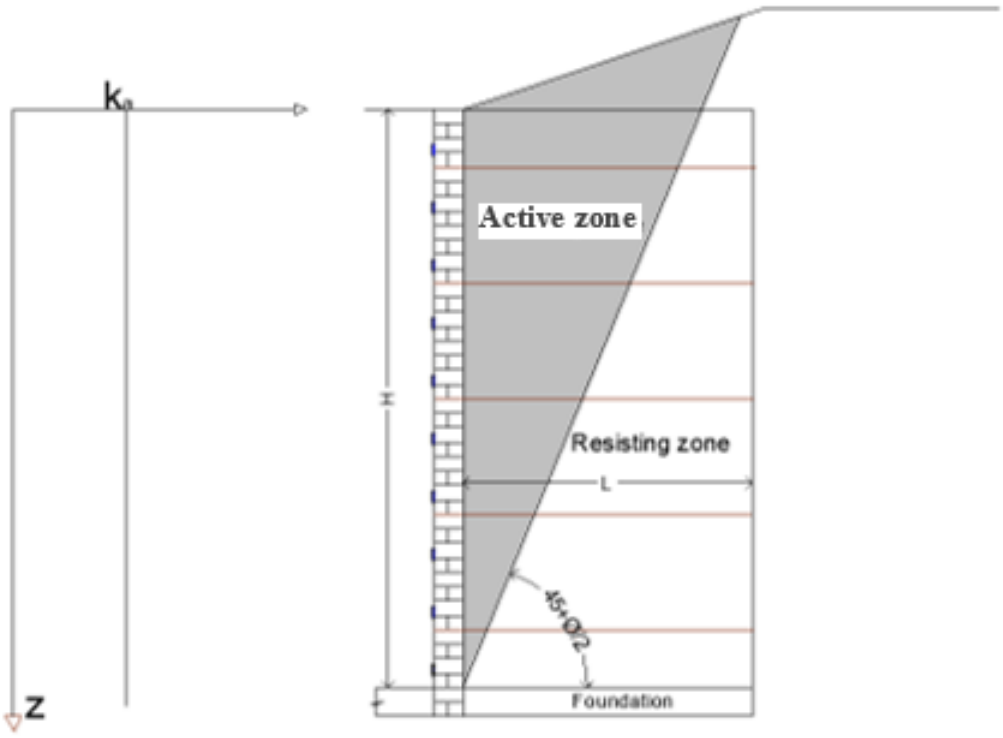

Figure 2.6 Tieback wedge method concept (after Anderson et al. 2012)

.

Simplified method

The simplified method is a modified version of the tieback wedge method, and it was developed to be a single design procedure for reinforced retaining walls with both extensible and inextensible types of reinforcement (Anderson et al 2012). This method uses the coherent gravity method's failure plane for retaining walls reinforced with inextensible reinforcement but the Rankine or Coulomb failure plane for retaining walls reinforced with extensible reinforcement. This method was adapted in the FHWA guideline (Elias et al., 2001).

2.3 Janssen's theory

In 1895 Janssen developed an equation to estimate the lateral pressure of corn on the side walls of a silo (Spirl 2006). Janssen developed his equation based on the results of the model tests that was performed to determine the pressure imposed by corn in a silo. The test results showed that the measured pressure on the bottom of the silo was lower than the weight of corn within the silo. Janssen (1985) assumed the lateral pressure was transmitted to the sidewalls and derived an equation to predict the lateral pressure on the sidewall. Janssen's theory can be applied to any granular material such as sand in geotechnical engineering.

In construction of reinforced retaining walls, soil is placed in layers which settles due to its self-weight and the load applied by additional soil layers above. Simultaneously, the wall provides a vertical shear force due to the friction that resists the settlement of soil. The vertical shear force reduces the soil overburden pressure, and hence reduces the lateral earth pressure. This phenomenon is known as the arching effect. Equation 2.1, referred to as the Janssen's equation, was derived based on Janssen's silo theory:

$$\sigma_h = \frac{\gamma B}{2tan\delta}(1 - e^{-2K\frac{Z}{B}tan\delta}) \quad \text{….. (2.1)}$$

where

γ = unit weight of backfill soil;

B= wall width;

Z= depth from top of wall;

H= wall height;

δ= friction angle between backfill soil and wall and between backfill soi and stable retained medium;

K = lateral earth pressure coefficient.

For the case with an non-deformable wall, K was defined by Jaky's empirical formula, i.e., 1-sin(φ'), where φ' is the angle of internal friction. The lateral earth pressure coefficient depends on the angle of internal friction. Because Janssen's theory was developed to estimate the lateral earth pressures with the boundary condition similar to that for the walls with limited fill space, this theoretical solution is useful when compared with the results of laboratory tests and numerical simulations.

2.4 Limited fill space retaining walls

AASHTO (2014) and FHWA (2009) recommend 0.7H (H is the wall height) but NCMA (2016) recommends (0.6H) as a minimum reinforcement length, L_{min} for the design of reinforced retaining walls. When roadways and other civil engineering structures are constructed in rugged, mountainous terrain, or adjacent to bedrock, or roads are widened adjacent to existing stabilized walls, it sometimes may be impractical to construct a wall with the required fill space width. In these cases, reinforced retaining walls have narrower fill space than the requirement in the design

guidelines. This type of walls is referred to as narrow walls or walls with limited fill space in the literature. In other words, a limited fill space geosynthetic reinforced retaining wall is defined as a GRR wall placed adjacent to bedrock, or an existing stable wall or slope that has an aspect ratio (L/H) less than that established in the current design guidelines. Figure 2.7 shows three cases where walls with limited fill space are required. Figure 2.7(a) shows a case where roadways are repaired and extended because of natural and environmental constraints in the mountain terrain. Figure 2.7(b) illustrates back-to-back GRR walls where the walls are constructed against each other and the space is limited by the distance between the walls. To meet increased traffic demand, widening of existing highways is sometimes needed but limited by the right of way. A possible solution is to build GRR walls adjacent to existing stabilized walls (Figure 2.7 (c)).

It is predictable that the mechanism of the limited fill space walls differs from that with satisfactory fill space. The differences may exist in the distribution of the lateral earth pressure, the failure surface, and the external failure. The following section briefly summarizes the previous studies conducted by researchers in terms of full-scale field, laboratory, analytical, and numerical studies. Most of these studies have focused on the mechanics of limited-space unyielding walls and provided insight into the effect of wall aspect ratio on the mechanics of the limited fill space walls.

(a) Roadway repair

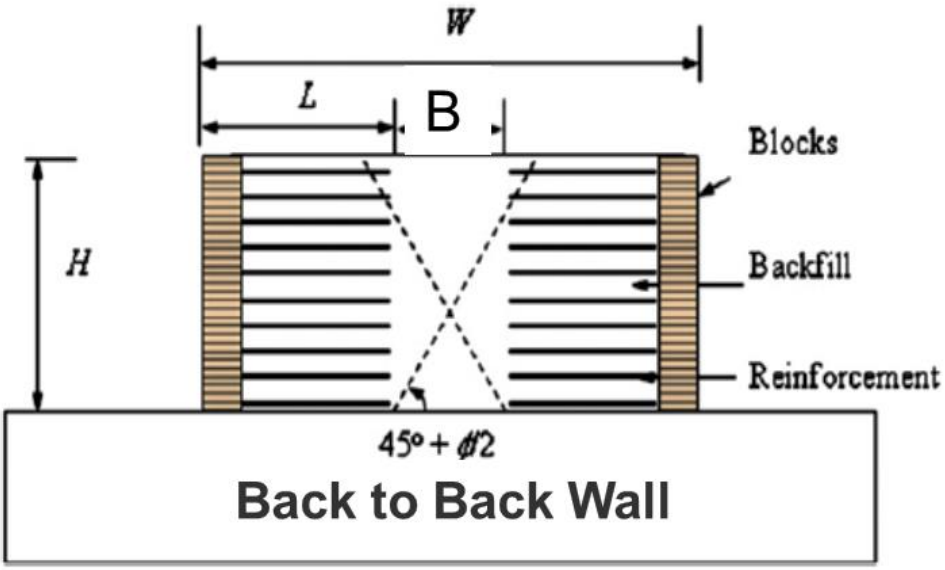

(b) Back-to-back walls (Han and Leshchinsky 2010)

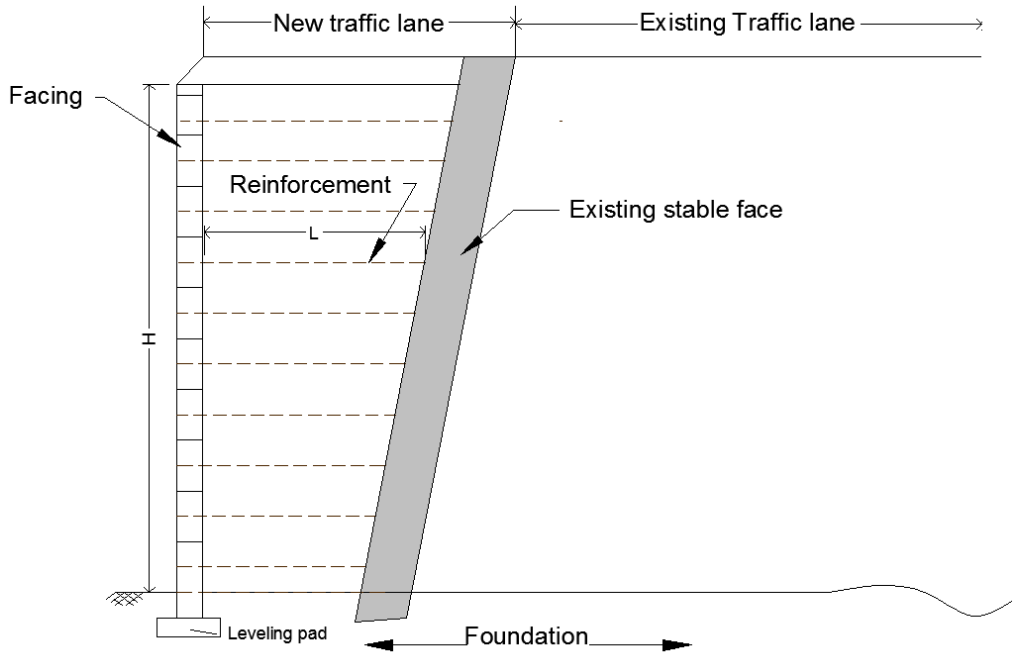

(c) Roadway widening (after Morrison et al, 2006)

Figure 2.7 Walls with limited fill space

2.4.1 Full-scale field test

Full-scale field test is an ideal method to understand the behavior of reinforced retaining walls; however, it is often too costly. According to the author's search, only one publication by Morrison et al. (2006) was identified on the full-scale field test on the walls with limited fill space in the literature and is briefly described below.

Morrison et al. (2006) conducted a full-scale field test on a shored MSE wall system at the FHWA Turner Fairbanks Highway Research Center (TFHRC) in McLean, Virginia. Shored wall is a retaining wall used to provide vertical or near-vertical support of an excavation. The test wall system consisted of an MSE wall with short reinforcement (0.25H – 0.39H) (H is the height of the wall). The field test included two walls, one connected to the shored wall and the other one unconnected. Figure 2.8 shows the connection detail for the connected wall system. The facing

batter of the MSE wall was 1H: 24V. Figure 2.9 presents the plan view of the full-scale Shored MSE wall while Figure 2.10 shows the wall cross section of the connected portion of the test wall. Loads were applied onto the test wall using two loaded footings with a dimension of 2.5 m by 1.0 m.

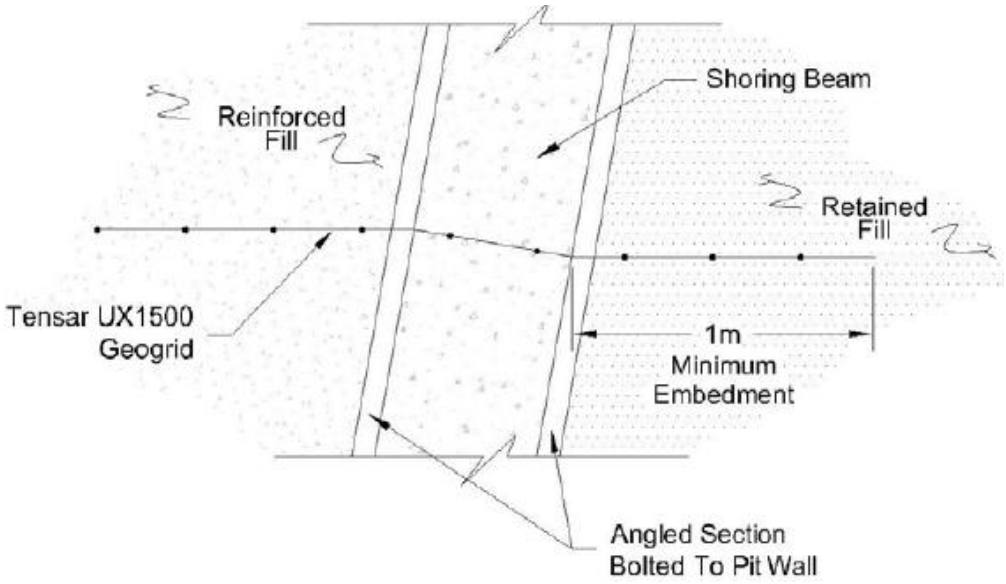

Figure 2.8 Connection detail for the connected wall system (Morrison et al. 2006)

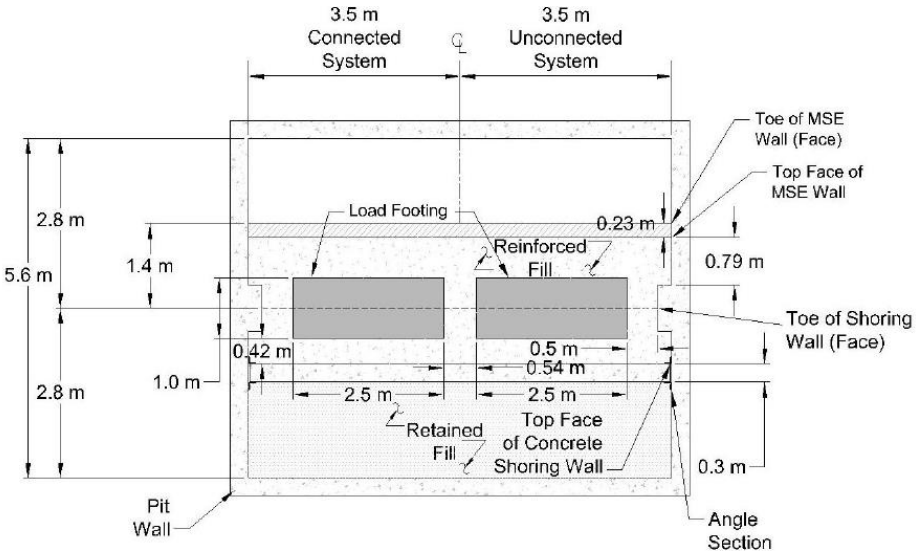

Figure 2.9 Plan view of the full-scale field test (Morrison et al. 2006)

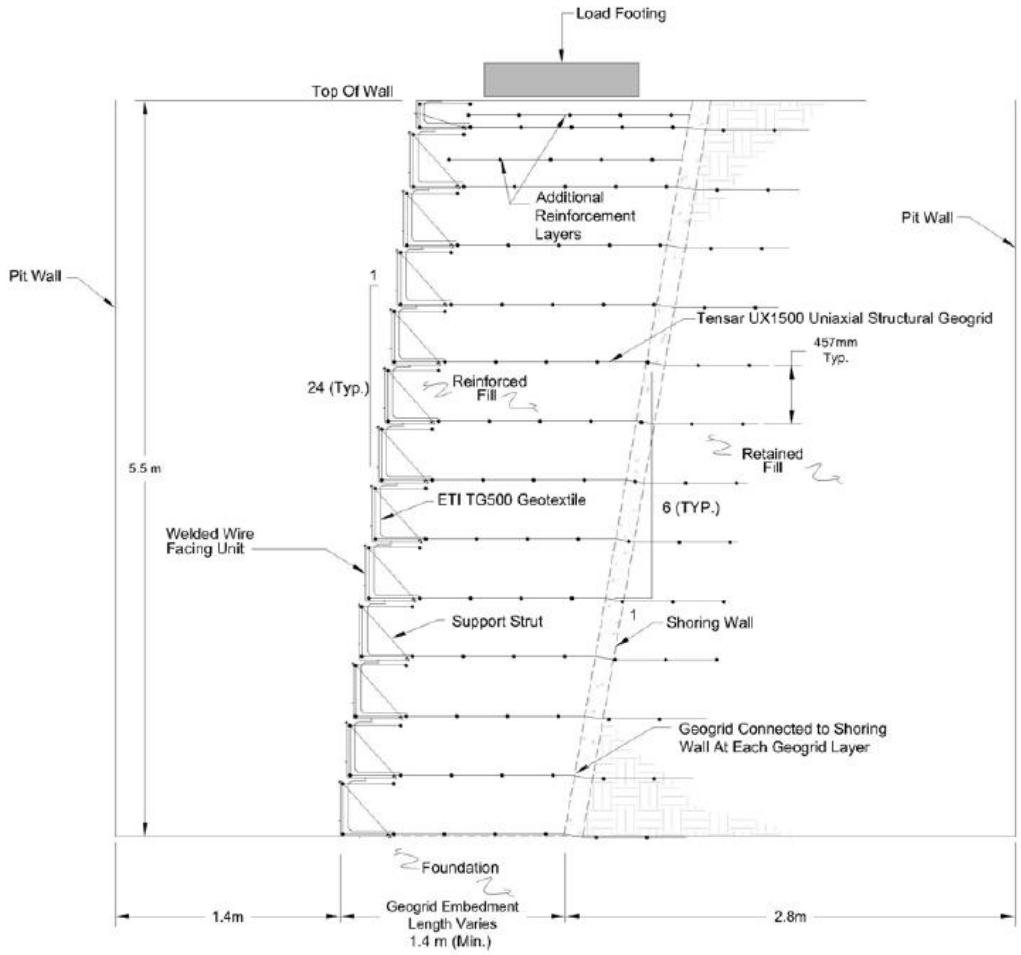

Figure 2.10 Full-scale field test wall cross section with the connected system (Morrison et al. 2006).

Morrison et al. (2006) observed that the field wall was stable under an applied pressure up to the maximum pressure of 356 kPa. The measured lateral earth pressure increased slightly with the increase of the footing load for both portions of the test wall as shown in Figure 2.11. Morrison et al. (2006) indicated that the measured lateral earth pressures were lower than the Rankine active earth pressures for both connected and unconnected walls, except for the uppermost pressure cells in the connected portion of the test wall. They also found that the measured vertical pressures well agreed with the estimated vertical pressure at zero load, but the Rankine method using 2:1 distribution concept underestimated the vertical earth pressure under a higher load.

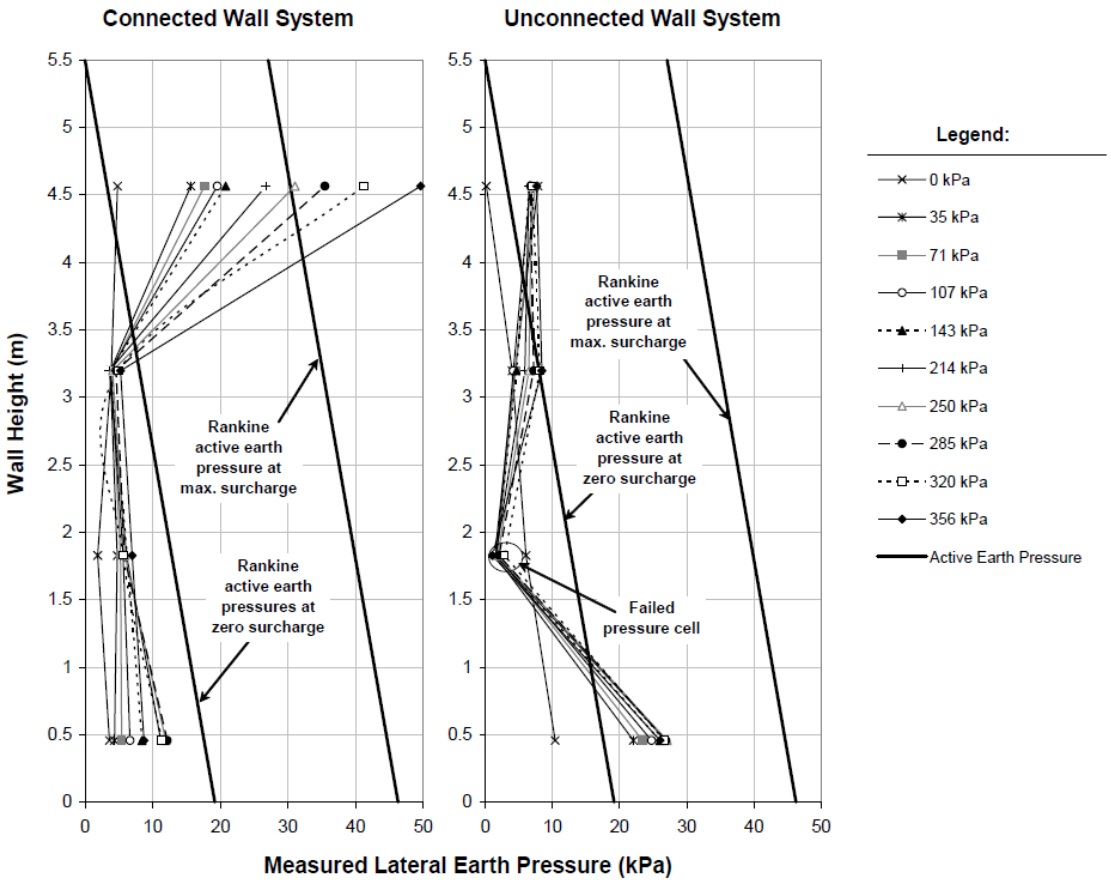

Figure 2.11 Earth pressure distributions for the full-scale field walls (Morrison et al. 2006)

2.4.2 Laboratory reduced-scale test

Laboratory reduced-scale model tests also have been conducted to investigate the limited fill space problem because model tests require less space and time and lower cost for construction and testing and can be run until failure. Several laboratory tests have been identified in the literature and are presented below.

Frydman and Keissar (1987)

Frydman and Keissar (1987) perfumed several centrifuge model tests to examine the earth pressure on non-deformable retaining walls near stable medium under both the at rest and active conditions. They constructed the models in an aluminum box (210 mm high x 100 mm wide x 327 mm long) and connected an aluminum plate (195 mm high x 100 mm wide x 20 mm thick) to the base of the box to simulate the retaining wall. A wooden block was used to simulate the stable medium. Frydman and Keissar (1987) coated the wooden block with the backfill soil so that the friction between the backfill material and the stable medium was essentially equal to the angle of internal friction of the backfill soil. The fill had density between 16.4 kN/m^3 at 70% relative density, the angle of internal friction (φ') equal to 36^o, and the angle of interface friction (δ) between the backfill material and the stable medium was 20^o - 25^o based on the direct shear tests.

They tested the models with various aspect ratios (L/H) ranging from 0.1 to 1.1 of the soil behind the wall. Figure 2.12 shows the results of the model tests. Frydman and Keissar (1987) compared their results with Janssen's equation, which was originally developed to estimate corn pressures at the bottom of a silo. Figure 13 shows a good agreement between the centrifuge test results and Janssen's equation. In addition, they stated that Janssen's equation could estimate the lateral earth pressures on the retaining walls under the at-rest conditions using K_o= 1-sin (φ').

Since Janssen's equation requires identical interface friction angle (δ) between the rock face and the material and between the material and the wall face, Frydman and Keissar (1987) suggested using the average interface friction angle. They concluded that the lateral earth pressure coefficient decreased with depth from the theoretical at-rest value near the top of the wall and attributed this phenomenon to a soil arching effect.

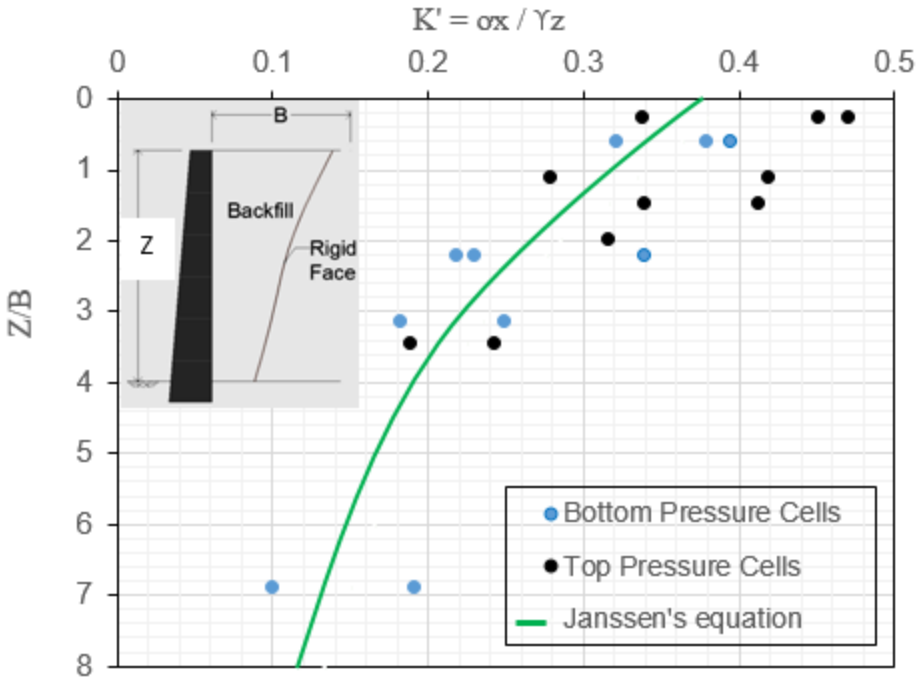

Figure 2.12 Lateral earth pressure coefficient versus Z/B (Frydman and Keissar 1987)

Take and Valsangkar (2001)

Take and Valsangkar (2001) performed a series of centrifuge tests to study the earth pressure on unyielding retaining walls with narrow backfill to evaluate Janssen's equation. Figures 2.13 and 2.14 show the model box and the wall configuration tested by Take and Valsangkar (2001**).** Since Janssen's equation depends on the wall aspect ratio, the interface friction angle, and the coefficient of earth pressure, this study considered these factors in the model tests and analyses. The wall aspect ratios ranging from 0.10 to 0.70 were investigated, and all the tests were conducted at an acceleration of 35.7g to simulate a 5 m high prototype wall. Their test results agreed with Frydman's finding that the measured earth pressure decreased from the theoretical at-rest value with an increase of the depth below the surface (Figure 2.15). In addition, Figure 2.16 shows that the measured lateral earth pressures acting on the unyielding model retaining walls are in good agreement with the Janssen arching theory (Spirl 2006)).

Take and Valsangkar (2001) indicated that the wall aspect ratio had a significant effect on the reduction of the earth pressure with narrow backfill. In addition, using an identical interface friction angle between the backfill soil and the stable wall and between the backfill soil and the wall, Janssen's equation resulted in fair agreement with the experimental results as shown in Figures 2.15 and 2.16. Although Janssen's equation describes the arching effect on the lateral earth pressure by a simple equation, the choices for the parameter K and the mobilized boundary friction angle during the transition from the at-rest condition to active condition require considerable engineering judgement (Take and Valsangkar 2001).

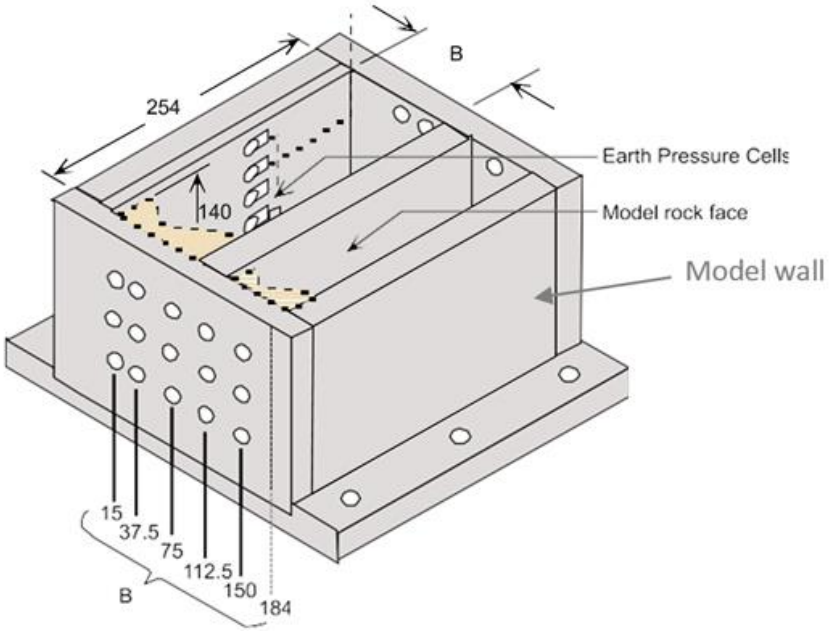

Figure 2.13 Model box for centrifuge tests (Take and Valsangkar 2001)

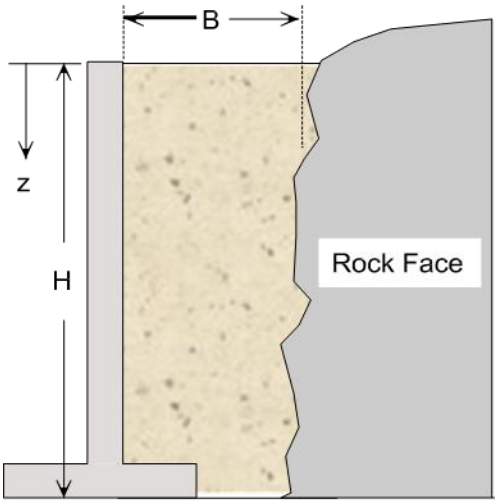

Figure 2.14 Geometry of the model tested by Take and Valsangkar (2001)

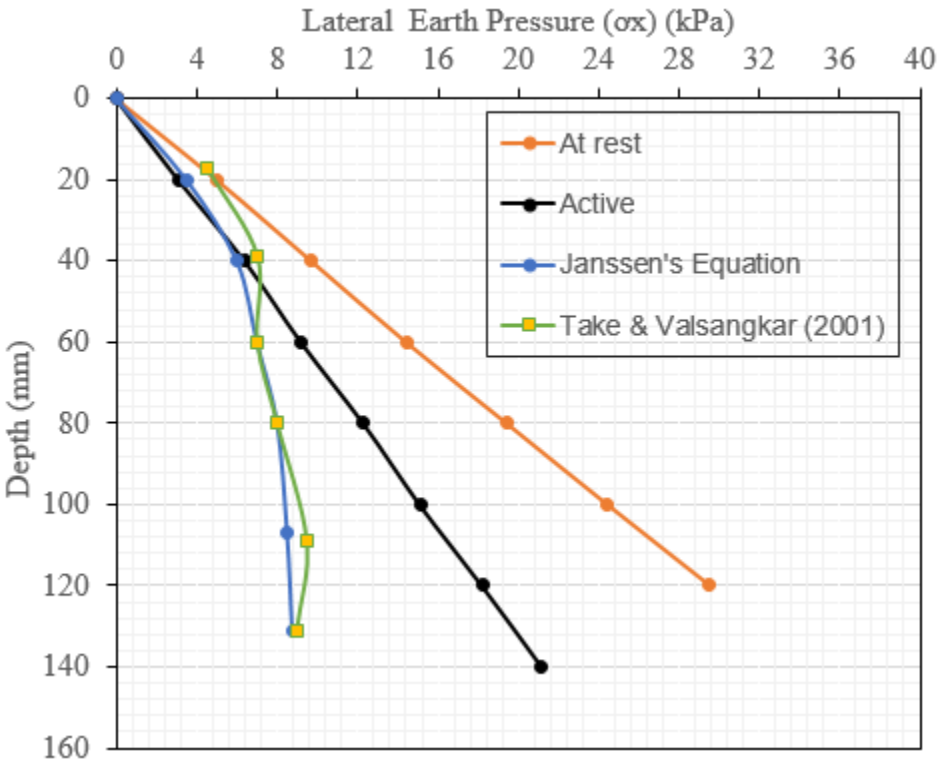

Figure 2.15 Comparison of lateral earth pressure coefficient verse (Z/B)

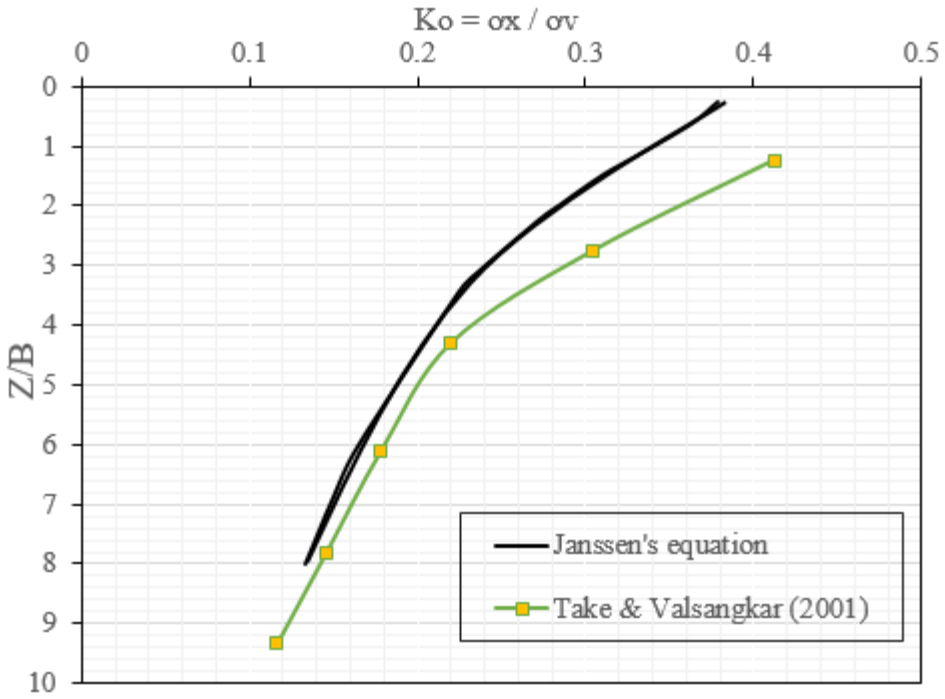

Figure 2.16 Lateral earth pressure coefficient versus Z/B

Woodruff (2003)

Woodruff (2003) performed centrifuge tests on 24 reinforced soil walls adjacent to a stable face. Figure 2.17 shows the test model setup. The wall models had L/H varying from 0.17 to 0.9, and all the reduced-scale walls were 230 mm tall with a wall facing batter of 11 (vertical) to 1 (horizontal). The reinforcement was folded backward at the rear to form a wrapped-around facing and overlapped by a secondary layer of 50 mm long in the centrifuge model. The model walls were placed in front of an aluminum box that simulates the stable face (rock face). All models were subjected to centrifugal acceleration until failure occurred. The type and location of failure surfaces were observed during the test.

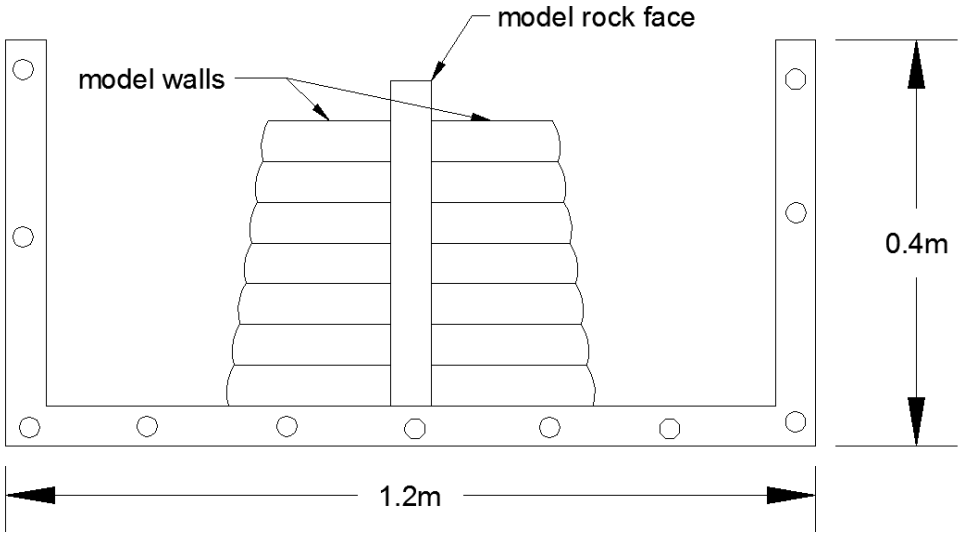

Figure 2.17 Test model setup (Woodruff, 2003)

Woodruff (2003) reported that the wall failed externally at L/H < 0.25 and internally at L/H >0.25. He observed that for L/H >0.6 the critical failure planes were linear, and the failure surfaces passed through the entire reinforced fill zone. However, the critical failure surfaces were bilinear for L/H <0.25. In addition, the inclination angle of the failure plane was less than that predicted by the Rankine failure plane (Figure 2.18).

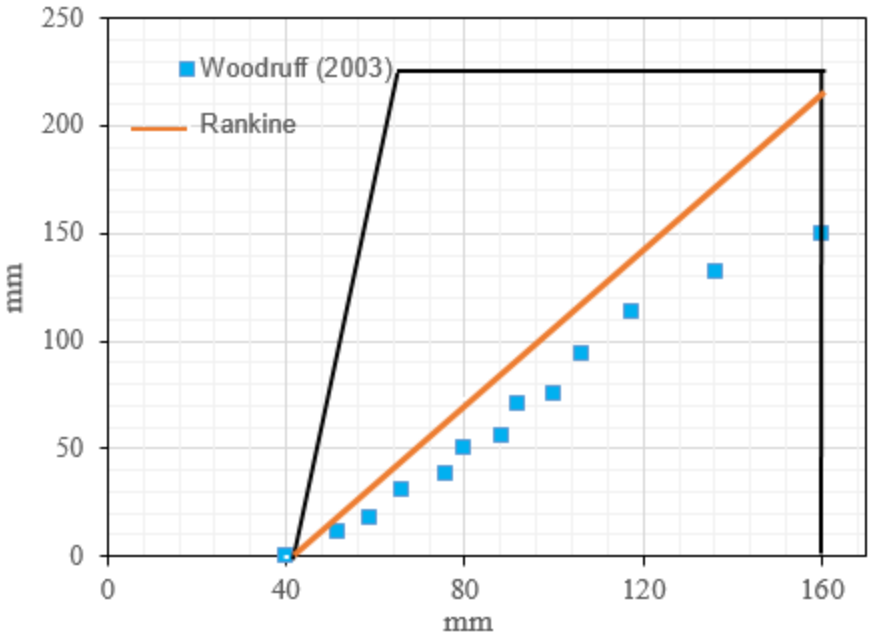

Figure 2.18 Cross-section of centrifuge model geometry showing a bilinear failure surface (After Woodruff 2003)

Morrison et al. (2006)

Morrison et al. (2006) also conducted 24 centrifuge model tests, a numerical study, and a full-scale field test. They investigated the wall aspect ratio (L/H), the reinforcement strength, the shoring interface, the reinforcement configuration at the shoring interface, and the shoring inclination. Morrison et al. (2006) indicated that the reduction of the reinforcement length to as little as 0.25H provided sufficient wall stability, even under a considerably high surcharge load. They did not observe the benefit of the rough shoring interface as compared with the smooth interface. In addition, they found that the smooth interface was more effective than the rough interface. Morrison et al. (2006) also observed that wrapping of the reinforcement around the back of the reinforced fill was effective and resulted in the reduction of the lateral earth pressure. They

observed that the reduction of the vertical spacing of the reinforcement also increased the stability of the wall.

Morrison et al. (2006) compared the Rankine active failure plane with the trend line of the tear failure locations on the reinforcement during centrifuge testing (Figure 2.19).

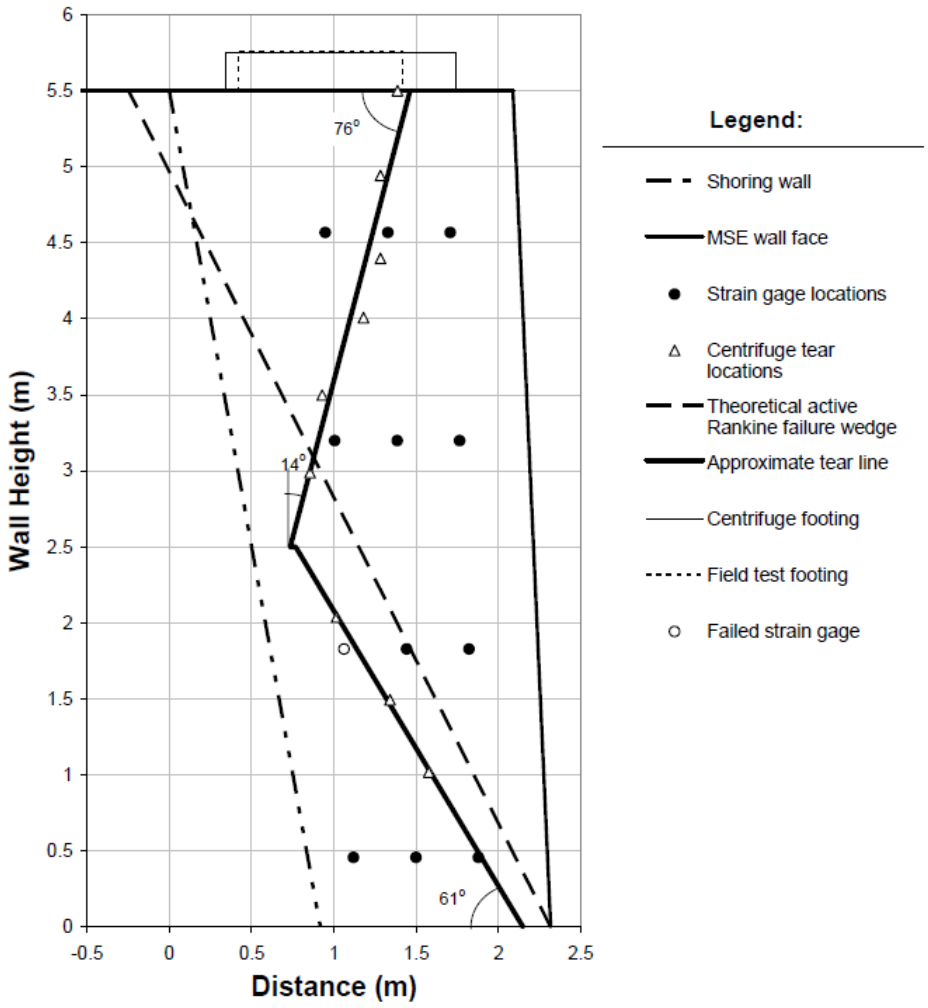

Figure 2.19 Comparison of the Rankine active failure plan with the actual failure line in the test (Morrison et al. 2006)

They found that the lower portion of the centrifuge test wall showed a failure plane, which was approximately parallel to the Rankine active failure plane; however, a much steeper failure plane than the Rankine active failure plane happened in the upper portion of the wall.

2.4.3 Limit equilibrium studies

Limit equilibrium methods have been commonly used all over the world to design many geotechnical engineering structures including geosynthetic reinforced retaining walls. The purpose of a limit equilibrium analysis is to calculate the maximum force allowed for equilibrium as compared with the shear strength of the soil. Several researchers have conducted limit equilibrium analyses for GRR walls with limited fill space and their findings are brief described below.

Leshchinsky et al. (2004)

Leshchinsky et al. (2004) conducted a limit equilibrium study on segmental GRR walls to modify the existing analysis procedures by considering limited fill space. Their limit equilibrium results were compared with those from the continuum mechanics-based method. Figure 2.20 illustrates the geometry of the model used by Leshchinsky et al. (2004) in their analysis. Their analysis models used the soil unit weight of 20 kN/m^3 and the internal friction angle between 20^o to 45^o. To eliminate the effect of global stability, they assumed the foundation as bedrock.

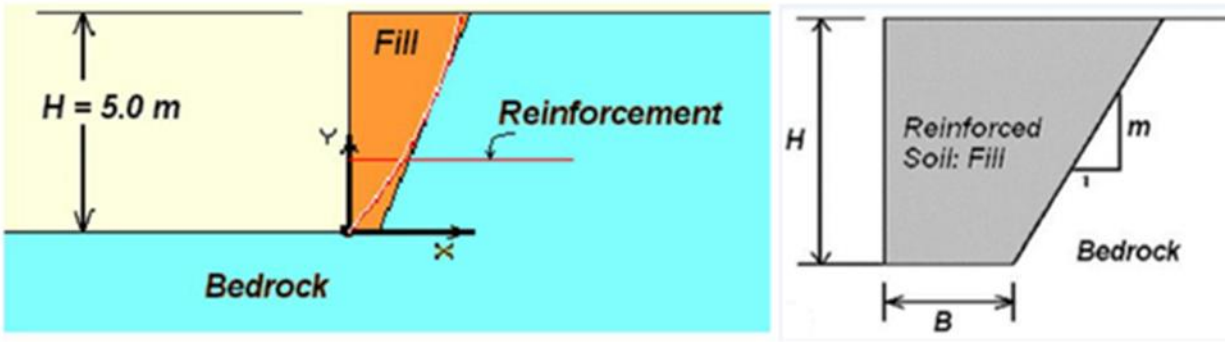

Figure 2.20 Geometry of the model used by Leshchinsky et al. (2004)

A single layer of reinforcement was simulated in the analysis. The reinforcement was placed at one-third of the height of the wall and considered as equivalent to multiple reinforcement layers at different heights.

To maintain the horizontal equilibrium, it was assumed that the equivalent reinforcement tensile resistance (T) calculated at a limit equilibrium state would be equal to the resultant force (P) caused by the weight of the soil. Based on this assumption and using the lateral earth pressure formula for conventional walls (Equation 2.2), Leshchinsky et al. (2004) developed a design chart (Figure 2.3) to estimate the coefficient of lateral earth pressure for different wall aspect ratio:

$$P = 0.5K_a'\gamma H^2 \quad \text{---------- (2.2)}$$

where

P is the resultant force of the lateral earth pressure in the limited space wall;

K_a' is the coefficient of lateral earth pressure considering the limited fill space;

γ is the unit weight of soil, and

H is the height of the wall.

Based on the equilibrium T= P:

$$K_a' = 2T/\gamma H^2 \text{---------- (2.3)}$$

Leshchinsky et al. (2004) stated that the design chart can be used for design of limited space GRR walls by selecting the geometrical parameters of the limited space width B and the slope of the stable retained medium m. Based on B, H, and m, the ratio K_a'/K_a from the chart can be found. Based on $K_a = \tan^2(45-\Phi/2)$, K_a' can be calculated and substituted for K_a in the design methods for GRR walls to determine the required strength of the reinforcement. However, this design chart is not applicable for some realistic cases (i.e., walls with complex boundary conditions). This chart indicated the decrease of the lateral earth pressure with the decrease of the wall aspect ratio (L/H).

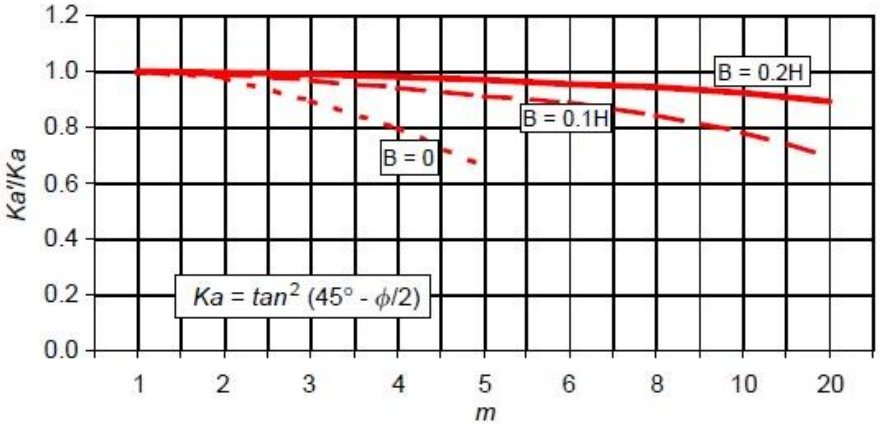

Figure 2.21 Design chart for limited-space GRR walls (Leshchinsky et al. 2004)

In addition, Leshchinsky et al. (2004) stated that because of the limited fill space there might not be sufficient anchorage length for the reinforcement and it must be anchored at its rear end. They also suggested some practical techniques to address this issue: (1) installing anchors into the bedrock and then connect the rear of the geosynthetics to these anchors or ties (e.g., use

horizontal U-shaped anchors; insert reinforcing geosynthetic strips into the loop and back fold); (2) using a common approach of placing fill over rock interface with a bench.

Lawson and Yee (2005)

Lawson and Yee (2005) conducted a limit equilibrium study using wedge stability analysis for the reinforced soil walls with limited fill space to estimate the coefficient of lateral earth pressure. Their study showed that the critical wedge angle converged to the Rankine failure angle at a large L_t/H ratio while it was above the Rankine failure plane at a small L_t/H ratio, where L_t is the width of the wall at the top and H is the height of the wall.

In their study, Lawson and Yee (2005) investigated the effect of the geometries of the stable face and the wall on the magnitude of lateral earth pressure and the location of critical failure surface. In addition, they presented a case study of a reinforced segmental block retaining wall with limited fill space, in which the reinforcement was connected to anchors.

Lawson and Yee (2005) considered planar and bilinear slip surfaces as shown in Figure 2.22(a) and calculated the values of K for various wall L_t/H ratios with a soil internal friction angle $\varphi' = 30°$. Lawson and Yee (2005) showed that when the wall aspect ratio (L_t/H) was greater than 0.5, the lateral earth pressure was equal to the Rankine active earth pressure as shown in Figure 22(b). However, for the walls with an aspect ratio (L_t/H) less than 0.5, the lateral earth pressure decreased with the decrease of L_t/H.

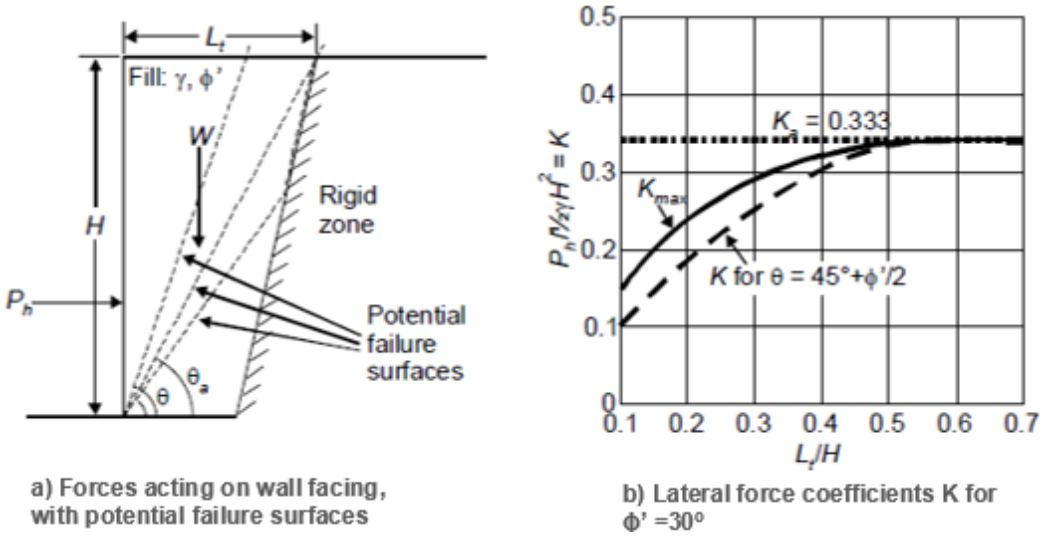

Figure 2.22 Lateral force acting on the wall face, the wedge failure plane angle, and the lateral earth pressure coefficient (Lawson and Yee 2005).

Lawson and Yee (2005) also estimated the maximum lateral earth pressure coefficient (K_{max}) for fills with various friction angles, ϕ along with various L_t/H ratios (Figure 2.23). They found that the coefficient of lateral earth pressure acting on the face of the wall is governed by the friction angle of the fill and the wall geometry.

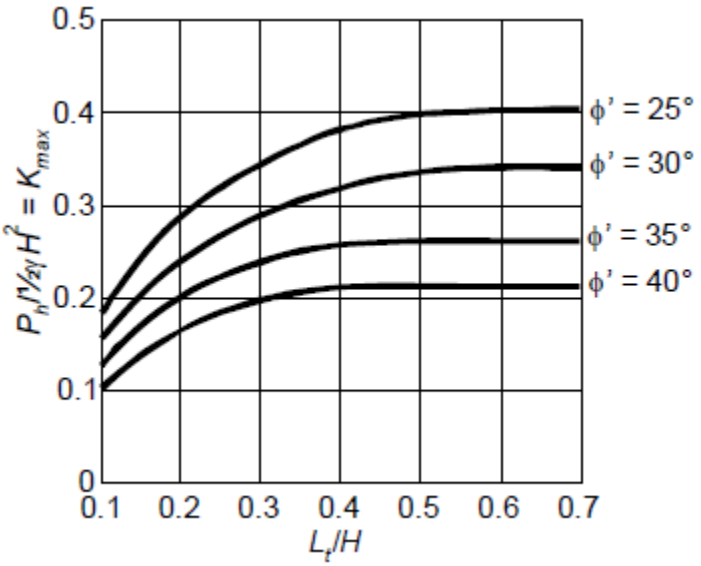

Figure 2.23 Maximum earth pressure coefficients Kmax for ϕ'= 25°, 30°, 35° and 40o (Lawson and Yee 2005)

In addition, Lawson and Yee (2005) proposed a simplified method to calculate the lateral stresses on the wall. Figure 2.24 shows the detail of this method.

Lawson and Yee (2005) also indicated that the reinforcement should have sufficient strength and proper spacing to support the lateral earth pressure acting on the wall face. Lawson and Yee (2005) suggested that to provide sufficient anchorage for the reinforcement, the reinforcement needs to be either connected to anchors or nails installed in the stable retaining medium or wrapped around the back of the reinforced fill.

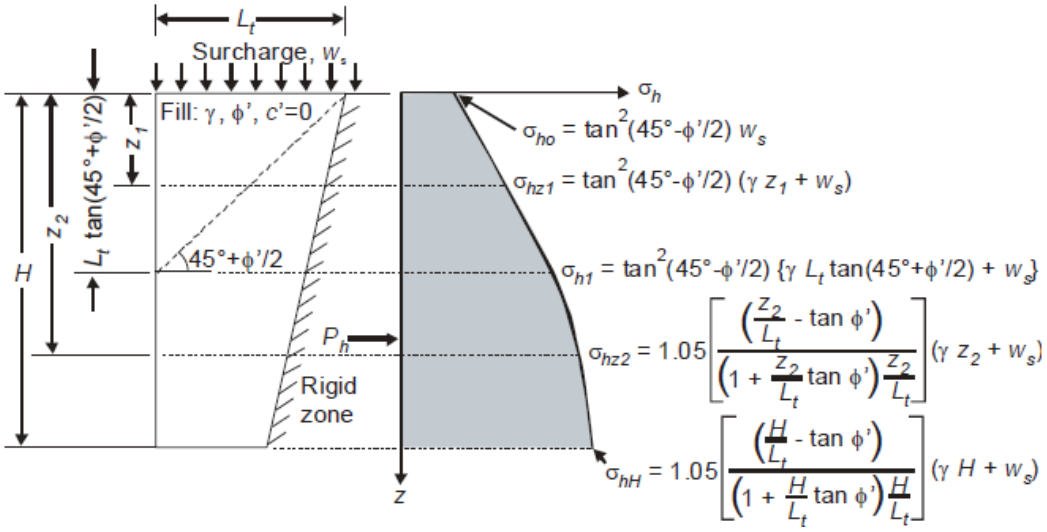

Figure 2.24 Lateral earth pressure distribution acting on the rear of the wall facing due to fill self-weight and surcharge (Lawson and Yee 2005).

Bilgin (2009)

Bilgin (2009) performed an analytical study to investigate the governing failure modes in determining the required minimum reinforcement length. He investigated the effect of several parameters, such as wall height, surcharge, reinforcement vertical spacing, reinforced fill width, fill unit weight, and fill friction angle, on the required reinforcement length. Bilgin (2009)

concluded that both the external and internal failure modes govern the required minimum reinforcement length, and the most common failure mode was pullout. In addition, it is possible to use reinforcement length shorter than 0.7H; however, special attention should be given to wall deformations if short reinforcement is used.

Yang et al. (2011)

Yang et al. (2011) investigated the critical failure plane in limited space GRR walls using the limited equilibrium method. They used the limit equilibrium program "UTEXAS4" developed at the University of Texas at Austin to conduct the analysis. They modeled the centrifuge tests conducted by Woodruff (2003) with B/H = 0.4, 0.6 and 0.7 using the "UTEXAS4" program.

Yang et al. (2011) indicated that for GRR walls with a low wall aspect ratio (L/H) the critical failure plane was not linear but bilinear. Figure 2.25 shows that for both the centrifuge and limit equilibrium results the critical failure surfaces went partially through the reinforced fill and partially along the interface between the reinforced fill and the stable face. They reported that the results from the limit equilibrium method well matched with the centrifuge test results and the inclination angle of the failure plane decreased with a decrease in the wall aspect ratio (L/H). Yang et al. (2011) also observed that the reinforcement type and the surcharge condition changed the location of the critical failure plane.

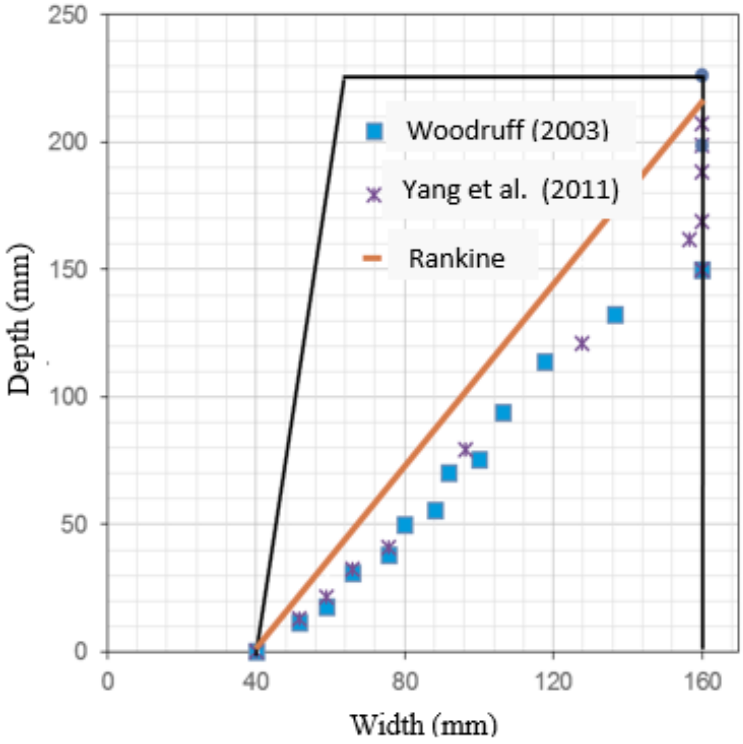

Figure 2.25 Critical failure surfaces (Yang et al. 2011)

Greco (2013)

Greco (2013) presented an analytical solution using the limit equilibrium method to evaluate the active wedge applied in the gravity retaining wall with limited fill space. As shown in Figure 2.26, he assumed three different failure mechanisms between the wall face and the stable face to investigate the shape of active wedge failure in limited fill space rigid walls. Greco (2013) reported that the coefficient of lateral earth pressure was not only less than that for Coulomb's theory but also less than that based on Frydman and Keissar (1987)'s finding. Figure 2.27 shows the distribution of the estimated lateral earth pressure coefficient against Z/B. Greco (2013) also found that the interface friction angle between the backfill and the boundaries had a significant effect on the lateral earth pressure coefficient as shown in Figure 2.28.

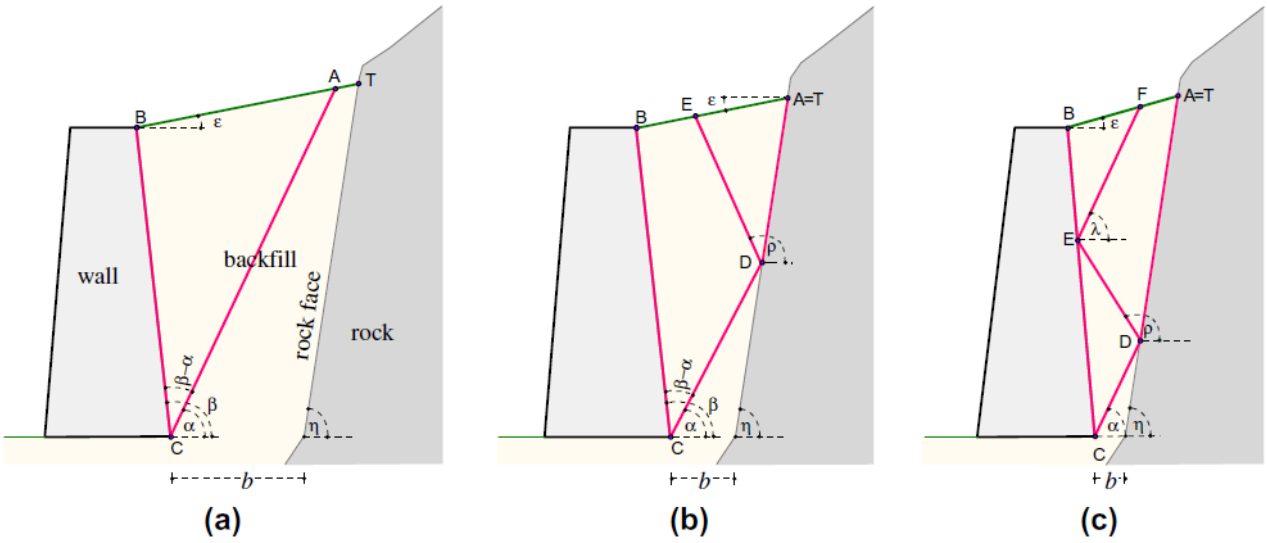

Figure 2.26 Mechanisms of failure between the wall face and the stable face (Greco 2013)

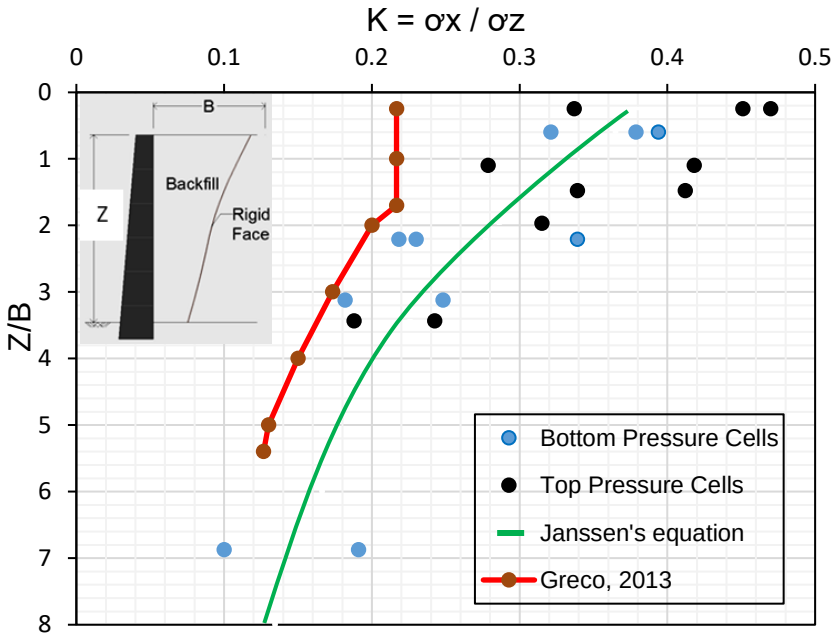

Figure 2.27 Coefficient of lateral earth pressure vs. Z/B

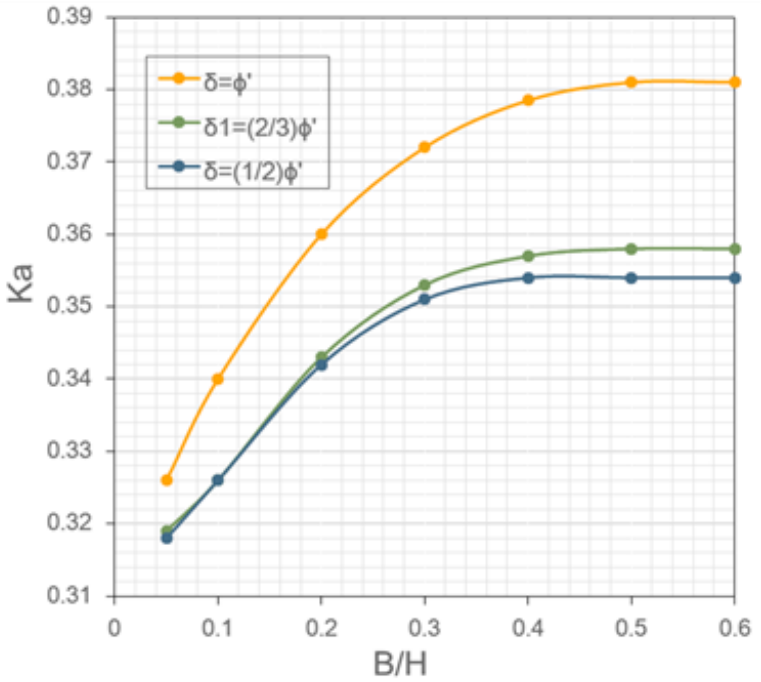

Figure 2.28 Effect of interface friction angle on Ka

2.4.4 Numerical studies

Numerical methods have been effectively used to analyze reinforced and unreinforced soil retaining walls. Both the finite element method (Karpurap and Bathurst 1995; Ling et al 199; Ling and Leshchinsky 2003; Skinner and Rowe 2005; Morrison et al. 2006; Kniss et al., 2007; Yang et al 2007; Yang et al. 2008; Fan and Fang 2010; Pukar and Kute 2013; Damians et al. 2013(mettalic), and 2015; and Mirmoradi and Ehrlich 2015; Yu et al. 2015a) and the finite difference method (Leshchinsky and Vulova 2001; Holtz and Lee 2002; Reddy et al. 2003; Leshchinsky et al.,2004; Hatami and Bathurst 2005 and 2006; Han and Leshchinsky; 2006b; Han and Leshchinsky, 2007; Han and Leshchinsky 2010; Huang et al. 2009, 2011, 2013 and 2014; Pukar and Kute 2013; Damians et al. 2014; Yu et al. 2015a; Yu et.al. 2016) have been

used to study GRR walls. Both methods have been verified to give satisfactory predictions of important performance features of full-scale walls in the field and reduced-scale model walls in the laboratory (Hatami and Bathurst 2005, 2006; Morrison et al. 2006; Fan and Fang 2010; Huang et al. 2009, 2010; Damians et al. 2015).

Numerical analysis of reinforced retaining walls requires the properties of the three components (e.g., backfill soil, reinforcement and wall facing) and the interface properties between these components. A summary of the material properties found in the reviewed numerical studies is presented below. The following sections summarizes the material properties found in the reviewed numerical studies and briefly describe the reviewed numerical studies on the limited fill space walls.

Soil Properties

Researchers used different soil constitutive models to simulate behavior of soil in geosynthetic reinforced retaining walls like:

(1) Soil stress dependent hyperbolic model with Mohr Coulomb failure criterion (Ling et al 1999; Holtz and Lee 2002; Ling and Leshchinsky 2003; Hatami and Bathurst 2005 and 2006)

(2) Linear elastic perfectly plastic material with Moher-Coulomb failure criterion (Leshchinsky and Vulova 2001; Reddy et. Al. 2003; Leshchinsky et al. 2004; Yang and Liu 2007; Han and Leshchinsky 2010; Huang et.al. 2011; Abdelouhab et al. 2011; Damians et al. 2014; Yu et al. 2016; Jiang 2016)

(3) Duncan-Chang hyperbolic soil model, and Lade's model with Mohr Coulomb failure criteria (Huang et al. 2009).

(4) Cap-yield soil model (Huang et.al. 2013 and 2014 and Jiang 2016). Linear elastic model (Pukar and Kute 2013 and Kniss et al. 2007), and (5) hardening soil model (Mirmoradi and Ehrlich 2015).

Reinforcement properties

Various structural elements were incorporated in FLAC to simulate the reinforcement in geotechnical structures, and the following have been used to simulate geosynthetic reinforcement in GRR walls:

(1) Linearly elastic cable element (Holtz and Lee 2002; Leshchinsky and Vulova 2001; Han and Leshchinsky 2010),

(2) Linearly elastic-geogrid element (Huang 2011, 2013 and 2014),

(3) Hyperbolic load strain time model for polypropylene geogrid and Moher-Coulomb for PET geogrid-cable element (Hatami and Bathurst 2005; 2006 and Huang et al 2009; Yu et al. 2016),

(4) A flexible beam structures (Reddy et al. 2003), and

(5) Linearly elastic and perfectly plastic strip element (Yue et al. 2015; and Jiang 2016).

Facing unit properties

Most of the facing units used in GRR walls are made of concrete and so linear elastic material were intensively used to simulate facing units (Holtz and Lee 2002; Leshchinsky and Vulova 2001; Mirmoradi and Ehrlich 2015; Hatami and Bathurst 2005 and 2006; Yu et al 2016 and Jiang 2016). One dimensional element- nonlinear material properties also was used to simulate the behavior of facing units in GRR walls (Ling et al 2001).

Interface properties

FLAC provides various interfaces to simulate the interaction between two different components (materials) of a geotechnical structure. For example, an interface between geosynthetic and backfill material, an interface between wall facing and backfill material, and an interface between the facing units in GRR walls.

Itasca (2014) defines interface as a connection between sub-grids that can slide or open. A combination of springs and sliders are used to model the interface behavior. A vertical spring with a tensile strength is used to simulate the behavior of interface in the normal direction (normal stiffness) and a horizontal spring and a slider is used to simulate the behavior of the interface in the tangent direction.

The following interface models were used to simulate the interaction between each of two adjacent components of GRR walls:

(1) Sliding or separation interface with Mohr-Coulomb shear-strength criterion (Ling et al 2000; Leshchinsky and Vulova 2001; Huang et al. 2009; Han and Leshchinsky 2010; Huang et al. 2011, 2013 and 2014, Yu et al. 2105; Jiang 2016), and

(2) Perfectly bonded (Holtz and Lee 2002; Hatami and Bathurst 2005 and 2006; Damians et al. 2013; Mirmoradi and Ehrlich 2015 and Yu et al. 2016).

Morrison et al. (2006)

Morrison et al. (2006) conducted a numerical study using the finite element program (PLAXIS) to simulate the full-scale test wall in the field, which was limited to the unconnected portion of the wall. They used the “Hardening-Soil” model to simulate the soil stress-strain behavior and the “geogrid” element to simulate the reinforcement. “Plate” elements were used to

simulate the MSE wall facing units. Morrison et al. (2006) used a “plate” element with elastic behavior to model the reinforced concrete footing. It was reported that this study showed a good agreement of the results between the numerical model and full-scale field test.

The full-scale field test, the centrifuge model tests, and the numerical model analysis indicated that the wall with the reinforcement length as short as 0.25H remained stable under a considerably higher surcharge load. Based on this finding, Morrison et al. (2006) recommended a minimum reinforcement length equivalent to 0.3H as measured from the top of the leveling pad for an SMSE wall system. In addition, the two upper reinforcement layers need to be extended to a minimum length of 0.6H or 1.5 m beyond the shored wall (Figure 2.29). However, they clearly declared that this guideline was specifically established for the use of soil nail walls as the shoring wall component. Morrison et al. (2006) did not recommend any rear connection because the experimental test results did not show the benefit of attaching the reinforcement to the shored wall, and the complexity of construction of connections.

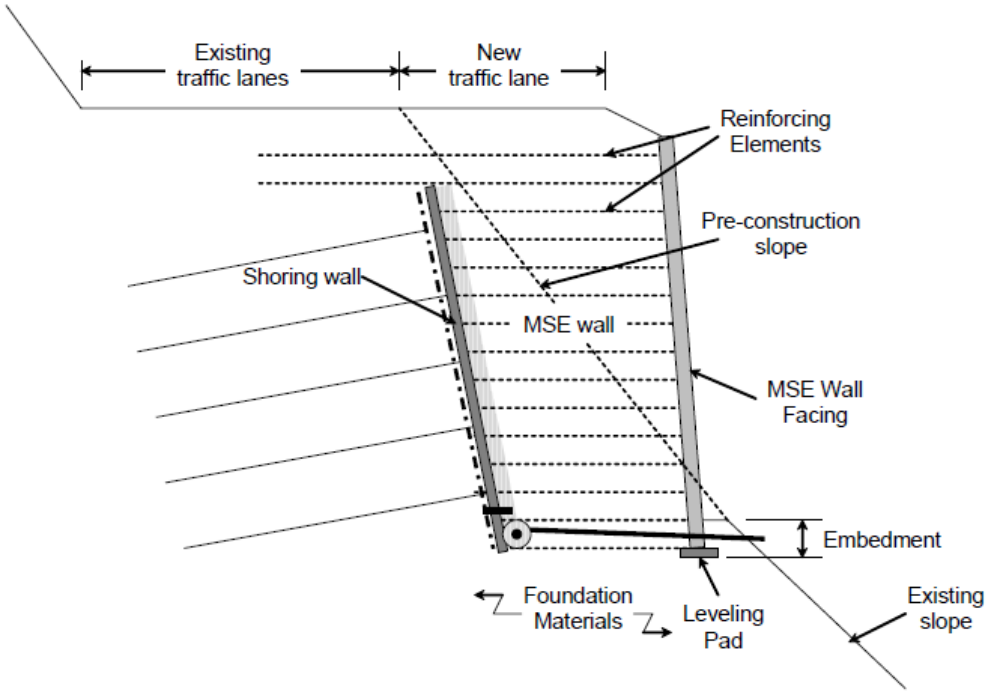

Figure 2.29 Typical cross section of a shored reinforced retaining wall system for steep terrains (Morrison et al. 2006).

Kniss et al. (2007)

Kniss et al. (2007) performed a series of numerical analyses to find the distribution of the lateral earth pressures behind limited fill space unyielding walls. Kniss et al. (2007) used three constitutive models to simulate the soil in the numerical software - PLAXIS: linear elastic, Mohr-Coulomb, and Hardening-Soil. A "fixed" boundary was used to simulate an unyielding wall condition. Kniss et al. (2007) used the interface elements available in PLAXIS to model the soil-wall interaction and its interface strength was controlled by an interface reduction factor that relates the interface strength to the shear strength of the soil.

Kniss et al. (2007) investigated the effect of a range of wall aspect ratios on the lateral earth pressures under at-rest and active conditions. They compared the lateral earth pressures predicted by the numerical method with the measured ones from the experimental tests and the

calculated one based on Janssen's arching theory. Good agreements were obtained among the calculated lateral earth pressures from the numerical analyses, those from the Janssen's equation, and the experimental measurements. All results showed the decrease of the lateral earth pressures with the decrease of the wall aspect ratio.

Yang and Liu (2007)

Yang and Liu (2007) performed a numerical analysis to assess the lateral earth pressure distributions in limited fill space walls with inextensible reinforcement. They investigated the effect of the wall aspect ratio (L/H) on the lateral earth pressure distribution along the wall face and the center of the limited fill space walls. The wall aspect ratio studied were 0.1, 0.3, 0.5, and 0.7. Yang and Liu (2007) used the finite element program - PLAXIS for the numerical analysis. Figure 2.30 shows the geometry of the model used by Yang and Liu (2007). They simulated the behavior of soil and the interface between the wall face and soil using an elastic-plastic model. "Plate" elements were used to simulate the wall face and "fixed" boundary conditions were used to model the stable medium.

Yang and Liu (2007) showed the decrease of the lateral earth pressure with the decrease of the wall aspect ratio, and concluded that the design of limited fill space walls using the design the FHWA design guidelines is conservative.

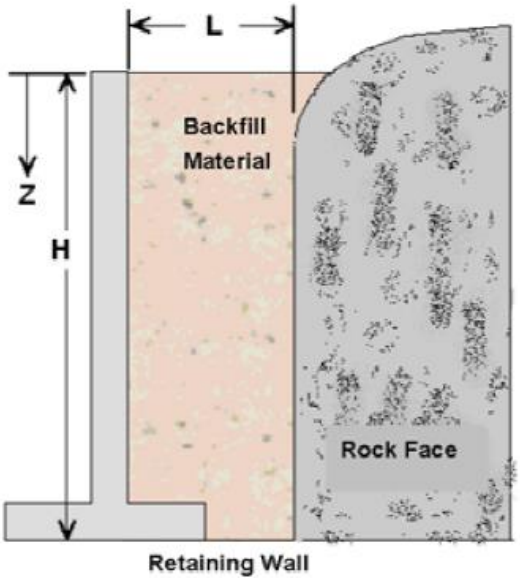

Figure 2.30 Model geometry simulated by Yang and Liu (2007)

Han and Leshchinsky (2010)

Han and Leshchinsky (2010) used the finite difference method incorporated in the numerical software - FLAC 2D and the limit equilibrium method in the software - ReSSA to study the effect of the wall width to height ratio on the internal and external stability of back-to-back MSE walls under static loading. In their study, they investigated the effect of the wall aspect ratio (wall width (B) to wall height (H)) on the critical failure plane, and the lateral earth pressure behind the reinforced fill zone. Reinforcement was modeled as a cable with grouted interface properties between cable and soil. They used the Mohr-Coulomb failure criteria for the strength between blocks, the strength of the reinforced and retained fill, and the strength of the foundation soil. Figure 2.31 shows the model geometry and material properties used by Han and Leshchinsky (2010).

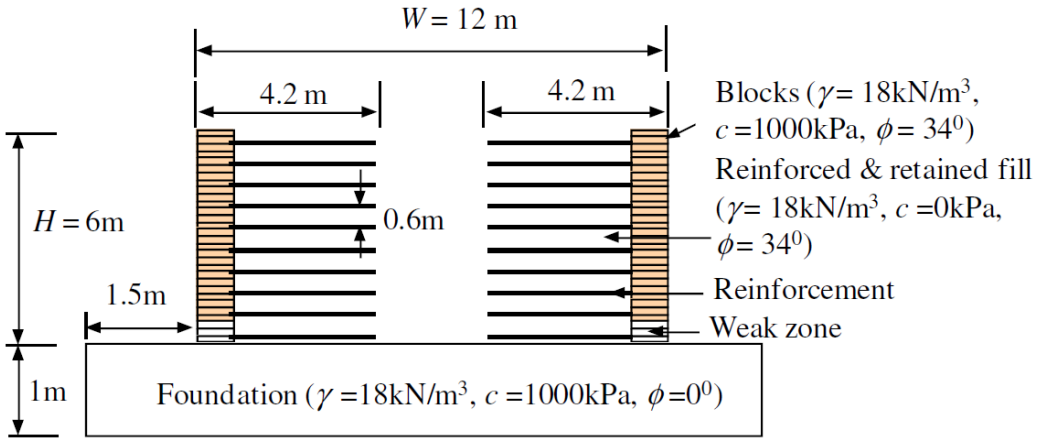

Figure 2.31 Back to back MSE model (Han and Leshchinsky 2010)

Figure 2.32 shows the critical failure planes in back to back walls. Han and Leshchinsky (2010I) reported that if there was no retained fill between these two walls, the failure surfaces entered the reinforced zone form another side. Thus, the critical failure plane was bilinear for the case without any retained fill between the two walls.

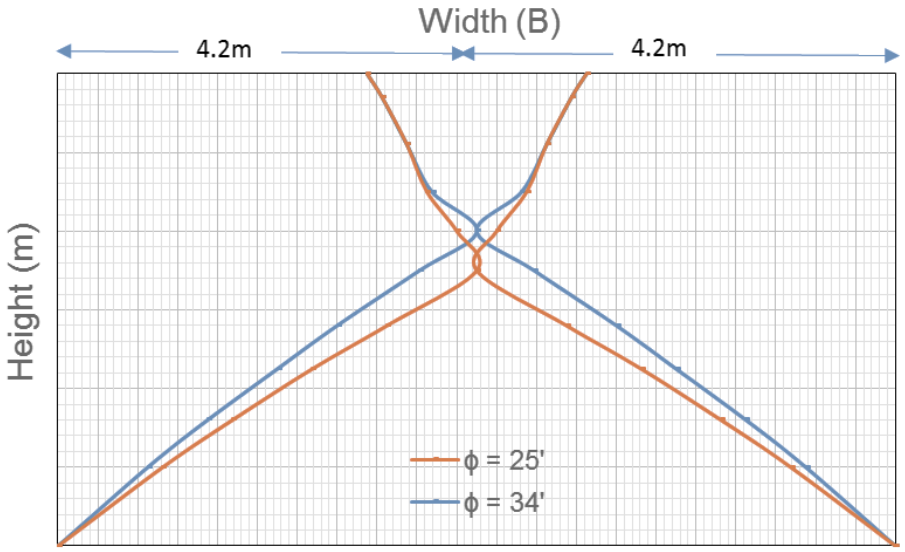

Figure 2.32 Critical failure planes in back-to-back walls (Han and Leshchinsky 2010)

Fan and Fang (2010)

Fan and Fang (2010) performed a numerical analysis to examine the distribution of the lateral earth pressures behind the wall face under limited fill space conditions for non-deformable walls. The effects of backfill geometry and the friction angle of the backfill on the distribution of the lateral earth pressure were examined. Fan and Fang (2010) used the finite element program - PLAXIS to assess the lateral earth pressure from at rest to active conditions for a non-deformable wall close to a stable medium. They used Mohr-Coulomb constitutive model to simulate the behavior of soil. Two types of interface (i.e., the interface between the wall and the backfill and the interface between the stable medium and the backfill) were considered. The stable medium behind the wall and the facing wall were modelled using the plates with linearly elastic behavior.

Fan and Fang (2010) estimated the lateral earth pressure distributions along the depth (z/H) at various wall displacements and at the β (wall batter) of 8^o and the b (bottom width of the wall) value of 0.5 m (Figure 2.33). They found that the coefficient of lateral earth pressure was much lower than that based on the Coulomb theory. It was also stated that the location of the rock face behind the retaining wall played an important role in the coefficient of lateral earth pressure distribution with depth (Figure 2.34). $K_{a(c)}$ is the coefficient of active earth pressure computed by the numerical analysis while $K_{a(Coulomb)}$ is the coefficient of active earth pressure based on the Coulomb solution.

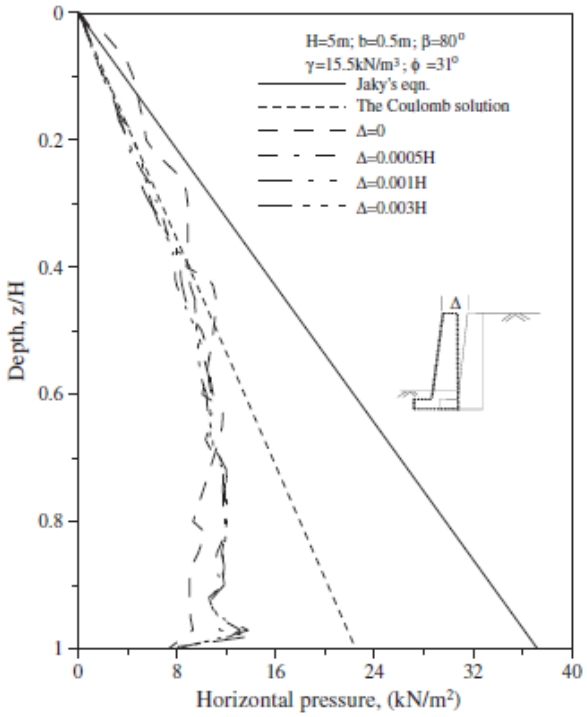

Figure 2.33 Distributions of lateral earth pressures with depth at various wall displacements (Fan and Fang 2010)

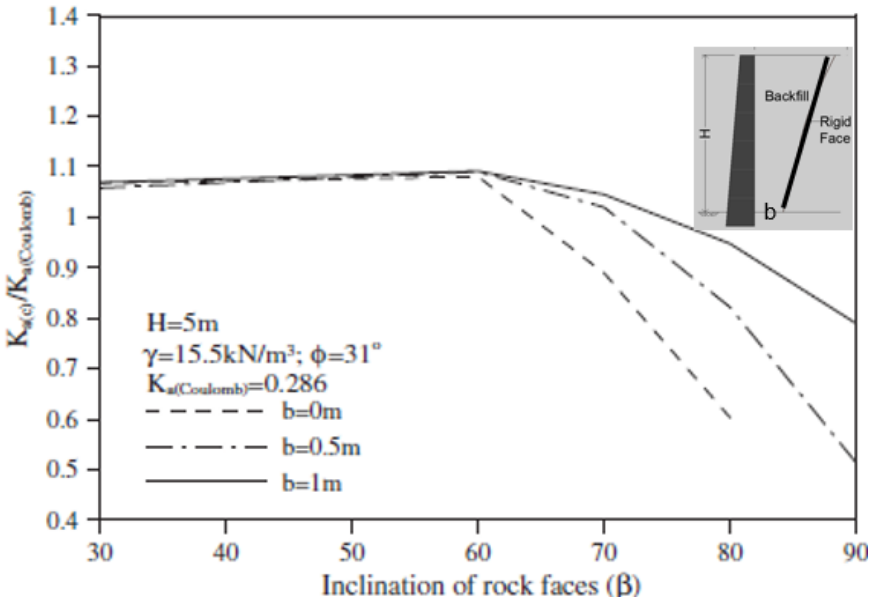

Figure 2.34 Distributions of lateral earth pressures with depth for various wall geometries (after Fan and Fang 2010)

.

Chapter 3 Model Scale Effect Analysis

3.1 Introduction

Full-scale (prototype) testing is ideal for understanding actual behavior of engineering-related structures. However, researchers often conduct tests on reduced-scale models in laboratory because these models require less space, time, and cost for construction, instrumentation, and testing. These models can also be run and monitored until failure. The results of laboratory reduced-scale model tests are used to develop and verify mathematical models for predicting the performance and behavior of full-scale models. To ensure reduced-scale models to correctly and reasonably reflect the behavior of full-scale models, it is required to develop a modeling technique, scaling laws between model and prototype, which account for all the variables governing the behavior or response of the full-scale structure. The concept of similarity and dimensional analysis can be used to find the scaling laws between reduced-scale and prototype models. Kline (1986) presented three methods for scale modeling applications: dimensional analysis, similitude theory, and method of governing equations. Many researchers have used the principle of dimensional analysis and similarity theory to account for the scale effect in various civil engineering structures (e.g., Noche 2013; Andrew 2013; Chadwick 2013; Wang et al. 2013; Khurmi 2006; Reddy et al. 2003; Ettema et al. 1998 and Neymand 1998).

Thus, to minimize uncertainty and increase confidence in the results of laboratory reduced-scale models, a scale effect analysis should be conducted to account for all parameters governing the behavior of the studied models. In this study, a dimensional analysis method, the Buckingham $\prod$-Theorem method, was used with the principle of similarity between the reduced-scale model and the prototype to examine possible scale effect on the behavior of geosynthetic-

reinforced retaining (GRR) walls. This process helped design the proper reduced-scale models for the laboratory study to be discussed in Chapter 4. The equations used by the Federal Highway Administration (FHWA) to calculate the maximum tensile stress of the reinforcement in GRR walls (FHWA 2009) were used to examine the scale effect and to verify the results of the dimensional analysis method. Then, a limit equilibrium method was used to derive a scaling law to evaluate the use of laboratory reduced-scale GRR model walls. The following sections present the details of the scale effect analysis.

3.2 Methods of approach

3.2.1 Dimensional analysis

Dimensional analysis is a mathematical technique dealing with the dimensions of physical quantities. This method is used to check equations, interpret experimental data, convert unit systems, and examine physical models. In this study, modeling was carried out based on the principle of similarity and dimensional analysis, and the Buckingham-∏ Theorem was used as the dimensional analysis method. The concept of this method is to find a dimensionless relationship between a set of parameters that influence the behavior of a system. In this study, a dimensional analysis was performed on the parameters that influence the stability of GRR walls. The Buckingham-∏ Theorem suggests the following steps.

Step 1. List all the parameters that are involved in the system and select the parameters to be investigated and denote the total number of parameters as n.

Factor of safety (FS) is usually used as a primary indicator to check the stability of a wall. The parameters affecting FS and their fundamental Force-Length-Time units are listed below:

H = height of wall [L]

L = width of wall [L]

L = length of reinforcement [L]

g = gravitational acceleration [LT^{-2}]

J = stiffness of reinforcement [FL^{-1}]

T = strength of reinforcement [FL^{-1}]

γ = unit weight [FL^{-3}]

q = surcharge [FL^{-2}]

ϕ = soil friction angle

This study considered wall height (H), reinforcement stiffness (J), reinforcement strength and length (T and L), soil unit weight (γ), and surcharge (q) as the parameters to be investigated. Therefore, the number of parameters (relevant variables) n = 6.

Step 2. Choose the repeating parameters (independent variables). Since the principle of similarity requires that the model should have a similar unit weight with a desired prototype model, and the scale factor for the geometry should always be one. H and γ have been selected as the repeating parameters (R_1 and R_2, respectively).

Step 3. Specify the number of primary dimensions (m): Force (F) and Length (L); therefore, m = 2.

Step 4. Calculate the number of Π-equations required: n-m = 6 - 2 = 4.

Step 5. Derive the Π-equation for each of the n-m parameters (variables).

The generic Π-equation will be: Π = (variable) $(R_1)^a (R_2)^b$

Where a, b are chosen so that the Π-equation become non-dimensional (i.e. Π = 1)

Since H and γ are the repeating parameters, variables are L, q, J, and T.

The Π-equations for (L) will be:

$$\pi_L = L\,(\gamma)^a(H)^b \quad \ldots\ldots\ldots\ldots\ldots\ldots \ldots (3.1)$$

$$\pi_L = L\,F^a L^{-3a} L^b \quad \ldots\ldots\ldots\ldots\ldots\ldots \ldots (3.1a)$$

$$\pi_L = L^1\,(L^1 F^{-3})^a (L^1)^b \quad \ldots\ldots\ldots\ldots\ldots\ldots \ldots (3.1b)$$

$$\pi_L = L^1\,F^a L^{-3a} L^b \quad \ldots\ldots\ldots\ldots\ldots\ldots \ldots (3.1c)$$

$$F^0 L^0 = L^1\,F^a L^{-3a} L^b \quad \ldots\ldots\ldots\ldots\ldots\ldots \ldots (3.1d)$$

$$F^0 L^0 = L^{1-3a+b}\,F^a \quad \ldots\ldots\ldots\ldots\ldots\ldots \ldots (3.1e)$$

Solve for a, b by equating exponents to make the quantity dimensionless,

$$a = 0 \ldots\ldots\ldots\ldots\ldots\ldots \ldots (3.1f)$$

$$1-3a + b = 0 \ldots\ldots\ldots\ldots\ldots\ldots \ldots (3.1g)$$

Since a = 0 (equation 3.1g):

$$b = -1 \ldots\ldots\ldots\ldots\ldots\ldots \ldots (3.1h)$$

Substituting the equation (3.1f) and (3.1h) with (a) and (b) in the equation (3.1):

$$\pi_L = \frac{L}{H} \quad \ldots\ldots\ldots\ldots\ldots\ldots (3.2)$$

The Π-equations for the rest of variables (q, J, and T) will be:

$$\pi_q = F L^{-2} F^a L^{-3a} L^b \quad \ldots\ldots\ldots\ldots\ldots\ldots (3.3)$$

$$\pi_J = F L^{-1} F^a L^{-3a} L^b \ldots\ldots\ldots\ldots\ldots\ldots (3.4)$$

$$\pi_T = FL^{-1}F^aL^{-3a}L^b \text{ ..... (3.5)}$$

Solve for a, and b such that the Π-equations are dimensionless (following the procedures implemented for the equation (3.1)), the following equations are obtained:

$$\pi_L = \frac{L}{H} \text{ ..... (3.6)}$$

$$\pi_q = \frac{q}{\gamma H} \text{ ..... (3.7)}$$

$$\pi_J = \frac{J}{\gamma H^2} \text{ ..... (3.8)}$$

$$\pi_T = \frac{T}{\gamma H^2} \text{ ..... (3.9)}$$

Using a reduced-scale model to simulate the behavior of a prototype structure requires a similar model and a prototype system in terms of the geometry, material and load. The soil used in both the model and prototype should have the same unit weight, and the same internal friction angle at the scaled normal stress. Considering the principle of similarity, the following relationships can be established between the reduced-scale model and the prototype:

$$H_m = NH_P \text{ ..... (3.10)}$$

$$g_m = g_P \text{ ..... (3.11)}$$

$$\gamma_m = \gamma_P \text{ ..... (3.12)}$$

The subscripts (m) and (p) are referred to the reduced-scale and prototype models, respectively. N is the scale factor, which is the ratio of a reduced-scale model to the prototype in this study.

All lengths of the prototype are therefore scaled down to those in the model by a factor (N). The corresponding Π-values are:

$$\pi_{L-m} = \frac{L_m}{H_m} = \pi_{L-p} = \frac{L_p}{H_p}$$

$$L_m = NL_p \quad \text{..... (3.13)}$$

$$\pi_{q-m} = \frac{q_m}{H_m \gamma_m} = \pi_{q-p} = \frac{q_p}{H_p \gamma_p}$$

$$q_m = Nq_p \quad \text{..... (3.14)}$$

$$\pi_J = \pi_T = \frac{J}{\gamma H^2}$$

$$\frac{J_m}{\gamma {H_m}^2} = \frac{J_p}{\gamma {H_p}^2}$$

$$J_m = N^2 J_p \quad \text{..... (3.15)}$$

Equation (3.15) reveals that the stiffness or the mechanical properties of the geosynthetic used in the laboratory-scale model should be scaled down by N^2. For example, if N=1/5 and the stiffness of the geogrid available in the market is 2000 kN/m, the stiffness of the laboratory-scaled geogrid should be 80 kN/m.

To examine the scale factor for the strain value in geosynthetic reinforcement between a prototype and a reduced scale model, Hook's law was applied to the strain in the elastic portion only. According to Hook's law $\sigma = E\epsilon$, the tensile stress of geosynthetic reinforcement can be

assumed as the surcharge (q) and written as q=Jϵ. Since $q_m = Nq_p$ (Equation 3.13) and $J_m = N^2 J_p$ (Equation 3.15):

$$q_m = J_m \in_m = Nq_p = N^2 J_p \in_p \ldots\ldots\ldots\ldots\ldots\ldots \text{(3.16a)}$$

$$\in_m = N \in_p \ldots\ldots\ldots\ldots\ldots\ldots \text{(3.16b)}$$

Equation (3.16b) indicates that the strain in the geosynthetic used in the reduced-scale model should be N times the strain in the geosynthetic used in the prototype model.

3.2.2 FHWA method for calculating the maximum tensile stress of reinforcement in GRR walls (2009)

The equations provided by FHWA (2009) to calculate the maximum tensile stress of reinforcement in GRR Walls were used to find the scale factor between the prototype and the reduced-scale model.

Based on the FHWA (2009), the maximum tensile stress, T_{MAX}, for a GRR wall with level backfill and surcharge can be calculated as follows:

$$T_{MAX} = k_r (\gamma d_i + q) s_v \ldots\ldots\ldots\ldots\ldots\ldots \text{(3.17)}$$

where

d_i is the distance from the reinforcement layer of interest to the top of the wall;

k_r is the coefficient of lateral earth pressure in the reinforced soil zone;

q is the applied surcharge;

S_v is the vertical spacing between the layers of the reinforcement;

γ is the unit weight of soil.

The maximum tension of the reinforcement for a reduced-scale model can be written as:

$$T_{MAX\text{-}m} = [k_r (\gamma d_i + q) s_v]_m \ldots\ldots\ldots\ldots\ldots\ldots \text{(3.18)}$$

$$T_{MAX-m} = [k_r (\gamma d_{im} + q_m)] s_{vm} \quad \ldots\ldots\ldots\ldots (3.19)$$

To find the scale factor between the prototype and the reduced scale model, the principle of similarity was applied to the parameters of the porotype between the reduced-scale models. In addition to Equations (3.10), (3.11), and (3.12), the following equations can be added:

$$d_{im} = N d_{ip} \ldots\ldots\ldots\ldots\ldots (3.20)$$

$$s_{vm} = N s_{vp} \ldots\ldots\ldots\ldots\ldots (3.21)$$

$$T_{MAX-m} = (k_r (\gamma N d_{iP} + N q_P)) N s_{vp}$$

$$T_{MAX-m} = N^2 ((k_r (\gamma d_{ip} + q_p)) s_{vp})$$

$$T_{MAX-m} = N^2 T_{MAX-p} \ldots\ldots\ldots\ldots\ldots\ldots (3.22)$$

Based on FHWA (2009), the maximum tension should be lower than the pullout resistance of the reinforcement, i.e.:

$$T_{MAX} \leq R_f F^* \sigma_v L_e C R_c \alpha \ldots\ldots\ldots\ldots\ldots\ldots (3.23)$$

where:

L_e = the anchorage length of reinforcement in the resisting zone;

T_{MAX} = the maximum reinforcement tension;

R_f = the resistance factor for reinforcement pullout;

F^* = the pullout resistance factor, $F^* = C_i^* \tan\phi$;

α = the scale correction factor;

σ_v = the nominal vertical stress at the reinforcement level in the resistant zone;

C= 2 for geogrid;

C_i = the interaction coefficient, typically 0.8 for geogrid;

R_c = the reinforcement coverage ratio, R_c = 1.0 in this study.

The maximum tension of the reinforcement required to resist pullout failure for the reduced-scale model can be written as:

$$T_{MAX\text{-}m} = (R_f F^* \sigma_v L_e C R_c \alpha)_m \ldots\ldots\ldots\ldots\ldots (3.24)$$

Applying the principle of similarity:

$$T_{MAX\text{-}m} = R_f F^* (N)\sigma_{vp} (N)L_{ep} C R_c \alpha \ldots\ldots\ldots (3.25)$$

$$T_{MAX\text{-}m} = N^2 T_{MAX\text{-}p} \quad \ldots\ldots\ldots\ldots\ldots\ldots\ldots\ldots .. (3.26)$$

Both Equations (3.22) and (3.26) show that the tensile strength of the geosynthetic used in the laboratory-scale model should be scaled down by N^2, which verifies the results obtained from the dimensional analysis (i.e., Equation 3.14).

3.2.3 Limit equilibrium method

Limit equilibrium methods have been commonly used to design major earth structures, including geosynthetic reinforced retaining structures (Ellis and Christopher 1997). One of the commonly used limit equilibrium methods is Bishop's simplified method that uses a circular arc slip surface for equilibrium analysis. Bishop's simplified method was modified to include reinforcement as a horizontal force intersecting the slip circle (Han and Leshchinsky 2004). This method has been built in the ReSSA Version 3.0 program (also referred to as ReSSA (3.0)), developed by the ADAMA Engineering. ReSSA (3.0) can analyze many slip circles based on user's predefined zone. ReSSA (3.0) can also generate a safety map, which identifies the critical zone based on the criterion set up by the user. ReSSA (3.0) has been developed to analyze geosynthetic reinforced slopes and walls (Han and Leshchinsky 2010, and Han and Leshchinsky 2004). Due to the simplicity of the method, this study used Bishop's simplified method built in the ReSSA program to analyze the scale effect of GRR walls and verify the results of the dimensional analysis method.

3.2.4 Modeling of problem

Figure 3.1 shows a typical geometry and material properties for the model used to analyze the scale effect of the GRR wall models. Three different scale factors, N = 1/5, 3, and 10 were used. Various models were studied to find the scale law (i.e., the correct scale factor) between the prototype and laboratory reduced-scale models for GRR walls. Table 3.1 shows the models investigated in this study.

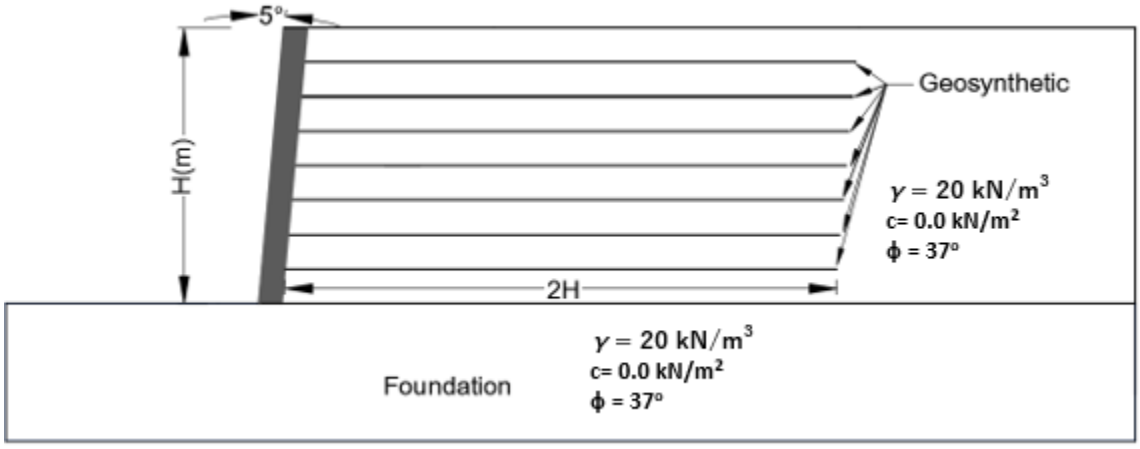

Figure 3.1 Typical GRR model

Models I, II, and sIII in Table 3.1 are referred to the unreinforced models without any load, with a uniform load (Q_u), and with a strip load (Q_s), respectively. The purpose for the analysis of unreiforced models was to determine the scale effect of the geometry of the model and the applied load when the geosynthetic (reinforcement) was not included. Models IV, V, and VI are referred to the reinforced models without any load, with a uniform load, and with a strip load, respectively.

Table 3.1 Models

Model Type	Description
Model I	Simple Model
Model II	Model with Uniform Surcharge
Model III	Model with Strip Load
Model IV	Simple Model with Reinforcement
Model V	Model with Uniform Surcharge & Reinforcement
Model VI	Model with Strip Load & Reinforcement

In this study, the required tensile strength of the reinforcement and/or the magnitude of the applied load for the full-scale model were first determined for the factor of safety equal to 1.0, using ReSSA (3.0). Then the critical slip surface and the factor of safety of the reduced-scale model were determined and then compared with those of the full-scale model. The size of the reduced-scale models was reduced based on the scale factor used (i.e., N = 1/5) and then the tensile strength value of the reinforcement and/or the magnitude of the applied load were varied until the computed factor of safety of the reduced-scale model became unity (i.e., equal to the factor of safety of the full-scale model). When the factor of safety of the reduced-scale model was equal to the factor of safety of the full-scale model (i.e., factor of safety = 1.0), the tensile strength of the reinforcement in the full-scale model was compared with that in the reduced-scale model to find the scale factor between these two models.

Results of limit equilibrium analysis for scale factor (N) =1/5

Table 3.2 shows the calculated factors of safety of Models I, II, and III. The prototype model simulated a full-scale wall of 6.0 m high and the reduced-scale (RS) models simulated the reduced-scale models of 1.2 m high, whose dimensions (i.e., height and width of the model) were reduced by the scale factor N =1/5. (note: all the factors of safety (FS) presented in this

dissertation are the minimum factors of safety obtained by ReSSA (3.0)). Table 3.2 shows that for Model I, the prototype and the reduced-scale models resulted in the same FS (i.e., 1.0) when the prototype dimensions were reduced by the scale factor (N=1/5). For Models II and III, it is observed that the reduced-scale models with the uniform and strip loads reduced by N and N^2, respectively, generated the same FS result as the prototype model. In other words, under uniform loading, the scale factor should be N (i.e., Q_U=20 kPa), while under strip loading, the scale factor should be N^2 (i.e., Q_S=4.8 kN/m).

Table 3.2 Unreinforced wall

Model I	**Case**	T_{ul} (kN/m)	Surcharge (Q)	FS
	Prototype	-	-	1.01
	RS	-	-	1.01
Model II	**Case**	T_{ul} (kN/m)	Q_U (kPa)	FS
	Prototype	-	100	1
	RS-1	-	100	0.85
	RS-2	-	20	1
Model III	**Case**	T_{ul} (kN/m)	Q_S (kN/m)	FS
	Prototype	-	120	1.02
	RS-1	-	24	0.94
	RS-2	-	4.8	1.02

Table 3.2 shows that Model III with the RS-1 case had a lower factor of safety (i.e., FS = 0.94) than that (1.0) of the prototype when the strip load was reduced by the scale factor N. The reason for this result is that the dimension (width) of the loading plate was also reduced by the scale factor N.

Table 3.3 shows the calculated FS results of the reinforced wall models (Model IV). The prototype model simulated a full-scale geosynthetic reinforced model wall of 6.0 m high while the RS cases simulated the reduced-scale models of 1.2 m high (i.e., N=1/5). The RS-1 case is a

model wall reinforced with the same tensile strength of the reinforcement (i.e., ultimate strength (T_{ul}) = 20 kN/m) as that of the prototype. The reinforcement strength in the RS-2 case was reduced by the scale factor of N while the reinforcement strength in the RS-3 case was reduced by N^2 (i.e., T_{ul} = 0.8 kN/m). All the cases were investigated to find the best-match case that simulated the prototype model. Table 3.3 indicates that when the reinforcement strength of the prototype was used in the reduced-scale model, the software was not capable of calculating the factor of safety for the model (i.e., N/A). The reduction of the tensile strength of reinforcement by the scale factor N (i.e., T_{ul} = 4 kN/m) in the reduced-scale model (i.e., RS-2) resulted in a much higher factor of safety (i.e., FS=19.56) than that of the prototype model (i.e., FS = 1.00). Table 3.3 also shows that when the tensile strength of the reinforcement in the RS-3 case was reduced by the scale factor of N^2, the calculated factor of safety, FS =1.02, which is the same as that of the prototype.

In addition, Figures 3.2, 3.3, 3.4, and 3.5 show the slip surfaces (10 critical circles) and the safety maps for the prototype and the RS-3 case, in which the tensile strength of reinforcement was reduced by N^2. Figures 3.2 to 3.5 show that the prototype and the RS-3 case had the same slip surfaces and safety maps, which indicate that the scale factor N^2 ought to be applied to the tensile strength of the reinforcement in the reduced-scale models to simulate the prototype model.

However, Figure 3.6 shows that when the tensile strength of the reinforcement in the RS-2 case was reduced by N (i.e., T_{ul} = 4 kN/m), different slip surfaces were developed as compared with those in the prototype model. This comparison indicates that because of the improper scale factor, the reduced-scale model yielded a different factor of safety and different slip surfaces than those of the prototype.

Table 3.3 Reinforced wall

	Case	T_{ul} (kN/m)	Surcharge (kPa)	F.S.
Model-IV	Prototype	20	0.0	1.02
	RS-1	20	0.0	N/A
	RS-2	4	0.0	19.56
	RS-3	0.8	0.0	1.02

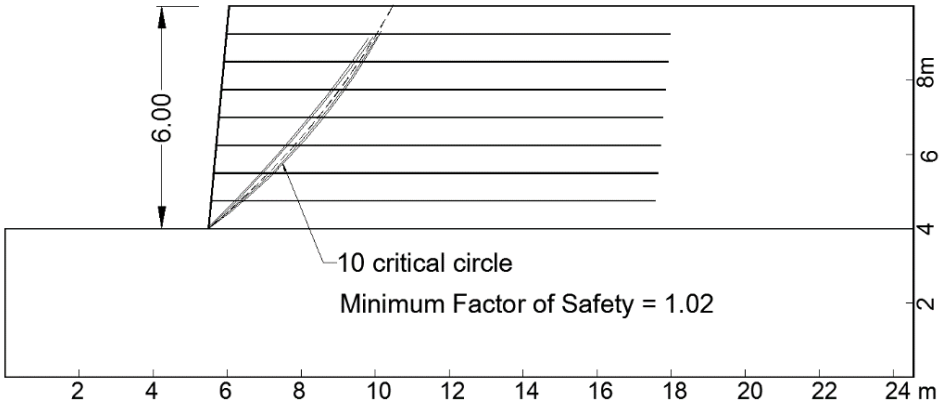

Figure 3.2 Model IV Prototype

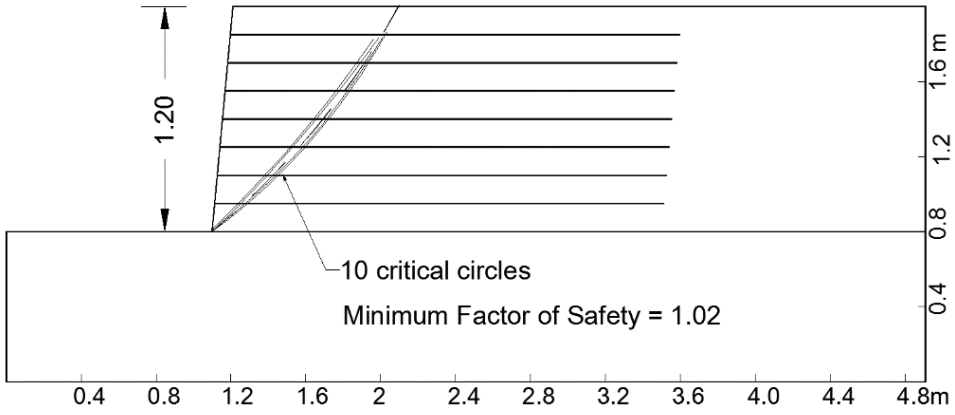

Figure 3.3 Model IV RS-3 Case

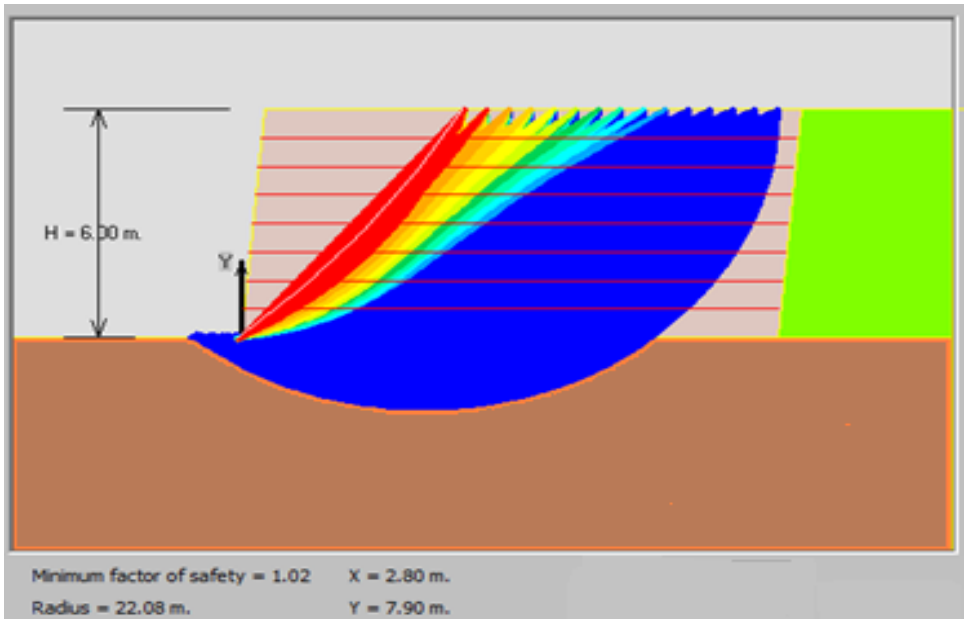

Figure 3.4 Model IV Prototype

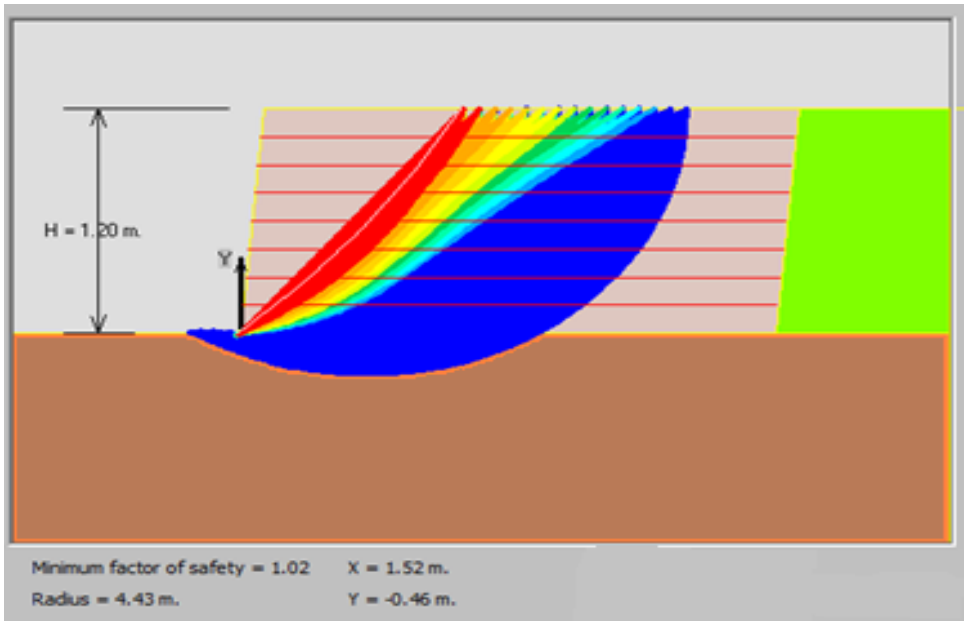

Figure 3.5 Model IV RS-3 Case

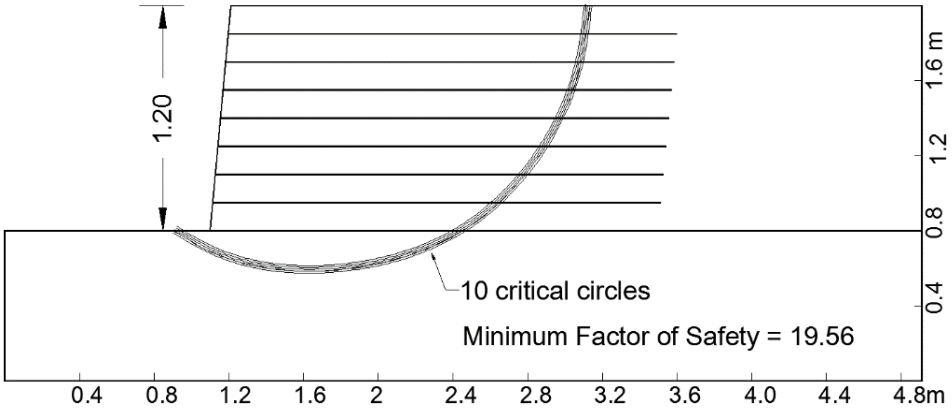

Figure 3.6 Model IV RS-2 Case

Table 3.4 shows the calculated FS results for the reinforced model walls under a uniform applied load (Model V). Various cases were considered to obtain correct scale factors between the prototype and the reduced-scale models. In this analysis, two parameters were studied, the tensile strength of the reinforcement and the magnitude of the applied surcharge. Same as for Model III, the prototype case simulated a full-scale reinforced wall of 6.0 high, which was subjected to an applied surcharge (Q_U) of 180 kPa. The RS cases simulated the reduced-scale models of 1.2 m high (N = 1/5). The RS-1-A case represents a model reinforced with the same reinforcement strength (i.e., T_{ul} = 50 kN/m) and subjected to the same applied surcharge (Q_U =180 kPa) as those of the prototype. The RS-1-B case is similar to the RS-1-A case except that an exclusion zone was introduced in the foundation of the RS-1-B case to avoid the critical slip surfaces passing through the foundation. The magnitude of the applied surcharge and the reinforcement strength were reduced by N in the RS-2 case. The RS-3 case had the same reinforcement strength (i.e., T_{ul} = 50 kN/m) and the reduced surcharge by N as that of the prototype was used. For the RS-4 case, the reinforcement strength was reduced by N^2 (i.e., T_{ul} = 2 kN/m) and the magnitude of the applied surcharge was reduced by N (i.e., Q_U = 36 kPa).

Table 3.4 Reinforced walls subjected to uniform surcharge

	Case	T_{ul} (kN/m)	Q_U (kPa)	FS
Model V	Prototype	50	180	1.0
	RS-1-A	50	180	2.36
	RS-1-B	50	180	2.64
	SR-2-A	10	36	3.97
	SR-2-B	10	36	6.82
	RS-3-A	50	36	3.7
	RS-3-B	50	36	76.42
	RS-4	2	36	1.0

Different factors of safety were obtained by applying different scale factor for the reinforcement and the surcharge. Figure 3.7 shows the critical failure surfaces for the prototype model with the minimum FS= 1.0., which is the baseline case for Model V cases.

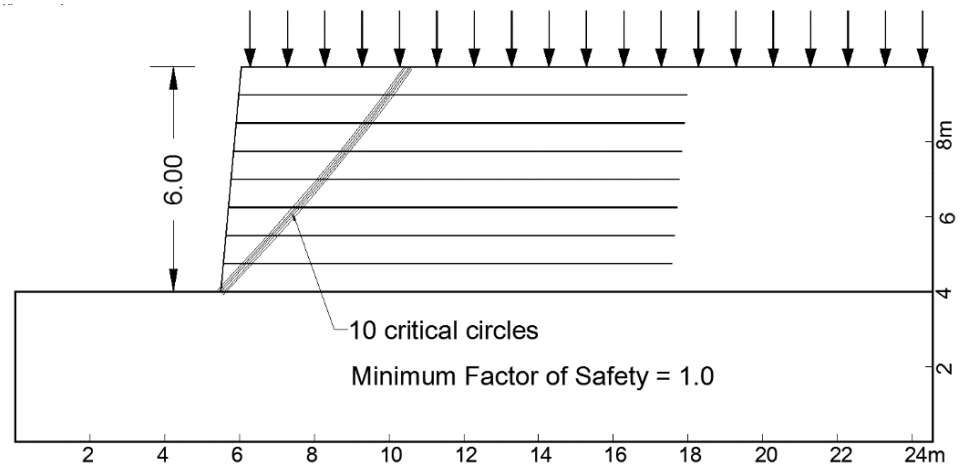

Figure 3.7 Model V Prototype

Table 3.4 shows that the RS-1-A case generated a higher factor of safety (i.e., FS = 2.36) than that of the prototype. The same model yielded even a higher factor of safety (i.e., FS = 2.64) when an exclusion was introduced in the foundation as in RS-1-B case. Figure 3.8 shows the

critical failure surfaces for the RS-1-B case, which are different from those of the prototype. The RS-2-A and RS-2-B cases, in which the reinforcement strength and the magnitude of the applied surcharge were reduced by N, also resulted in higher factors of safety than those of the prototype.

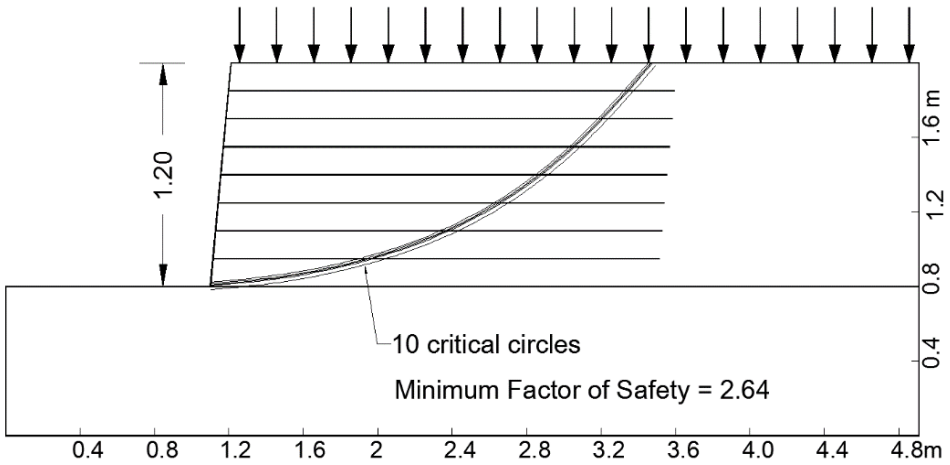

Figure 3.8 Model V RS-1-B Case

Table 3.4 also shows that the minimum factor of safety for the RS-2-A was 3.97 and became 6.82 when an exclusion zone was introduced to the foundation of the RS-2-B case. Figures 3.9 and 3.10 show the critical failure surfaces for the RS-2-A and RS-2-B cases are different from those of the prototype in Figure 3.7 because of the improper scale factor.

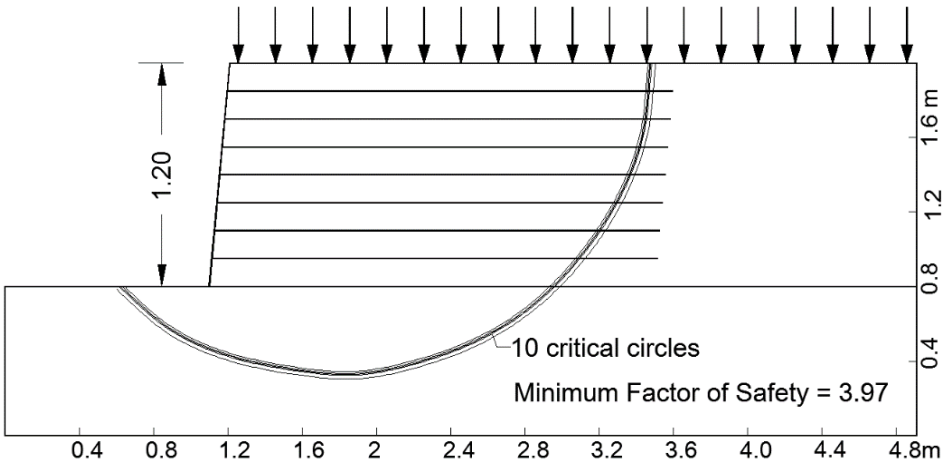

Figure 3.9 Model V RS-2-A Case

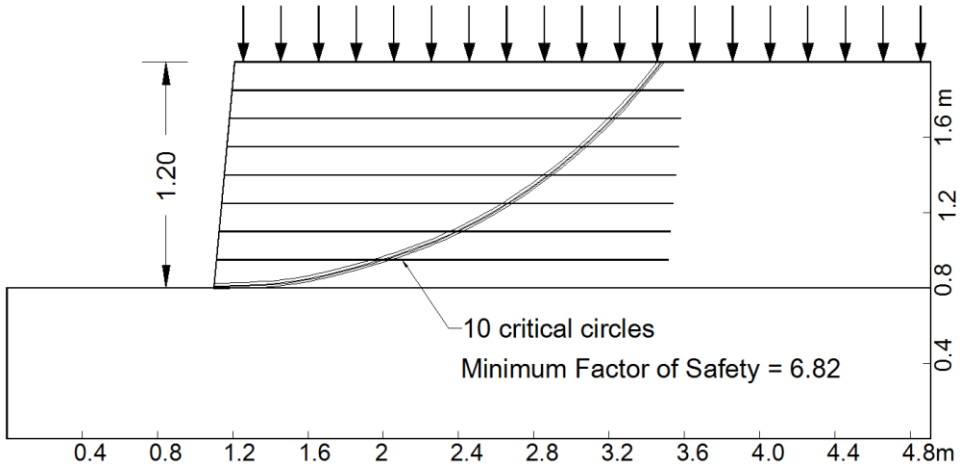

Figure 3.10 Model V RS-2-B Case

Nonetheless, the RS-4 case shows that the reduction of the tensile strength of the reinforcement by N^2 (i.e., T_{ul} = 2 kN/m) and the uniform applied surcharge by N (i.e., Q_U = 36 kPa) generated the same factor of safety as that of the prototype (i.e., FS = 1.0). Figure 3.11 shows that the reduction of the tensile strength of the reinforcement by N^2 and the magnitude of the uniform surcharge by N in the RS-54 case not only generated the same factor of safety but also the same critical slip surfaces as those of the prototype as shown in Figure 3.8.

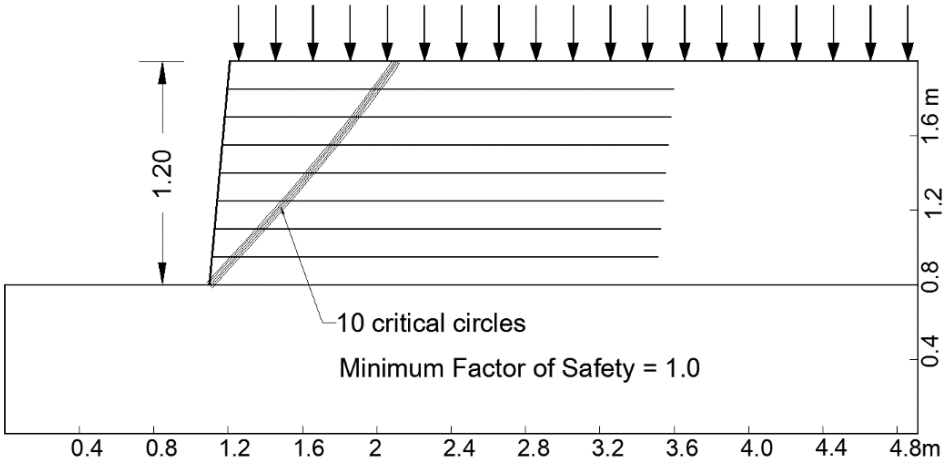

Figure 3.11 Model V RS-4

Table 3.5 shows the calculated FS results for the reinforced retaining wall models subjected to strip loading (Model VI). Various cases were analyzed to obtain the correct scale factors between the prototype and reduced-scale models. In Model VI, two parameters were examined, the tensile strength of the reinforcement and the applied surcharge. Similar to the Model V cases, the prototype case simulated a full-scale reinforced wall of 6.0 m high, which was subjected to a strip surcharge (Q_S) of 480 kPa. The RS cases simulated the reduced scale models of 1.2 m high (N=1/5). The RS-1 case represents a model with the same reinforcement strength (i.e., T_{ul} = 50 kN/m) and same applied surcharge (i.e., Q_S = 480 kN/m) as those of the prototype model. In the RS-2 case, the same reinforcement strength as that of the prototype (i.e., T_{ul} = 50 kN/m) was used, but the applied surcharge was reduced by the scale factor N (i.e., Q_S = 96 kN/m). Additionally, The RS-3 case represents a model, in which the reinforcement strength and the applied surcharge were reduced by the scale factor N (i.e., T_{ul} = 10 kN/m, and Q_S = 96 kN/m). For the RS-4 case, the reinforcement strength was reduced by the scale factor N and the magnitude of the applied surcharge was reduced by N^2. Both the magnitude of the applied

surcharge and the reinforcement strength were reduced by N^2 in the RS-5 case (i.e., T_{ul} = 2 kN/m, and Q_S = 19.2 kN/m).

Table 3.5 Reinforced walls under strip loading

	Case	T_{ul} (kN/m)	Q_S (kN/m)	FS
Model VI	Prototype	50	480	1.01
	RS-1	50	480	0.8
	RS-2	50	96	7.81
	RS-3	10	96	1.18
	RS-4	10	19.2	20.53
	RS-5	2	19.2	1.01

Table 3.5 indicates that when the reinforcement strength and the magnitude of the strip surcharge were scaled down by N^2 (i.e., T_{ul} = 2 kN/m and Q_S = 19.2 kN/m) in the RS-5 case, the same factor of safety as that for the prototype was yielded. Figure 3.12 and 3.13 show that the RS-5 case, in which both the reinforcement strength and the magnitude of the applied strip surcharge were scaled down by N^2, had the same slip surfaces as the prototype.

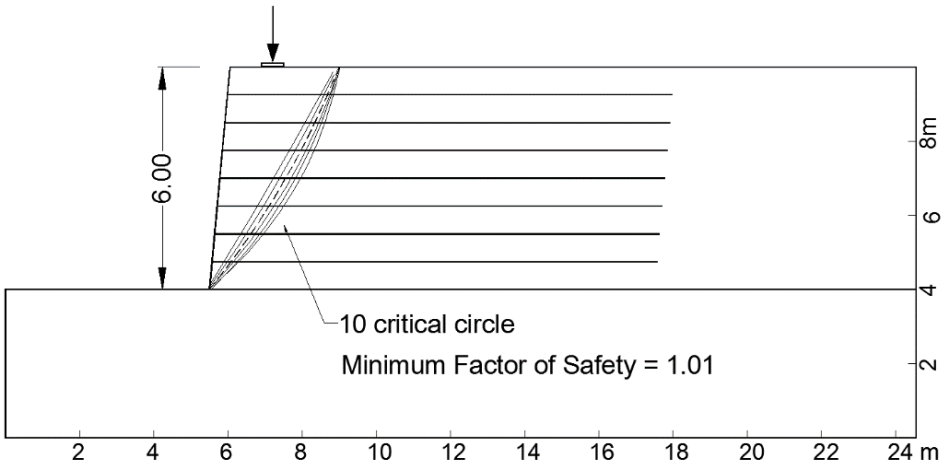

Figure 3.12 Model-VI-Prototype

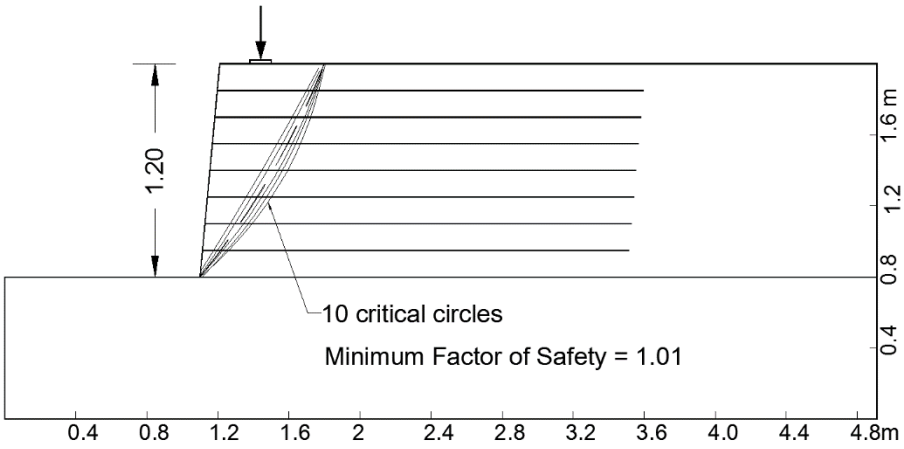

Figure 3.13 Model VI RS-5 Case

Similarly, Figures 3.14 and 3.15 show that the RS-5 case had the same safety map as the prototype when the reinforcement strength and the magnitude of the applied strip surcharge were scaled down by N^2 in the RS-5 case. On the other hand, the reduced scale model (RS-1) with the same reinforcement strength and the same applied surcharge of the prototype resulted in a lower factor of safety (i.e., FS = 0.8) than that of the prototype. This result is due to the use of the higher applied surcharge (i.e., Q_S = 480 kN/m) than the scaled applied surcharge (i.e., Q_S = 19.2 kN/m).

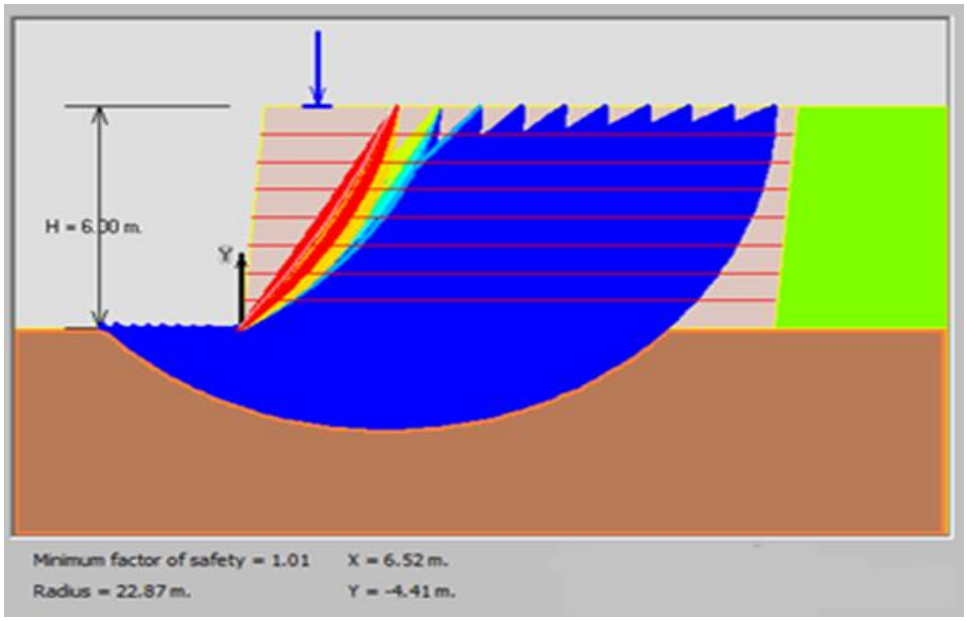

Figure 3.14 Model VI Prototype

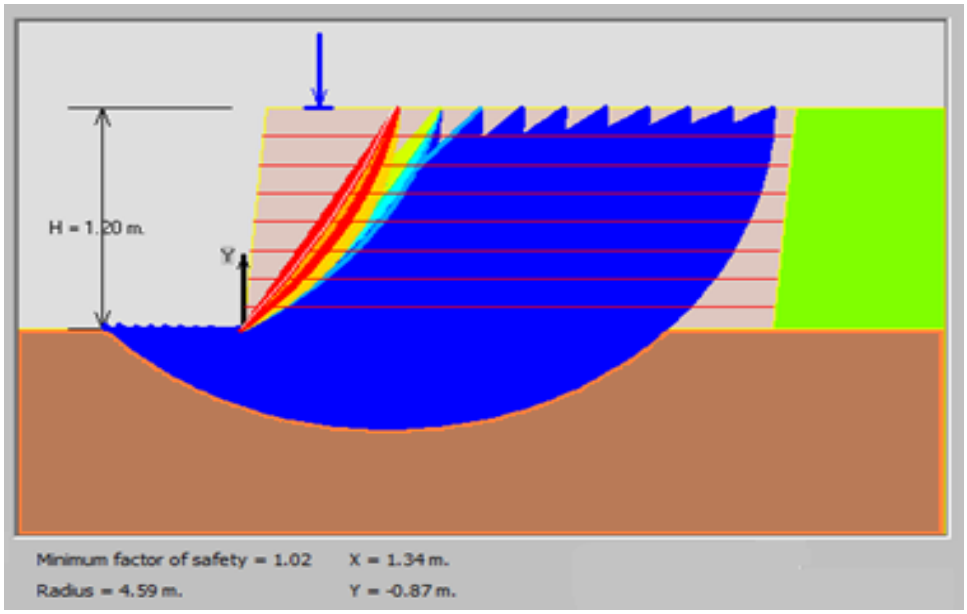

Figure 3.15 Model VI RS-5 Case

Table 3.5 also shows that the use of the same reinforcement strength as that of the prototype in a reduced scale model (i.e., the RS-2) and the scaled magnitude of the applied

surcharge by N (Q_S = 96 kN/m) resulted in a much higher factor of safety (i.e., FS = 7.82) than that of the prototype. However, the RS-2 case had very similar critical slip surfaces as the prototype (i.e., Figure 3.11 vs. Figure 3.16).

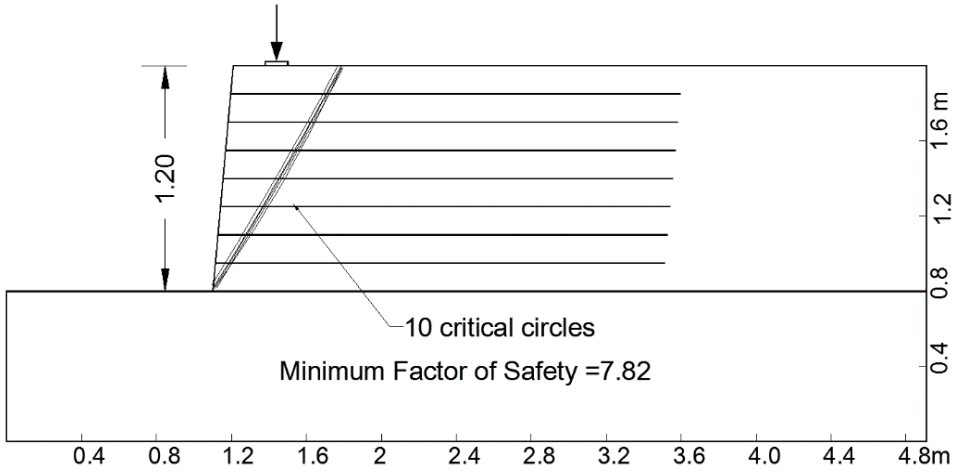

Figure 3.16 Model VI RS-2

In addtion, when the strength of the reinforcement scaled by N (i.e., T_{ul} = 10 kN/m) and the magnitude of the applied load reduced by N^2 (i.e., Q_S = 19.2 kN/m) in the RS-4 case, it yielded a higher factor of safety (i.e., FS = 20.53) than the RS-5 case and the prototype (i.e., FS = 1.01). Figure 3.17 shows the critical failure surfaces of the RS-4 case, which are different from those of the prototype or the RS-5 case, indicating that the improper use of a scale factor for a reduced-scale model could result in different slip surfaces.

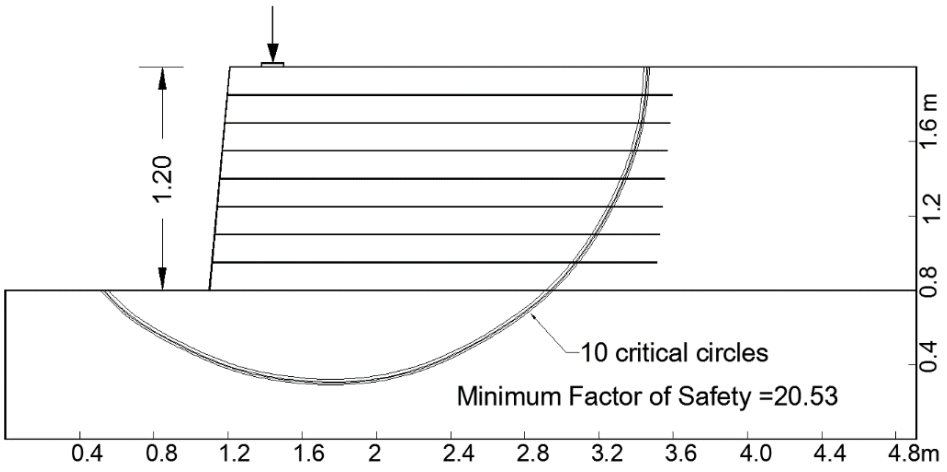

Figure 3.17 Model VI RS-4

Results of limit equilibrium analysis for scale factors (N) = 1/3 and 1/10

Further analyses were done in this study to check whether the same conclusions were still valid for other scale factors. In these analyses, a reduced-scale model was used as the baseline case to predict the behavior of a prototype (i.e., a full-scale model). Table 3.6 shows the results of these analyses.

Based on the results of the earlier analyses (i.e., N =1/5), the scale factor N^2 was applied to the reinforcement strength and the applied strip surcharge (considering the width of the loading plate was scaled by N), and the scale factor N was applied to the uniform surcharge.

All the cases in the Model I had no applied surcharge, while the Model II and Model III cases were subjected to uniform and strip surcharge, respectively.

Tables 3.3, 3.4, and 3.5 presented the results of the RS-3, RS-4, and RS-5 cases, respectively. These three models represent the reduced-scale model walls of 1.2 m high, subjected to zero surcharge, a uniform surcharge (Q_U = 36 kPa), and a strip surcharge (Q_S = 19.2 kN/m), respectively. The FS-1 and FS-2 cases in all the models represent the full-scale model walls of 3.6 m (N= 1/3) and 12.0 m (N=1/10), respectively.

Table 3.6 Reinforced walls for N = 1/3 and 1/10

Model I	**Case**	T_{ul} (kN/m)	Surcharge (Q)	FS
	RS-3	0.8	0.0	1.02
	FS-1	7.2	0.0	1.02
	FS-2	80	0.0	1.02
Model II	**Case**	T_{ul} (kN/m)	Q_U (kPa)	FS
	RS-4	2	36	1.0
	FS-1	18	108	1.0
	FS-2	200	360	1.0
Model 3	**Case**	T_{ul} (kN/m)	Q_S (kN/m)	FS
	RS-5	2	19.2	1.02
	FS-1	18	172.8	1.03
	FS-2	200	1920	1.02

Table 3.6 shows that the increase of the reinforcement strength by N^2 in the Model I cases (i.e., T_{ul} = 7.2 kN/m in the FS-1 case with N=3.0, and T_{ul} = 80 kN/m in the FS-2 case with N=10) generated the same factor of safety as that of the reduced-scale model (i.e. FS=1.02). Figures 3.18 and 3.19 show the critical slip surfaces and the factors of safety generated by ReSSA (3.0) for the FS-1 and FS-2 cases.

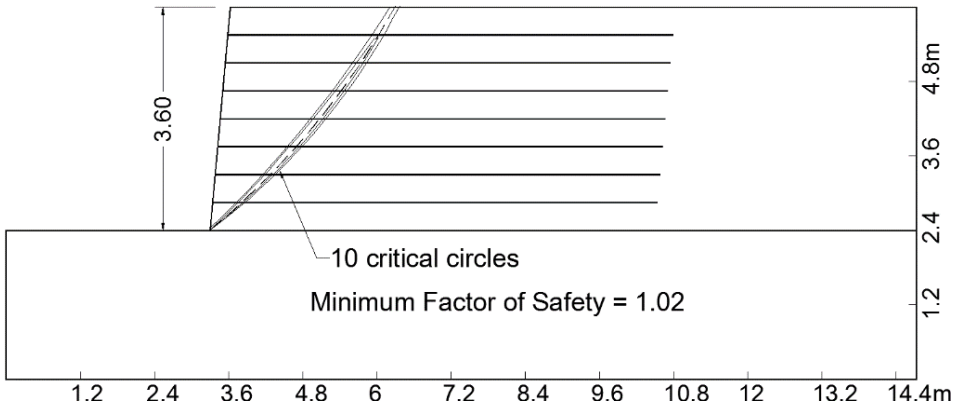

Figure 3.18 Model I FS-1

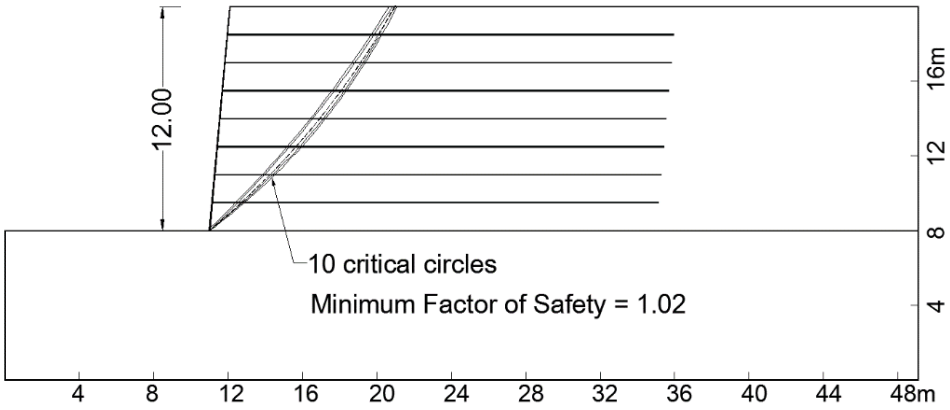

Figure 3.19 Model I FS-2

Figures 3.18 and 3.19 also show that the analysis yielded the same slip surfaces for both cases (FS-1 and FS-2). As compared with Figure 3.3, Figures 3.18 and 3.19 show the same slip surfaces as those of the RS-3 case.

Table 3.6 also shows that the increase of the reinforcement strength by N^2 in the Model II cases (i.e., T_{ul} = 18 kN/m for the FS-1 case with N=1/3, and T_{ul} = 200 kN/m for the FS 2 case with N=1/10) and the magnitude of the applied surcharge by N (i.e., Q_U = 108 kPa for the FS-1 case, and Q_U = 360 kPa for the FS-2 case) resulted in the same factor of safety as that of the RS-1 case (i.e., FS=1.0).

Figures 3.20 and 3.21 show that the increase of the strength of the reinforcement and the magnitude of the applied surcharge by N^2 (i.e., Q_S = 172.8 kN/m in the FS-1 case with N=1/3 and Q_S = 1920 kN/m in the FS-2 case with N=1/10) to the reduced-scale model resulted in the same factor of safety and slip surfaces as those of the baseline model (Figure 3.13). These results and comparisons indicate that the reduced-scale models can be used to predict the behavior of the prototype model in term of the factor of safety and slip surfaces.

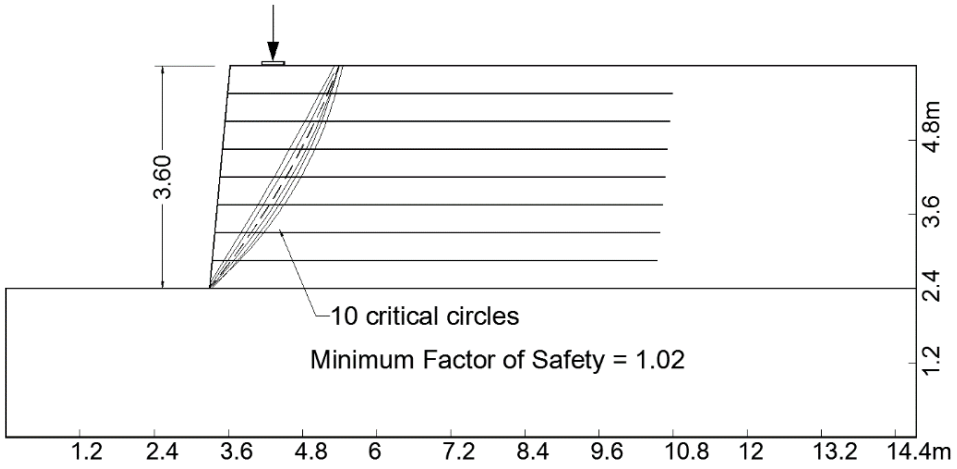

Figure 3.20 Model III FS-1

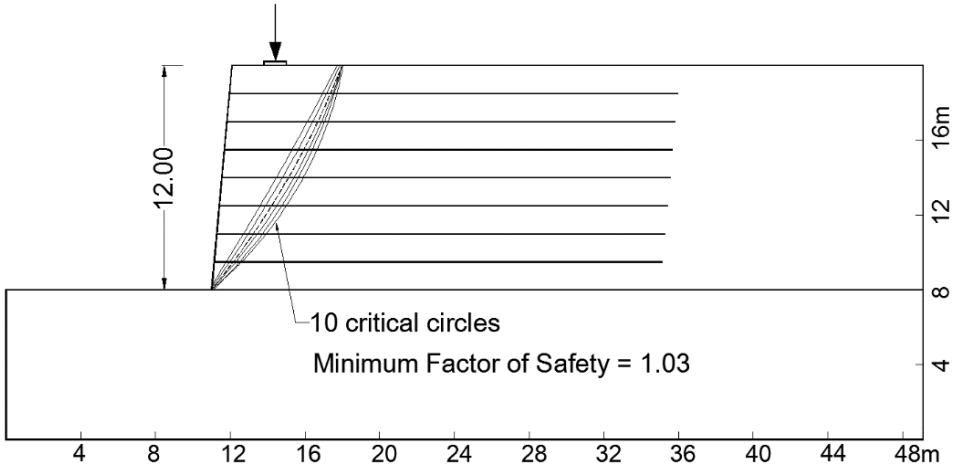

Figure 3.21 Model III FS-2

In summary, all three methods (i.e., the dimensional analysis, the FHWA equations, and the limit equilibrium method) used in the above analyses resulted in the same scale factor. Table 3.7 presents the scale factors used for different parameters in prototype and reduced-scale model walls in this study. These scale factors were used in this study to design the reduced-scale model tests to be discussed in Chapter 4.

Table 3.7 Scale factors for various parameters

Parameters	**Scale Factor**
Model Height (H)	N
Model Length (L)	N
Reinforcement Stiffness (J)	N^2
Uniform Surcharge (Q)	N
Strip Surcharge (q)	N^2

Chapter 4 Laboratory Model Tests

4.1 Introduction

An experimental program was designed and conducted to study the behavior of geosynthetic reinforced retaining (GRR) walls with limited fill space under static loading. This chapter presents the layouts of the model tests, the properties of the material used, the test instrumentation, and the measurement methods.

4.2 Test plan

A series of limited space GRR wall models constructed in front of a stable face were planned to test under static footing loading. The models were tested under plane strain conditions. Table 4.1 presents the detail of the model test plans. The model walls were 1.0 m high, 0.45 m wide and had various lengths, which simulated three-meter high full-scale walls. Therefore, the scale ratio (i.e., the ratio between the model size (reduced-scale) to the prototype size (full-scale) = 1/3). The stable face was modeled by a solid wooden block.

Figures 4.1 to 4.6 illustrate the layouts of all the model tests conducted in this study. Figure 4.1 illustrates the layout for the A1 model test, which simulates a typical GRR wall with reinforcement length of 0.7H (H is the height of the wall) and retained backfill (retained medium) of 0.5H wide.

The A1 model test is the only model that had retained backfill. The purpose of testing this model (the A1 model test) was to examine the effect of retained fill on the behavior of GRR walls. Figure 4.2 shows the test layouts for the models with reinforcement length of 0.7H and no retained backfill to simulate the wall with the minimum reinforcement requirement and constructed in front of a stable face. Figure 4.2 (a) shows the A2-I model test while Figure 4.2(b) shows the A2-II

model test. These two model tests are almost identical except for different footing offsets. The A2-II model test was conducted as the control model test.

Table 4.1 Model test details

Model	Wall Width	Reinforcement spacing (m)	Reinforcement rear connection	Retained medium	Footing* offset (m)
A1	0.7H	0.2	not connected	0.5H retained fill	0.2
A2-I	0.7H	0.2	not connected	stable	0.2
A3-I	0.5H	0.2	not connected	stable	0.2
A4	0.3H	0.2	not connected	stable	0.05
B1	0.3H	0.1	not connected	stable	0.05
C1	0.3H	0.2	connected	stable	0.05
C2	0.3H	0.2	connected**	stable	0.05
C3	0.3H	0.2	bent upward	stable	0.05
C4	0.5H	0.2	bent upward	stable	0.05
A2-II	0.7H	0.2	not connected	stable	0.05
A3-II	0.5H	0.2	not connected	stable	0.05

* Distance from the back of wall facing to the near edge of the footing;
** Two top layers connected

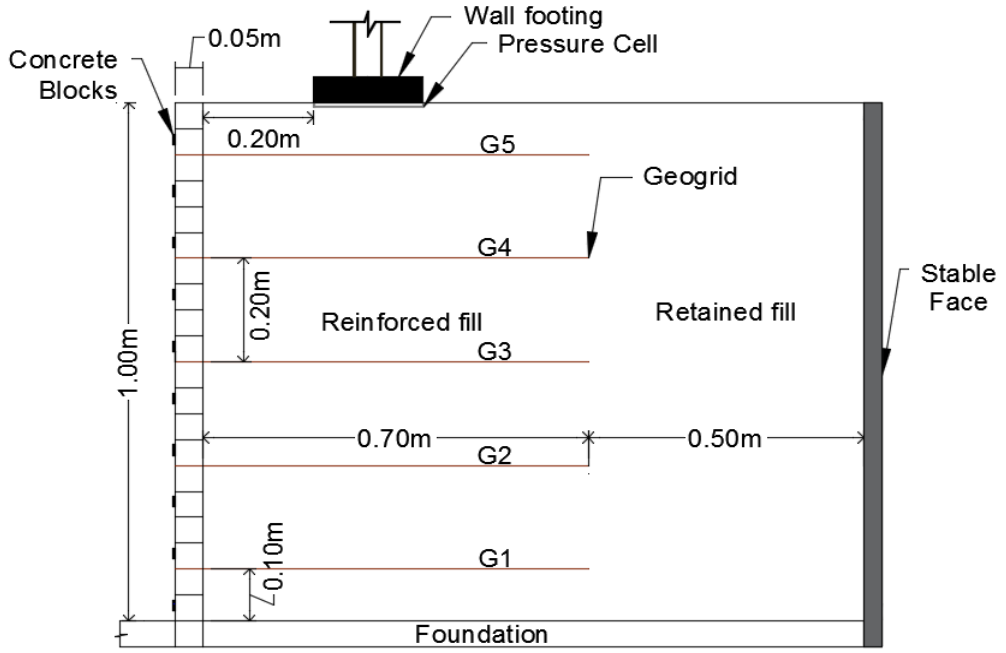

Figure 4.1 Test layout for A1 model

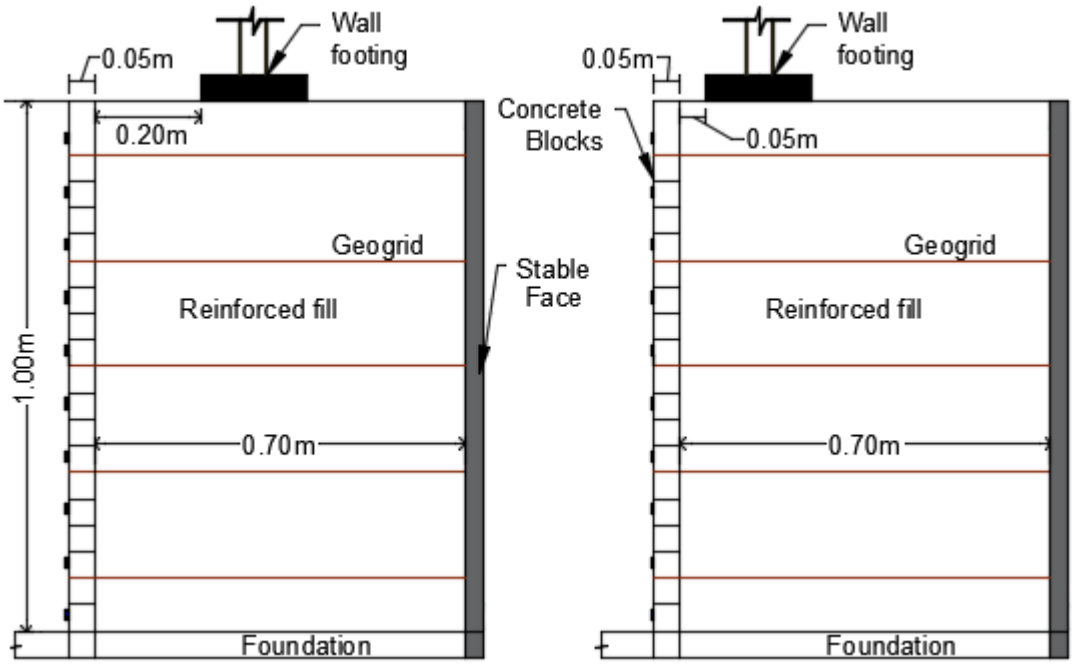

(a) (b)

Figure 4.2 Test layouts for (a) the A2-I model and (b) the A2-II model

Figure 4.3 shows the test layouts for both the A3-I model and the A3-II model. These two model tests were almost identical and had reinforcement length of 0.5H but they had different footing offsets. The A3 models were planned to simulate GRR walls with reinforcement length of 0.5H, constructed in front of a stable wall and subjected to a footing load. Figure 4.4 illustrates the A4 model and the B1 model, which had reinforcement length of 0.3H. However, the B1 model had smaller vertical spacing of reinforcement (i.e., reinforcement vertical spacing = 100 mm) than the A4 model.

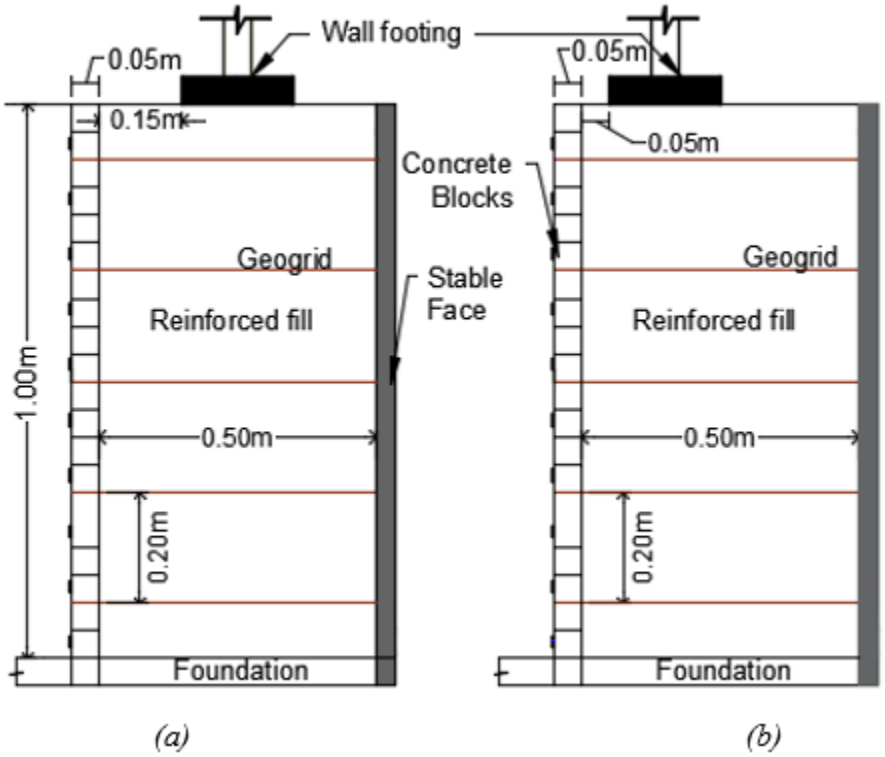

Figure 4.3 Test layouts for (a) the A3-I model and (b) the A3-II model

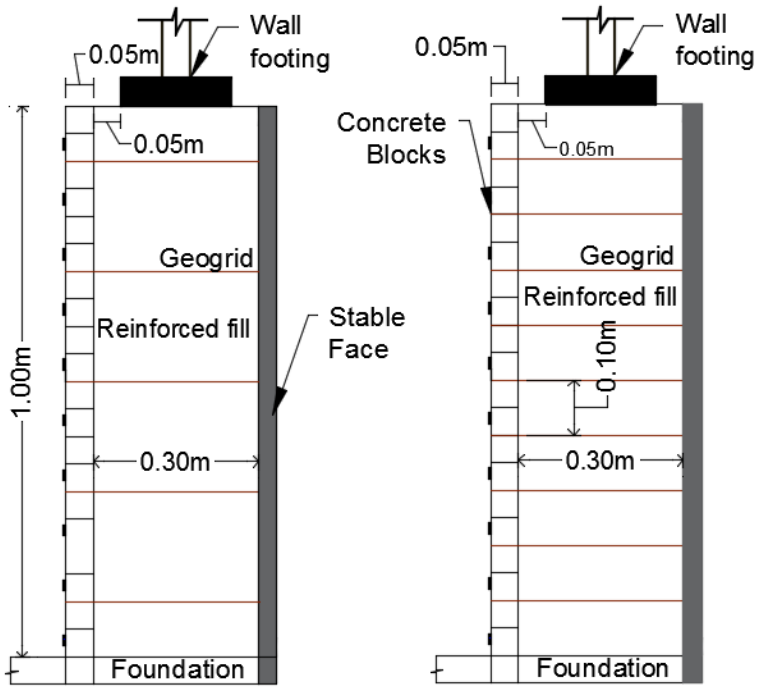

(a) (b)

Figure 4.4 Test layouts for (a) the A4 model and (b) the B1 model

Figure 4.5 illustrates the C1 model and the C2 model that had reinforcement layers connected (fixed) to the stable face at the rear. Both models had the same reinforcement length (i.e., L=0.3H) and the same footing offset distance. Four layers out of five layers of the reinforcement were connected to the stable face at the rear in the C1 model, while only the two uppermost layers of the reinforcement in the C2 model were connected to the stable face at the rear (i.e., connecting the rear of the reinforcement to the stable face by the use of anchors, ties, or connectors). Figure 4.5(a) shows the enlarged view of the connectors built to connect the rear of the reinforcement to the stable face. The purpose of connecting the reinforcement to the stable face was to examine the effect of rear connection on the performance of limited fill space walls as suggested by Leshchinsky et al. (2004) and Lawson and Yee (2005).

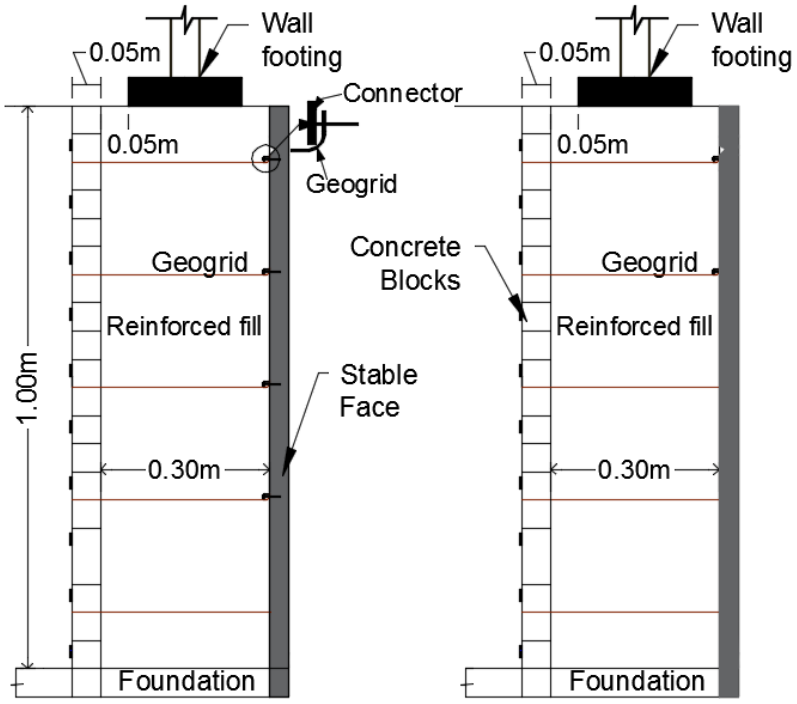

Figure 4.5 Test layouts for (a) the C1 model and (b) the C2 model

Figure 4.6 illustrates the C3 model and the C4 model tests that had all reinforcement layers bent upward with a bent length of 0.2 m at the rear along the stable face. The C3 model wall had reinforcement length of 0.3H while the C4 model wall had reinforcement length of 0.5H.

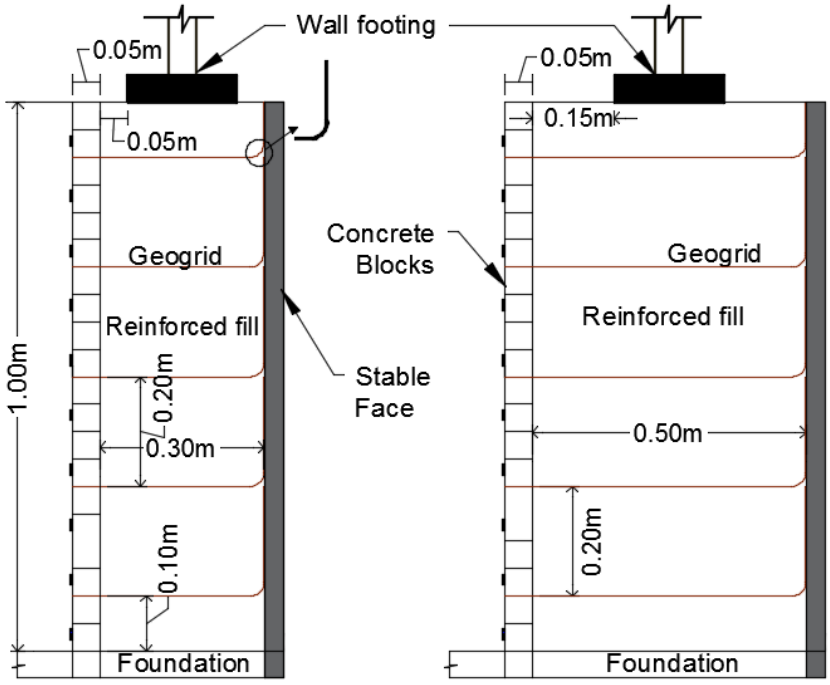

(a) (b)

Figure 4.6 Test layouts for (a) the C3 model and (b) the C4 model

4.3 Test box

The inside dimensions of the test box were 2.4 m long, 0.45 m wide, and 1.1 m high. The main body of the box was made of structural steel sections. Figure 4.7 shows the schematic view of the test box. Two sides of the box were made of 20-mm thick transparent glass plates, which allowed for visualizing and mapping of distortions, such as wall deformation, failure plane, and footing settlement, during the test. To minimize the boundary effect due to the friction of the sides of the box, lubricant was applied onto the glass plate from inside.

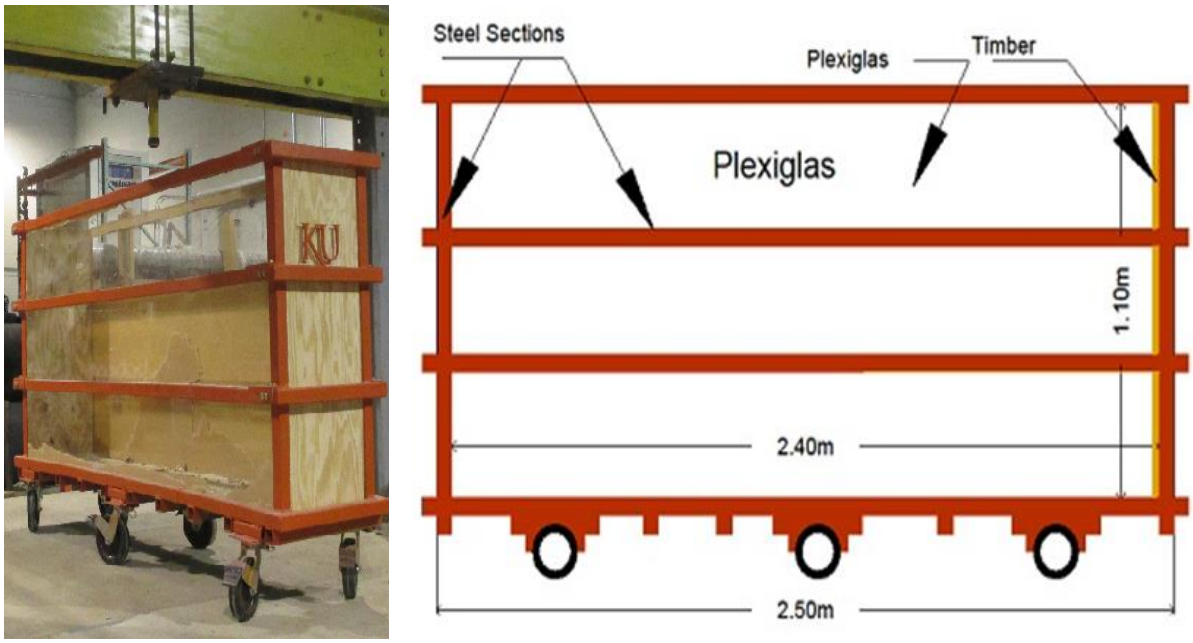

Figure 4.7 Schematic view of the box for model tests

4.4 Footing

The rigid strip footing was made from a 25-mm thick steel plate. The steel plate was reinforced by two steel profiles to minimize its bending under loading. The footing was 200 mm wide and 450 mm long. To ensure a plane strain condition, the length of the footing was approximately equal to the internal width of the test box with a small gap between the footing and the glass plates.

4.5 Materials

4.5.1 Backfill

Kansas River sand (Figure 4.8) was used as backfill for all the model tests conducted in this study. The sand was classified as a poorly graded sand (SP) according to the Unified Soil Classification System. Figure 4.9 shows the particle size distribution of the sand used in this

study. Laboratory tests in accordance with ASTM D4254-00 and ASTM D4253-00 were conducted to determine the minimum and maximum densities of the sand, respectively. The relative density of sand (R_d) was determined from the following equation:

$$R_d\,(\%) = \frac{\gamma_{dmax}\,(\gamma_d - \gamma_{dmin})}{\gamma_d\,(\gamma_{dmax} - \gamma_{dmin})} x\ 100 \qquad \ldots\ 4.1$$

where

$\gamma_{d\,min}$= the minimum dry unit weight (kN/m^3),

$\gamma_{d\,max}$ = the maximum dry unit weight (kN/m^3),

γ_d = the dry unit weight that corresponds to a specified relative density (kN/m^3).

The sand was compacted to a relative density R_d =70%, which corresponds to the dry unit weight 17.8 kN/m^3 in the model tests.

Figure 4.8 Kansas River sand

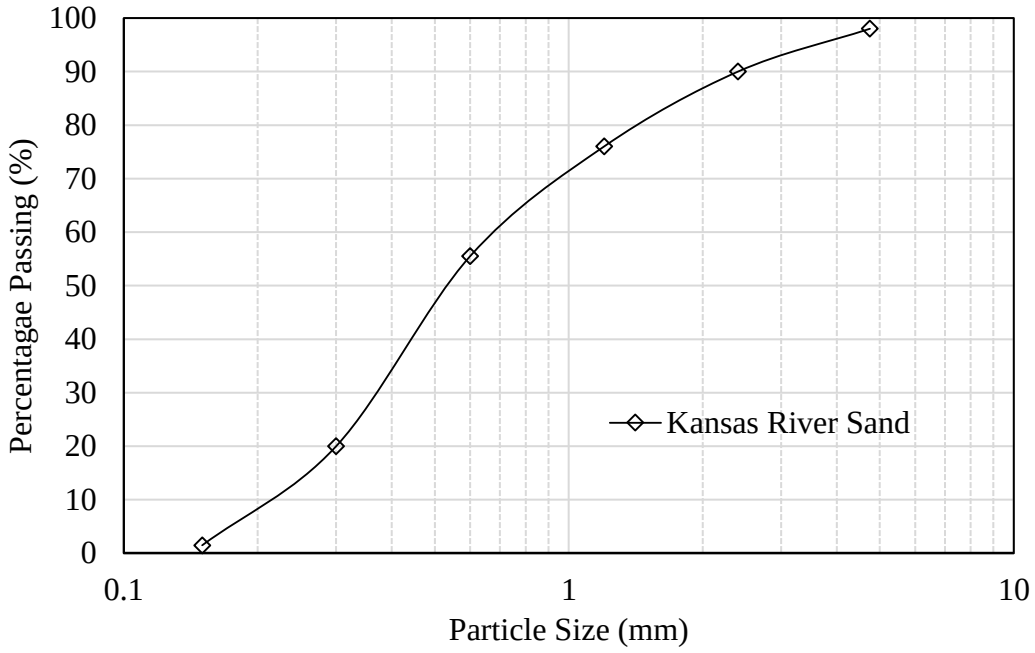

Figure 4.9 Particle size distribution of the Kansas River sand

Three triaxial compression tests (ASTM D7181) at different confining stresses (34.5, 68.9, and 103.3 kPa) were performed on the sand compacted at approximately 70% relative density to determine the shear strength parameters, c (cohesion) and Φ (internal friction angle). Figure 4.10 shows the results of the triaxial compression tests of Kansas River Sand used in this study, and Table 4.2 shows the properties of the sand.

Table 4.2 Properties of backfill material

Properties	Value
Minimum dry unit weight, $\gamma_{d\ min}$ (kN/m^3)	16.1
Maximum dry unit weight, $\gamma_{d\ max}$ (kN/m^3)	18.9
Uniformity coefficient ,C_u	3.18
curvature coefficient, C_c	0.93
Cohesion (kPa)	0
Internal friction angle, Φ	37^O

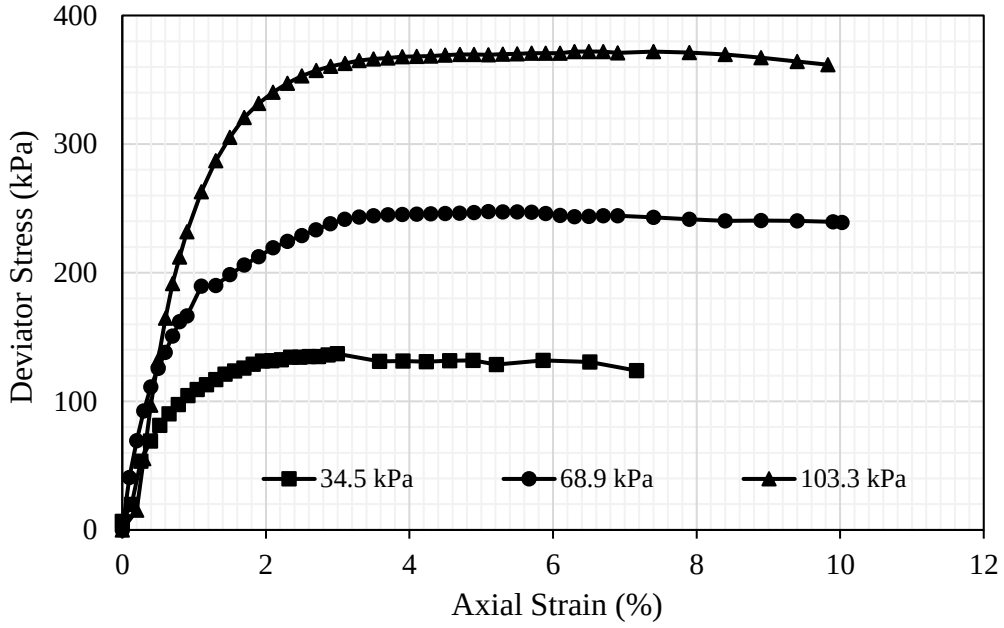

Figure 4.10 Triaxial compression test results of the Kansas River sand

4.5.2 Wall facing

Facing is a component of the reinforced soil retaining wall system used to prevent the soil from raveling out between the rows of reinforcement. The wall facing was made with individual modular concrete blocks, which were prepared by cutting plain concrete blocks available in the market. Each block was 150 mm long (exposed face length), 50 mm high, 50 mm wide (dimension perpendicular to the wall face). In practice, block heights range from 100 to 300 mm, with 200 mm as typical. Block length (exposed face length) usually varies from 200 to 450 mm. Block width (dimension perpendicular to the wall face) varies from 200 and 600 mm (FHWA, 2009). Considering the scale ratio of 1/3, the block heights should range from 33 to 100 mm, exposed face length should vary from 67 to 150 mm, and the dimension perpendicular to the wall face should range between 67 to 200 mm. The dimensions of the wall facing units used in this

study were in the ranges as stated above. Figure 4.11 shows the concrete blocks used for the wall facing.

Figure 4.11 Concrete blocks used for wall facing

4.5.3 Geosynthetic reinforcement

Punched-drawn biaxial geogrid (BX) made of polypropylene material was used in the model tests. Table 3.3 presents the properties of the biaxial geogrid used in this study, which were provided by the manufacturer (Tensar International). Table 4.3 shows that the geogrid had ultimate tensile strengths of 12.4 kN/m in the machine direction (MD) and 19 kN/m in the cross-machine direction (XD). However, in practice, uniaxial geogrids are commonly used in GRR walls. Thus, in this study, to create a configuration of uniaxial geogrid, three ribs of a biaxial geogrid in the machine direction (transverse ribs) were removed every four ribs. This modification was first used by Xiao et al. (2016) and then by Kakrasul et al. (2016) and Rahmaninezhad et al. (2016).

Punched-drawn uniaxial geogrids typically have the aperture size in the longitudinal direction of 300 - 500 mm. Accounting for the scale ratio of 1/3, the aperture of the model geogrid in the longitudinal direction should be in the range of 100 to 160 mm. The model geogrid used in this study had the aperture length of 140 mm, which is within this range. Figure 4.12 shows a sample of the geogrid used in this study. To determine the tensile strength of the geogrid in the cross-machine direction after the removal of some ribs, Xiao et al. (2016) conducted tensile strength tests with and without removed ribs following ASTM D6637. Xiao et al. (2016) showed that the removal of the transverse ribs reduced the ultimate tensile strength of the geogrid in the cross-machine direction by 7%. In this study, the cross-machine direction of the biaxial was the same as the longitudinal direction of the uniaxial geogrid. Xiao et al. (2016) found that the tensile strength of the geogrid in the cross-machine direction was 17.6 kN/m after the removal of partial ribs.

Table 4.3 Geogrid properties

Index properties	Units	MD Values	XMD Values
Aperture dimensions	mm	24	33
Minimum rib thickness	mm	0.76	0.76
Tensile strength at 2% strain	kN/m	4.1	6.6
Tensile strength at 5% strain	kN/m	8.5	13.4
Ultimate tensile strength	kN/m	12.4	19.0
Structural Integrity			
Junction Efficiency	%	93	-
Flexural Stiffness	Mg-cm	750,000	-
Aperture Stability	m-N/deg	0.65	-

Note: MD stands for the machine direction; XMD stands for the cross-machine direction.

The typical tensile strengths of punched-drawn uniaxial geogrids used in practice range from 58 to 210 kN/m (Tensar International, 2012). Based on the results of the scale effect analysis conducted in this study; the mechanical properties of geosynthetic materials used in the 1-g laboratory-scale models should be scaled down by N^2, where N is the ratio of the prototype size (full scale) and the model size (reduced scale). To account for the scale ratio of 1/3, the tensile strength of the model geogrid should be reduced to 1/9 that of a field geogrid. Thus, the tensile strength of the model geogrid should be in the range of 6.4 to 23.3 kN/m. The tensile strength of the model geogrid used in this study (i.e., 17.5 kN/m) was within this range.

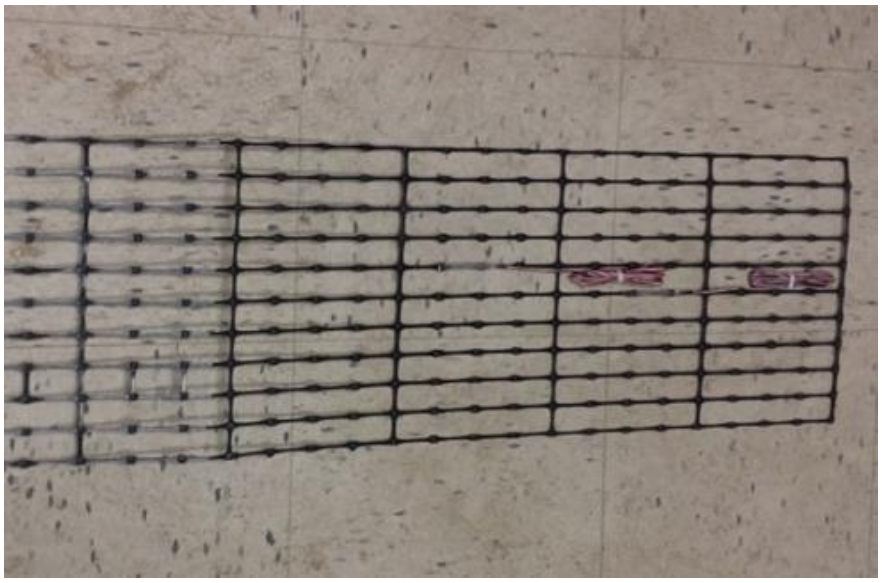

Figure 4.12 Geogrid sample used for the pullout test

In addition, to determine soil/reinforcement interface properties for the modified geogrid, a set of the pullout tests in accordance with ASTM D6706-01 (2013) were carried out in a large pullout box in the geotechnical laboratory of the University of Kansas. Weldu et al. (2016) described the pullout box in detail in their study. A 370 mm wide and 765 mm long geogrid was

used in the pullout test. Figure 4.13 shows a prepared geogrid sample used in the pullout test. The pullout tests were conducted under three normal stresses (14.6, 11.8, and 8.4 kPa). Figure 4.14 shows the results of the pullout tests. The pullout resistances at 20 mm displacement of the modified geogrid under the normal stresses of 14.6, 11.8, and 8.4 kPa, were 15.9, 9.4, and 5.6 kN/m, respectively. The friction coefficient at the soil/reinforcement interface (*f*) was calculated from the following equations:

$$f = \frac{\tau_{max}}{\sigma_v} \qquad \ldots. \ 4.2$$

$$\tau_{max} = \frac{P_{max}}{CA} \quad \ldots. \ 4.3$$

where P_{max} = the maximum pullout load applied on the geogrid;

τ_{max} = the maximum shear stress applied in the geogrid;

A = the area of the geogrid (length x width of the geogrid);

C = the overall reinforcement surface area geometry factor based on the gross perimeter of the reinforcement (equal to 2 for strip, grid, and sheet-type reinforcements);

f = the friction coefficient at the soil/reinforcement interface;

σ_v = the vertical stress applied on the reinforcement.

Based on the test results, the interaction coefficient at the soil/reinforcement interface was 0.85.

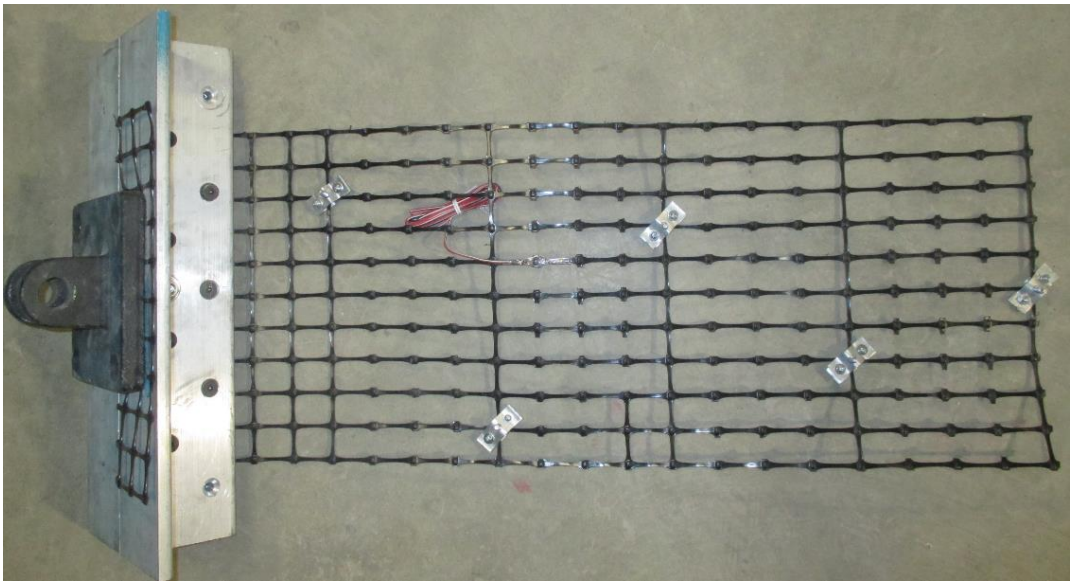

Figure 4.13 Geogrid sample used for the pullout test

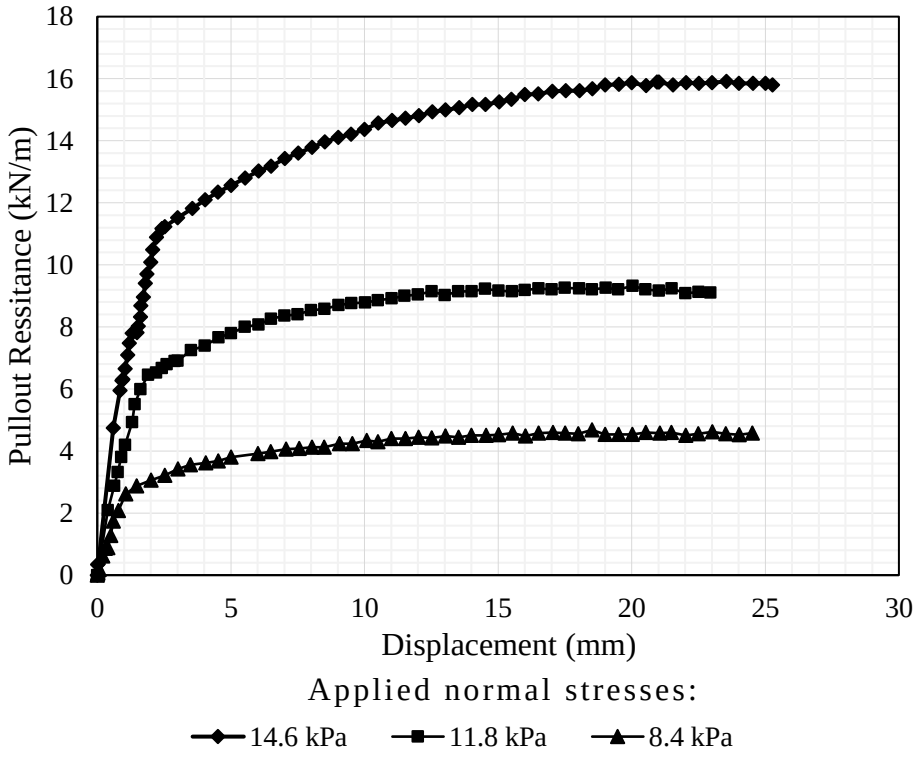

Figure 4.14 Pullout resistance versus displacement of the uniaxial geogrid

4.6 Model test construction

Each model was constructed from the bottom to the top of the wall. The construction of the model started with placing a 5-cm thick layer of Kansas River sand as the foundation and a concrete block as the leveling pad. Figure 4.15 shows the foundation (5-cm thick sand) and the leveling pad. The next step was the placement of facing units (concrete blocks) and 20-cm thick sand in two layers, followed by the placement of the geogrid and the connection to the facing units. Figure 4.16 shows the placement of the first layer of facing units while Figure 4.17 shows the placement of the first layer of sand and geogrid. The geogrid was connected to the facing units by metal pins, which simulate Mechanical connection by mechanical fasteners, such as bolts, screw or rivets, in the field. Figure 4.17 also shows the metal pins used to connect geogrid to the facing units.

The sand layers were compacted to the relative density of approximately 70%, using hand tools. Wooden blocks were placed in front of the facing to support the wall during construction and removed prior to the application of the load. The same procedures were followed until the end of construction. Since blocks and sand in the reduced-scale wall were light, they were easy to move during the construction. Wooden blocks were therefore used in front of wall facing to minimize their movement. Figure 4.18 shows the technique of supporting the model wall during construction. In the field, blocks and fill are relatively heavy, their movement during construction is minimum; therefore, no wall facing support is needed. However, a similar technique is used in practice in case of using concrete panels to temporarily support the facing units during construction.

For each model, five layers of geogrid were placed at 200 mm vertical spacing except for the B1 model, where the geogrids were placed at 100 mm vertical spacing.

.

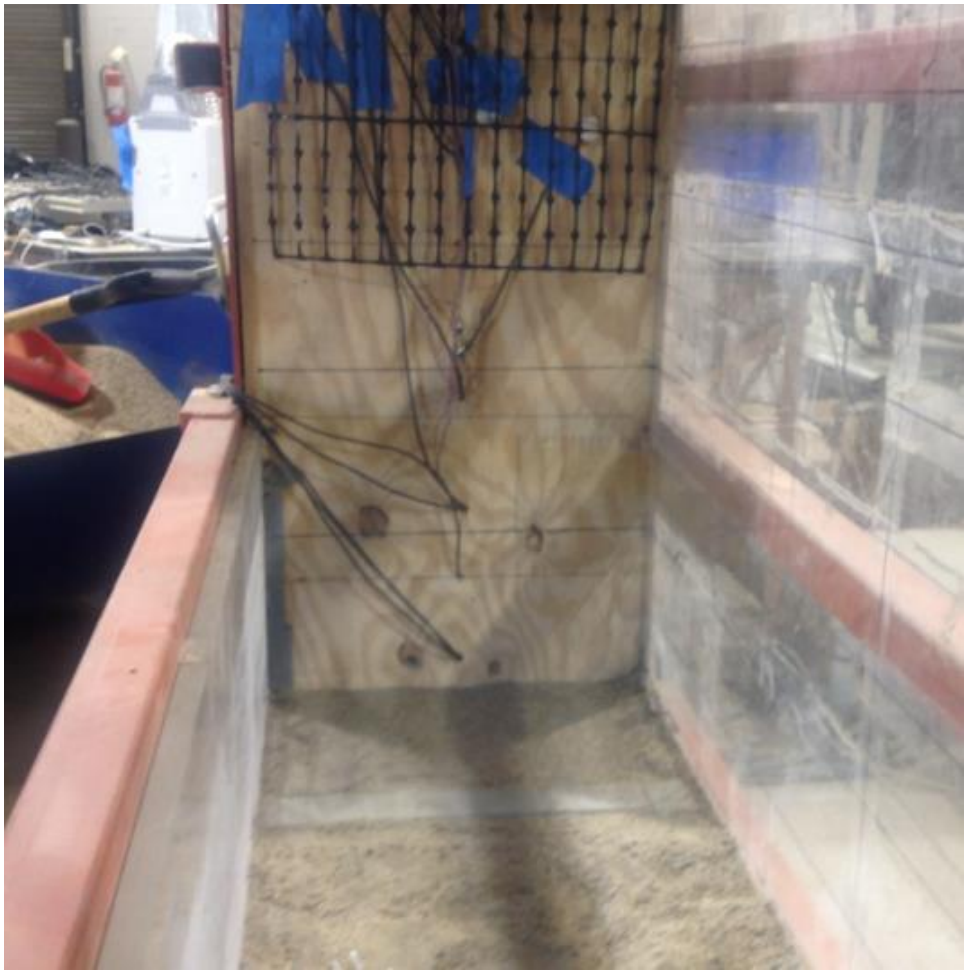

Figure 4.15 The foundation sand and the leveling pad

Figure 4.16 Placement of the first layer of the facing

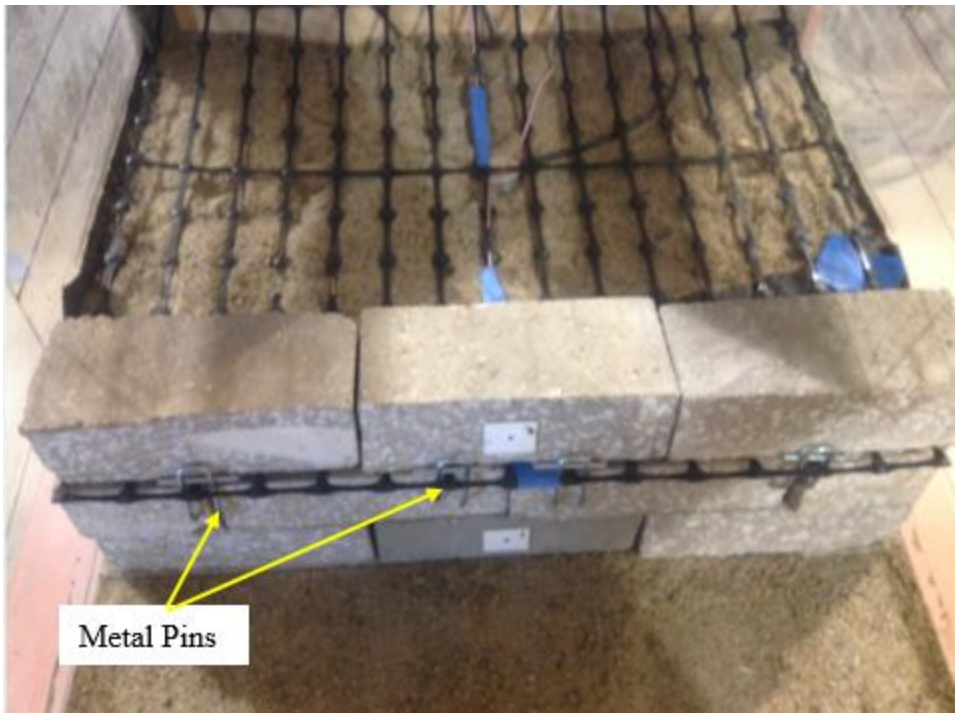

Figure 4.17 Placement of the first fayer of sand and the geogrid

Figure 4.18 Supporting blocks for the model wall during construction

In addition, thin and low-strength gardening sheets were used between the facing units and the backfill to retain the sand behind the facing and prevent it from flowing out (Figure 4.19).

Figure 4.19 Placement of the gardening sheet

Some models (i.e., the C1, C2, C3, and C 4 models) had different geogrid configurations at the rear. Figure 4.20 shows the bent-upward configuration of geogrid used in the C3 and C4 models. In these models, the geogrid layers were smoothly curved at 90^{o} at their rear and along the stable rear face.

The geogrid layers in the C1 and C2 models were connected to the stable rear face. A wooden strip was installed, and the geogrid was back-folded and inserted between the wooden strip and the stable rear face. Subsequently, the geogrid was fixed by the wooden bar using nails. Figure 4.21 shows how the geogrid was connected to the stable rear face as used in the C1 and C2 models to simulate the geogrid fixture condition. All models were vertical with a zero-degree facing batter during the construction.

Figure 4.20 Bent-upward geogrid

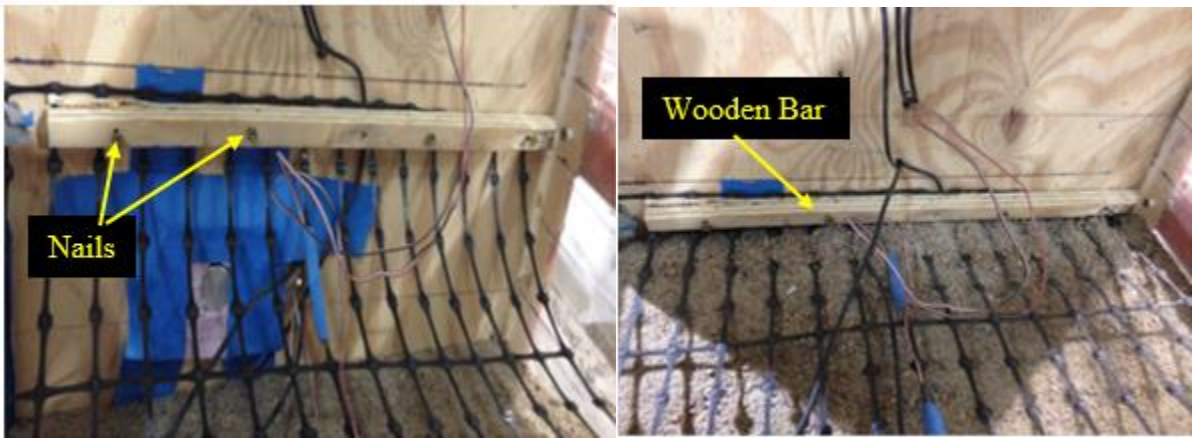

Figure 4.21 Connected geogrid at rear

4.7 Test setup and instrumentation

Several strain gauge-type pressure cells of 25 mm in diameter with capacities of 200 to 500 kPa were used to measure the vertical and horizontal earth pressures in the models. Figure 4.22 shows the earth pressure cells and their layout at the bottom of a model. A laser tape having an accuracy of 0.1 mm was used in this study to measure the settlement of the loading plate and the lateral displacements of the wall facing.

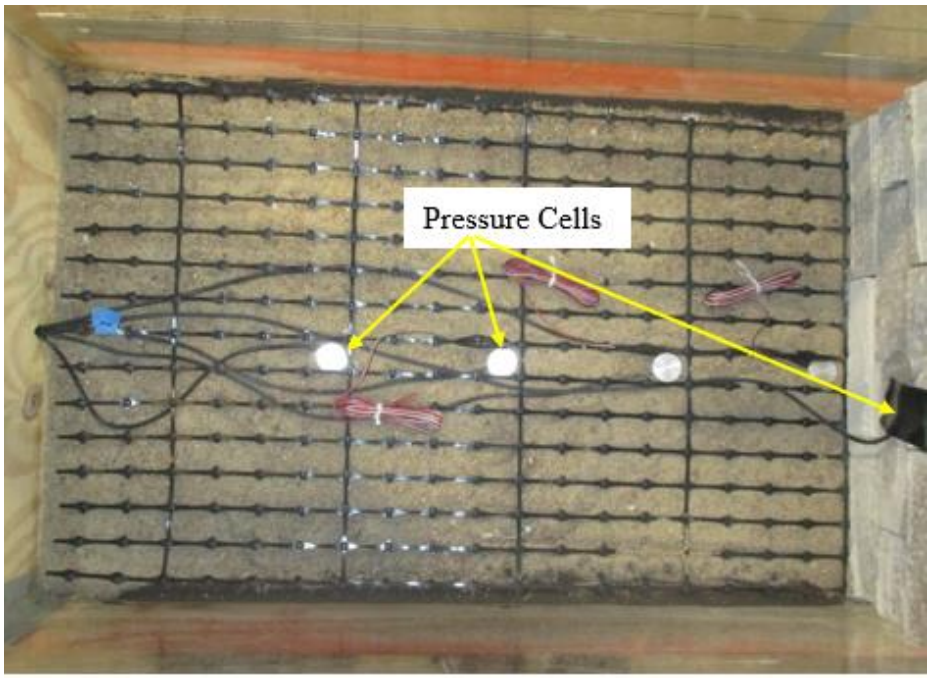

Figure 4.22 Layout of earth pressure cells

Figure 4.23 shows the laser type used in this study. In addition, two digital cameras were used to capture the wall deformation and evaluate possible slip surfaces during loading stages. Marks on facing units and on the footing loading plate were installed to measure wall deformations, and footing settlements, respectively. Figure 4.24 shows the displacement targets installed on the front of a model while Figure 4.25 shows the camera and displacement targets installed on the side of a model. Figure 4.26 illustrates a typical model cross section with the

location of the applied load, pressure cells, deformation mark references, and camera bench marks.

Figure 4.23 Laser tape

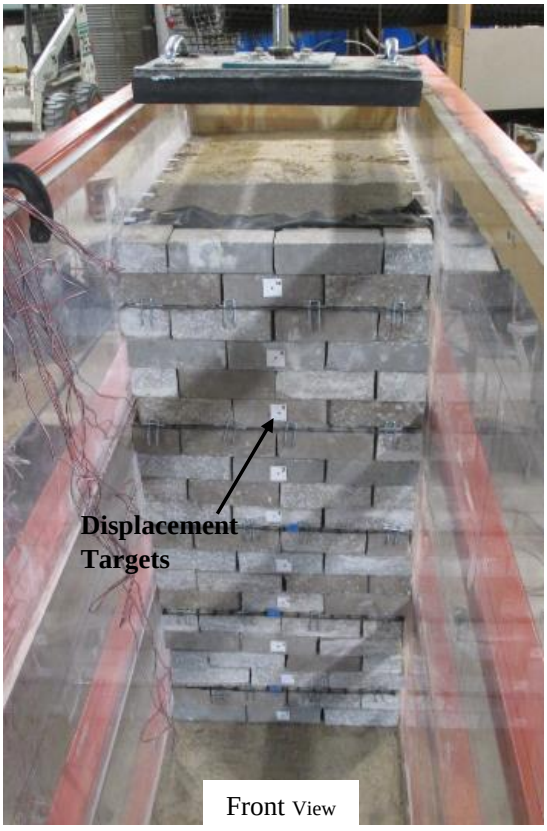

Figure 4.24 Displacement targets on the front of a model

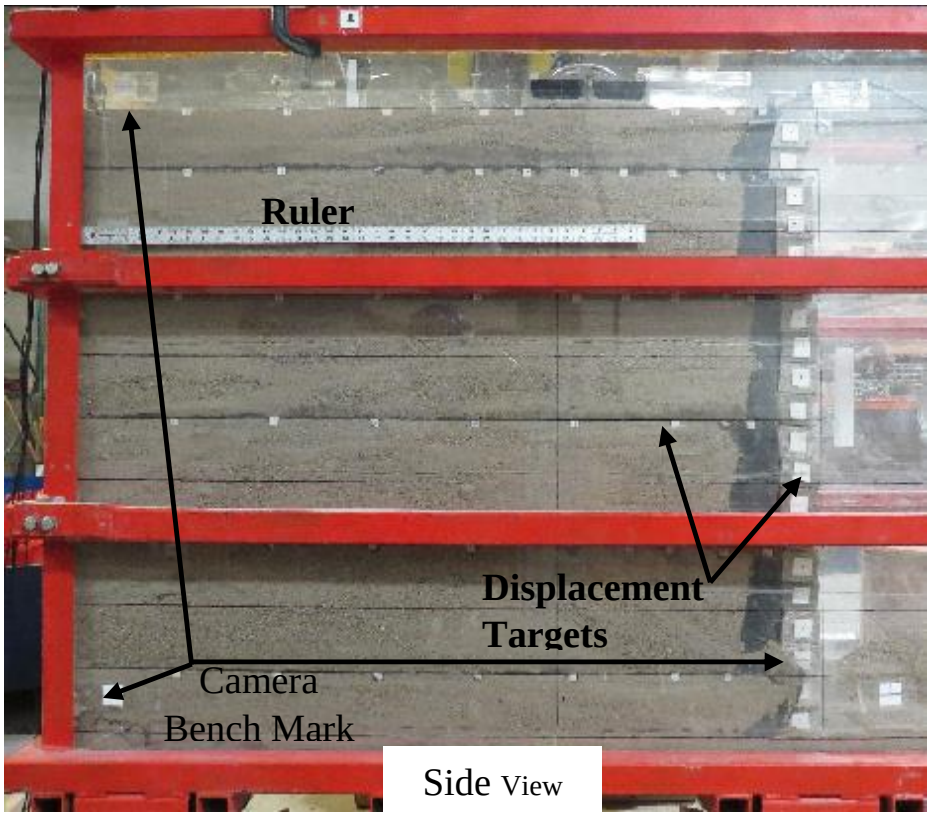

Figure 4.25 Camera and displacement targets on the side of a model

4.8 Test procedures and measurements

In each model test, a load was applied on the top of the model through the footing (200 mm wide and 450 mm long). The loading system consisted of a hydraulic jack, which was controlled manually via a check and control valve and a pressure dial gauge. After the construction of the model wall, initial readings were taken for the instruments prior to the application of the load. After the application of each load, the load was maintained until all the measurements were taken. A data acquisition system (Figure 4.27) connected to a personal computer was used to measure and record the lateral and vertical earth pressures through the installed pressure cells during loading. Figure 4.28 shows the schematic view of the test setup.

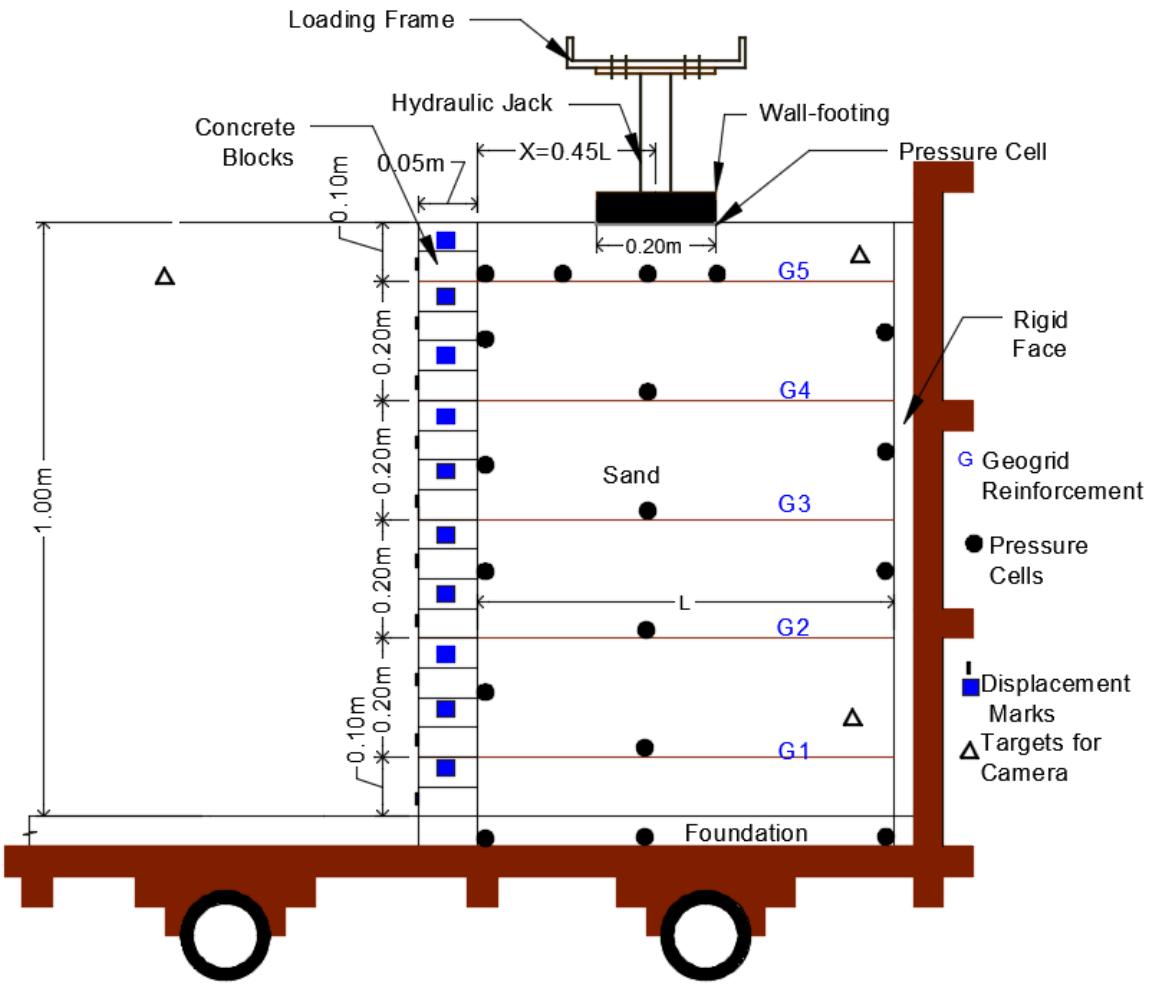

Figure 4.26 A Typical layout of the model test

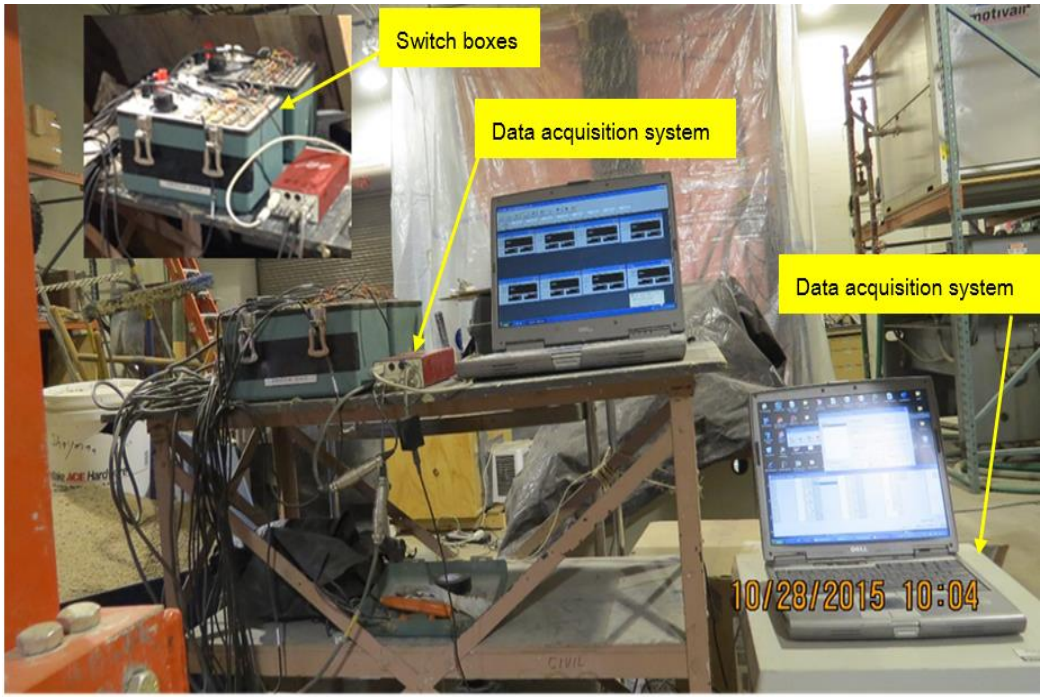

Figure 4.27 Data measuring and recording system

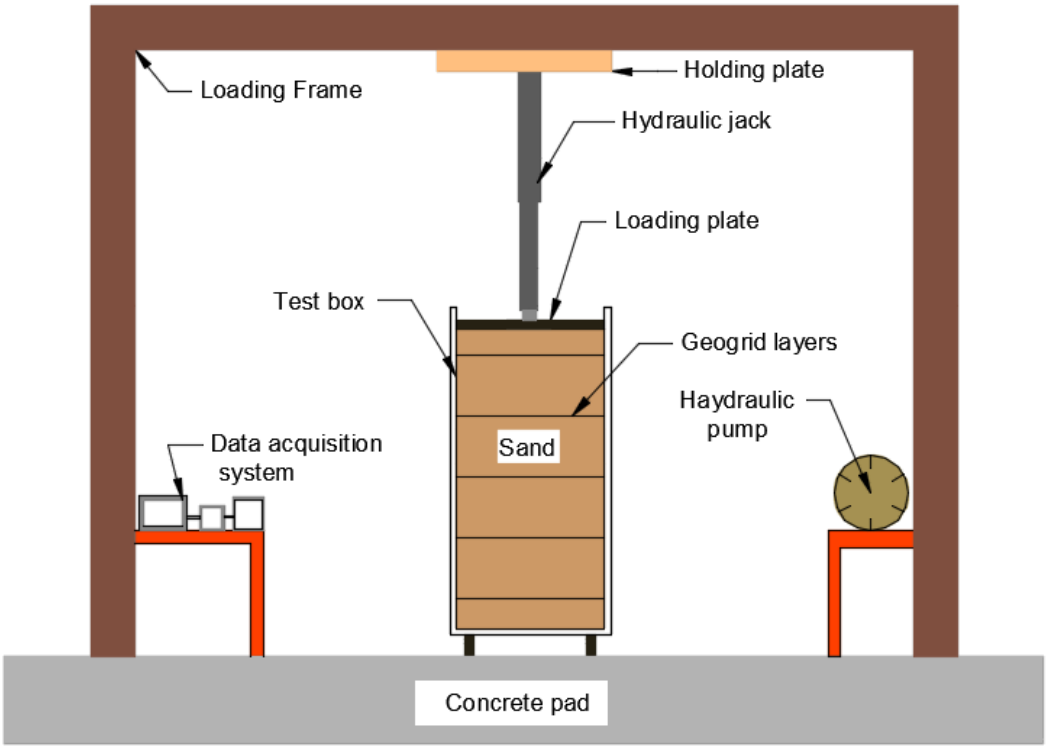

Figure 4.28 Schematic view of test setup

The wall facing deformation and the footing settlement were measured using the laser tape through the installed marks on the facing units and on the loading plate. A fixed benchmark for the laser tape and a reflected mark on a target object (i.e. a model wall) were required to attain the desired measurement (i.e., the distance between the laser tape and the reflected mark). In addition to the benchmarks attached on the wall facing, a number of fixed benchmarks were installed at the end of the box along the model height and perpendicular to the benchmarks on the wall facing (Figure 4.29). The measurements provided by the laser tape were recorded manually because the laser tape used in this study could only store up to four successive measurements. Tape readings were taken at each loading stage during the test. Furthermore, photos were taken on either side of the model at each loading stage to capture wall movement, lateral wall displacements, and footing settlement during the test using two cameras. Figure 4.29 also shows the locations of the camera and calibration benchmarks.

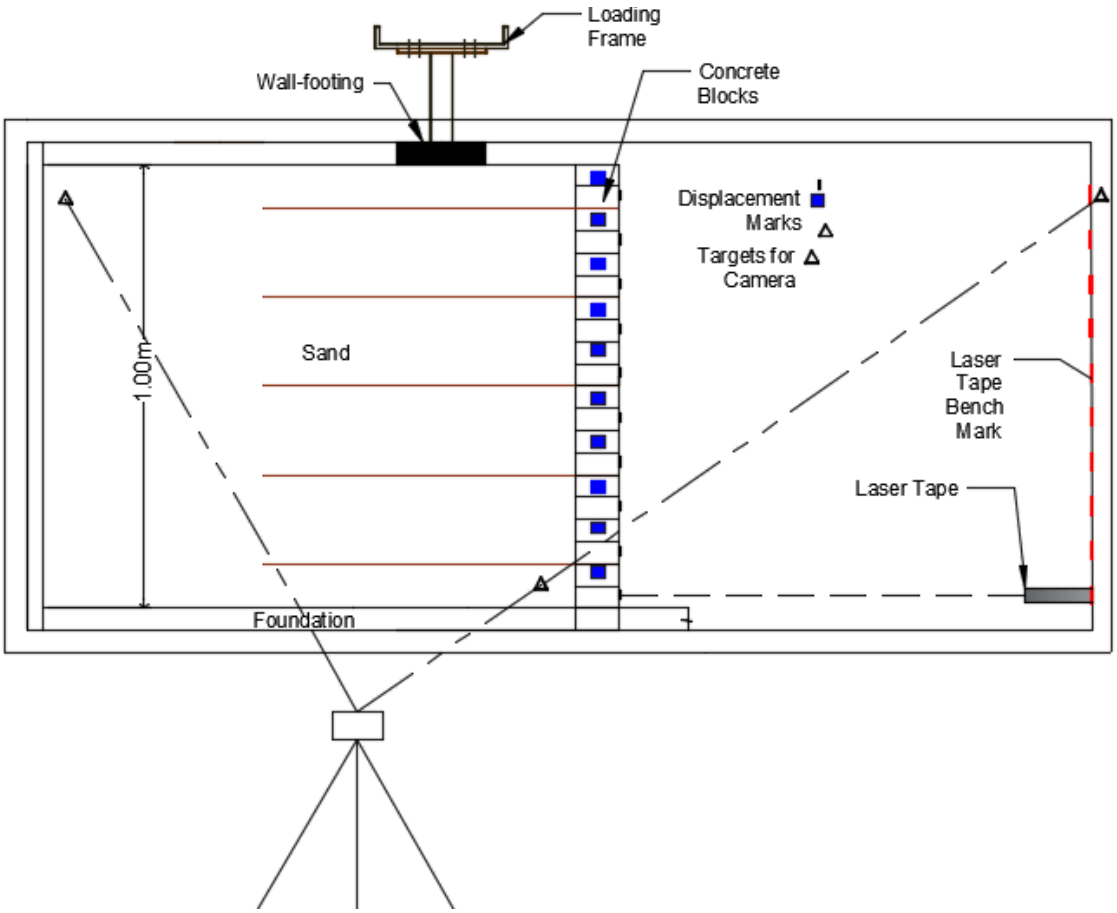

Figure 4.29 Camera and laser tape setup

Chapter 5 Experimental Model Test Results and Discussions

5.1 Introduction

This chapter presents the results of the laboratory model tests conducted in this study. The results include (1) wall deformation, (2) footing settlement, and (3) vertical pressure distribution, and (4) lateral earth pressure distribution.

5.2 Wall deformation

Wall deformation is referred to as the lateral displacement (deformation) of the wall facing and the internal deformation of a wall model test. The presentation of the wall deformations is organized based on their influence parameters considered in this study.

5.2.1 Effect of backfill space

Figure 5.1 shows the measured lateral displacement of the wall facing versus the wall height (H) under footing loading for the A1 model test. The A1 model test had 0.7H reinforcement fill width (also reinforcement length) and 0.5H retained fill. The footing offset distance (the distance from the back of the wall facing to the near edge of the footing o) was 0.2 m in the A1 model test. Figure 5.1 shows that the lateral displacement of the wall facing increased with an increase of applied load. Most of the displacements occurred above the mid-height of the wall (i.e., from H = 0.5 m to H = 0.9 m). The maximum displacement was 36 mm (approximately 3.6% of the wall height) at the maximum applied load (i.e., the applied footing pressure of 225 kPa).

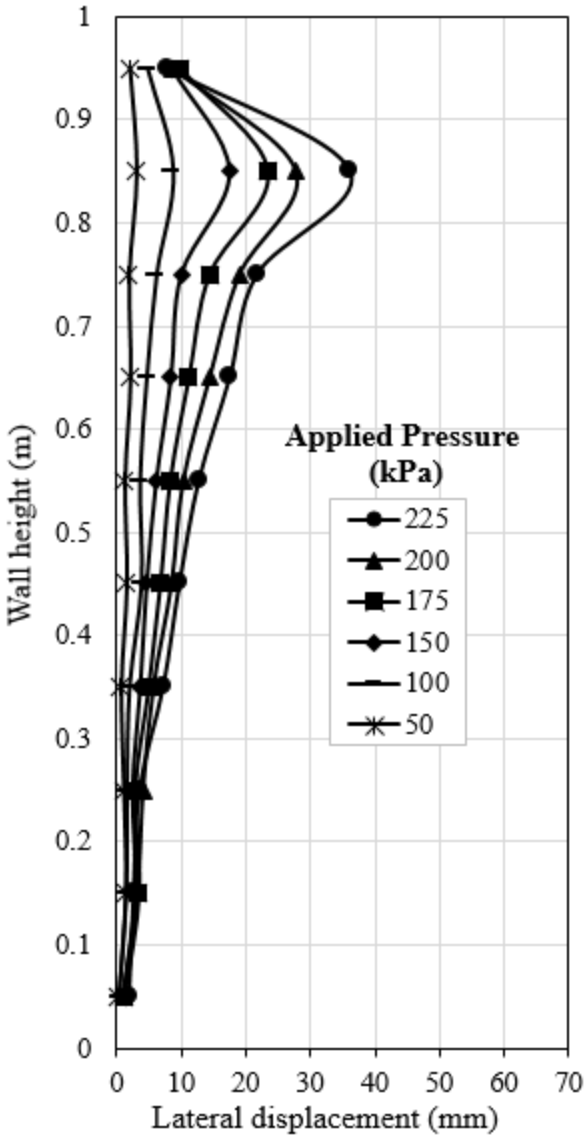

Figure 5.1 Lateral wall facing displacement versus height for the A1 model test

Figure 5.2 shows the measured lateral displacement of the wall facing versus the wall height under footing loading for the A2-I model test. The A2-I model test had 0.7H reinforcement length and no retained fill. The A2-I model test had the same footing offset distance as that of the A1 model test (i.e., the offset distance was 0.2 m in the A2-I model test). Figure 5.2 shows that the lateral displacement of the wall facing increased with an increase of applied load. Most of the displacements occurred above the mid-height of the wall. The

maximum measured displacement was 34 mm (approximately 3.4% of the wall height) at the maximum applied load (i.e., the applied footing pressure of 225 kPa).

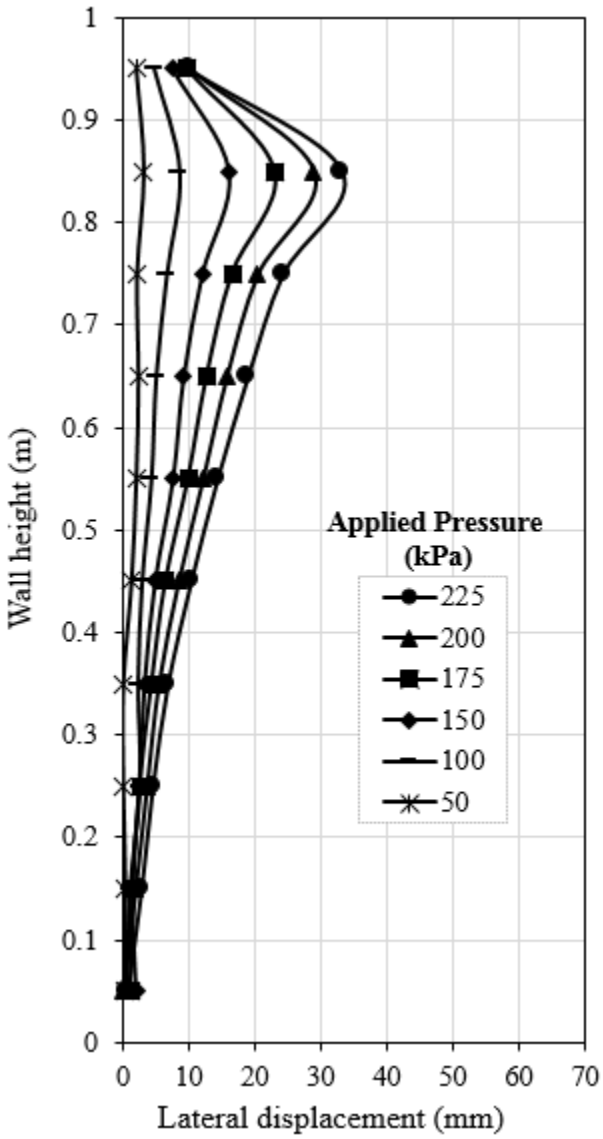

Figure 5.2 Lateral wall facing displacement versus height for the A2-I model test

Figure 5.2 shows that the A2-I model test had a slightly smaller maximum lateral displacement than that of the A1 model test (Figure 5.1) at the maximum applied load. However, the A2-I model test had slightly larger lateral displacements than the A1 model test below the

height corresponding to the maximum lateral displacement. This slight difference might be due to the difference in the stress (pressure) distributions in these two model tests. In the A2-I model test, there was a stable rigid medium behind the reinforced fill that acted as a rigid boundary, distorting the stress distribution and forcing the fill to move towards the wall facing. In addition, the maximum lateral displacement of the wall facing occurred at a depth approximately equal to the width of the applied loading plate from the top of the wall.

Figures 5.3 and 5.4 show the internal deformations at the verge of failure for the A1 and A2-I model tests, respectively. Figures 5.3 and 5.4 show the movement of the reinforcement (dotted lines) under loading relative to their original locations (solid yellow lines) and the movement of the soil as well. The movement of the reinforcement was indicated by the movement of black sand placed at each layer during construction.

Both figures show that the uppermost reinforcement had obvious vertical deformations under footing loading, but other reinforcement layers had small vertical deformations. This result indicates that the influence depth of the footing load was shallower than 1.5 times the footing width.

Even though the deformed shape and movement of the reinforcement layers were almost the same in the A1 and A2-I model tests, the movement of the soil was different in these two models. In the A2-I model test, the stable medium behind the reinforced fill constrained the soil movement and resulted in shifting of the soil movement and pushing the soil towards the facing units.

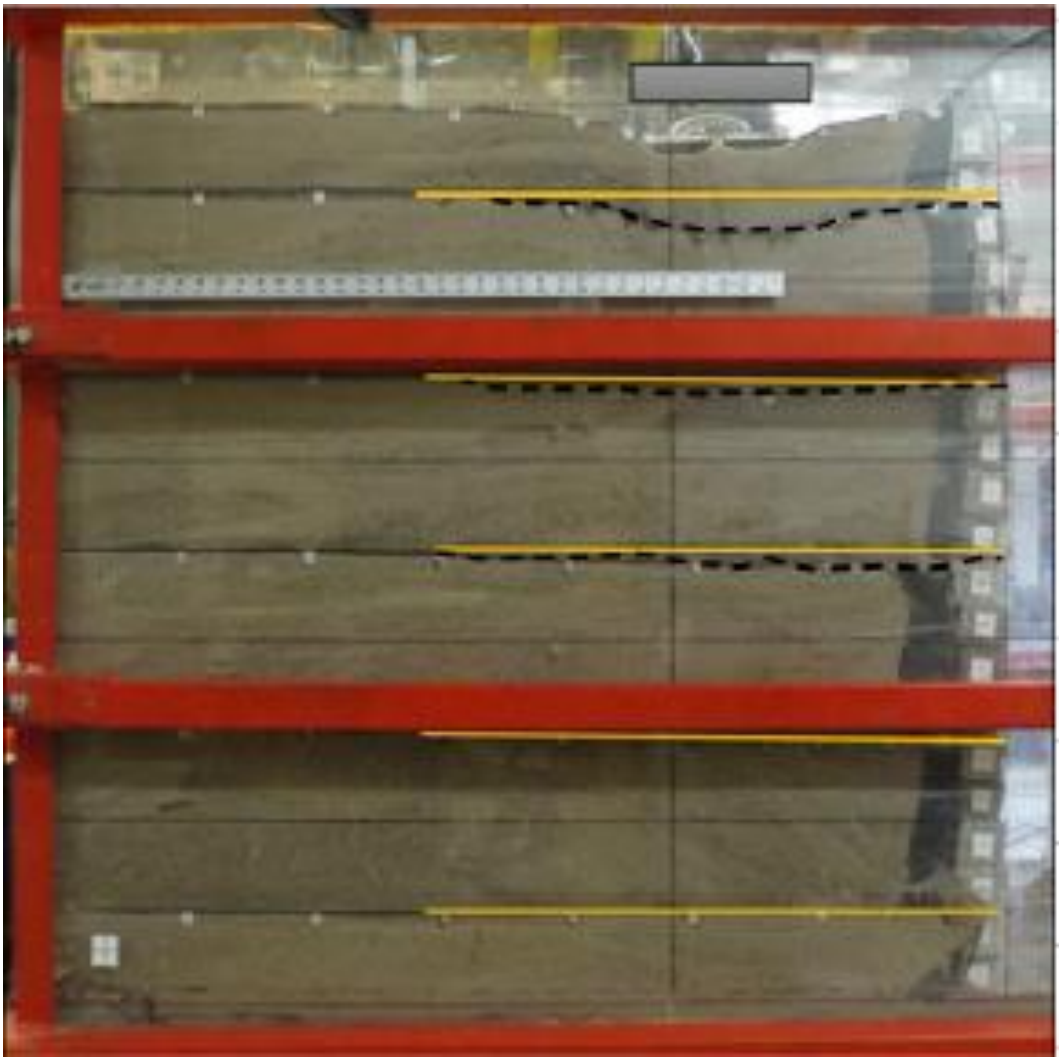

Figure 5.3 The A1 model test wall on the verge of failure

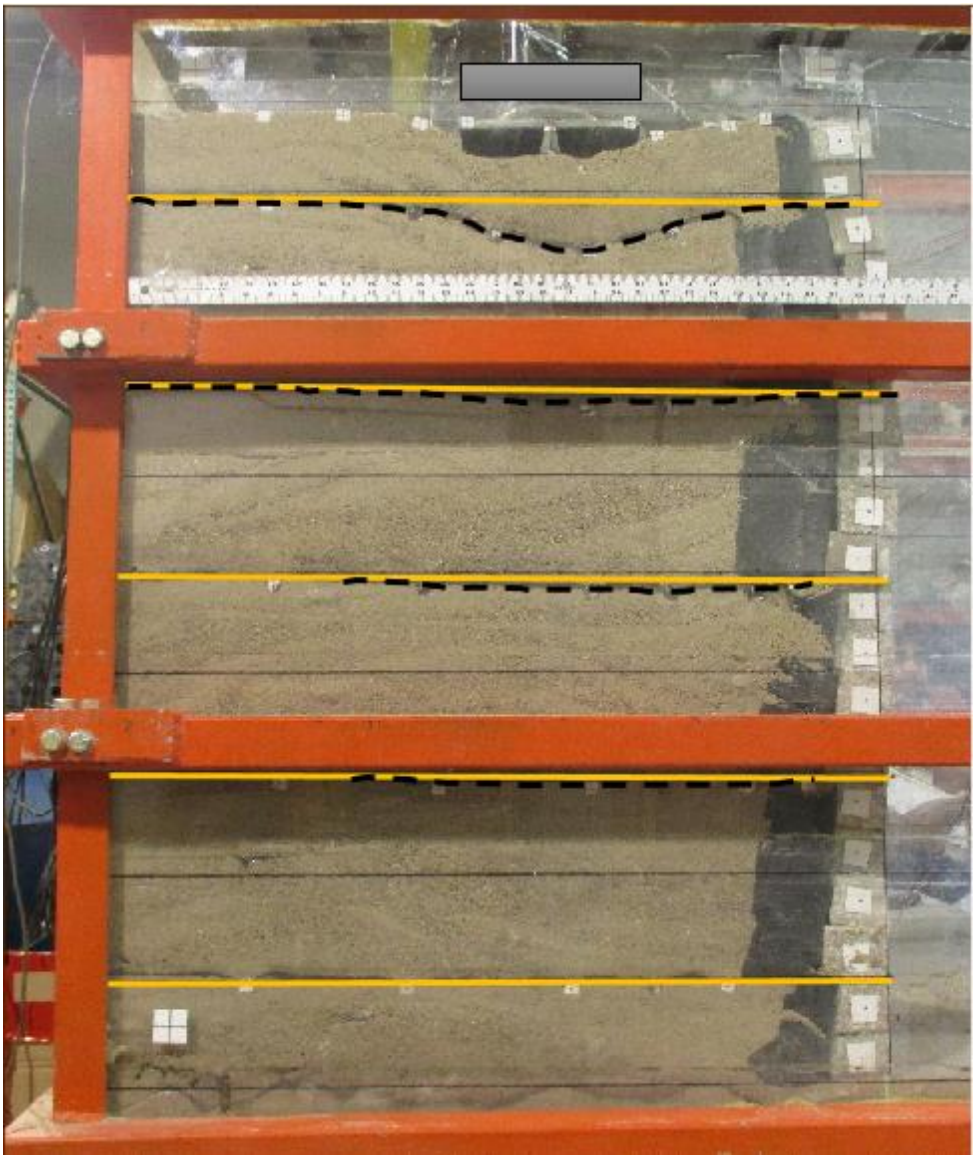

Figure 5.4 The A2-I model test wall on the verge of failure

5.2.2 Effect of reinforced fill width

Figure 5.5 shows the measured lateral displacement of the wall facing versus the wall height under footing loading for the A2-II model test. The A2-II model test had 0.7H reinforcement length and no retained fill. The A2-II model test is identical to the A2-I model test

except that the A2-II model test had a different footing offset. The footing offset distance was 0.05 m in the A2-II model test.

Figure 5.5 shows that the lateral displacement of the wall facing increased approximately with the same increment with an increase of applied load except for a rapid increase in the displacement after the footing pressure of 200 kPa as the maximum applied load was applied. This figure shows that almost the entire wall facing displaced under the applied load, and the maximum displacement occurred at the depth of less than the footing width. In addition, the maximum measured displacement was 48 mm (approximately 4.8 % of the wall height) at the maximum applied pressure of 200 kPa.

Figure 5.6 shows the measured lateral displacement of the wall facing versus the wall height under footing loading for the A3-II model test. The A3-II model test had 0.5H reinforcement length and no retained fill. The A3-II model test and the A2-II model test had the same footing offset, which was 0.05 m.

Figure 5.6 shows that, same as that in the A2-II model test, the lateral displacement of the wall facing in the A3-II model test, increased approximately in the same increment with an increase of applied load except for the displacement increasing at a greater rate after the footing pressure of 200 kPa was applied. This figure also shows that the maximum measured displacement was 60 mm (approximately 6 % of the wall height) at the maximum applied load (i.e., the applied footing pressure of 200 kPa), and it occurred at the depth of less than the footing width.

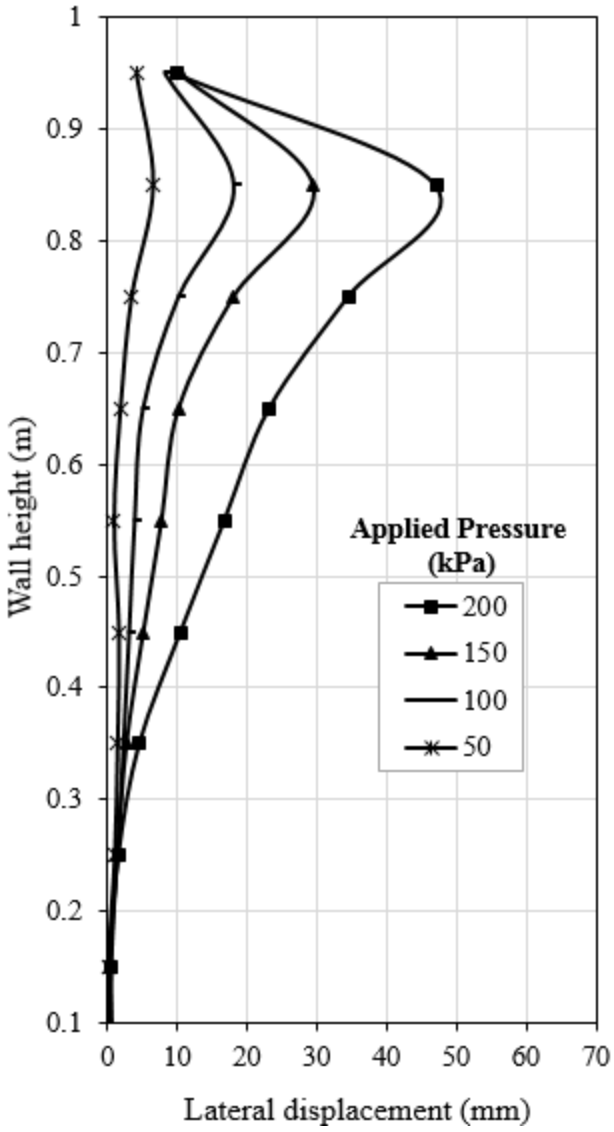

Figure 5.5 Lateral wall facing displacement versus height for the A2-II model test

Figures 5.5 and 5.6 show that the A3-II model test had slightly larger displacements along the depth of the wall than those of the A2-II model test under the applied pressure of 50 kPa up to 150 kPa. These figures also show that the reduction of the reinforcement length from 0.7H (i.e., the A2-II model test) to 0.5H (i.e., the A3-II model test) resulted in 25% larger maximum displacement at the maximum applied load (i.e., 60 mm displacement at 200 kPa) than that of the A2-II model test (i.e. 48 mm displacement at 200 kPa). In addition, the reduction of

the reinforcement length from 0.7H to 0.5H increased the overall displacement below the depth corresponding to the maximum lateral displacement under the maximum applied load. This difference might result from the existence of the rigid boundary at a close distance in the case of the A3-II model test, which changed the stress distribution and forced the soil to move towards the lower portion of the wall facing.

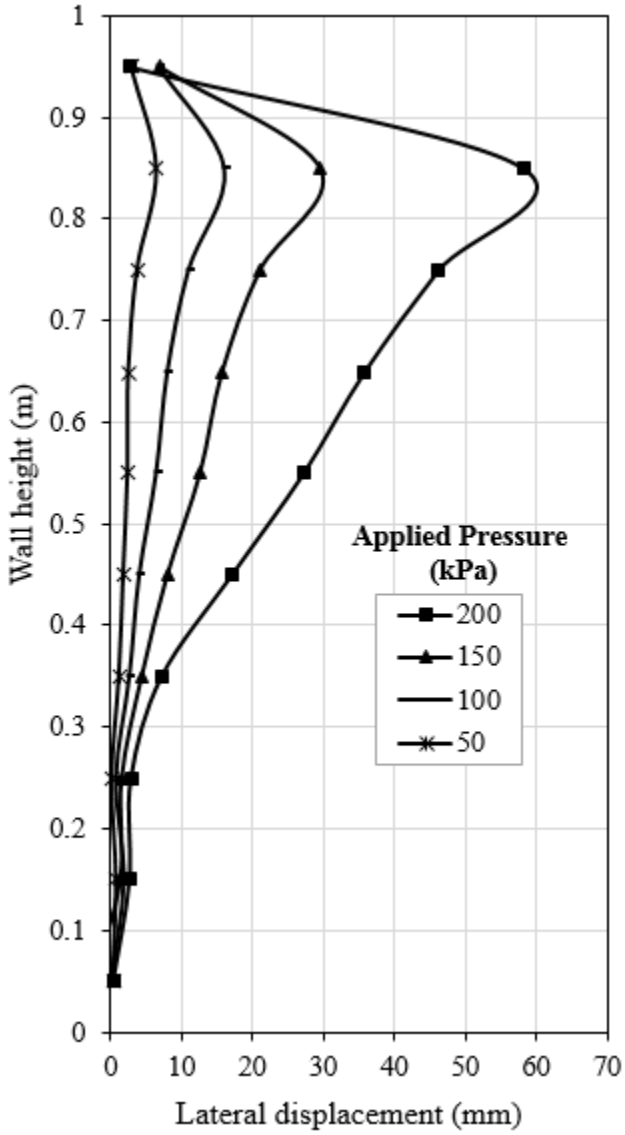

Figure 5.6 Lateral wall facing displacement versus height for the A3-II model test

Figure 5.7 shows the measured lateral displacement of the wall facing versus the wall height under footing loading for the A4 model test. The A4 model test had 0.3H reinforcement length and no retained fill. The A4 model test had the same footing offset distance as that of the A3-II and A2-II model tests, which was 0.05 m.

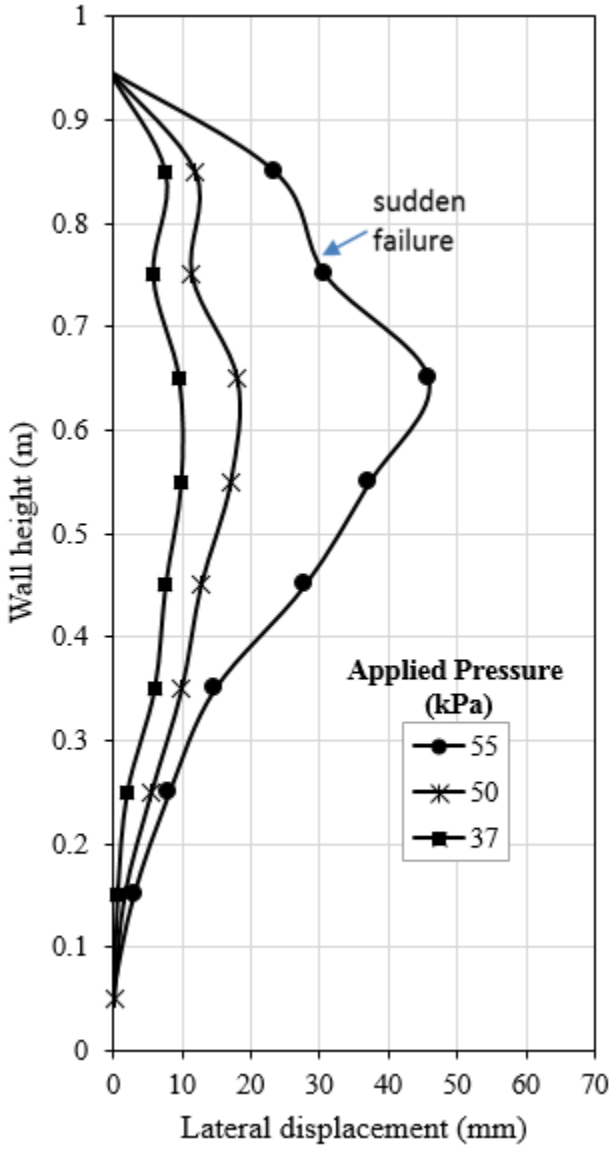

Figure 5.7 Lateral wall facing displacement versus height for the A4 model test

Figure 5.7 shows that the reduction of the reinforcement length from 0.5H (i.e., the A3-II model test) to 0.3H (i.e., the A4 model test) resulted in excessive wall facing displacements. The maximum displacement in the A4 model test was three times larger than the maximum displacement in the A2-II model test under the same applied pressure. For example, the facing wall in the A4 model test displaced about 18 mm at the applied pressure of 50 kPa, while the A2-II model test displaced only 6 mm at the same applied pressure. Therefore, the walls with reinforcement shorter than 0.5H would result in large lateral displacement.

In addition, sudden failure occurred in the A4 model test after a footing pressure of 55 kPa was applied because the reinforcements did not have enough length to provide sufficient anchorage required for maintaining the stability of the model. Therefore, the wall with reinforcement shorter than 0.5H resulted in a significant reduction in the ultimate bearing capacity of the footing on the wall.

Moreover, the maximum displacement at failure in the A4 model test occurred at the depth of (1/3) H from the top of the wall, which was deeper than those for the A2-II and A3-II model tests. Based on the modified 2:1 stress distribution method (FHWA 2009 and Morrison et al. 2006), the footing width, and the wall width, the distribution of the vertical pressure was almost the same from the top to the bottom of the model wall (i.e. the A4 model test).

Figures 5.8**,** 5.9, and 5.10 show the internal deformations of the A2-II, A3-II, and A4 model tests, respectively. These figures show the movements of the reinforcement layers (dotted lines) under the maximum applied load relative to their original locations (solid yellow lines), and the movements of the soil and facing units as well.

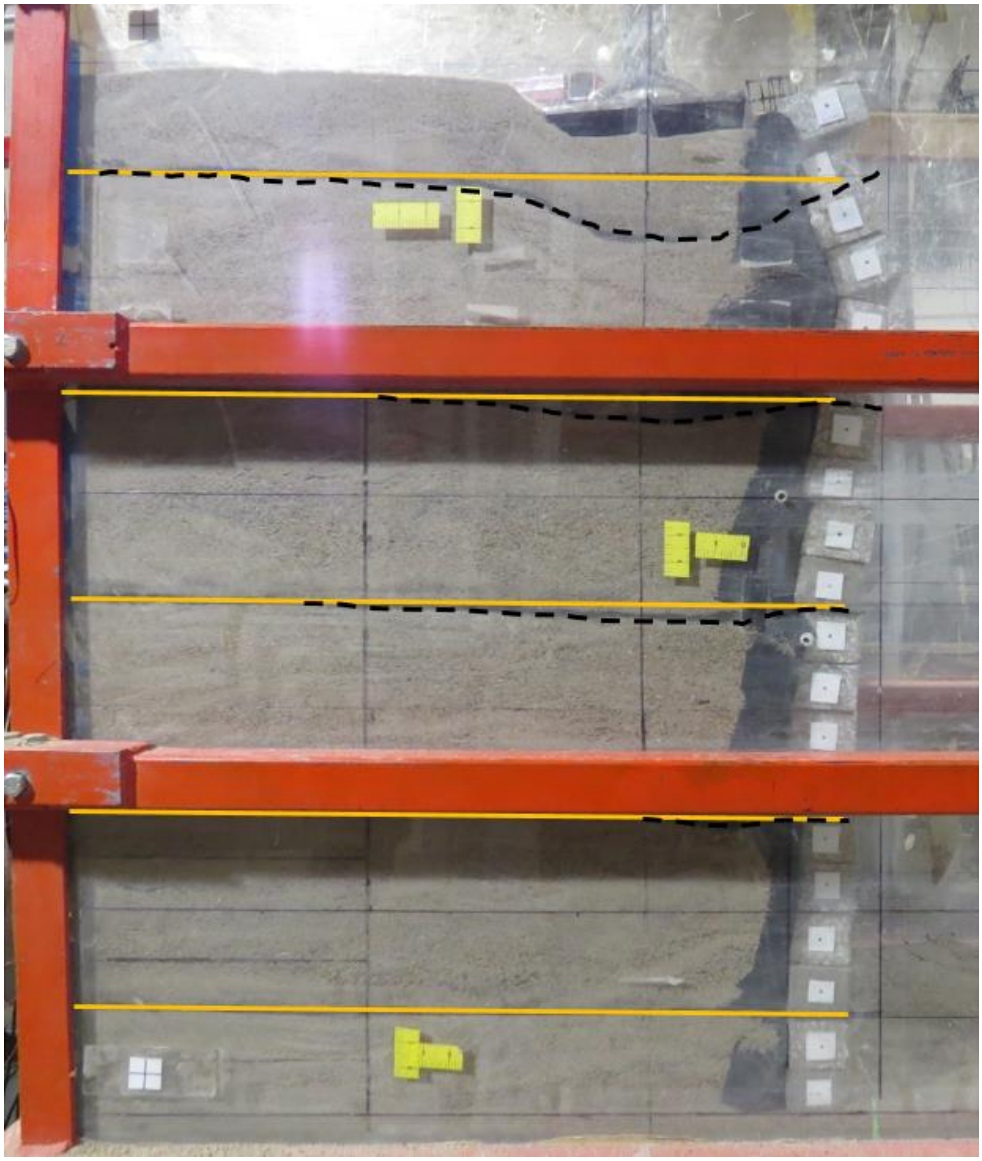

Figure 5.8 The A2-II model test wall on the verge of failure

Figures 5.8 and 5.9 show that the A2-II and A3-II model tests had almost the same influence depth of the footing load, which was approximately two times the footing width. In addition, the fourth and fifth facing units from the top of both A2-II and A3-II model tests behaved almost the same. The facing units moved away from each other and were forced out of the wall.

Figure 5.9 The A3-II model test wall on the verge of failure

On the other hand, Figure 5.10 clearly shows that the influence depth of the footing load in the A4 model test was more than those in the A2-II and A3-II model tests. The influence depth of the footing load in the A4 model test was more than 2.5 times the footing width, while the influence depths of the footing load in the A2-II and A3-II model tests were approximately 2.0 times the footing width.

Figure 5.10 The A4 model test wall on the verge of failure

In addition, the A4 model test had more vertical compression than that in the A2-II and A3-II model tests. These differences can be explained using the wall cross sections as shown in Figure 5.11. When the wall had longer reinforcement (i.e., Figure 5.11(a) and/or (b) as compared with Figure 5.11(c)), the applied load was distributed to a wider area so that the vertical stress decreased with the depth rapidly.

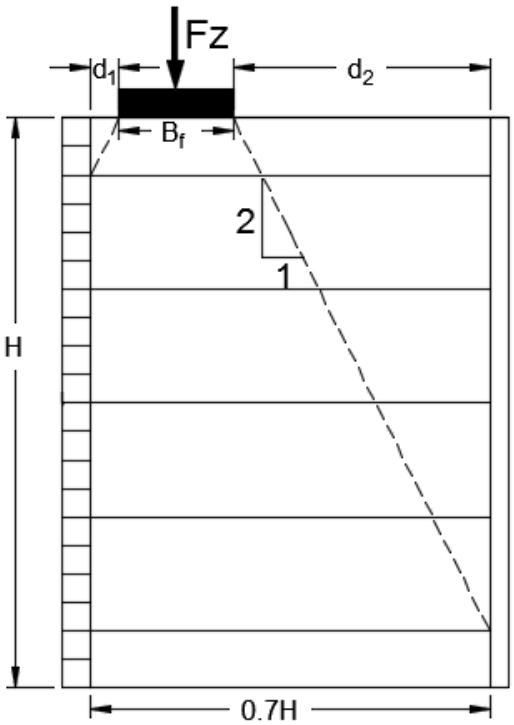

(a)

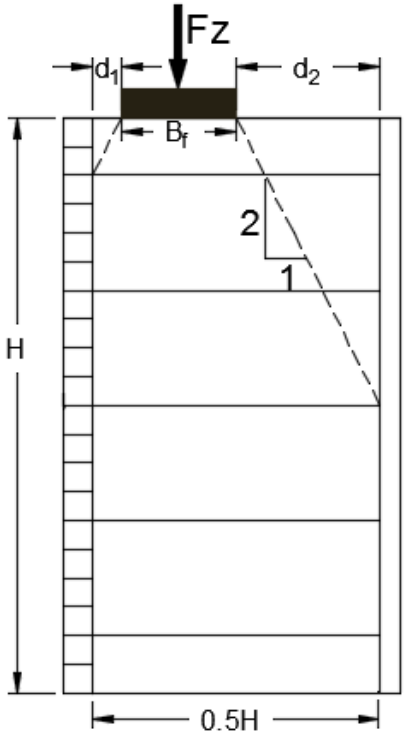

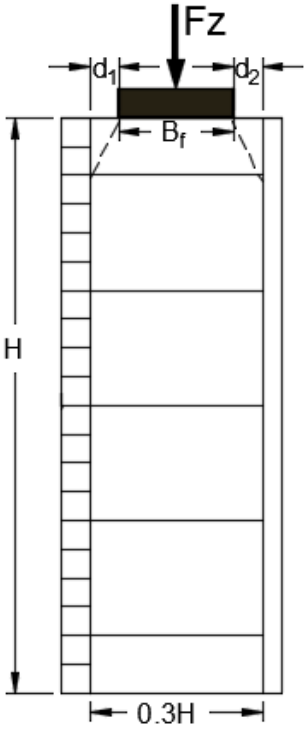

(b) (c)

Figure 5.11 Distribution of the applied load with depth for walls with the reinforcement length of (a) 0.7H, (b) 0.5H, and (c) 0.3H

However, when the wall had shorter reinforcement (i.e., Figure 5.11(c)), the applied load was distributed to a narrower area so that the vertical stress decreased with the depth slowly. As a result, the wall with shorter reinforcement had higher vertical stresses, a deeper influence depth, and more deformations than that with longer reinforcement.

5.2.3 Effect of footing offset distance

Both A2-I and A2-II model tests had the same reinforcement length (i.e., reinforcement length = 0.7H) but different footing offset distances. The footing offset distance was 0.15 m in the A2-I model test, while it was 0.05 m in the A2-II model test. Figures 5.2 and 5.5 show the effect of footing offset distance on the lateral wall facing displacement in the A2-I model test and the A2-II model test. Likely, Figures 5.4 and 5.8 show the effect of the footing offset on the wall deformation.

Figure 5.5 shows that the reduction of the footing offset distance from 0.2 to 0.05 m resulted in a substantial increase in the lateral facing displacement under the same applied load. The maximum measured displacement was approximately 23 mm in the A2-I model test, while the maximum measured displacement was approximately 48 mm in the A2-II model test under the same applied load (i.e. at the applied footing pressure of 200 kPa).

Because of the closer footing offset distance, almost the entire wall facing of the A2-II model test deformed (Figure 5.8) under the applied load in the model as compared to that of the A2-I model. Figure 5.12(a) shows that when the footing was closer to the wall facing as in the case of the A2-II model test, the applied pressure was distributed over a narrower area next to the wall facing, which resulted in higher pressure on the wall facing and thus larger deformation.

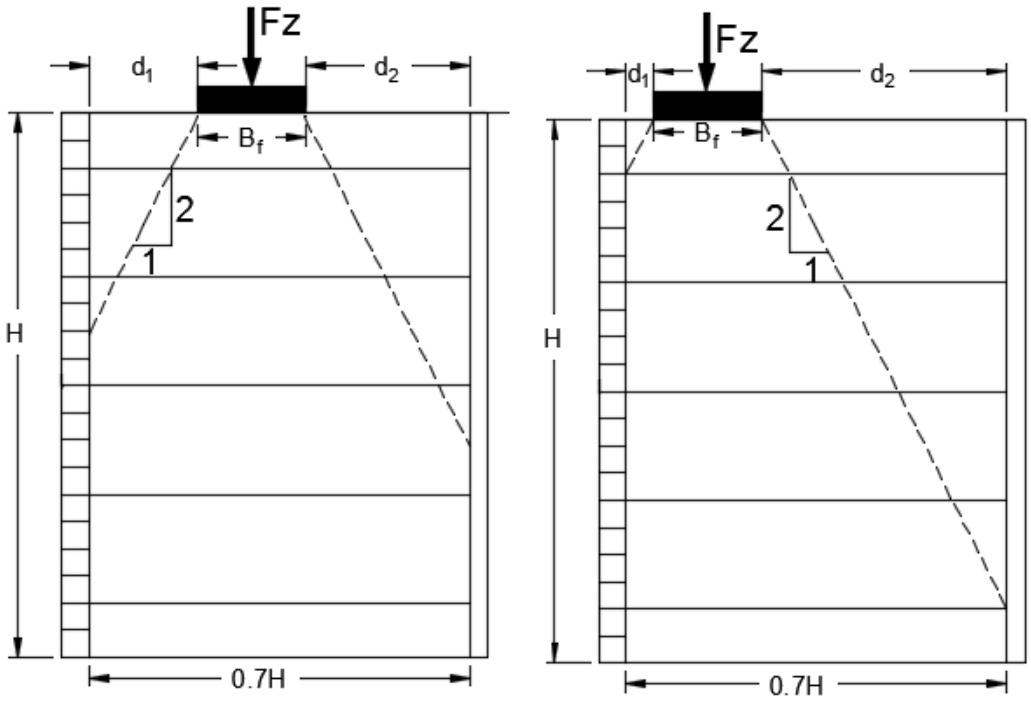

(a)

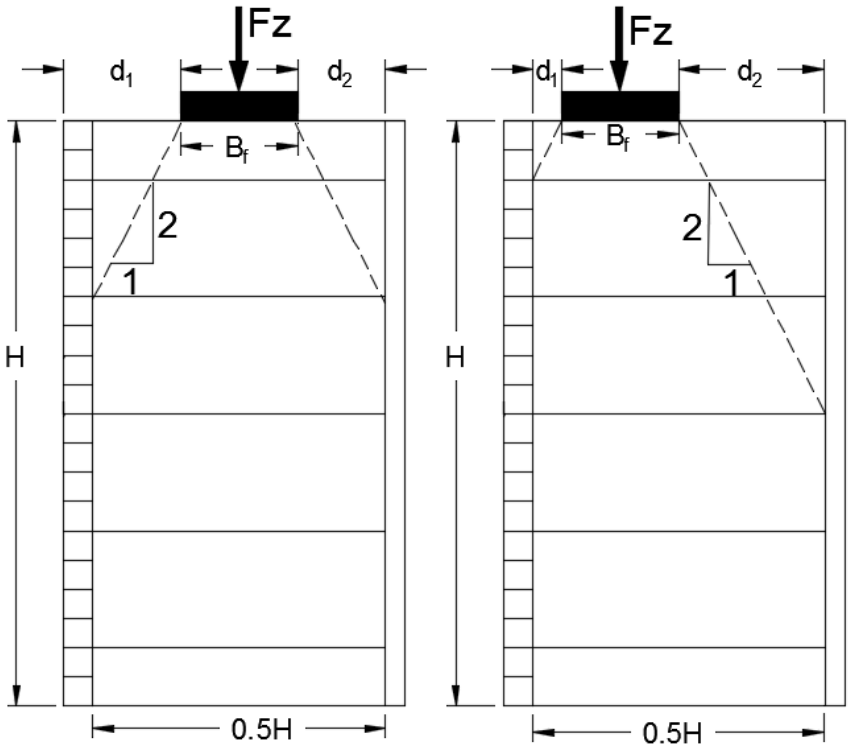

(b)

Figure 5.12 Effects of footing offset distances on the distribution of the applied load with depth for different wall widths

Figure 5.13 shows the measured lateral displacement of the wall facing versus the wall height under footing loading for the A3-I model test. The A3-I model test had 0.5H reinforcement length and no retained fill. The A3-I model test is identical to the A3-II model test except that they had different footing offset distances. The footing offset distance was 0.15 m in the A3-I model test, while it was 0.05 m in the A3-II model test.

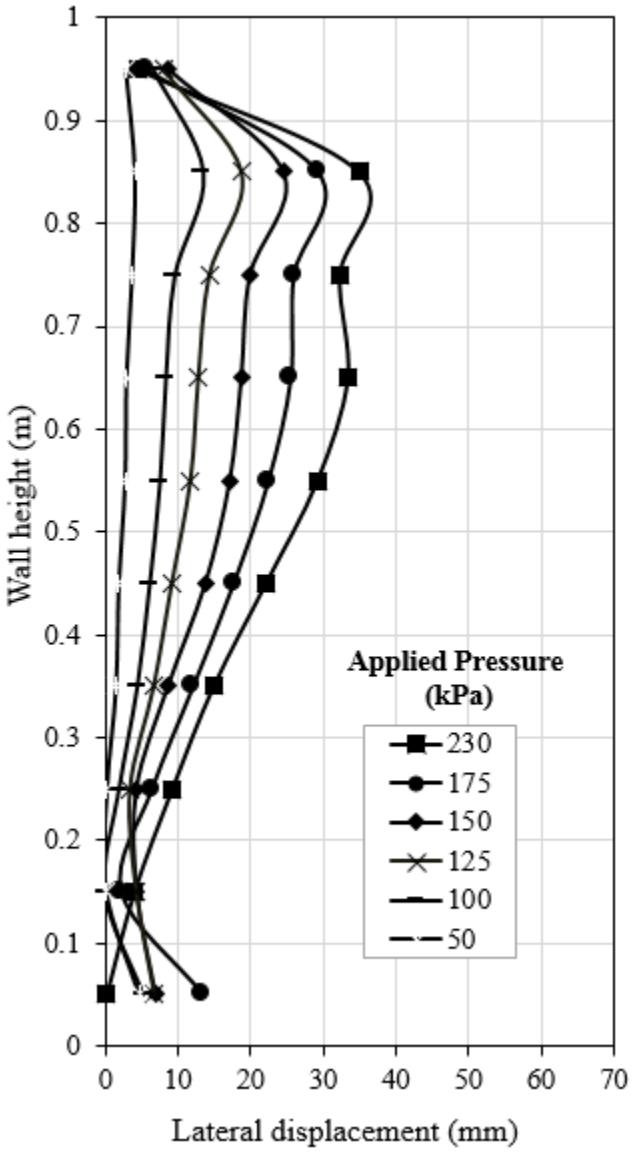

Figure 5.13 Lateral wall facing displacement versus height for the A3-I model test

Compared with Figure 5.6, Figure 5.13 shows that the increase of the footing offset distance from 0.05 m to 0.15 m resulted in considerable reduction in the maximum lateral facing displacement under the maximum applied load in the model. The maximum measured lateral displacement was approximately 60 mm in the A3-II model test under the applied footing pressure of 200 kPa, while the maximum measured displacement was approximately 35 mm in the A3-I model test under the applied footing pressure of 230 kPa. However, the overall lateral facing displacement was almost the same in both models (A3-I and A3-II model tests) under the same applied load. For example, the average lateral facing displacements (i.e., the displacement area) were approximately 12.6 mm in the A3-I model and 13.0 mm in the A3-II model under the applied footing pressure of 150 kPa.

Figure 5.14 shows the deformed test wall in the A3-I model test after the application of the maximum applied load. The picture shows the movements of the reinforcement layers (dotted lines), the facing units, and the soil under loading in this model. This figure shows that the A3-I model test had more vertical compression as compared with that of the A3-II model test. In addition, the influence depth of the footing load in the A3-I model test was more than that in the A3-II model test. The influence depth of the footing load in the A3-I model test was more than 2.5 times the footing width, while the influence depth of the footing load in the A3-II model test was approximately 2.0 times the footing width.

Figure 5.14 shows that nearly the same deformation occurred from the depth of 0.35 to 0.9 m in the A3-I wall model, while Figure 5.9 shows that most of the deformation occurred from the depth of 0.6 to 0.9 m in the A3-II wall model.

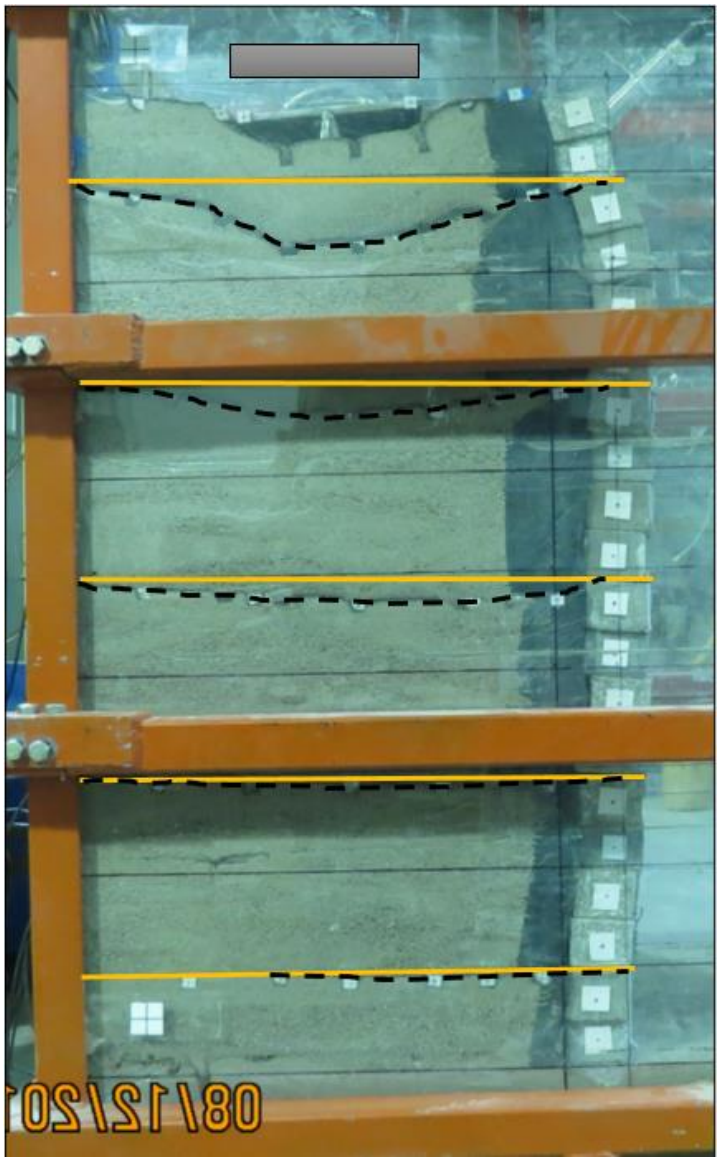

Figure 5.14 The A3-I model test wall on the verge of failure

5.2.4 Effect of reinforcement vertical spacing

Figure 5.15 shows the measured lateral displacement of the wall facing versus the wall height under footing loading for the B1 model test. The B1 model test had 0.3H reinforcement length and no retained fill. The B1 model test is identical to the A4 model test except that the B1 model test had closer vertical spacing between the reinforcement layers than the A4 model test.

The vertical spacing between the reinforcement layers was 0.1 m in the B1 model test. The offset distance of the footing was 0.05 m in the B1 model test.

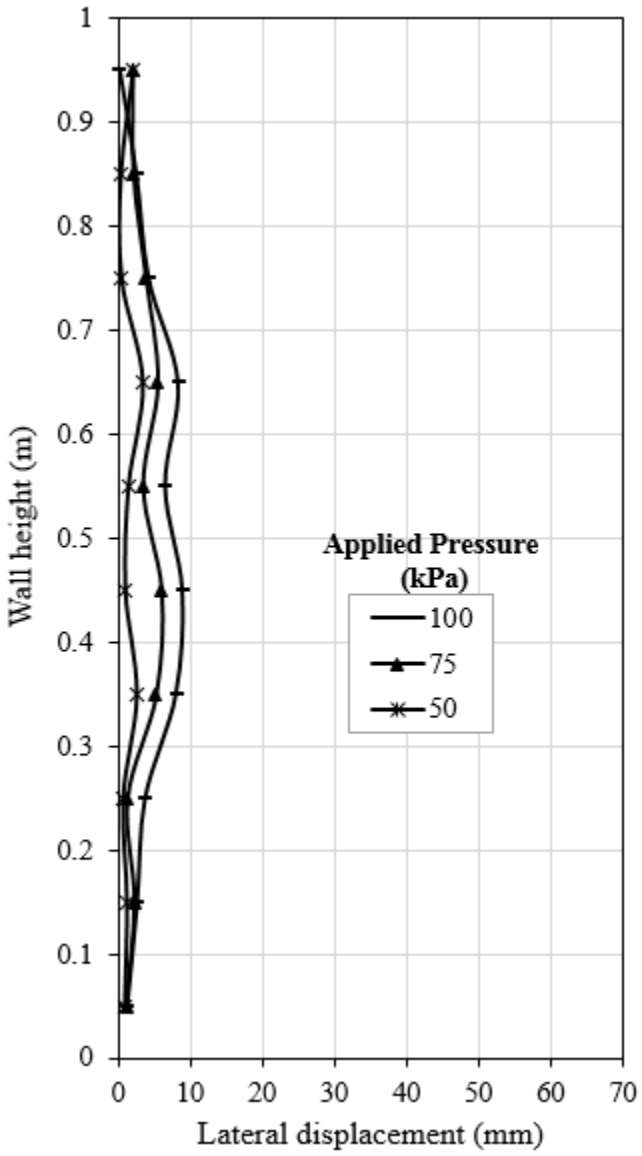

Figure 5.15 Lateral wall facing displacement versus height for the B1 model test

Compared to the A4 model test (Figure 5.7), the B1 model test had smaller than ¼ times the maximum measured displacement at the same applied load as shown in Figure 5.15. For example, the maximum measured displacement in the A4 model test was 18 mm, while the maximum measured displacement in the B1 model test was only 4 mm under the applied footing pressure of 50 kPa. The B1 model test had even smaller maximum displacement than the A2-II model test. However, the A2-II model test had the overall wall facing displacement two times (i.e., the average lateral facing displacement was 3.2 mm) smaller than the B1 model test (i.e., average lateral facing displacement was 6.0 mm). Figure 5.15 also shows that the maximum lateral facing displacement occurred approximately at (1/2) H from the top of the wall.

Figure 5.16 shows the internal deformations of the B1 model test. This figure shows the movements of the reinforcement layers (dotted lines) under the maximum applied load relative to their original locations (solid yellow lines) and the movement of the soil. Figure 5.16 shows that the B1 model test had a similar shape of lateral deformation to that of the A4 model test. In addition, the B1 model test had almost the same influence depth of the footing load (i.e., 2.5 times the footing width) as that of the A4 model test.

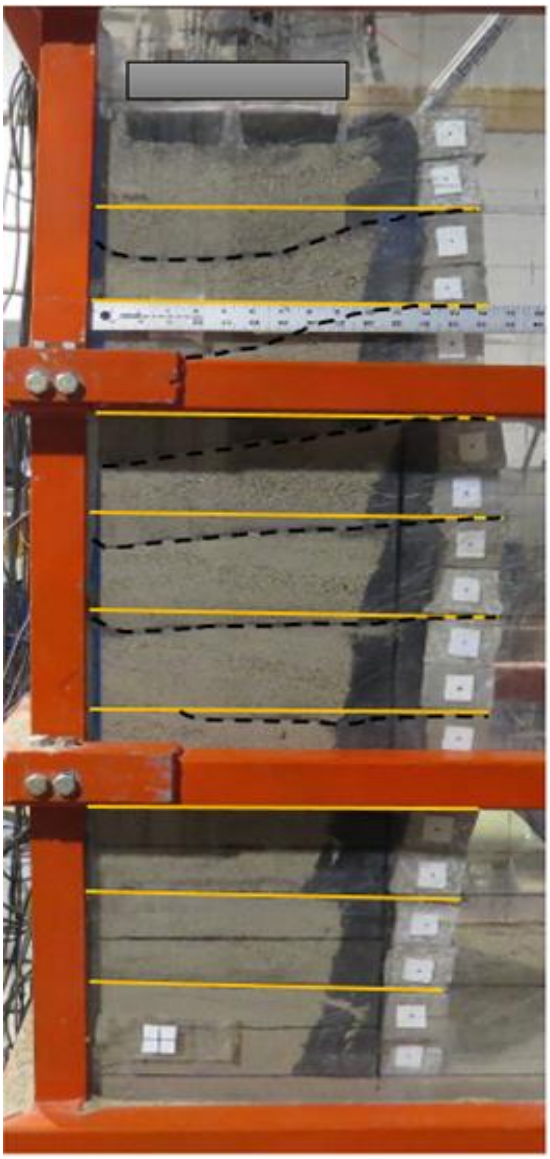

Figure 5.16 The B1 model test wall on the verge of failure

5.2.5 Effect of reinforcement rear connection

Figure 5.17 shows the measured lateral displacement of the wall facing versus the wall height under footing loading for the C1 model test. This model test had 0.3H reinforcement length and no retained fill, same as the A4 model test. In the C1 model test, top four reinforcement layers were mechanically connected to the stable medium at the rear to provide

sufficient anchorage for the reinforcement layers. This figure shows that the connection of the reinforcement layers to the stable medium resulted in substantial reduction in the displacement of the wall facing as compared with that in the A4 model test under the same loading condition. For example, the maximum measured displacement was only about 4 mm in the C1 model test under the applied footing pressure of 50 kPa, while the maximum displacement of 18 mm was measured in the A4 model test under the same applied load. In addition, as compared to the A2-II model test, the C1 model test even showed better performance by having 25% smaller maximum lateral displacement under the same applied pressure.

Figure 5.18 shows the measured lateral displacement of the wall facing versus the wall height under footing loading for the C2 model test. This model had 0.3H reinforcement length and no retained fill, same as the C1 model test. In the C2 model test, two uppermost reinforcement layers were mechanically connected to the stable medium at the rear to provide sufficient anchorage for the reinforcement layers. This figure shows that even fixing of the two uppermost reinforcement layers to the stable medium resulted in substantial reduction in the displacement of the wall facing as compared with that in the A4 model test under the same applied load.

In addition, the C2 model test had even smaller maximum lateral facing displacements than the C1 model test under the applied footing pressure of 25 kPa to 225 kPa. However, the C2 model test failed suddenly after the footing pressure was applied more than 225 kPa.

Figure 5.18 also shows that fixing the uppermost reinforcement layers to the stable wall as in the C2 model test, resulted in lowering the location of the maximum lateral facing displacement and changing the shape of the displacement profile, as compared with the C2 model test.

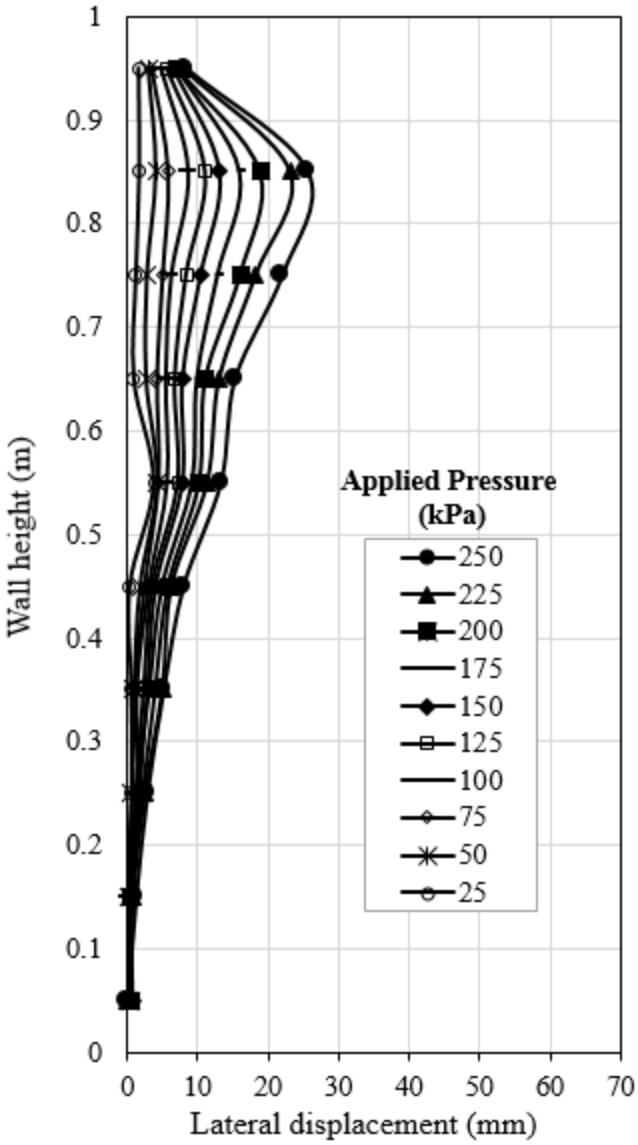

Figure 5.17 Lateral wall facing displacement versus height for the C1 model test

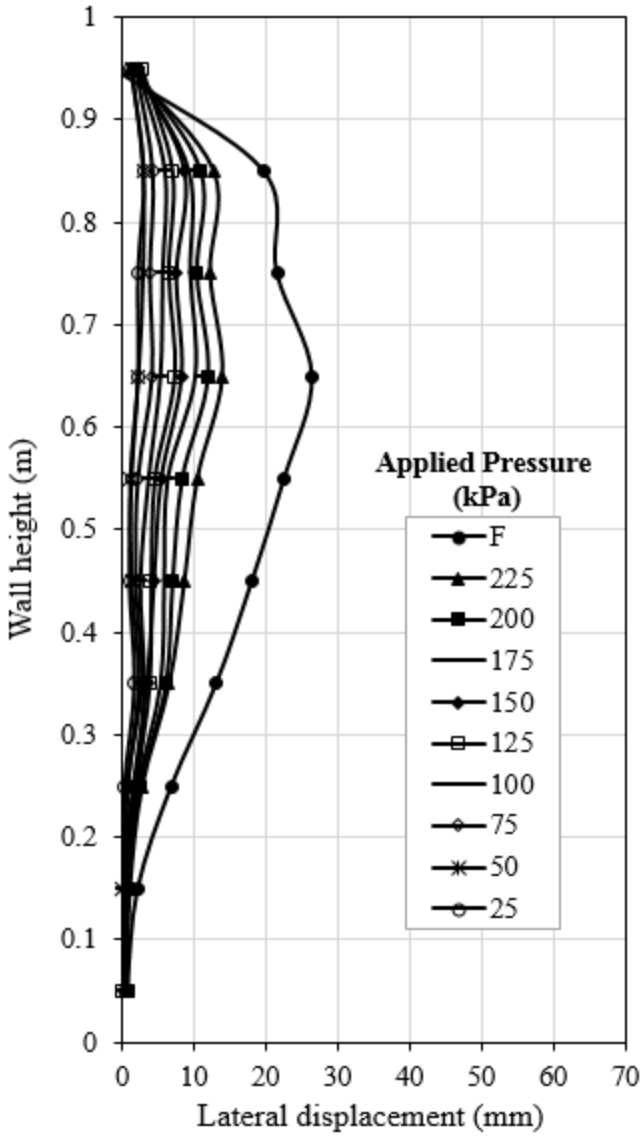

Figure 5.18 Lateral wall facing displacement versus height for the C2 model test

Figure 5.19 shows the measured lateral displacement of the wall facing under loading in the C3 model test. This model is identical to the A4 model test except that in the C3 model test, the reinforcement layers were bent upward at the end by 0.2 m along the back of the reinforced fill (i.e., between the back of the reinforced fill and the stable rigid medium). The C3 model test showed that upward-bending of the reinforcement layers around the back of the reinforced fill resulted in a significant reduction of the lateral displacement in the model as compared with that

in the A4 model test under the same applied pressure of 55 kPa. For example, the A4 model test failed suddenly under the applied pressure of 55 kPa; however, the C3 model test displaced only around 10 mm under the same applied pressure.

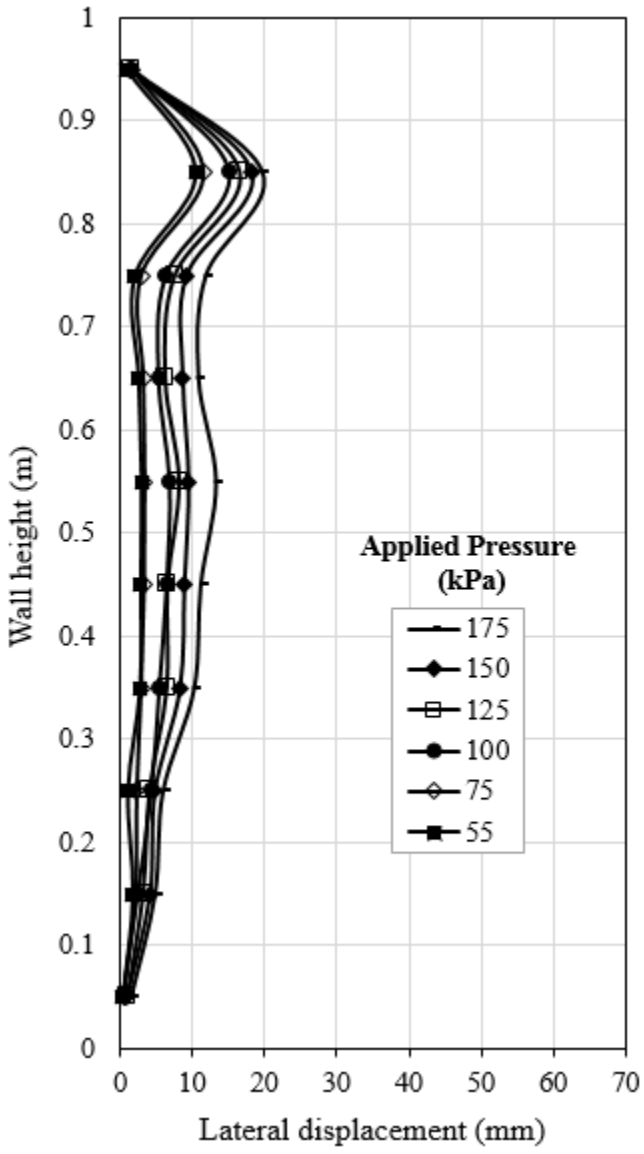

Figure 5.19 Lateral wall facing displacement versus height for the C3 model test

Figures 5.17 and 5.18 show that the connection of the reinforcement layers onto the stable medium was slightly more effective in reducing the lateral displacement of the wall than

that by upward-bending of the reinforcement layers along the stable medium (e.g., at the applied pressure of 175 kPa). It should be noted that in this comparison the C1 model was tested to a higher pressure (i.e., 250 kPa) than the C3 model (i.e., 175 kPa).

Figures 5.20, 5.21, and 5.22 show the deformed test walls in the C1 model test, the C2 model test, and the C3 model test after the application of the maximum load. The pictures show the movements of the geogrids (dotted lines) and the soil under loading in these three models. Figures 5.21 and 5.22 show the deformed wall tests in the C2 and C3 model tests before and at the failure.

Figure 5.20 shows that the rear connection of the reinforcement in the C1 model test minimized the downward movement of the reinforcement at the rear even under the maximum applied load. On the other hand, in the C2 and C3 model tests, the reinforcement moved downward and then was pulled out at the rear.

Figure 5.20 The C1 model test wall on the verge of failure

(a) (b)

Figure 5.21 The C2 model test (a) before failure and (b) at failure

(a) (b)

Figure 5.22 The C3 model test wall (a) before failure and (b) at failure

Figure 5.23 shows the measured lateral displacement of the wall facing under loading in the C4 model test. In this model test, the reinforcement layers were bent upward at the end by 0.2 m between the back of the reinforced fill and the stable rigid medium. The C4 model test had the same footing offset distance and reinforcement length as that of the A3-I model test.

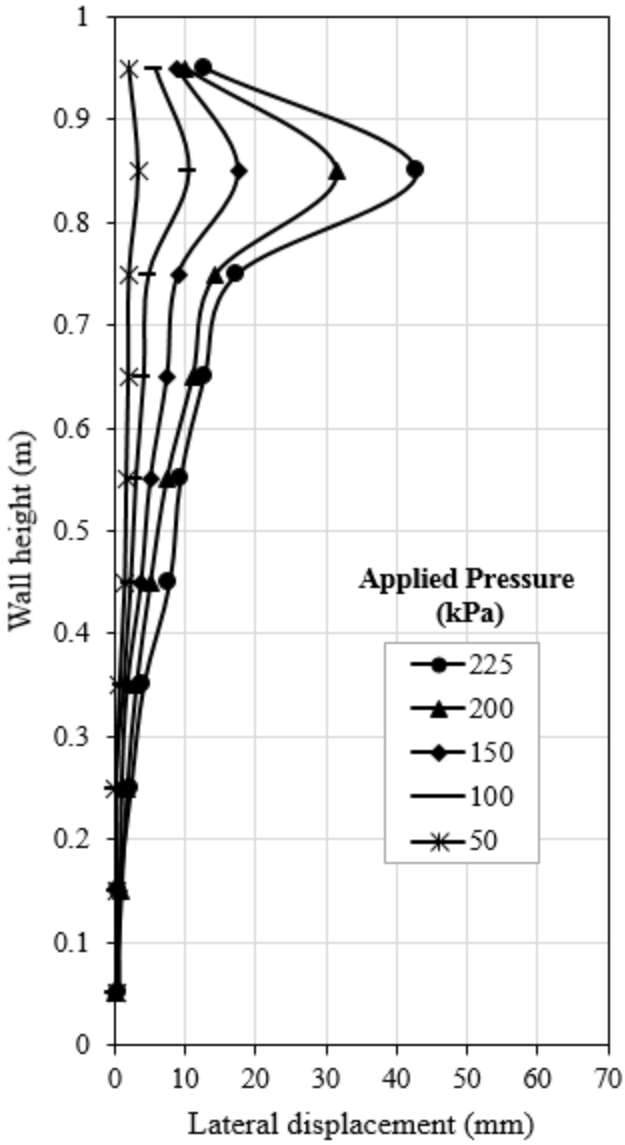

Figure 5.23 Lateral wall facing displacement versus height for the C4 model test

Figure 5.23 shows that the C4 model test had a larger maximum lateral facing displacement under the maximum applied pressure of 225 kPa as compared with that of the A3-I model test (Figure 5.13) under the maximum applied pressure of 230 kPa. However, the C4 model test showed that upward-bending of the reinforcement layers around the back of the reinforced fill resulted in a considerable reduction of the average lateral displacement as

compared with that of the A3-I model test at the same applied load. For example, the average lateral facing displacement of the C4 model test was approximately 6.4 mm at the applied footing pressure of 150 kPa, while the average lateral facing displacement of the A3-I model test was 12.30 mm under the same applied load.

Figure 5.24 shows the internal deformations of the C4 model test on the verge of failure. This figure shows the movements of the reinforcement layers (dotted lines) under the maximum applied load relative to their original locations (solid yellow lines) and the movement of the soil.

Figure 5.24 also shows that upward-bending of the reinforcement layers around the back of the reinforced fill minimized the downward movements of all reinforcement layers under the maximum applied load except for the top layer, which was deformed under the applied load. In addition, the influence depth of the footing load in the C4 model test was less than that of the A3-I model test. The influence depth of the footing was 1.5 times the footing width.

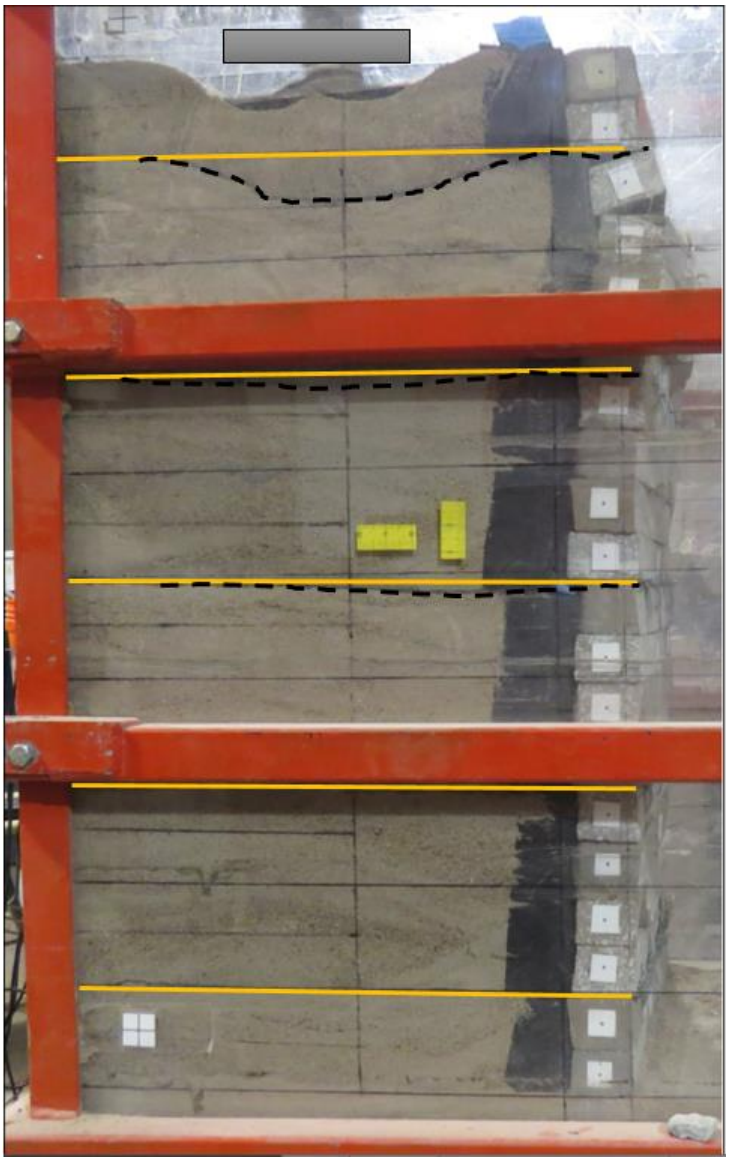

Figure 5.24 The C4 model test wall on the verge of failure

5.3 Settlement of footing

This section presents the effects of different parameters on the applied pressure-settlement curves of the footing in the model wall tests conducted in this study.

5.3.1 Effect of backfill space

Figure 5.25 shows the applied pressure-settlement curves of the footing in the A1 and A2-I model tests. Both model tests had the same reinforcement length (i.e., 0.7H) and footing offset distance except that the A2-I model test had no retained fill. This figure shows that the A2-I model test had a higher ultimate bearing capacity and a smaller settlement than the A1 model test.

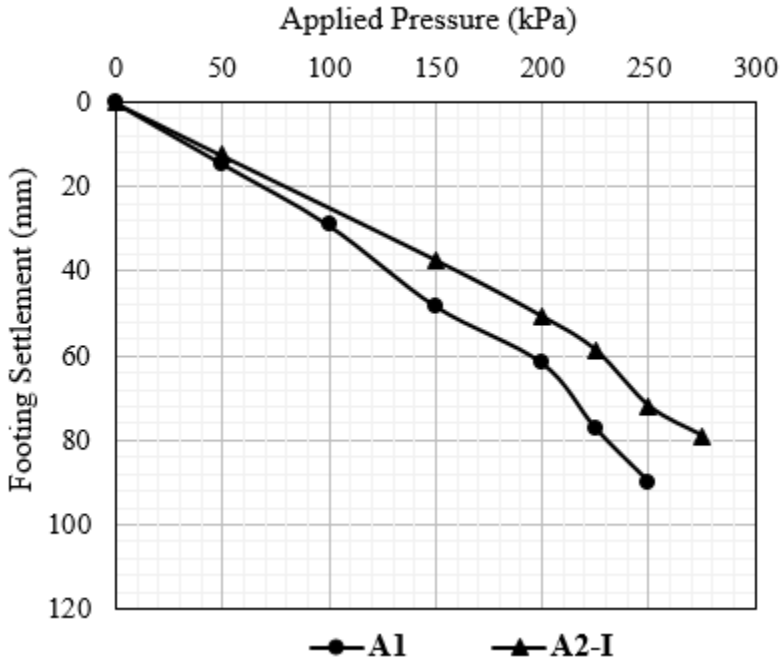

Figure 5.25 Pressure-settlement curves of the footing in the A1 and A2-I model tests

5.3.2 Effect of reinforced fill width

Figure 5.26 shows the applied pressure-settlement curves of the footing in the A2-II, A3-II, and A4 model tests. The A2-II model test had 0.7H reinforcement length, the A3-II model test had 0.5H reinforcement length, and the A4 model test had 0.3H reinforcement length. These three model tests had the same footing offset distance (i.e., 0.05 m). This figure shows that the A2-II and A3-II model tests had almost the same pressure-settlement curve under the applied footing pressure up to 150 kPa. However, the A2-II model test had smaller footing settlement after the applied footing pressure was higher than 150 kPa. In other words, the reduction of the reinforcement length from 0.7H (i.e., the A2-II model test) to 0.5H (i.e., the A3-II model test) resulted in almost the same footing settlement of the footing under the applied pressure of 150 kPa and lower, but slightly larger footing settlement of the footing under a higher applied load. For example, the A2-II model test had about 80 mm footing settlement at the applied footing pressure of 200 kPa, while the A3-II model test had 100 mm settlement at the same applied pressure, which is about 25% increase.

Further reduction in the reinforced fill width from 0.5H to 0.3H resulted in excessive settlement of the footing and a sudden failure of the model test as observed in the A4 model test. For example, the A4 model test had 60 mm settlement at the applied footing pressure of 50 kPa, while the A3-II model test had only 20 mm settlement at the same applied pressure.

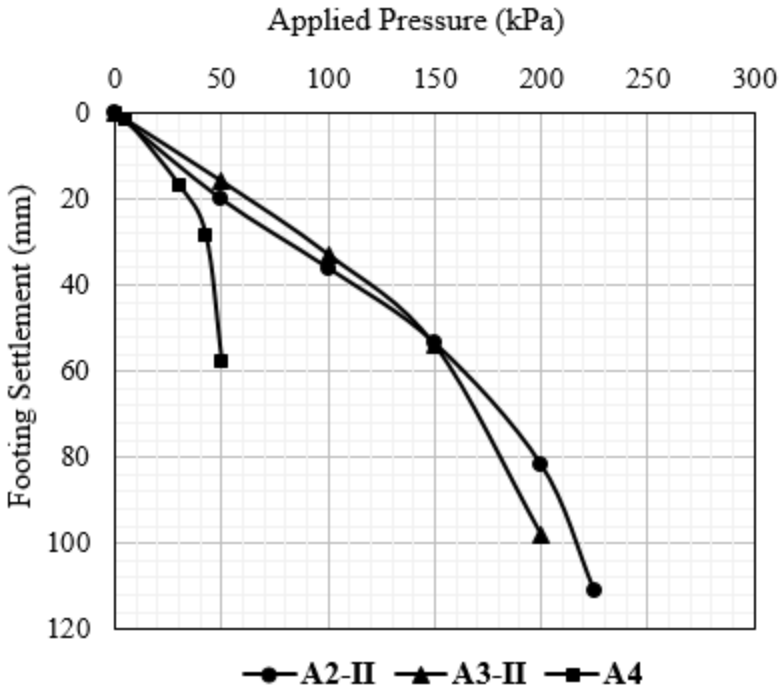

Figure 5.26 Pressure-settlement curves of the footing in the A2-II, A3-II and A4 model tests

5.3.3 Effect of footing offset distance

Figure 5.27shows the applied pressure-settlement curves of the footing in the A2-I and A2-II model tests (these two curves are presented together for the comparison purpose). The A2-I model test had a different footing offset distance from the A2-II model test. The footing offset distances were 0.2 and 0.05 m the in the A2-I and A2-II model tests, respectively.

The pressure-settlement curves in Figure 5.27 show that the A2-II model test had larger footing settlement than the A2-I model test and the difference in their settlement values increased with an increase of the applied load. In other words, the reduction of the footing offset distance from 0.2 m (i.e., in the A2-I model test) to 0.05 m (i.e., in the A2-II model test) resulted in larger settlement and lower bearing capacity of the footing. For example, the A2-I model test had about 51 mm footing settlement at 200 kPa, while the A2-II model test had 81 mm settlement at the same applied pressure, which is about 50 % increase.

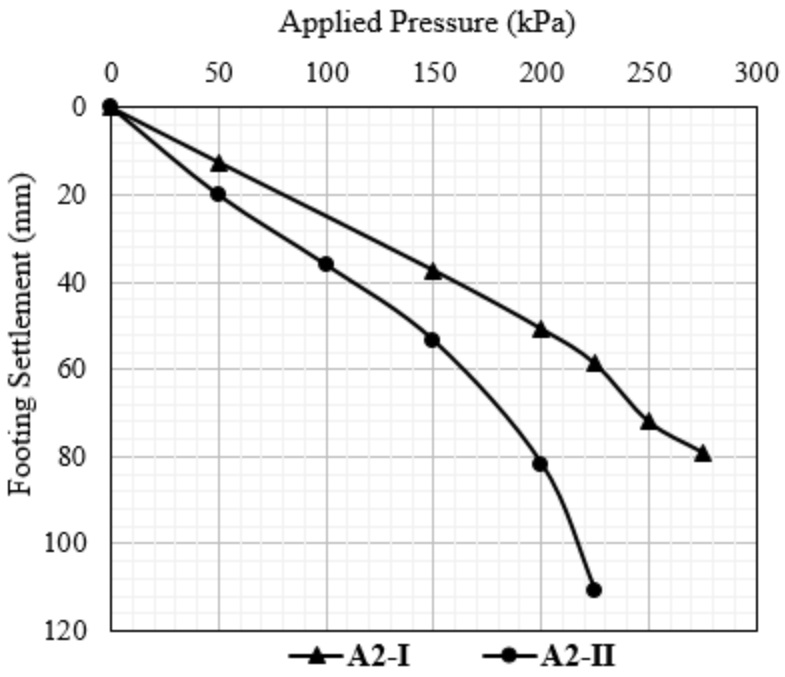

Figure 5.27 Pressure-settlement curve of the footing in the A2-I model test

Figure 5.28 shows the applied pressure-settlement curves of the footing in the A3-I and A3-II model tests. These two models had the same reinforcement length (i.e., 0.5H reinforcement length), but different footing offset distances. The footing offset distances were 0.15 and 0.05 m the in the A3-I and A3-II model tests, respectively.

This figure shows that the A3-II model test had smaller footing settlement than the A3-I model test under the applied footing pressure lower than 150 kPa. However, the A3-I model test had smaller footing settlement than the A3-II model test after the application of the footing pressure higher than 150 kPa. For example, the A3-I model test had about 33 mm footing settlement at 100 kPa, while the A3-II model test had about 28 mm settlement at the same applied pressure, which is about 15% decrease. However, the A3-I model test had about 80 mm footing settlement at 200 kPa, while the A3-II model test had 100 mm settlement at the same applied pressure, which is about 25% increase. Consequently, the reduction of the footing offset

distance from 0.15 m (i.e., in the A3-I model test) to 0.05 m (i.e., in the A3-II model test) resulted in slightly smaller footing settlement of the footing under a relatively low load, but larger footing settlement of the footing under a high load.

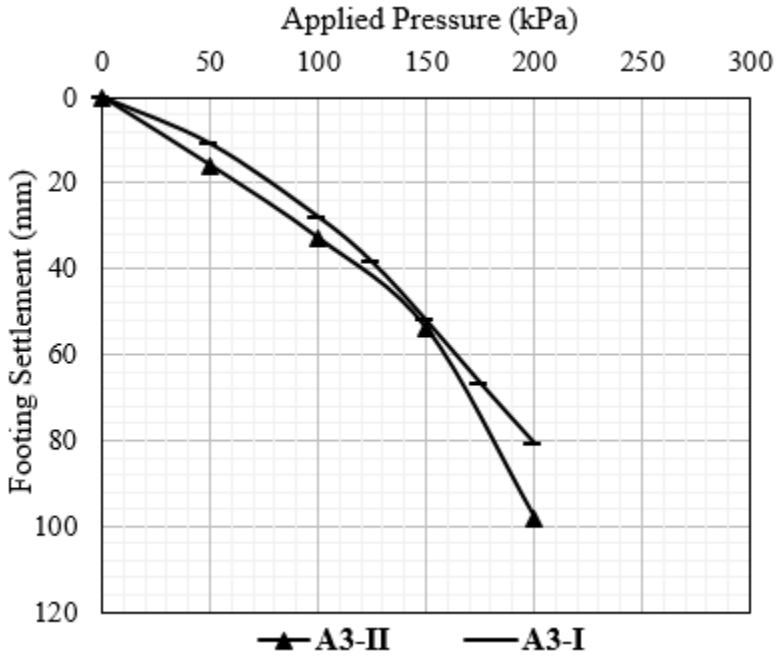

Figure 5.28 Pressure-settlement curve of the footing in the A3-I model test

5.3.4 Effect of reinforcement vertical spacing

Figure 5.29 shows the applied pressure-settlement curves of the footing in the B1 model test and the A4 model test. Both model tests had the same reinforcement length (i.e., 0.3H) except that the B1 model test had different reinforcement vertical spacing (i.e., 0.1 m) from the A4 model test (i.e., 0.2 m). Both model tests had the same footing offset distance (i.e., 0.05 m).

This figure shows that the reduction in the vertical spacing of the reinforcement from 0.2 m (i.e., the A4 model test) to 0.1 m (i.e., the B1 model test) resulted in a substantial increase in the bearing capacity of the footing and reduction in the footing settlement. For example, the A4

model test had about 60 mm footing settlement under the applied footing pressure of 50 kPa, while the B1 model test had only 9 mm settlement at the same applied pressure, which is ?% reduction.

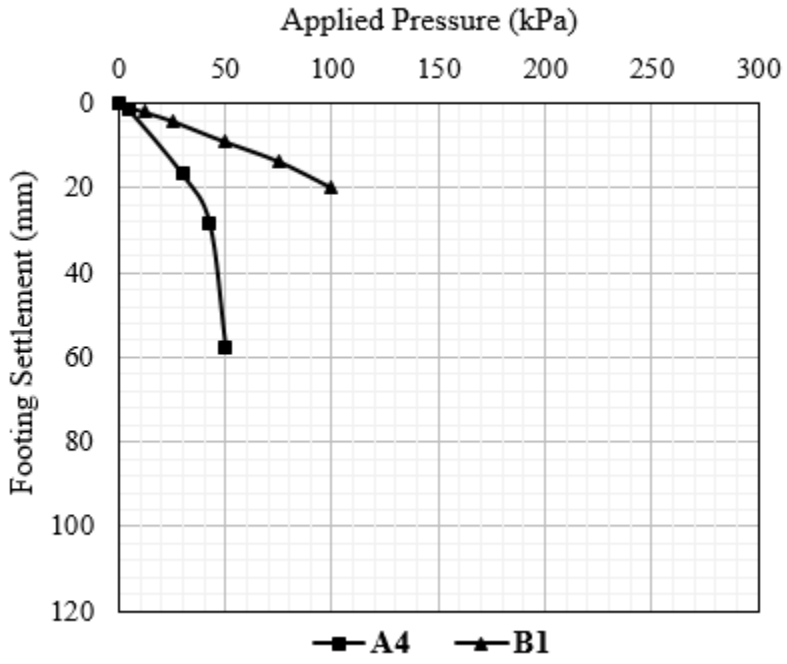

Figure 5.29 Pressure-settlement curves of the footing in the B1 model test

5.3.5 Effect of reinforcement rear connection

Figure 5.30shows the applied pressure-settlement curves of the footing in the C1, C2, and C3 model tests. These three model tests had the same reinforcement length (i.e. 0.3H) and footing offset distance, but different reinforcement rear connection. The C1 model test had four reinforcement layers out of five connected to the stable medium at the rear. The C2 model test had the two uppermost reinforcement layers connected to the stable medium at the rear. The C3 model test had all the reinforcement layers out five bent up at the rear along the stable medium. The applied pressure-settlement curve of the footing in the A4 model test is presented in this figure as well for the comparison purpose.

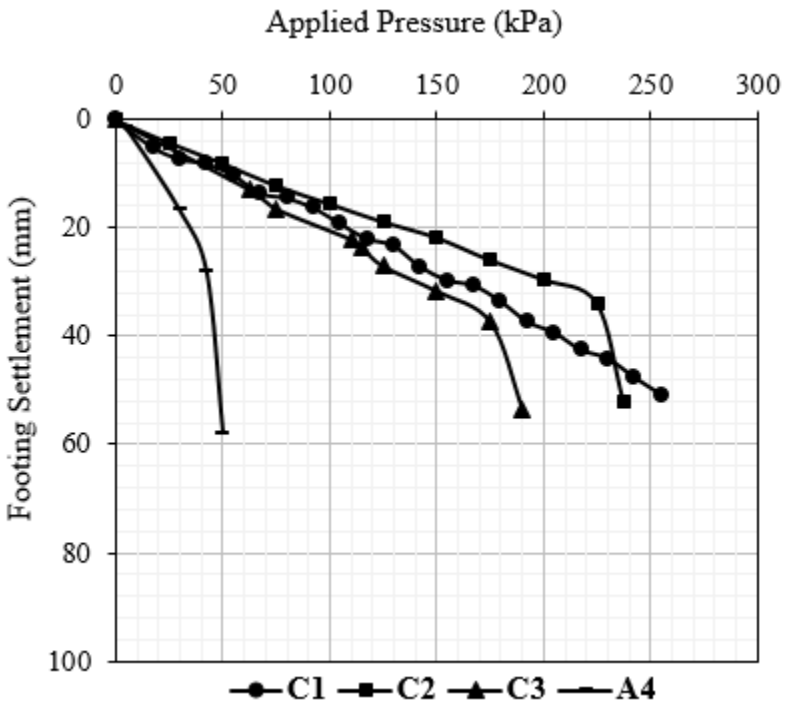

Figure 5.30 Pressure-settlement curves of the footing in the C1, C2, and C3 model tests

Figure 5.30 demonstrates that the connection of the reinforcement layers to the stable medium resulted in a considerable reduction in the footing settlement, and significant increase of the bearing capacity of the footing in the C1 and C2 model tests. For example, at the applied footing pressure of 50 kPa, the C1 and C2 model tests had only 10 mm footing settlement, while the A4 model test had almost 58 mm footing settlement at the same applied pressure. Figure 5.30 also shows that upward-bending of the reinforcement at the end of the reinforced fill in the C3 model test substantially reduced the footing settlement as compared with the A4 model test. The C3 model test had similar behavior to the C1 model test up to the applied footing pressure of approximately 180 kPa. In addition, the connection of the reinforcement layers to the stable medium increased the ultimate bearing capacity by 500% as compared with that of the A4 model

test. Upward-bending of the reinforcement at the end of the reinforced fill increased the bearing capacity by approximately four times as compared with that of the A4 model test.

Figure 5.31 shows the applied pressure-settlement curves of the footing in the A3-I and C4 model tests. These two models had 0.5H reinforcement length and the same footing offset distance (i.e. 0.25 m). However, the C4 model test had four reinforcement layers out of five bent up at the rear along the stable medium.

This figure shows that the A3-I and C4 model tests had almost the same pressure-settlement curves under relatively low applied pressure (i.e., the applied footing pressure lower than 75 kPa). However, the C4 model test showed that upward-bending of the reinforcement at the end of the reinforced fill substantially increased the bearing capacity of the footing and significantly reduced the footing settlement as compared with that of the A3-I model test. For example, the A3-I model test had about 81 mm footing settlement under the applied footing pressure of 200 kPa, while the C4 model test had 52 mm footing settlement under the same applied pressure, which is more that 50% reduction.

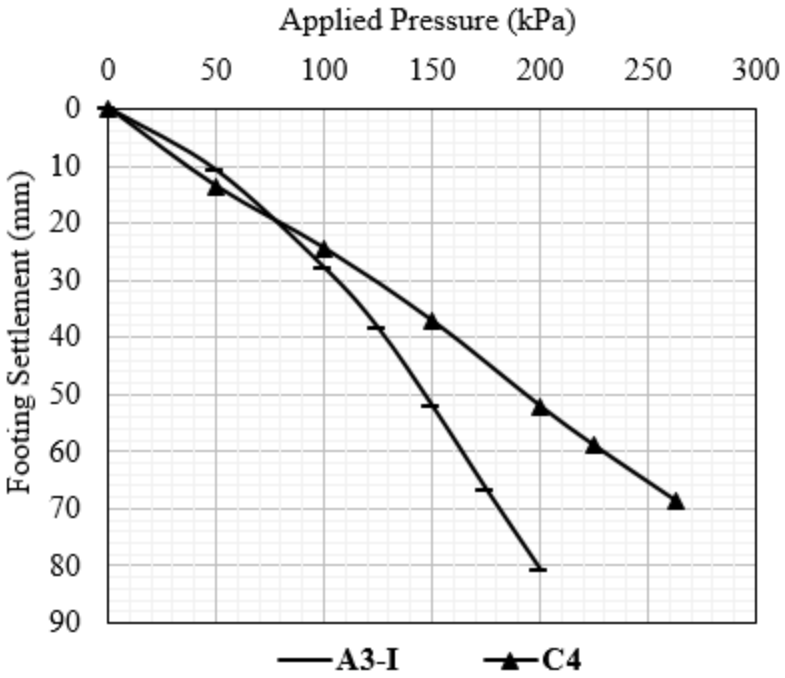

Figure 5.31 Pressure-settlement curve of the footing in the A3-I and C4 model tests

5.4 Vertical earth pressure

This section presents the measured vertical earth pressures in the model tests conducted in this study. The vertical earth pressures were measured below the centerline of the footing along the depth in all the model tests. For the comparison purpose, the vertical earth pressure distribution based on the 2:1 stress distribution method (FHWA 2009 and Morrison et al. 2006) as shown in Figure 5.32 was also calculated and is presented in this section.

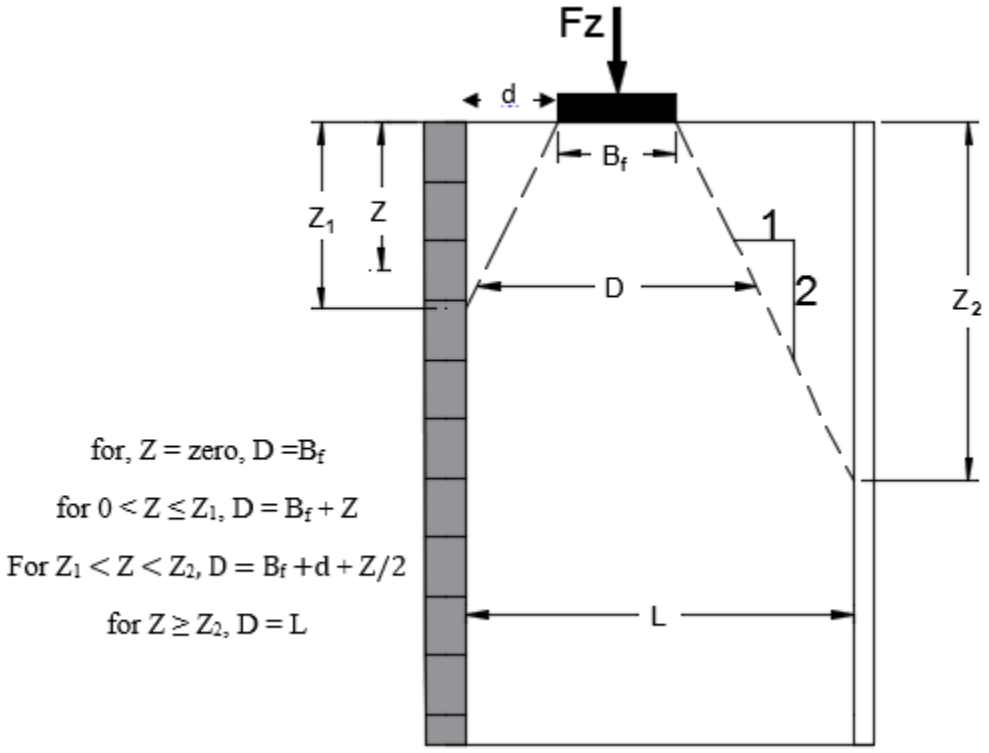

Figure 5.32 Modified 2:1 stress distribution method (after FHWA 2009 and Morrison et al. 2006)

In this method, the vertical pressure resulting from the applied footing load is assumed to distribute uniformly on an area bounded by 2(V):1(H) can be estimated by dividing the applied footing load by D1 (Equation 5.1). Using Equation (5.1) and Figure 5.31, the vertical pressures

were calculated for various applied footing loads and are plotted along with the measured vertical earth pressures presented in this section.

$$\Delta\sigma_v = \frac{F_Z}{D1} \text{ …….. (5.1)}$$

The term 2:1 used in the figures shown in this section is referred to as the 2:1 stress distribution method used by Morrison et al. (2006) and adopted by FHWA (2009).

Figure 5.33 shows the distribution of the measured vertical earth pressure versus depth under footing loading for the A2-I model test and the A2-II model test. Both model tests had 0.7H reinforcement length, but different footing offset distances (i.e., the footing offset distances were 0.2 m in the A2-I model test and 0.05 m in the A2-II model test).

The figures show that the measured vertical earth pressures in the A2-I and A2-II model tests increased with the increase of the applied footing pressure. In addition, the distributions of the measured vertical earth pressures had similar trends in both models for all the applied footing pressures. Figure 5.33(a) shows that the measured vertical earth pressures in the A2-II model test agreed well with the vertical pressures calculated based on the 2:1 method. Even though there is a fair agreement between the measured and calculated vertical earth pressures in the A2-I model test in Figure 5.33(a), the vertical earth pressures measured within the bottom portion of the wall (i.e., at the depths of 0.9 and 1.0 m) were lower than those calculated at the same depths.

The terms TEST and 2:1 used in the legends of the figures presented in this chapter are referred as to the data measured from the experiments tests, and the data calculated based on 2:1 distribution method (Equation (5.1)).

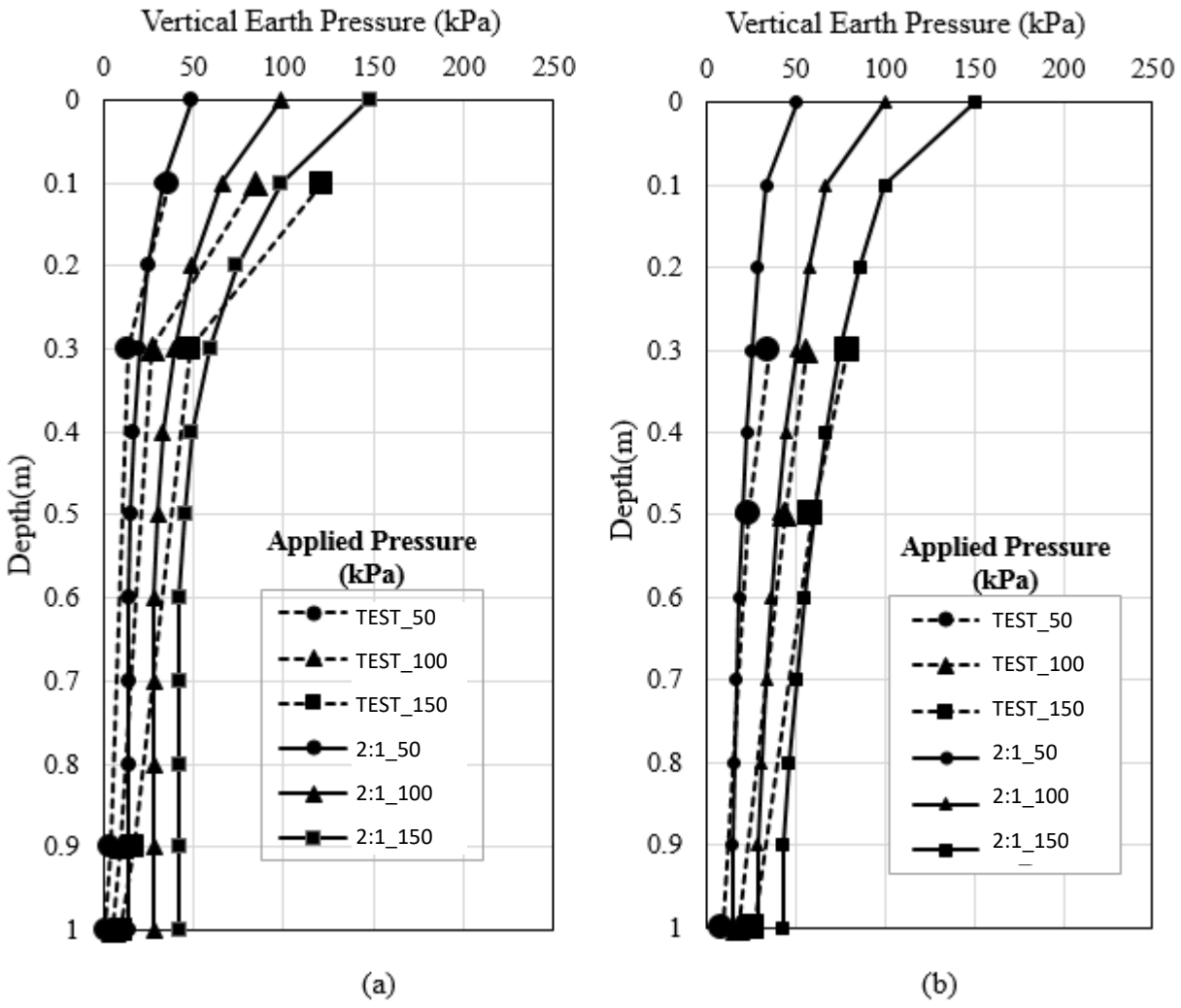

Figure 5.33 Vertical earth pressure distributions versus depth for (a) the A2-I model test and (b) the A2-II model test

Figure 5.32 also shows that the pressure cells in the A2-II model test measured higher vertical pressures than those in the A2-I model test. For example, the measured vertical earth pressure at the depth of 0.2 m in the A2-II model test was approximately 77 kPa under the applied footing pressure of 150 kPa, while in the A2-I model test, the measured vertical earth pressure at the same depth was approximately 50 kPa under the same applied footing pressure. These differences are due to the different footing offset distances for the two models. As

illustrated in Figure 5.14 (a), when the footing was close to the facing wall (i.e., in the case of the A2-II model test), the applied load was distributed to a narrower area and hence higher vertical stresses at the same the depth.

Figure 5.34 shows the distribution of the measured vertical earth pressure and the vertical pressures calculated based on the 2:1 method versus depth under footing loading for the A3-I and the A3-II model test. Both model tests had 0.5H reinforcement length, but different footing offset distances. The footing offset distances were 0.15 m in the A3-I model test, and 0.05 m in the A3-II model test.

Figure 5.34 shows that the measured vertical earth pressures increased with the increase of the applied footing pressure and had the similar trends for all the applied footing pressures in both the A3-I and A3-II model tests). This figure also shows that the measured vertical earth pressures at the depths of 0.1 m and 0.3 m in the A3-I model test in Figure 5.34 (a) matched well those calculated at the same depths. However, the vertical earth pressures measured below the depth of 0.3 m are lower than those calculated at the same depth.

In addition, like the A2-II model test in Figure 5.32(b), the vertical earth pressures measured in the A3-II model test were higher than those in the A2-I model test at the same depth and under the same applied footing pressure. These differences are also because of the different footing offset distances in the two models, which adversely affected the pressure distribution with the depth of the walls. Figure 5.14 (b) illustrates the effect of the footing offset distance on the pressure distribution in the models that had 0.5H reinforced fill width.

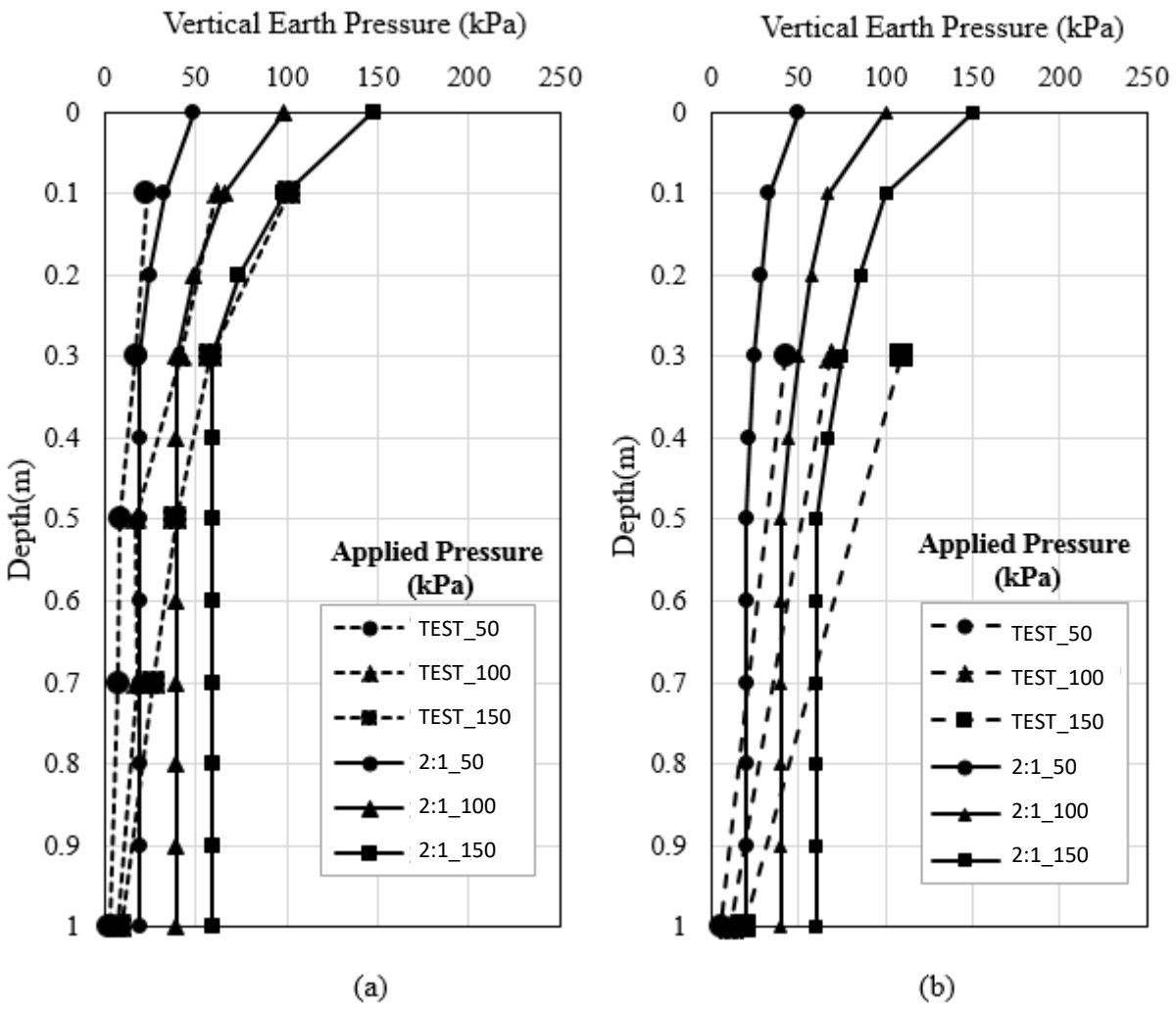

Figure 5.34 Vertical earth pressure distributions versus depth for (a) the A3-I model test and (b) the A3-II model test

Figures 5.35 and 5.36 show the distributions of the measured vertical earth pressure versus depth under footing loading for the A4 model test and the B1 model test. Both models had the same reinforcement length (i.e., 0.3H) and footing offset distance (i.e., 0.05 m). However, the B1 model test had smaller vertical spacing between the reinforcement layers (i.e., 0.1 m) than that of the A4 model test. The calculated vertical pressures from the 2:1 distribution method are also shown in these figures.

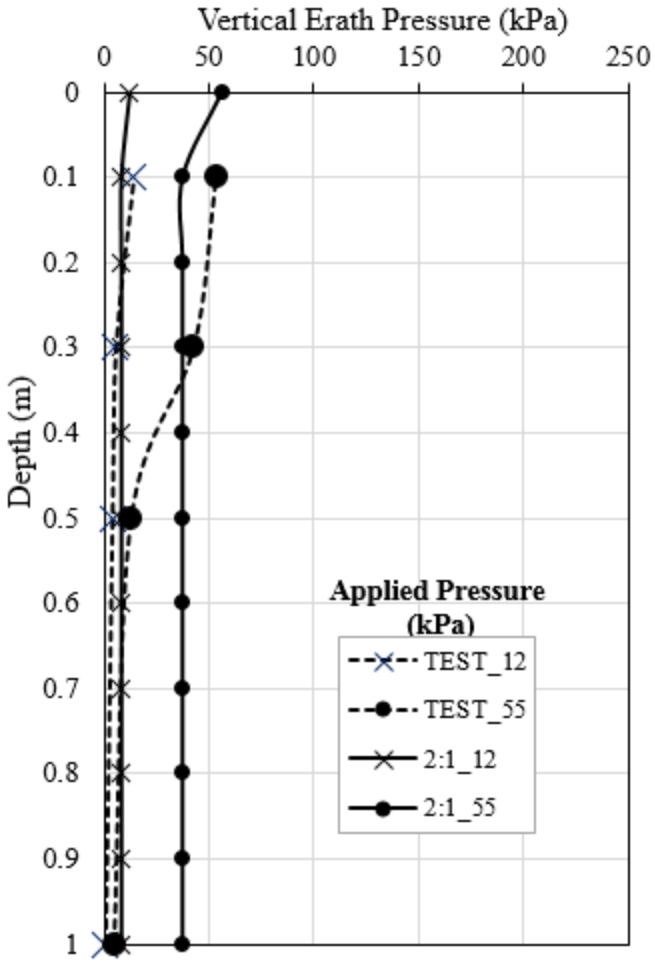

Figure 5.35 Vertical earth pressure distribution versus depth for the A4 model test

Figure 5.35 shows that at the low applied footing pressure (i.e., 12 kPa), the 2:1 method appears to provide a reasonable estimate of the vertical earth pressures along the depth of the model. However, at the higher applied pressure (i.e., 55 kPa), the 2:1 method appears to overestimate the vertical pressure in the model, especially for the depth deeper than 0.3 m.

Similar to the A4 model test, the measured vertical earth pressures in the B1 model test are lower than the vertical pressures calculated based on the 2:1 method.

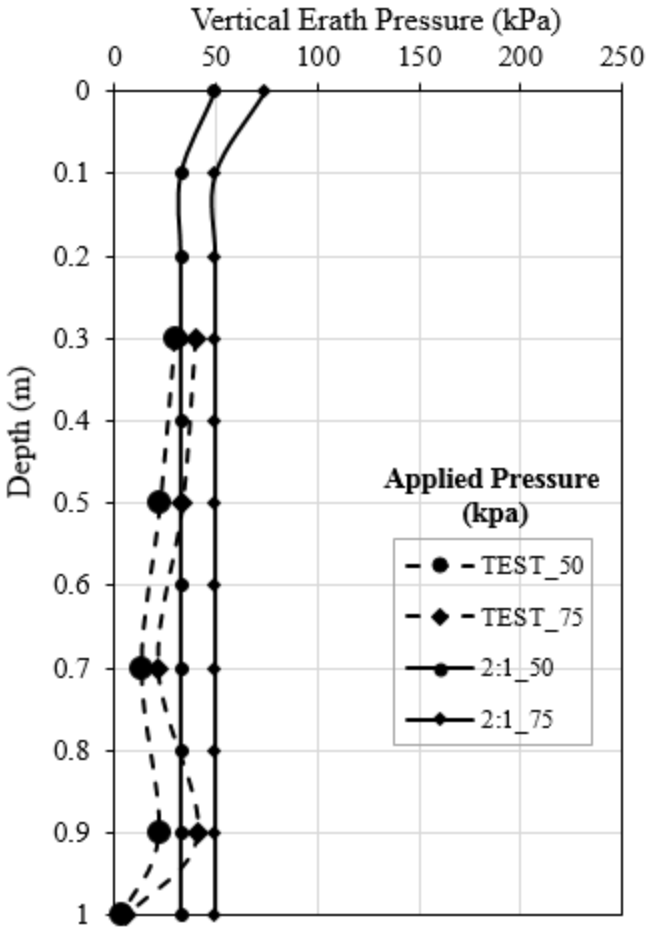

Figure 5.36 Vertical earth pressure distribution versus depth for the B1 model test

The differences between the measured and calculated vertical earth pressures may be due to two main reasons. First, the 2:1 pressure distribution method (Figure 5.32) is applicable to a footing on a half-space level ground. In this study, the footing width (i.e., 0.2 m) was close to the model width (i.e., 0.3 m). As a result, the distribution of the vertical pressure is almost the same from the top to the bottom of the model wall (i.e., the vertical earth pressure does not decrease with depth) as illustrated in Figure 5.11(c). Second, the effect of the side wall friction is not considered in the 2:1 distribution method. The side friction generates shear stresses along the wall facing and the stable medium and hence reduce the vertical pressure with depth.

Figure 5.37 shows the measured vertical earth pressure versus depth under the applied footing load for the C1 model test and the C2 model test. Both models had the same reinforcement length (0.3H). In these models, however, four reinforcement layers in the C1 model test and two top layers in the C2 model test were mechanically connected to the stable medium.

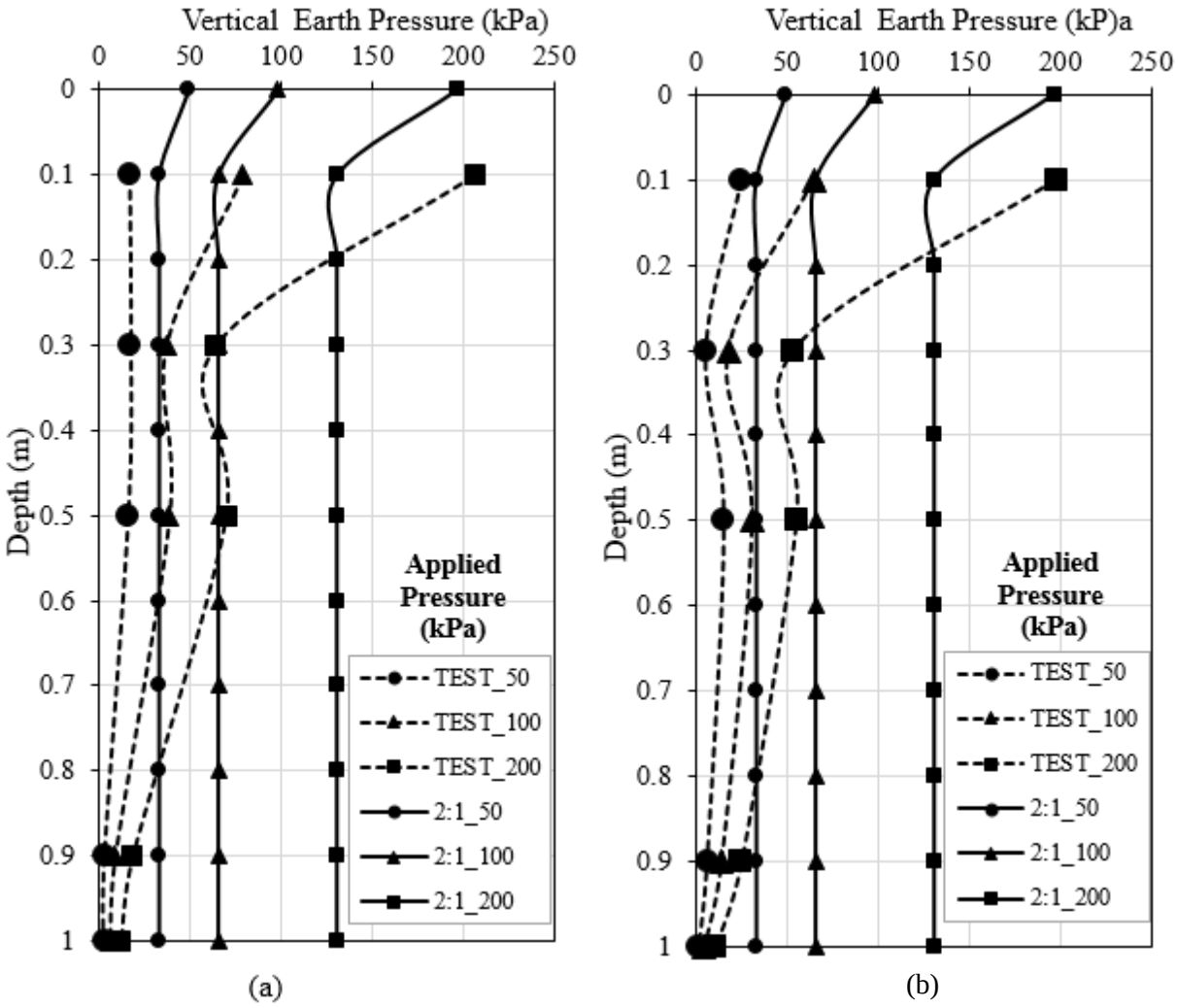

Figure 5.37 Vertical earth pressure distribution versus depth for (a) the C1 model test and (b) the C2 model test

Figure 5.37 shows that both models had similar trend of the measured vertical earth pressure distributions under all applied footing pressures, in which the measured vertical earth pressures increased with the increase of the applied footing pressure. This figure also shows that, except for the vertical earth pressures measured at the top (i.e., at the depth of 0.9 m), the measured vertical earth pressures are lower than those calculated using the 2:1 distribution method. This conclusion is consistent with the conclusion from the A4 and B1 model tests. Both conclusions make the 2:1 method questionable for limited fill space walls, especially, when the wall width is less than 0.5H.

Figure 5.38 shows the distribution of the measured vertical earth pressure and the vertical pressure calculated based on the 2:1 method versus depth under the applied footing load in the C3 model test. This model had 0.3H reinforcement length, in which the reinforcement layers were bent upward at the end by 0.2 m between the back of the reinforced fill and the stable medium. Like other models (e.g., the A4, B1, C1, and C2 model tests), the measured vertical earth pressures in the C3 model test were lower than the vertical pressures calculated by the 2:1 distribution method.

Figure 5.39 shows the distribution of the measured vertical earth pressure versus depth under the applied footing load in the C4 model test. This model had 0.5H reinforcement length, in which the reinforcement layers were bent upward at the end by 0.2 m between the back of the reinforced fill and the stable retained medium. This figure shows that the measured vertical earth pressures increased with the increase of the applied footing pressure, which is similar to that in the A3-I model test. Both the C4 and A3-I model tests had the same reinforced fill width and footing offset distance.

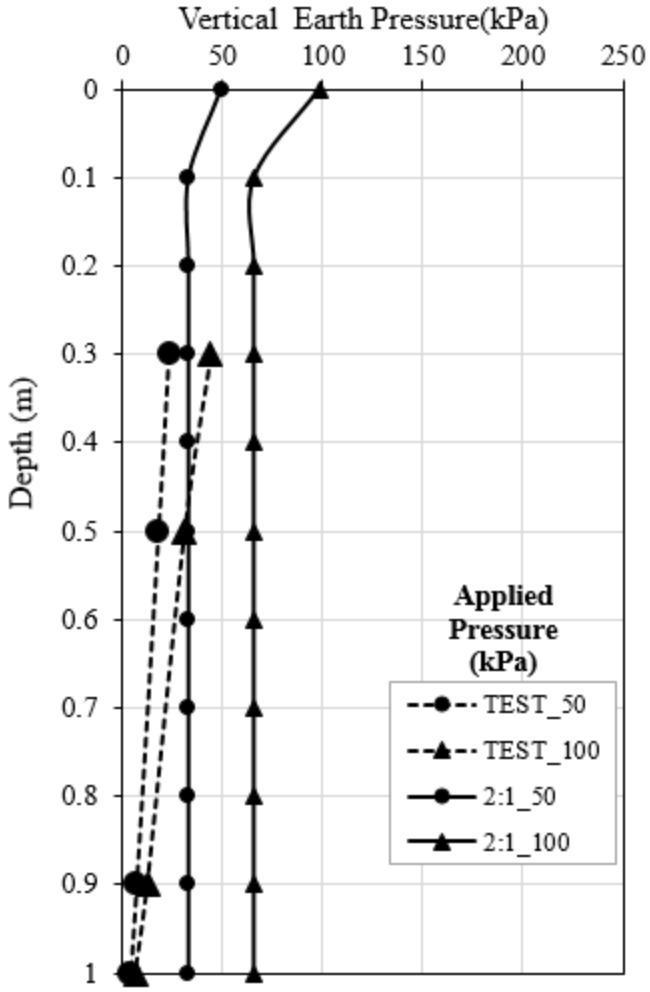

Figure 5.38 Vertical earth pressure distribution versus depth for the C3 model test

Figure 5.39 shows a very good agreement between the measured and the calculated vertical earth pressures at the wall depth of 0.3 m. However, the measured vertical earth pressures are lower than those calculated by the 2:1 method below the depth of 0.3 m. In addition, their differences became more with depth. This conclusion is consistent with the conclusion from the A3-I model test.

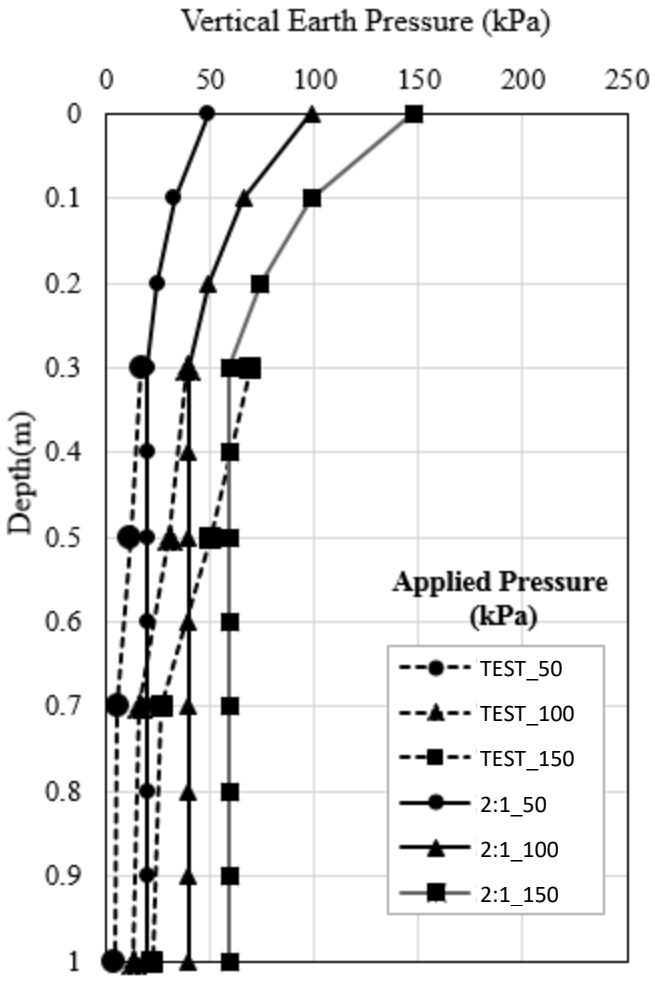

Figure 5.39 Vertical earth pressure distribution versus depth for the C4 model test

5.5 Lateral earth pressure

This section presents the measured lateral earth pressures on the wall facing in the model tests conducted in this study. For the comparison purpose, the lateral earth pressures were calculated based on the existing analytical methods and are presented in this section. These analytical methods include: (1) the Rankine theory for an active condition and (2) the equation developed based on Janssen's arching theory.

Based on the Rankine theory for the active condition, the lateral earth pressure at a desired depth is equal to the coefficient of active lateral earth pressure times the vertical pressure at the same depth. The coefficient of lateral earth pressure based on the Rankine active condition was calculated using Equation (5.2), and the 2:1 distribution method (Figure 5.32) was used to calculate the vertical pressure at a desired depth. The lateral pressures on the wall facing were then calculated and plotted for various applied footing loads using Equation (5.3).

$$k_{a(R)} = \frac{(1-\sin\phi)}{(1+\sin\phi)} \quad \text{..... (5.2)}$$

where:

$k_{a(R)}$ is the coefficient of active lateral earth pressure,

ϕ is the internal friction angle of the backfill material (i.e., $\phi = 37^{o}$ was used based on the trixial test),

$$\sigma_{h(R)} = k_{a(R)} * \sigma_{v} \quad \text{..... (5.3)}$$

where:

$\sigma_{h(R)}$ is the lateral earth pressure on the wall facing,

$k_{a(R)}$ is the coefficient of active lateral earth pressure from Equation (5.2),

σ_v is the vertical applied pressure calculated based on the 2:1 distribution method using Equation (5.1).

Equation (5.4), which was derived based on Janssen's arching theory (Yang and Tang 2017), was also used to calculate the coefficient of lateral earth pressure:

$$k_J = \frac{B}{2z\tan\delta}\left(1 - e^{-2K\frac{Z}{B}\tan\delta}\right) \quad \text{..... (5.4)}$$

where:

k_J is the coefficient of lateral earth pressure derived based on Janssen's arching theory,

B is the backfill width,

Z is the depth from the top of the wall,

H is the wall height,

δ is the friction angle between the backfill and wall and the backfill and the stable wall (assumed equal in this study),

K is the lateral earth pressure coefficient, which was calcualted uisng Equation (5.5) (Frydman and Keissar 1987):

$$K = \frac{(\sin^2\phi+1)-\sqrt{(\sin^2\phi+1)^2-(1-\sin^2\phi)(4\tan^2\delta-\sin^2\phi+1)}}{(4\tan^2\delta-\sin^2\phi+1)} \text{..... (5.5)}$$

where:

ϕ is the internal friction angle of the backfill material (i.e., $\phi = 37^o$ was used based on the trixial test).

The lateral earth pressure on the facing wall was calculated using Equation (5.6):

$$\sigma_{h(J)} = k_J * \sigma_v \quad \ldots\ldots\ldots\ldots\ldots\ldots \quad (5.6)$$

where

$\sigma_{h(J)}$ is the lateral earth pressure on the wall facing,

k_J is the coefficient of lateral earth pressure from Equation (5.4),

σ_v is the vertical applied pressure calculated based on the 2:1 distribution method using Equation (5.1).

Since Equation (5.4) requires the interface friction angle (δ) between the boundaries (wall facing and the stable wall) and the backfill to be known, $\delta = 26^o$ was assumed for the calcualtions.

Figure 5.40 compares the measured lateral earth pressures under the footing load for the A2-I and A2-II model tests. Both model tests had same reinforcement length, but different footing offset distances. The footing offset distances were 0.3 m in the A2-I model test, and 0.15 m in the A2-II model test. The calculated lateral earth pressures based on Rankine's active earth pressure theory using Equation (5.3) and Janssen's arching theory using Equation (5.6) are also plotted in the following figures. Note: the symbols, R_2:1 and J_2:1, used in the following figures are referred to as the lateral pressures calculated based on Rankine's active earth pressure theory and Janssen's arching theory, respectively, with the vertical pressures calculated using the 2:1 distribution method.

These figures show that the measured lateral earth pressures generally increased with the increase of the applied footing load. In addition, the measured pressures of both the A2-I and A2-II model tests show the similar trends under all the applied footing loads.

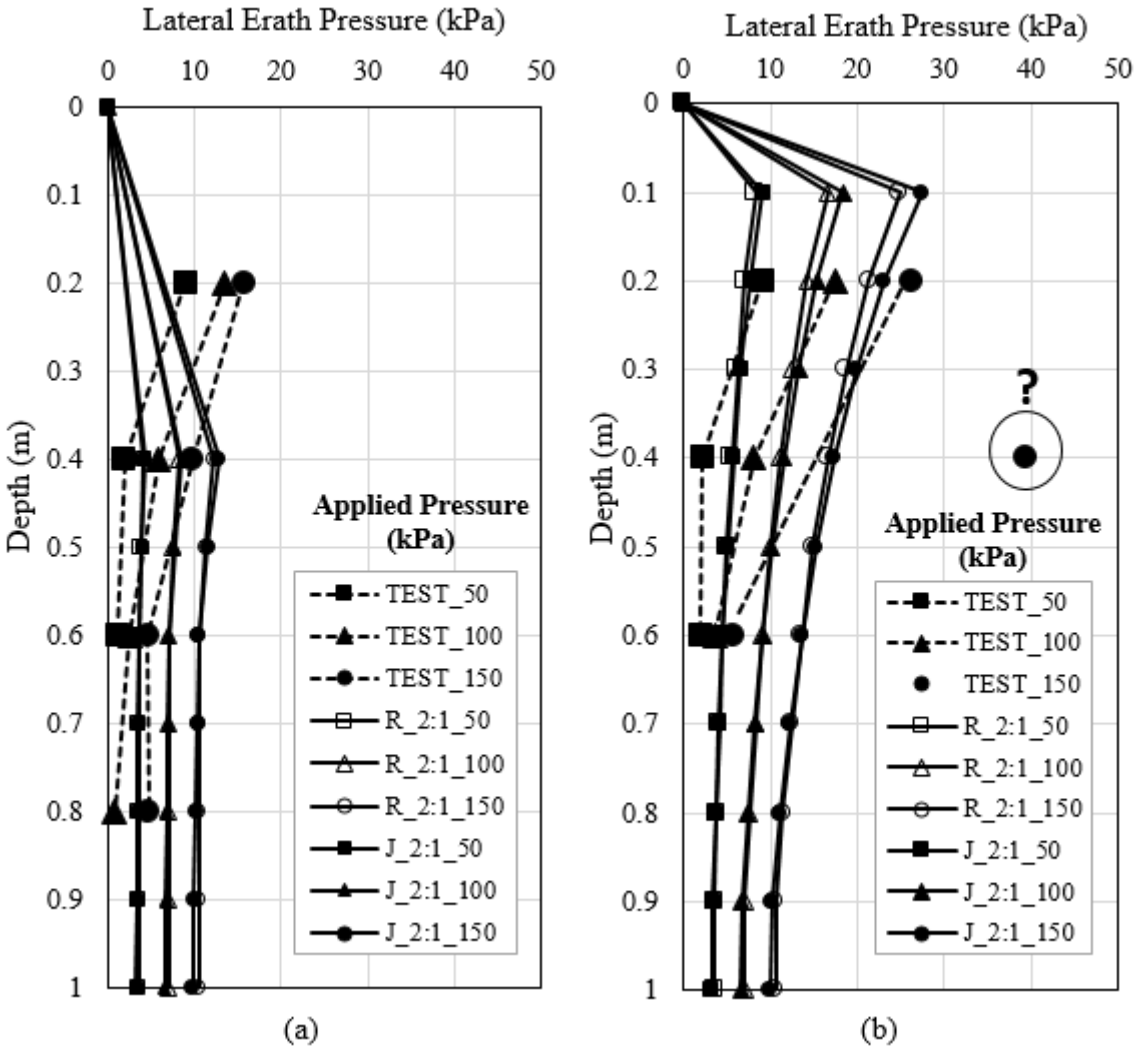

Figure 5.40 Lateral earth pressure distribution versus depth for (a) the A2-I model test and (b) the A2-II model test

However, the pressure cells in the A2-II model test recorded higher lateral earth pressures than those in the A2-I model test. For example, the measured lateral earth pressures at the depth of 0.2 and 0.3 m in the A2-II model test were approximately 17 kPa and 8 kPa, respectively, under the applied footing pressure of 100 kPa, while in the A2-I model test, the measured lateral earth pressures at the same depths were approximately 13 kPa and 8 kPa under the same applied

footing pressure. These differences are due to the differences in the footing offset for the two models. As illustrated in Figure 5.14 (a), when the footing was close to the wall facing (i.e. in the case of the A2-II model test), the applied load was distributed to a narrower area, resulting in higher vertical pressure and hence higher lateral pressure.

Figure 5.40 also shows that the lateral pressures calculated based on Equations (5.3) and (5.6) are almost the same. In addition, the measured lateral earth pressures matched well the calculated lateral pressures at the depth of 0.2 m in case of A2-II model test. Even at the depth of 0.4 m there is a fair agreement between the measured and the calculated earth pressures. However, the measured lateral earth pressures for the pressure cells at the lower elevation (i.e., at the depth lower than 0.4 m) are lower than the calculated earth pressures at the same depth.

Figure 5.41 compares the measured lateral earth pressures under the footing load for the A3-I and A3-II model tests. Both model tests had 0.5H reinforcement length, but different footing offset distances. The footing offset distances were 0.25 m in the A3-I model test, and 0.15m in the A3-II model test. This figure also compares the lateral pressures calculated based on Rankine's active condition using Equation (5.3) and Janssen's arching theory using Equation (5.6).

Figure 5.41 shows that the measured lateral earth pressures increased with the increase of the applied footing load with similar trends under all the applied footing loads in both the A3-I model test and the A3-II model test. Figure 5.41 also shows that the measured lateral earth pressures matched well the calculated lateral earth pressures. Except the lateral earth pressures measured at the depth 0.f 0.2m in case of A3-I model test were higher than the calculated lateral earth pressures. Figure 5.41 also shows that the earth pressures calculated based on Equations (5.3) and (5.6) are almost the same except that the calculated earth pressures from Janssen's

equation (i.e., J_2:1 lines) are slightly lower than those calculated from Rankine's theory (i.e., R_2:1 lines) at the depth of 0.8 m and lower.

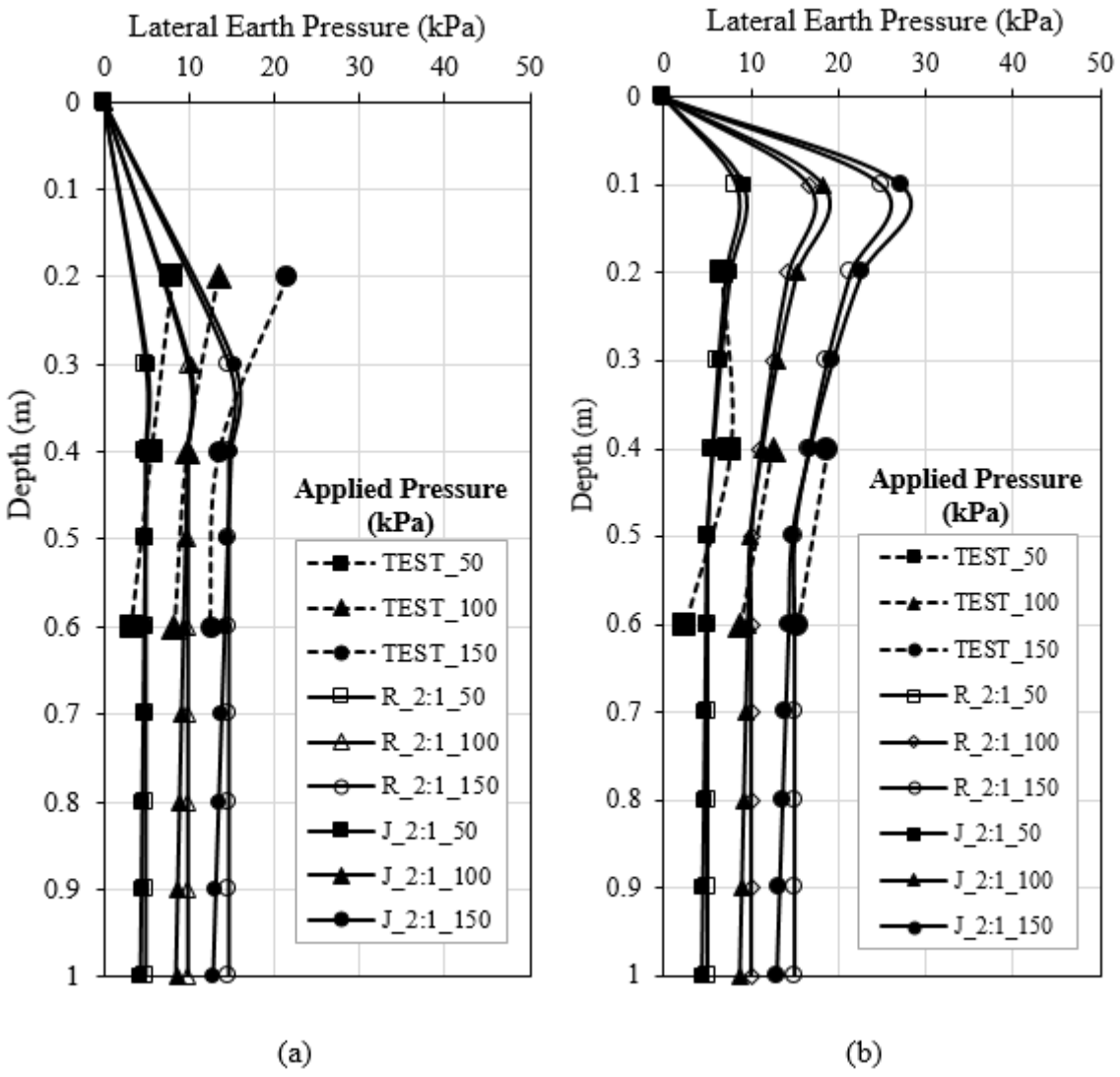

Figure 5.41 Lateral earth pressure distribution versus depth for (a) the A3-I model test and (b) the A3-II model test

Like the A2-II model test in Figure 5.40 (b), the pressure cells in the A3-II model test recorded higher lateral earth pressures than those in the A2-I model test at the same depth and

under the same applied footing load. The differences are also because of their differences in the footing offset distance in the two models, which adversely affected the pressure distribution along the depth of the walls. Figure 5.14 (b) illustrates the effect of the footing offset distance on pressure distribution in the models with 0.5H reinforced fill width.

Figures 5.42 and 5.43 show the measured lateral earth pressures versus depth under the footing load for the A4 and B1 model tests, respectively. Both models had the same reinforcement length and footing offset distance, but the B1 model test had smaller vertical spacing of the reinforcement layers. The lateral earth pressures calculated based on Equations (5.3) and (5.6) are also shown in these figures.

Figure 5.42 shows that at low applied footing pressure (i.e., 12 kPa) the measured lateral earth pressures matched well the calculated earth pressures. At the higher applied pressure (i.e., 55 kPa), the measured lateral earth pressures did not match well the calculated earth pressures, especially compared to the lateral pressures calculated based on the Rankine active condition. However, Figure 5.43 shows that the measured lateral earth pressures in the B1 model test matched well the calculated lateral pressures based on Equation (5.6).

In addition, Figures 5.42 and 5.43 show that the lateral pressures calculated based on Equation (5.6) are lower than those calculated based on Equation (5.3).

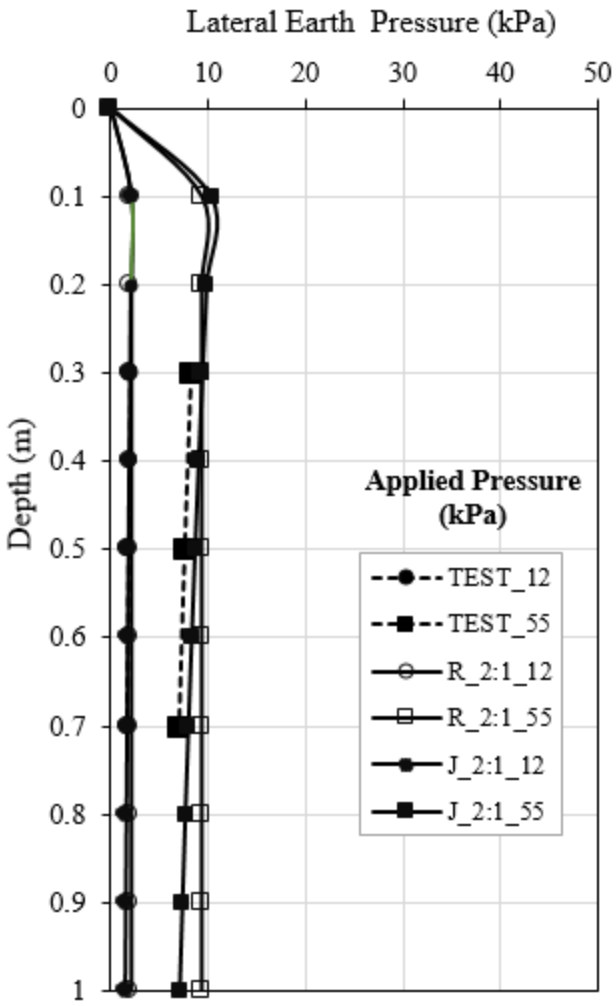

Figure 5.42 Lateral earth pressure distribution versus depth for the A4 model test

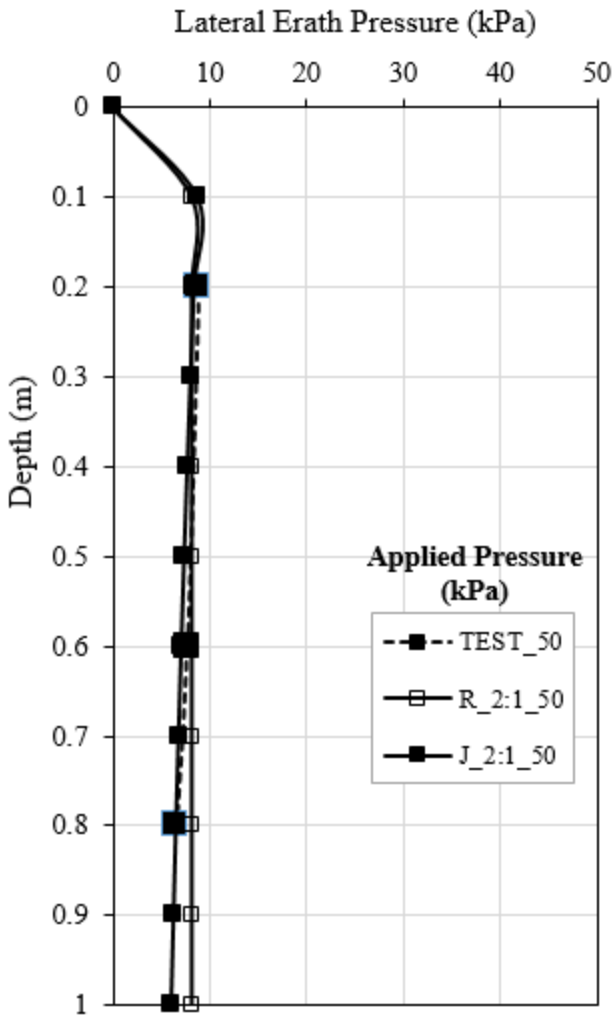

Figure 5.43 Lateral earth pressure distribution versus depth for the B1 model test

Figure 5.44 compares the measured lateral earth pressures under the footing load for the C1 model test and the C2 model test. Both models had the same reinforcement length (0.3H). In these models, four reinforcement layers in the C1 model test, and two uppermost layers in the C2 model test were mechanically connected to the stable medium. This figure also compares the lateral pressures calculated using Equations (5.3) and (5.6).

The measured lateral earth pressures generally increased with the increase of the applied footing load. However, the pressure cells located at the depths of 0.6 and 0.8 m in the C1 model

test behaved somewhat differently. Similar behavior was observed and reported by Morrison et al. (2006) for a full-scale wall field test. The wall had reinforcements connected to a stable face and a geometry proportional to the C1 model test.

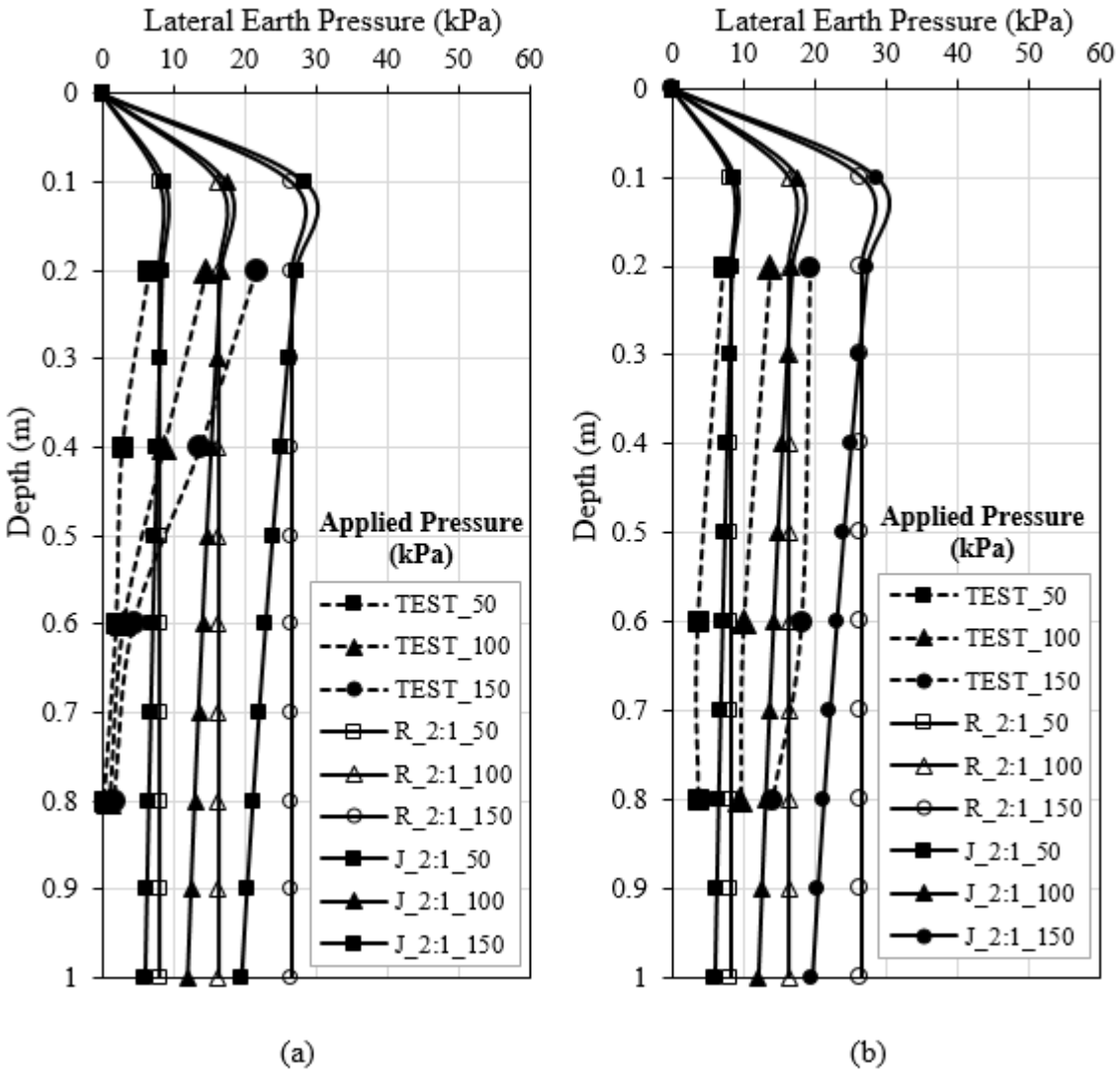

Figure 5.44 Lateral earth pressure distribution versus depth for (a) the C1 model test and (b) the C2 model test

Figure 5.45 shows the measured lateral earth pressure and the lateral pressures calculated using Equations (5.3) and (5.6) versus depth under the applied footing load in the C3 model test.

This model had 0.3H reinforcement length, in which the reinforcement layers were bent upward at the end by 0.2 m between the back of the reinforced fill and the stable medium.

This figure shows that the measured lateral earth pressures increased with the increase of the applied footing load. The measured lateral earth pressures in the C3 model test were lower than and approximately parallel to the calculated lateral pressures. This finding is consistent with those for the measured lateral earth pressures in the other models, such as the A4, B1, C1, and C2 model tests.

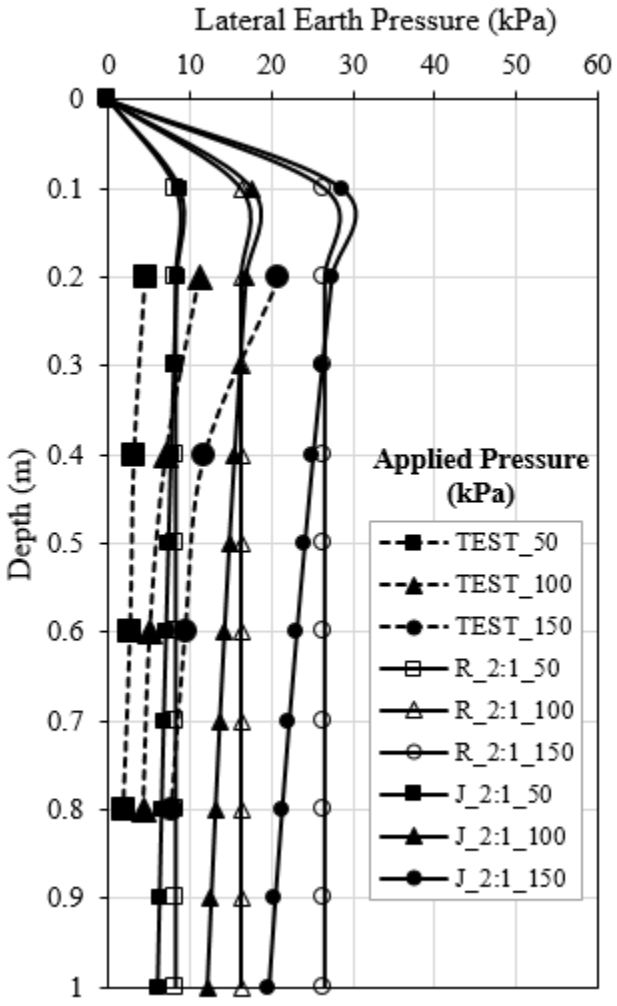

Figure 5.45 Lateral earth pressure distribution versus depth for the C3 model test

Figure 5.46 shows the measured lateral earth pressures for the C4 model test under the applied footing load. The model had 0.5H reinforcement length, in which four reinforcement layers out five were bent up at the rear along the stable medium. The lateral earth pressures calculated based on Equations (5.3) and (5.6) and the 2:1 distribution method, are also shown in the figure.

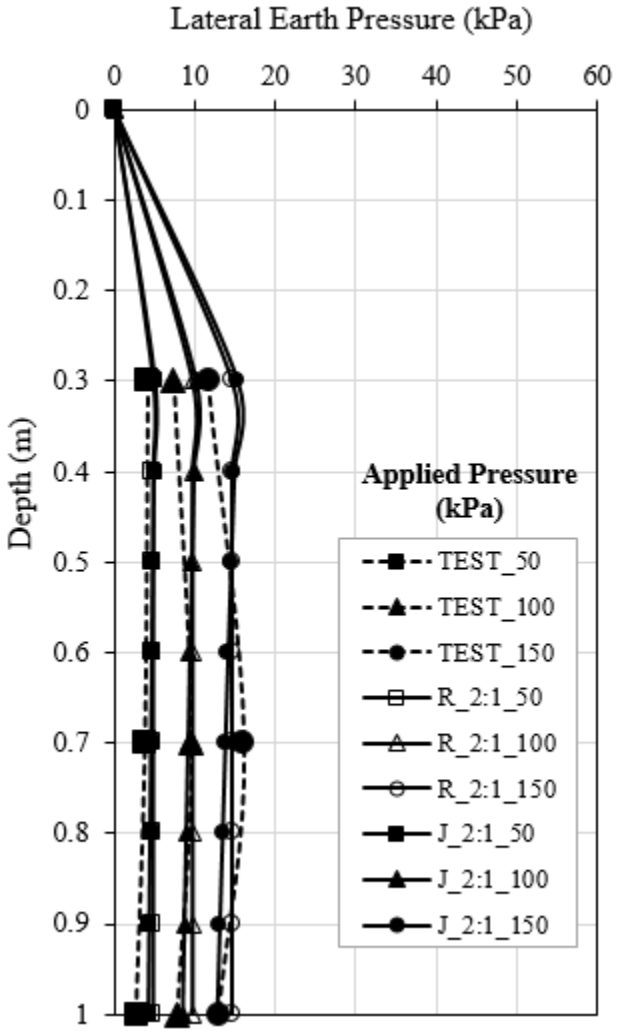

Figure 5.46 Lateral earth pressure distribution versus depth for the C4 model test

Figure 5.47 presents that the measured lateral earth pressures generally increased with the increase of the applied footing load. In addition, the measured lateral earth pressures matched well the calculated lateral pressures. This result is consistent with the result of the A3-I model test in Figure 5.41 (a). The C4 model test had the same footing offset distance as that of the A3-I model test.

To conclude, the measured lateral earth pressures for the all models with 0.3H reinforced fill width (e.g., the A4, B1, C1, C2, and C3 model tests), are lower than those calculated based on Rankine's active condition using Equation (5.3) and Janssen's arching theory using Equation (5.6). In addition, the lateral pressures calculated using Equation (5.6) are lower than those calculated using Equation (5.6) for all the considered footing loads. Therefore, the coefficient of lateral earth pressure (K) at a given depth was calculated and plotted to compare with the coefficient of lateral earth pressure calculated based on Rankine's active condition using Equation (5.2) and Janssen's equation using Equation (5.4). K is defined as the ratio of the measured lateral earth pressure (σ_{hm}) to the calculated vertical pressure using the 2:1 distribution method (σ_v), which is $K = \sigma_{hm} / \sigma_v$. Figure 5.47 shows the variation of lateral earth pressure coefficient based on the measured data (K), Rankine's active condition using Equation (5.2), and Janssen's arching theory using Equation (5.4), with depth for the C1, C2, and C3 wall models.

The terms TEST_50_C1, TEST_50_C2, TEST_50_C3 and so on are referred to as the data calculated under the applied footing load of 50 kPa for the C1, C2, and C3, respectively.

This figure shows that the lateral earth pressure coefficients calculated based on the measured data are lower than those calculated based on Equations (5.2) and (5.4) under all the applied footing pressures. In other words, the existing analytical methods may overestimate the

lateral earth pressure induced by footing loading for the walls with reinforcement width less than 0.5H.

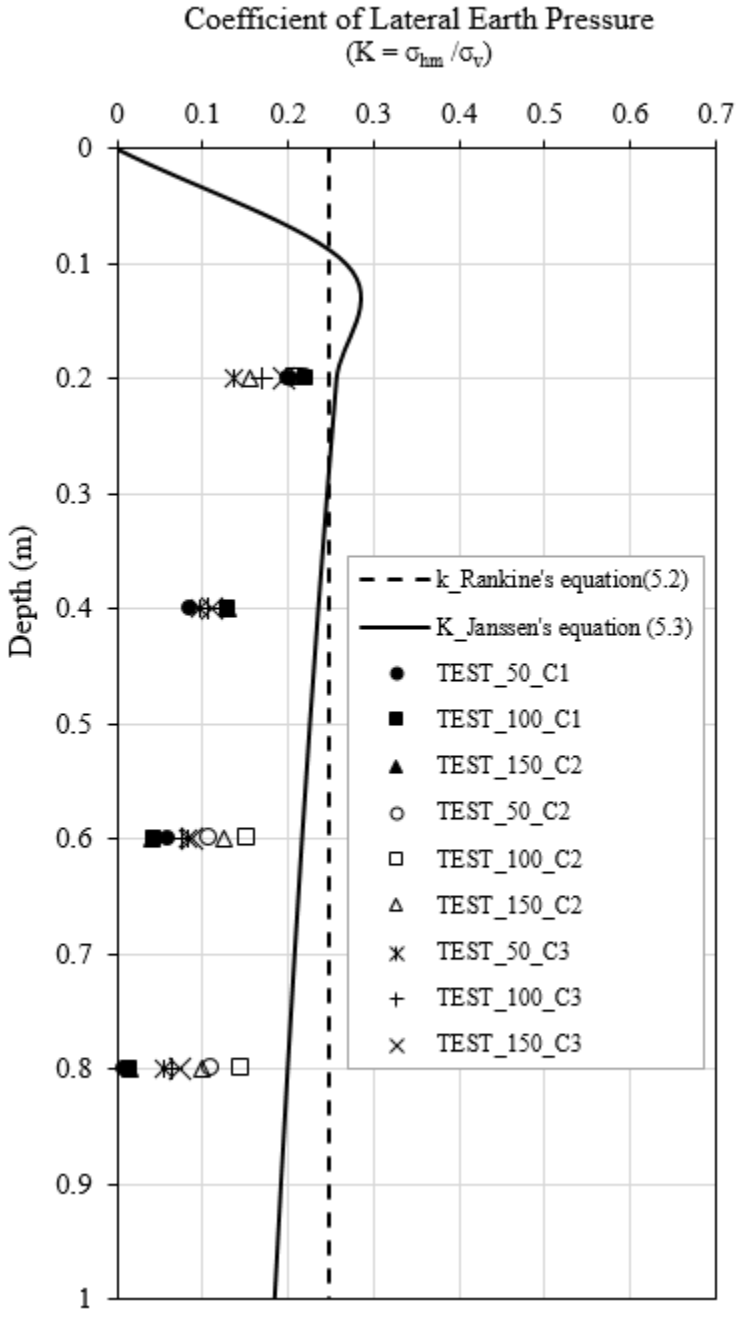

Figure 5.47 Variations of lateral earth pressure coefficient versus depth for the C1, C2 and C3 model tests

Chapter 6 Numerical Simulation

6.1 Introduction

This chapter describes the selection and calibration of the parameters used in the numerical models to simulate the experimental models conducted in the current study. The parameters include the material properties (e.g. backfill soil, facing units, and geosynthetic reinforcement) and the interfaces properties (e.g. interface between facing unit (block) and block, interface between block and backfill soil, and interface between backfill soil and geosynthetic reinforcement). Figure 6.1 shows the material and interface parameters required for numerical analysis of geosynthetic reinforced retaining (GRR) walls.

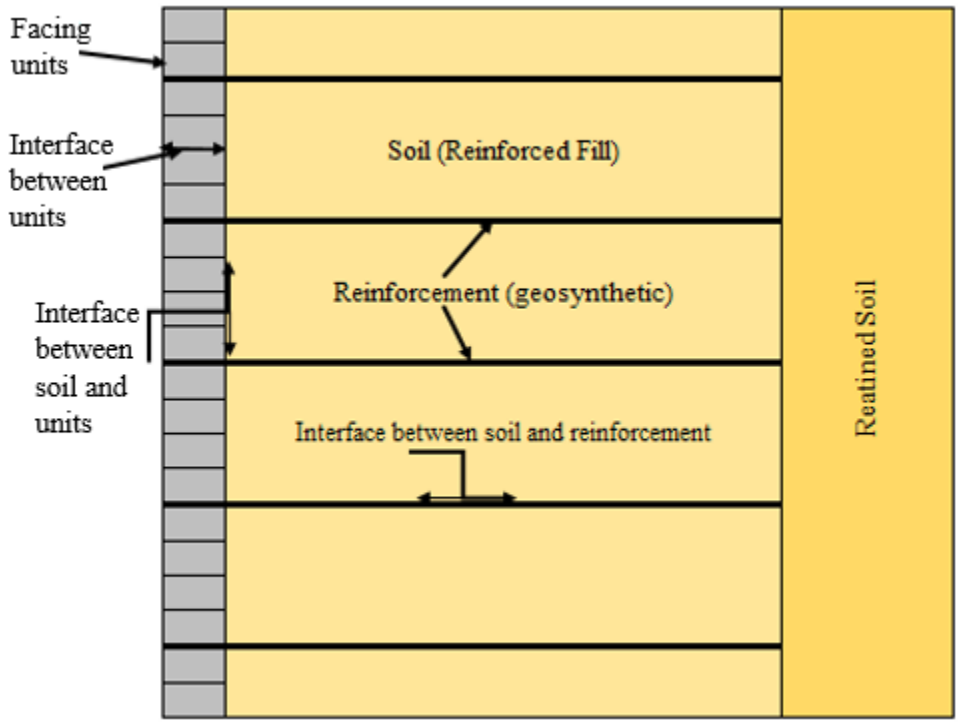

Figure 6.1 Typical parameters used in numerical simulations of a GRR walls

In addition, the experimental findings were verified using the numerical simulations and the results were also presented in this chapter.

Fast Lagrangian Analytical of Continua (FLAC), a two-dimensional (2D) finite difference program, i.e., FLAC2D Version 8.0, was used in this study. This program uses an explicit finite difference method to solve problems with initial and boundary conditions. The program supports several constitutive models, structural elements, and interface properties to model various geotechnical materials and structures (e.g., geosynthetic reinforced retaining walls).

6.2 Parameters for numerical simulation

FLAC 2D Version 8.0 was employed to perform numerical simulation of GRR wall models with limited fill space. This section presents the parameter selection and model calibration performed to estimate the properties of the reinforced fill material and geosynthetic reinforcement used in the experimental model tests, and soil-reinforcement interaction.

6.2.1 Material properties

Reinforced fill

In this study, the Mohr-Coulomb (MC) model was used to simulate the behavior of the backfill soil in FLAC. The model (MC) is linearly elastic and perfectly plastic with an MC failure criterion. A few researchers used the MC model in numerical modeling of GRR walls and showed that the MC model had capabilities to reasonably simulate the behavior of soil in GRR walls (e.g., Leshchinsky et al. 2004; Yang and Liu 2007; Han and Leshchinsky 2010; Huang et al. 2011; Damians et al. 2014; Yu et al. 2016; Jiang 2016). Figure 6.2 shows the stress-strain relationship of the MC model. This figure shows that the stress linearly increases

with strain and failure occurs when the stress reaches a shear strength (σ_y), and then the soil behavior becomes perfectly plastic. The yield stress can be determined using Equation (6.1), based on the MC failure criterion as shown in Figure 6.3.

$$\sigma'_y = c + \sigma'_c \tan\phi' \quad \ldots\ldots\ldots\ldots\ldots\ldots (6.1)$$

where

σ'_y is the shear strength of the soil,

c is the cohesion of the soil,

σ'_c is the effective confining stress applied on the soil, and

ϕ' is the effective friction angle of the soil.

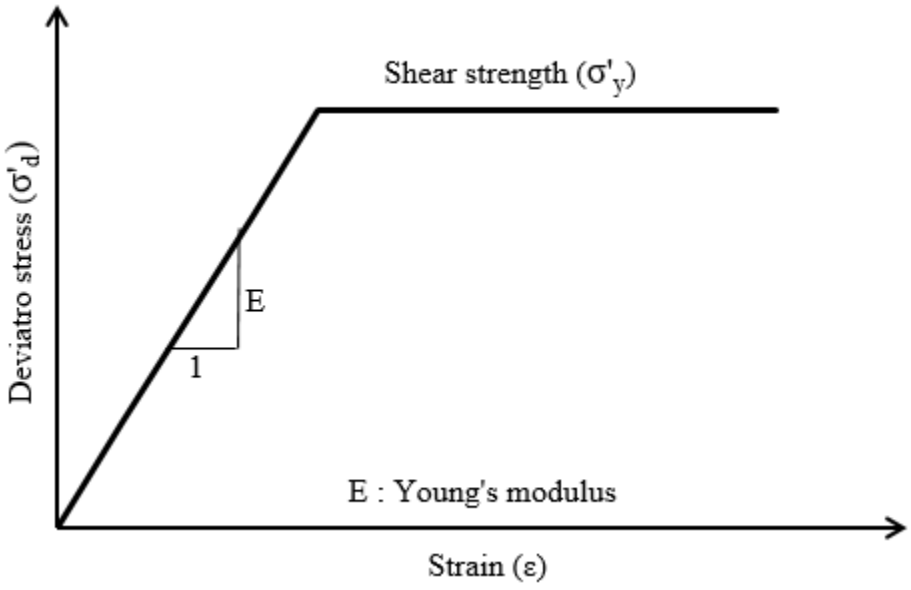

Figure 6.2 Stress-strain relationship for the Mohr-Coulomb model

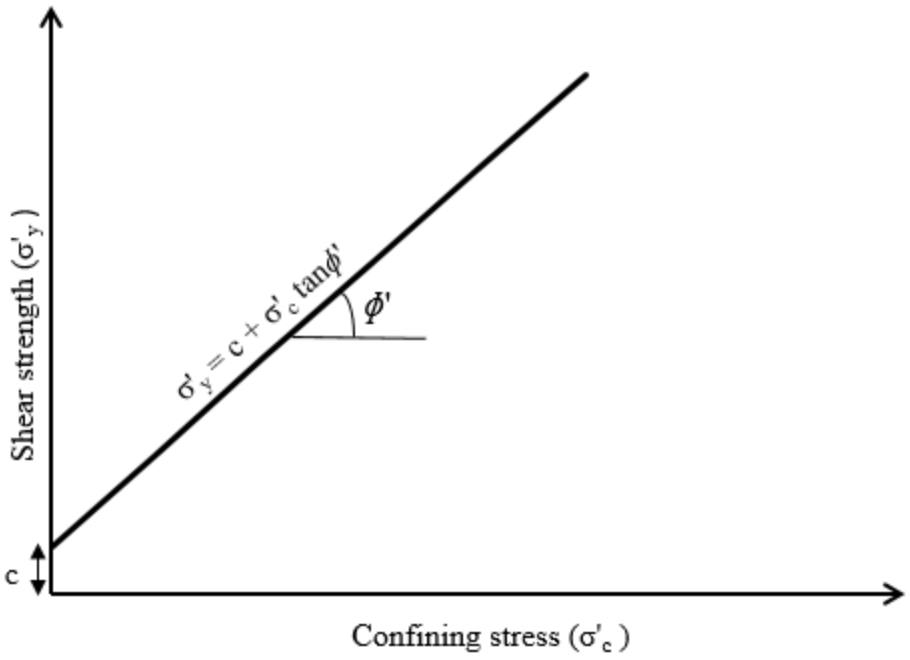

Figure 6.3 The MC failure criterion

The parameters of the Mohr-Coulomb model required for numerical simulation are: the friction angle (ϕ'), cohesion (c'), dilation angle (ψ), Young's modulus (E), and Poisson's ratio (ν) of the soil. Table 6.2 presents the parameters used in the MC model for the soil in this study. The unit weight (γ) was determined from the average unit weight of the samples prepared for triaxial tests. Young's modulus was determined from the initial slope of the stress-strain relationship of the soil. Poisson's ratio was assumed to be 0.25. The friction angle of the backfill soil was determined from the results of the triaxial tests conducted at three confining stresses of 34.5, 68.9, and 103.4 kPa. Considering a plane strain condition, the friction angle of the soil was converted to the friction angle in a plane strain condition using $\phi_p = 1.12\phi_t$ (Kulhway and Mayne 1990), where ϕ_p is the friction angle from plane strain compression tests and ϕ_t is the friction angle from triaxial compression tests.

Table 6.1 Parameters of the Mohr-Coulomb model for the backfill soil

Parameters	Value
γ (kN/m^3)	17.5
E (MPa)	23
ν	0.25
ϕ_p (^{o})	40.7
ψ (^{o})	0
c' (kPa)	0

Figures 6.4 compares the stress-strain relationship of the backfill material computed by the numerical simulation with that obtained from the triaxial tests. This figure shows a good agreement between the results of the numerical simulation and those of the triaxial tests. This comparison demonstrates the capability of the MC model to simulate the behavior of the backfill material used in this study.

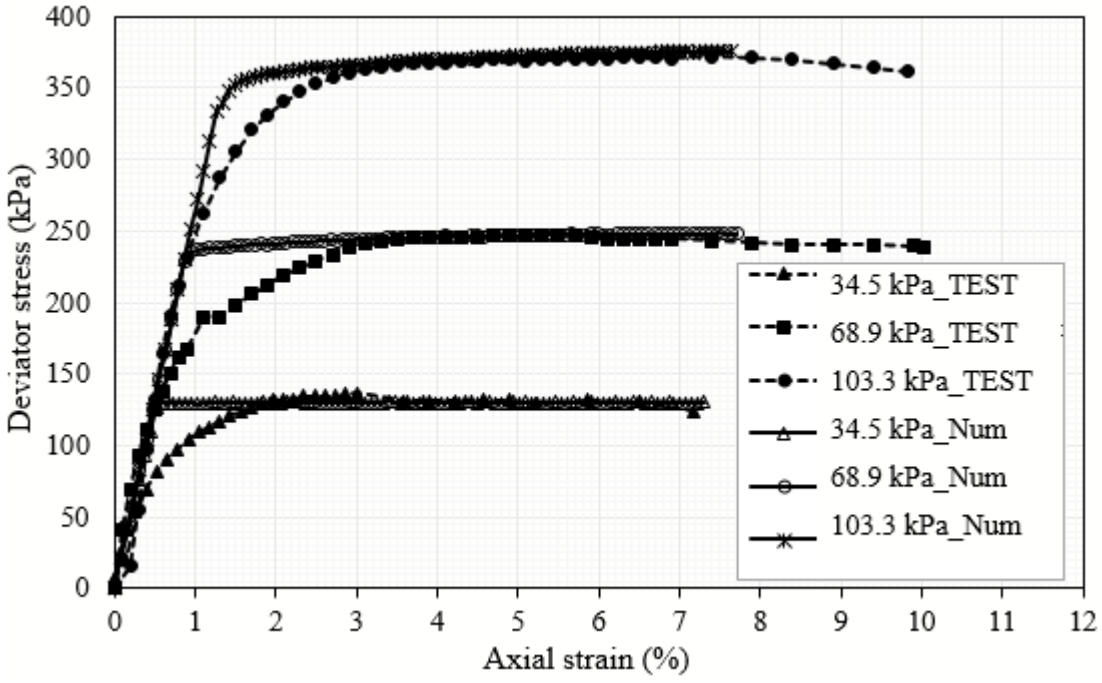

Figure 6.4 Stress-strain relationship of the backfill soil

Geosynthetic reinforcement

A structural element named strip element, which was especially designed for the simulation of reinforcement in reinforced retaining walls (Itasca 2014), was used in this study. Strip elements represent thin reinforcing strips placed in layers within a backfill soil to provide structural support (Itasca 2014). The strip element can yield in tension or compression but cannot sustain a bending moment. The strip element was modeled as a linearly elastic perfectly plastic material. Table 6.2 presents the parameters of the geosynthetic reinforcement used in the numerical simulation in this study, which were based on the data provided by the manufacturer unless mentioned.

Table 6.2 Parameters of geosynthetic in numerical simulation

Parameter	Value
Secant stiffness @ 2%, J (kN/m)	435
Yield strength (kN/m)	17.6*
Tensile failure strain (%)	10

*(Xiao et al. 2016)

Facing units

The facing blocks were modeled as a linear-elastic material. Their typical Young's modulus and Poisson's ratio as 20 GPa and 0.2, respectively were used. The average unit weight of blocks was 23 kN/m^3, which was based on the weight of four blocks divided by their volume. The parameters of the facing units are provided in Table 6.3.

Table 6.3 Parameters of facing units in numerical simulation

Parameter	Value
γ (kN/m3)	23
E (GPa)	20
ν (Poisson's ratio)	0.2

6.2.2 Interface properties

Interface parameters between two dissimilar materials (e.g., soil and reinforcement, soil and facing blocks, and block and block) play a vital role in the performance of the GRR walls and the results of the numerical simulation. All these interfaces were modeled with linearly elastic perfectly plastic constitutive laws with the MC failure criterion. Figure 6.5 shows the mechanics of an interface. Figure 6.5(a) shows a typical shear stress-relative displacement relationship of the interface while Figure 6.5(b) shows the MC failure criterion of the interface. These figures show that the shear stress linearly increases with an increase in the relative displacement until it reaches the maximum shear stress and the interface starts to fail. The maximum shear stress depends on the effective normal stress, the friction angle of the interface, and the interface cohesion. Equation (6. 2) gives the formula to calculate the maximum shear stress, which is based on the MC failure criterion as shown in Figure 6.5 (b):

$$\tau_{max} = c_i + \sigma'_n tan\phi'_i \quad \ldots\ldots\ldots\ldots (6.2)$$

where

τ_{max} is the maximum interface shear stress,

c_i is the interface cohesion,

σ'_n is the effective normal stress, and

ϕ'_i is the interface friction angle.

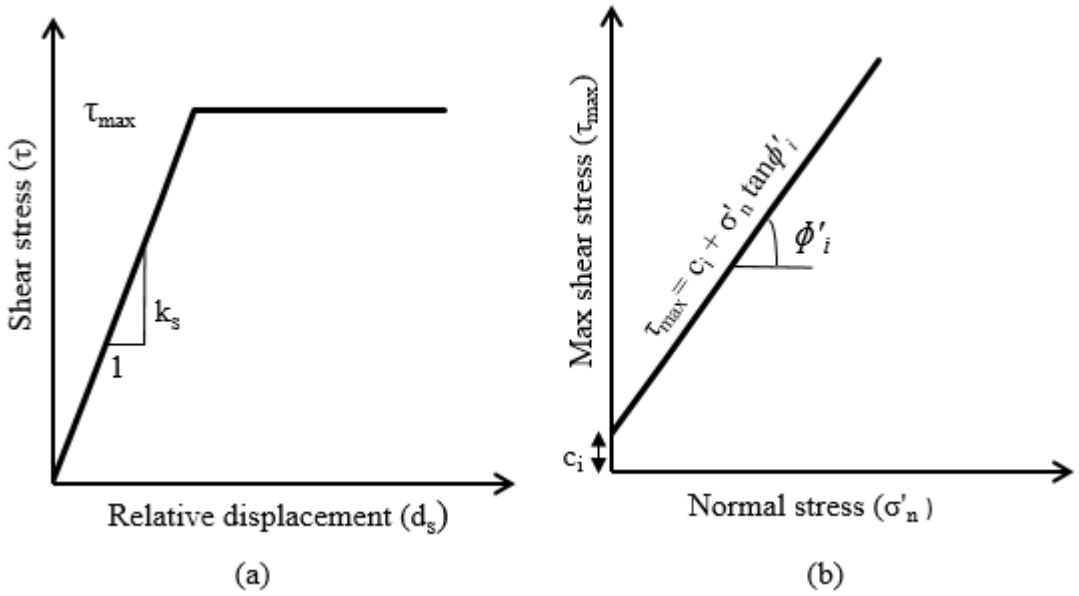

Figure 6.5 Mechanics of an interface: (a) the shear stress-relative displacement relationship for an interface and (b) the MC failure criterion for an interface

The details of the properties for different interfaces used in the numerical simulations conducted in this study are presented below.

Interface between reinforcement and backfill

A 2D numerical model was developed to simulate the pullout tests described in Chapter four and calibrate the interface properties between the reinforcement and the backfill soil. In the numerical simulation, the backfill soil was modeled as a linearly elastic perfectly plastic material with the MC failure criterion. Table 6.1 presents the properties used for the backfill soil in this model.

A strip element was used to simulate the reinforcement in the numerical simulation, which requires several parameters including the interface parameters between reinforcement

and soil, such as friction angle of the interface, interface cohesion, soil-reinforcement shear stiffness interface, and initial and minimum apparent friction coefficient.

Table 6.2 presents the properties used for the strip element. The interface properties between the reinforcement and the backfill soil are summarized in Table 6.4.

Table 6.4 Parameters of the reinforcement-soil interface in the numerical model

Parameters	**Value**
Interface cohesion, C_i (kN/m^2)	0.0
Friction angle of interface, ϕ'_i (^{o})	32
Shear stiffness, k_s (MN/m/m)	10
Initial apparent friction coefficient	0.8
Min. apparent friction coefficient	0.8

The pullout force and displacement relationships for the reinforcement in the soil computed by the numerical simulation and from tests are presented in Figure 6.6. Both the numerical simulation and the experimental tests show that the pullout force increased with an increase in the normal pressure. Figure 6.6 shows that the numerical results are generally in a fair agreement with those from the experimental tests. The differences between the test results and the numerical results are more obvious under the higher normal pressure (i.e., 10 kPa).

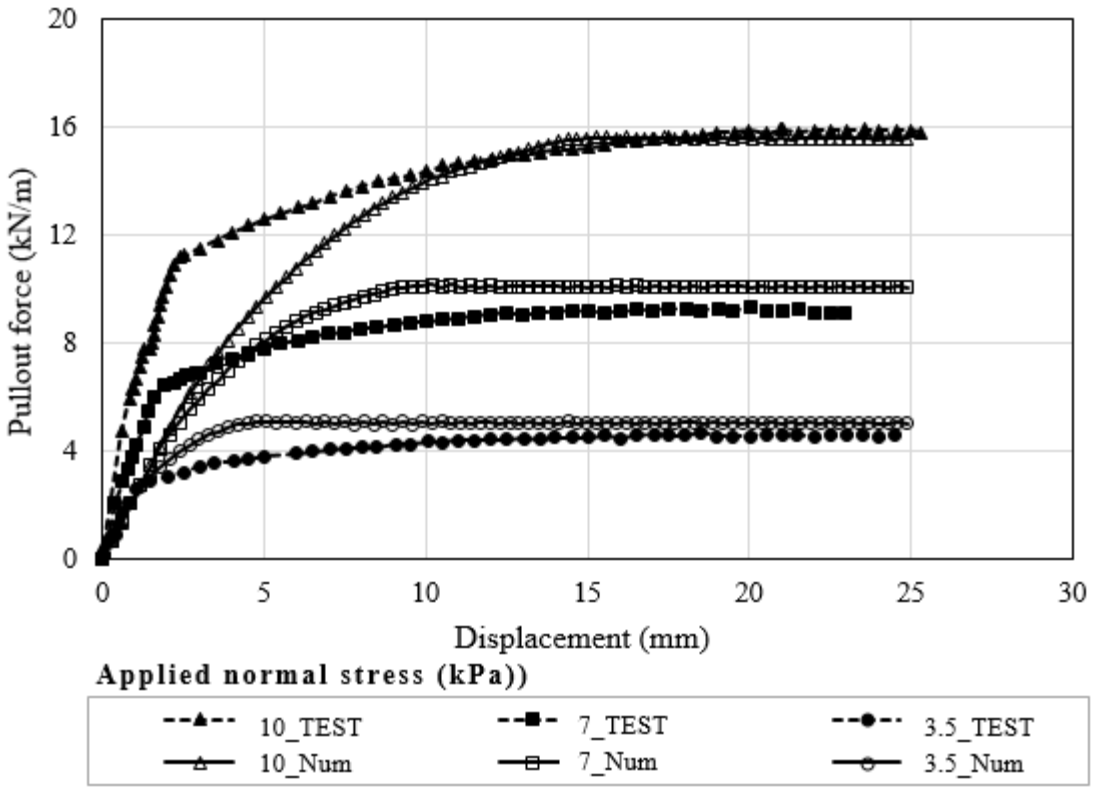

Figure 6.6 Numerical and experimental results of the pullout tests

Interfaces between facing blocks and between backfill and block

An interface was created to simulate the interaction between facing units, which were stacked on each other in the model to form the wall facing. Each block was 50 mm high and 150 mm wide (nominal). In a plane strain condition, only the interface between the top face of a block and the bottom face of another one was considered. The effect of interaction between side faces of blocks was neglected.

An interface between the blocks and the backfill soil was also created to simulate the interaction between these two materials. Table 6.6 presents the properties of the interfaces between the facing units and between the facing units and the backfill soil. Hatami and Bathurst (2006) reported a 57^{o} interface friction angle between the facing units, which was

also used in this study. Xiao et al. (2016) used 75 kPa cohesion between the facing units for the mechanical connection system (i.e. the connection between the reinforcement and the block), which was used in this study as well.

The friction angle of interface between the backfill soil and the facing units was assumed as 2/3 of the internal friction angle of the backfill soil.

The normal and shear stiffness of the interfaces between the facing blocks and between facing blocks and the backfill soil were determined from the model calibration presented in section 6.4.

Table 6.5 Interface properties between block and block, and soil and block

Parameter	**Value**	
	Block-Block	Soil-Block
Friction angle ϕ (^{o})	57	26
Dilation angle ψ (^{o})	0	0
Cohesion c (kPa)	75	0
Normal stiffness K_n (MN/m/m)) *	1000	100
Shear stiffness K_s (MN/m/m)) *	100	10

*determined based on the model calibration described in section 6.4.

6.3 Numerical simulation of model wall tests

The numerical model was first calibrated using the results of one model test and then verified by other model test results. This section describes the geometry and the construction of the numerical model.

6.3.1 Geometry of model

The numerical software, FLAC 2D 8.0, was used to simulate six model tests: A2-I, A2-II, A3-II, A4, B1, and C1 model tests. The A2-I and A2-II model tests had the same wall width (i.e., 0.7H reinforcement length), no retained fill, but different footing offset distances. The A3-II model test had 0.5H reinforcement length, no retained fill. The A4, B1 and C1 model tests had the same wall width (i.e., 0.3H reinforcement length), no retained fill, but different reinforcement configurations. All the simulated model tests had the footing offset distance of 0.05 m except for the A2-I model test, which had 0.2 m footing offset distance. Figure 6.7 shows the configuration of the numerical model used to simulate the A3-II wall model test by calibrating the parameters. This figure shows the geometry, boundary conditions, interfaces, and loading condition of the model. The details of the geometries of all the model tests are presented in Chapter four.

Since the model tests were conducted under a plane strain condition, 2D numerical models were developed instead of 3D numerical models. The numerical models consisted of reinforced fill, reinforcement, facing units, stable rigid medium, and foundation. The interaction between backfill soil and reinforcement, backfill soil and facing units, and facing units were also considered in the numerical models as shown in Figure 6.7. No interface between backfill soil and the stable rigid medium was considered. Morrison et al. (2006)

reported that the model with smooth interface between the shoring wall and the backfill soil behaved similarly as the model with rough interface.

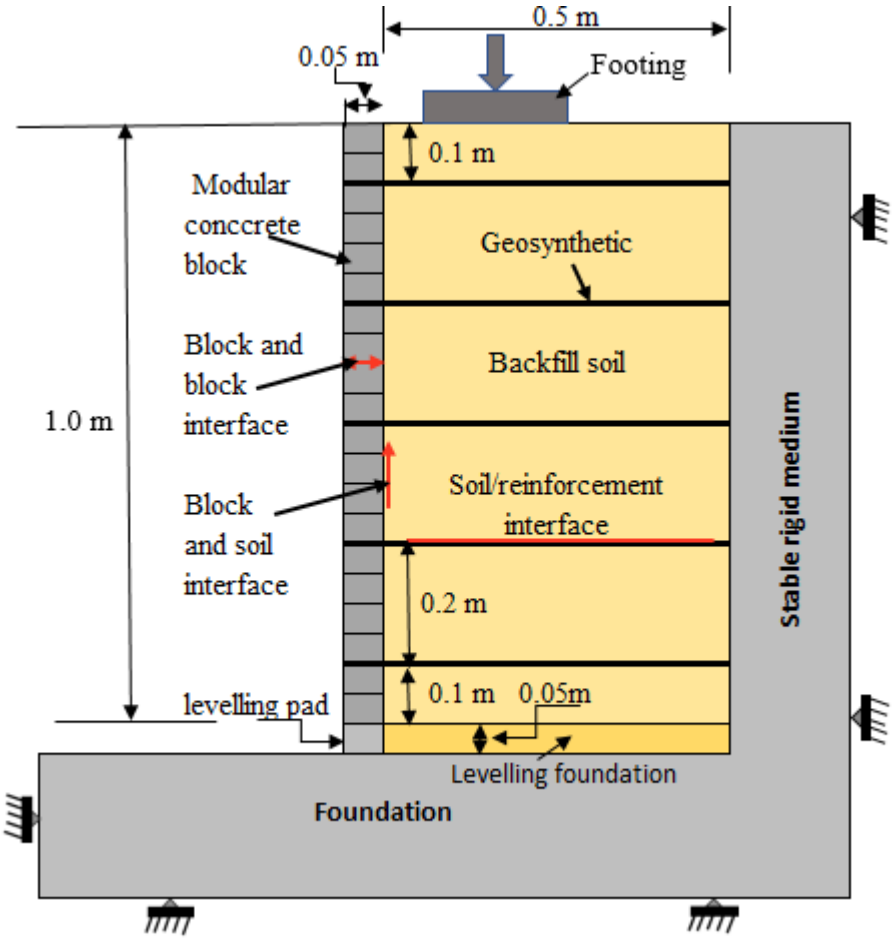

Figure 6.7 Geometry of the A3-II model

The backfill soil was modeled as a linear elastic perfectly plastic material with the Mohr-Coulomb (MC) failure criterion. Strip elements incorporated in FLAC2D was utilized to simulate the reinforcement and modeled as a linear elastic perfectly plastic material with the MC failure criterion. The facing units were modeled as a linearly elastic material. The

properties of backfill soil, reinforcement, and facing units are presented in Tables 6.1, 6.2, and 6.3 respectively.

In addition, interface elements were utilized to simulate the interaction between backfill soil and reinforcement, between backfill soil and facing units, and between facing units. All the interfaces were modeled as sliding or separation interface with the MC failure criterion. The properties of their interfaces are presented in Tables 6.4 and 6.5.

Since the experimental models were constructed inside a test box, the bottom of the box was considered as the foundation while the backside of the box was considered as the stable rigid medium. They were both modeled as linear elastic materials with high stiffness. The schematic detail of the test box is shown in Chapter four (Figure 4.1). The loading plate (footing) was also modeled as a linearly elastic material.

6.3.2 Construction of model

In the laboratory, the model walls were constructed inside a test box. Before the construction of a model wall, a model to simulate the box test was created, which included a stable rigid medium and a foundation and was first solved for initial equilibrium. After that, a wall model was constructed in stages as described below:

(1) A block as a levelling pad and a thin layer of backfill soil (50 mm) were placed to simulate the procedure used in the laboratory, and then this system was solved for the initial equilibrium.

(2) A layer of the wall facing units, the backfill soil, and the reinforcement were installed in the numerical model. A pin element was used as the connection between the reinforcement and the blocks to simulate the mechanical connection used in the model tests.

(3) Corresponding interfaces (i.e., the interface between blocks and the interface between the block and backfill soil) were assigned. The interface between backfill soil and the reinforcement was incorporated in the strip element.

(4) Each layer of the wall facing was fixed in the x-direction (i.e., a fixed boundary condition was applied) to simulate the blocks used to support the wall facing units during construction of the experimental model. Subsequently, the numerical model was solved to reach a new equilibrium.

(5) Steps (2) to (4) were repeated until the top of the wall.

(6) The facing wall support (i.e., the fixed boundary condition) was removed layer by layer from the top to the bottom of the wall as performed in the experimental test. The model was solved to reach equilibrium after removing each of the support.

(7) Finally, a load was applied in equal increments through a loading footing. After each load increment, the system was solved into equilibrium. The performance data were reduced, including the displacement of the wall facing, the settlement of the loading footing, the strain of the geosynthetic reinforcement, and the distribution of the vertical and lateral earth pressures in the model.

6.4 Calibration of the parameters used for simulation of model wall tests

A3-II wall model test was simulated to calibrate the parameters used in the numerical model and determine the numerical results were compared to the experimental results and were presented in this section. The normal and shear stiffness of interfaces between facing blocks and between facing block and backfill soil presented earlier in Table 6.5 were determined through this calibration process.

6.4.1 Wall facing displacement

Figure 6.8 presents the lateral displacements of the wall facing computed by the numerical analysis (Num) in the figure and measured in the experimental test (TEST) along the wall height under various footing loadings.

This figure shows that the wall facing displacements increased with the increase of the applied footing pressure with a similar trend in both the experimental test and the numerical analysis. In addition, most of the displacements occurred above the mid-height of the wall and approached to the maximum value at approximately 4/5 of the wall height or at the depth equal to the width of the footing (i.e., at depth of 0.2 m). Figure 6.18 shows that the lateral displacements of the wall facing computed by the numerical analysis matched those measured in the experimental test under all applied footing pressures.

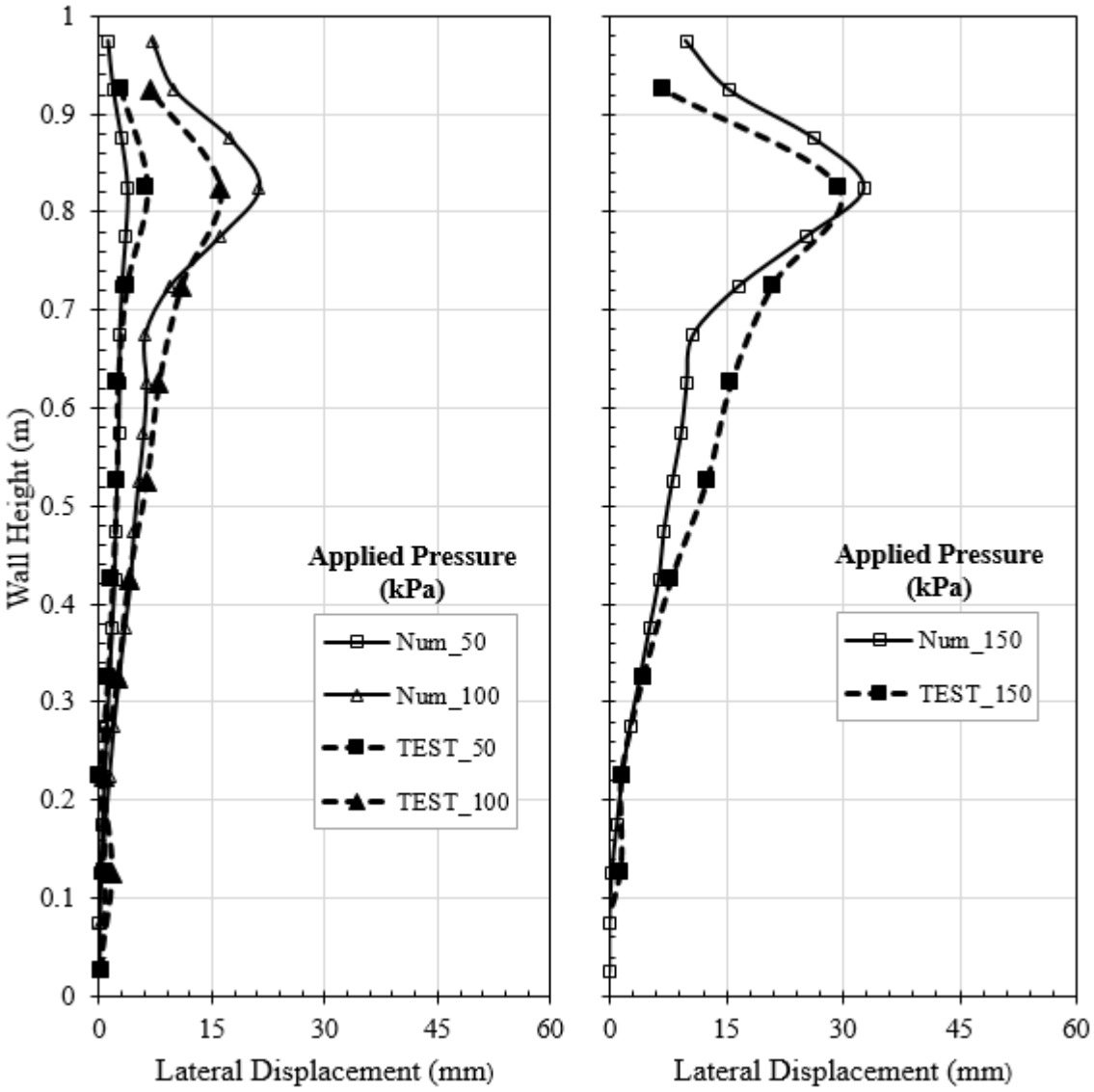

Figure 6.8 Lateral wall facing displacement versus wall height for the A3-II model

6.4.2 Pressure-settlement curve

Figure 6.9 compares the pressure-settlement curve of the footing computed by the numerical analysis with that measured in the experimental test. The settlement of the footing increased approximately linearly with increase of the applied footing pressure and then rapidly increased after the footing pressure was higher than 150 kPa. This figure shows that the footing

settlement computed by the numerical analysis agreed with that measured in the experimental test under all the applied footing pressures.

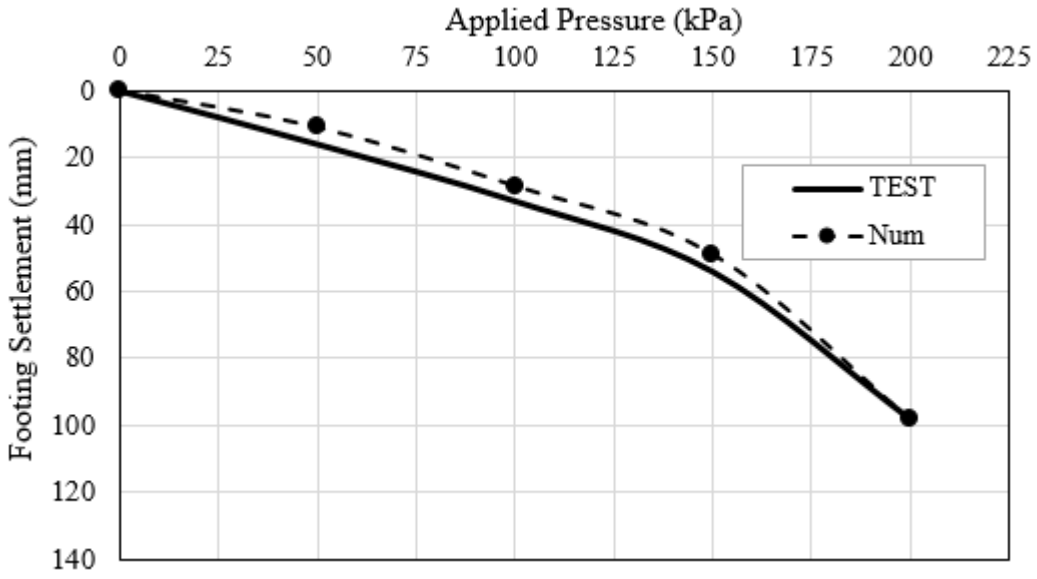

Figure 6.9 Pressure-settlement curve of the footing in the A3-II model

6.4.3 Vertical earth pressure distribution

Figure 6.10(a) compares the vertical earth pressures computed by the numerical analysis below the centerline of the footing along the depth with those measured in the experimental test while Figure 6.10(b) compares the results of the numerical analysis with those calculated using the 2:1 distribution method. Note: the term R_ 2:1 in the figure indicates the lateral earth pressures calculated based on Equation (5.3).These figures show that the vertical earth pressures computed by the numerical analysis increased with the increase of the applied footing pressure. In addition, the vertical earth pressures decreased with the depth under all the applied footing pressures. As shown in Figure 6.10(a), the numerical results matched the measured vertical earth

pressures at the depth of 0.3 m. However, the vertical earth pressures measured at the bottom of the wall model were lower than those computed by the numerical analysis at the same depth.

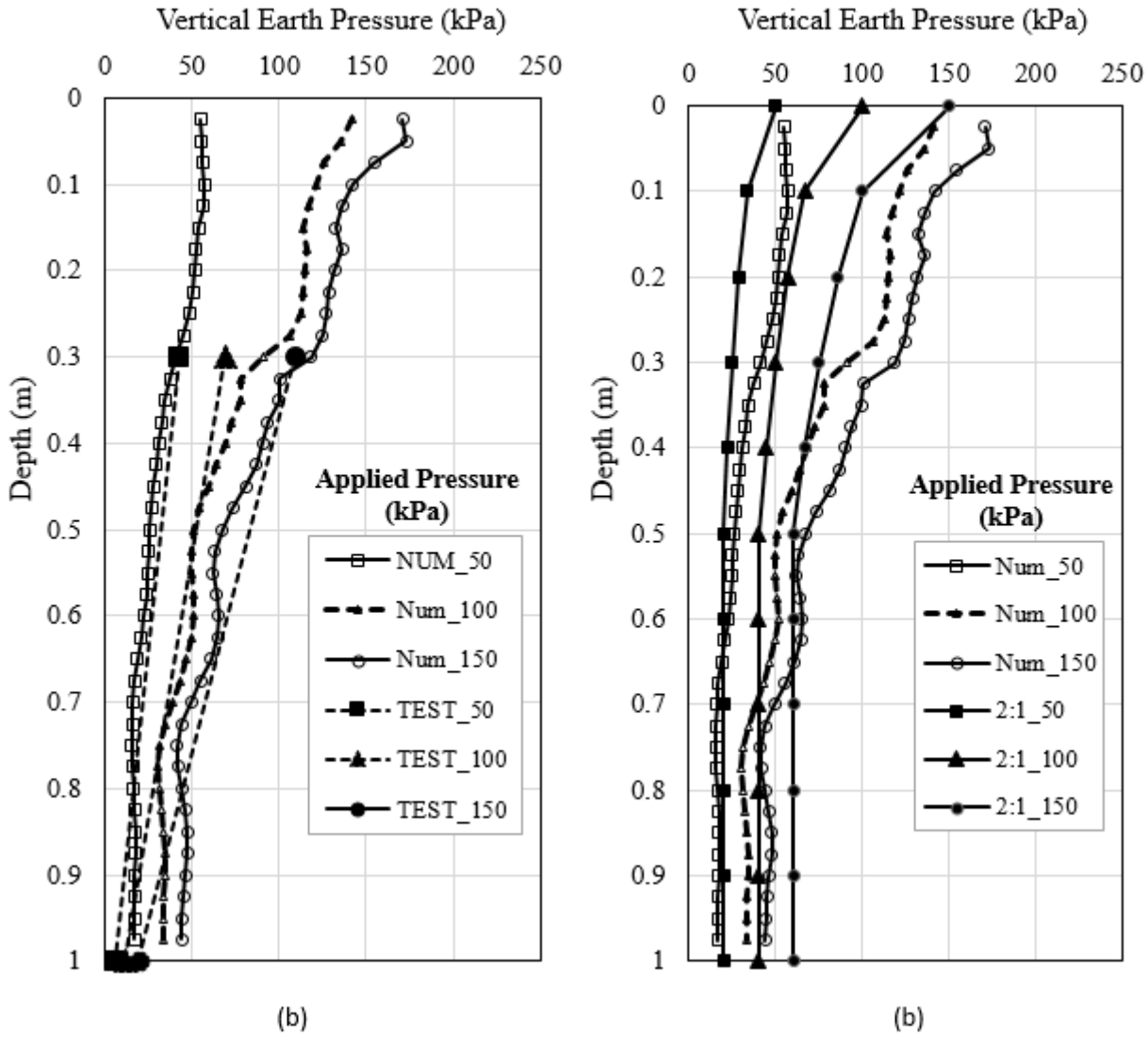

Figure 6.10 Vertical earth pressure distribution verse depth for the A3-II model: (a) Numerical versus test results and (b) numerical versus calculated results by the 2:1 distribution method

Furthermore, Figure 6.10(b) shows that the distribution of the vertical earth pressures computed by the numerical analysis agreed reasonably with those calculated based on the 2:1

distribution method from the mid-height of the wall model to the bottom of the wall. However, the vertical earth pressures calculated based on the 2:1 distribution method were slightly lower than those computed by the numerical analysis from the mid-height of the wall model to the top of the wall (i.e., at the depth less than 0.5 m).

Figure 6.11 presents the distributions of the vertical earth pressure along the wall width at the wall height of 0.9 m computed by the numerical analysis and measured in the experimental test under various footing loading, which show fair agreement.

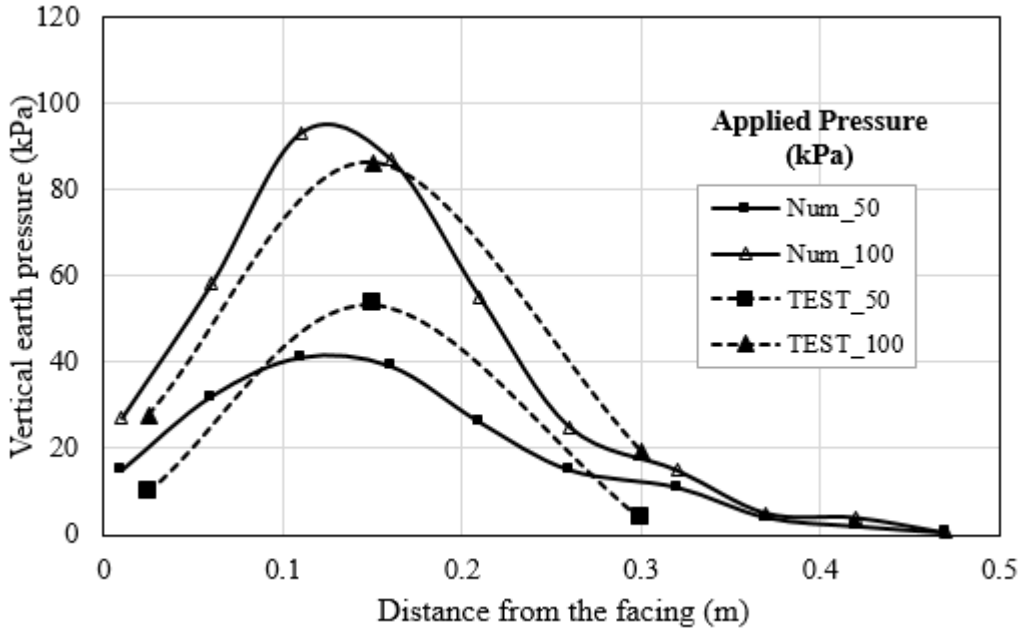

Figure 6.11 Vertical earth pressure distribution versus wall width at the wall height of 0.9 m for the A3-II model

6.4.4 Lateral earth pressure distribution

Figure 6.12(a) compares the lateral earth pressures computed by the numerical analysis with those measured in the experimental test. Figure 6.12(b) shows the lateral earth pressures on

the wall facing computed by the numerical analysis compared to those calculated based on the Rankine lateral earth pressure theory and the vertical pressure using the 2:1 distribution method.

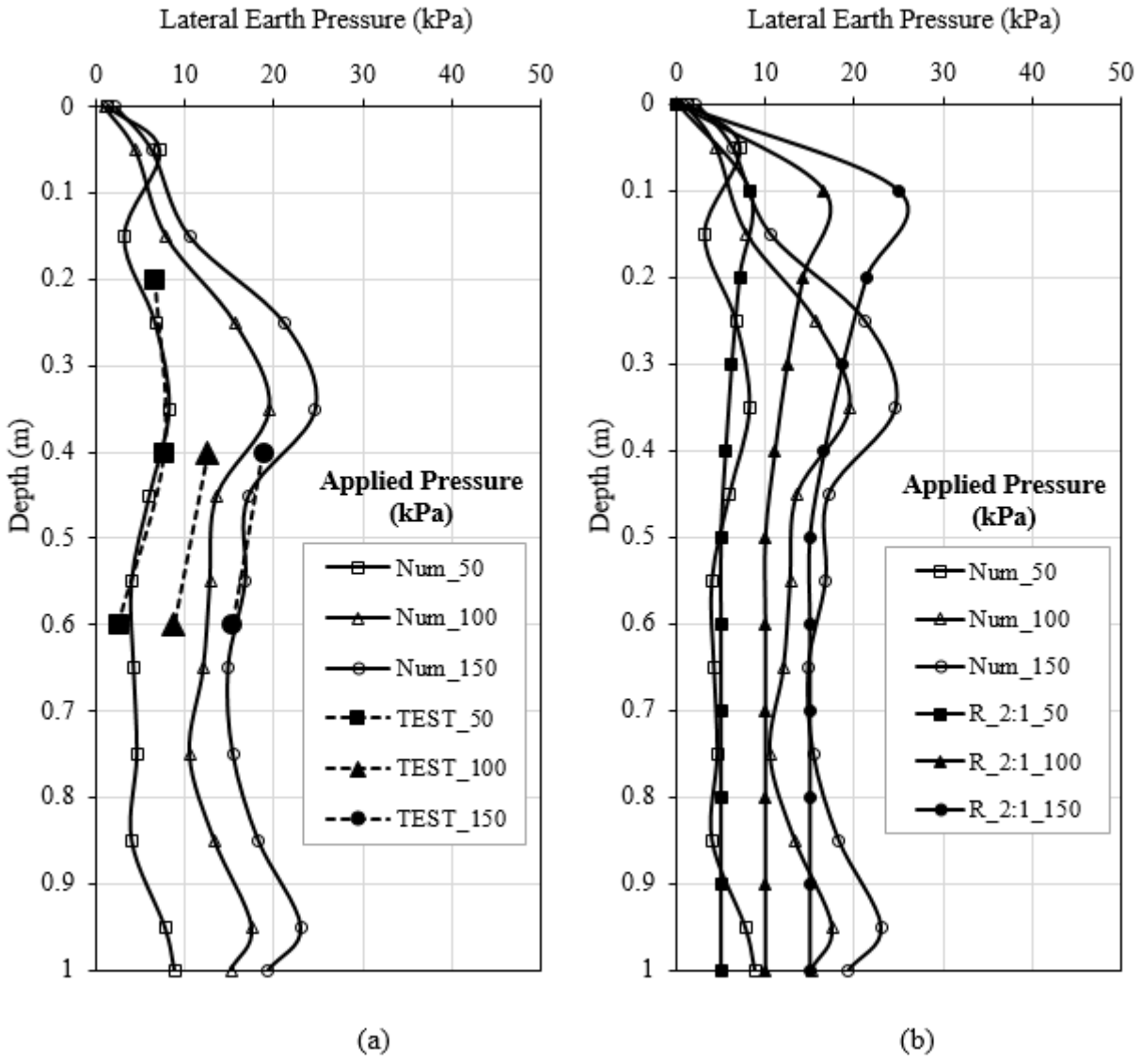

Figure 6.12 Lateral earth pressure distribution versus depth for the A3-II model test: (a) Numerical versus test results and (b) numerical versus calculated results based on the Rankine theory

Figure 6.12 shows that the measured lateral earth pressures increased with the increase of the applied footing load. In addition, the lateral earth pressures computed by the numerical analysis increased approximately linearly with depth from the top of the wall to the depth of 0.35 m. Subsequently, the lateral earth pressures decreased somehow and then became considerably constant the depth of 0.45 m to the bottom of the wall.

Figure 6.12(a) shows the lateral earth pressures on the wall facing computed by the numerical analysis are well compared with those measured in the experimental test. Figure 6.12(b) shows the lateral earth pressures on the wall facing computed by the numerical analysis are compared with those calculated based on the Rankine theory and the 2:1 distribution method.

6.5 Verification of the experimental test results

Several wall model tests were simulated to verify the experimental findings and the results were presented in this section.

6.5.1 A2-I wall model test

Wall facing displacement

Figure 6.13 shows the lateral displacements of the wall facing with the wall height under various footing loadings computed by the numerical model versus those by measured in the model test. This figure shows that the wall facing displacements increased with the increase of the applied footing pressure with the similar trend in both the experimental test and the numerical analysis. In addition, most of the displacements occurred above the mid-height of the wall and approached to the maximum value approximately at 4/5 of the wall height or at the depth equal to the width of the footing (i.e., at the depth of 0.2 m).

Figure 6.13 also shows a very good agreement in the lateral displacements of the wall facing computed by the numerical analysis and those measured in the experimental test. Under the high applied footing pressure (i.e., the applied footing pressure of 150 kPa), the lateral displacements computed by the numerical analysis had slightly larger maximum displacement than those measured from the experimental test.

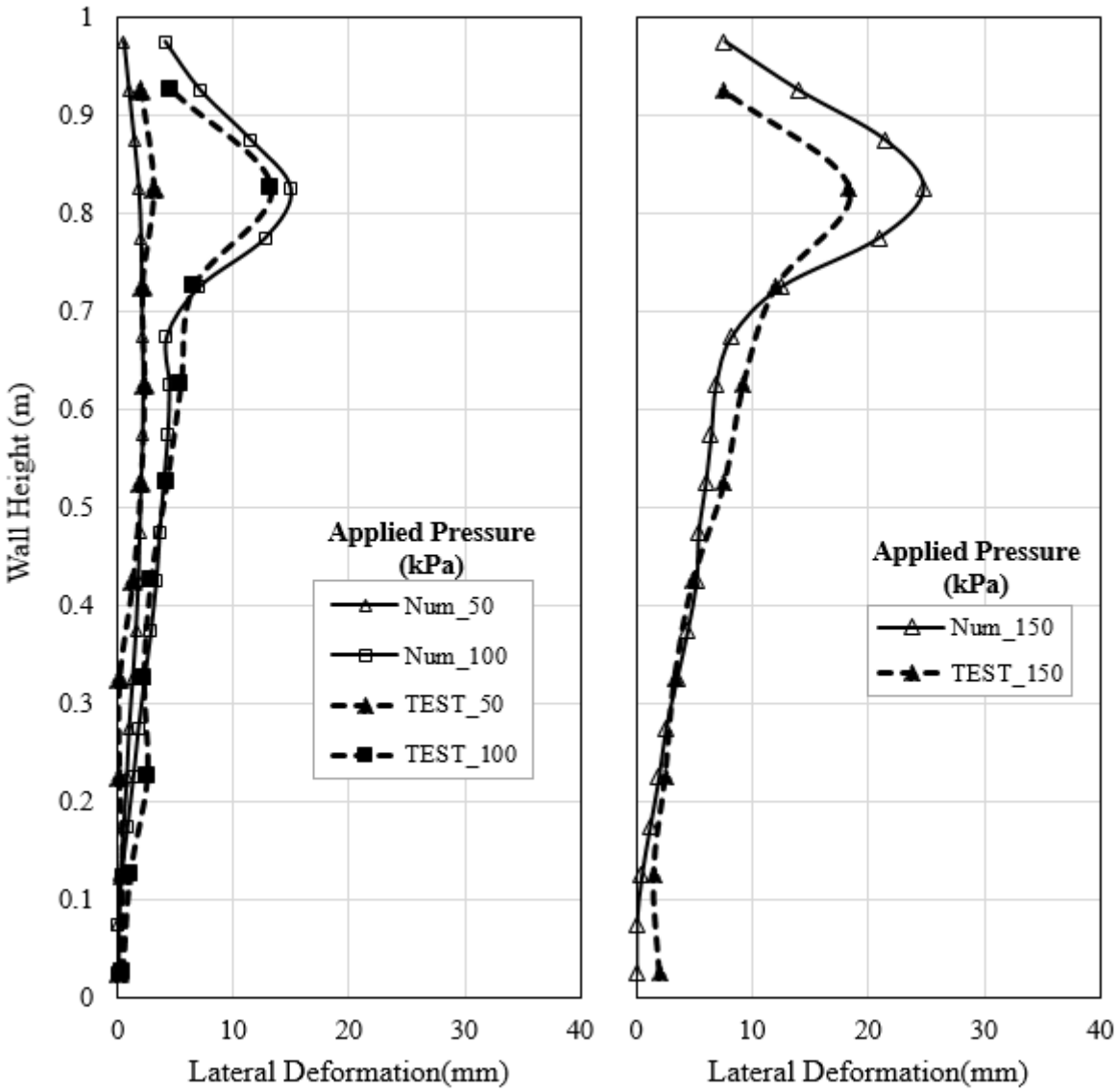

Figure 6.13 Lateral wall facing displacement versus wall height for the A2-I model

Pressure-settlement curve

Figure 6.14 presents the pressure-settlement curve of the footing on the GRR wall computed by the numerical analysis compared to that measured from the experimental test of the A2-I model. This figure shows that the footing settlement computed by the numerical analysis is in good agreement with that measured from the experimental test under the applied footing pressure of 150 kPa and lower.

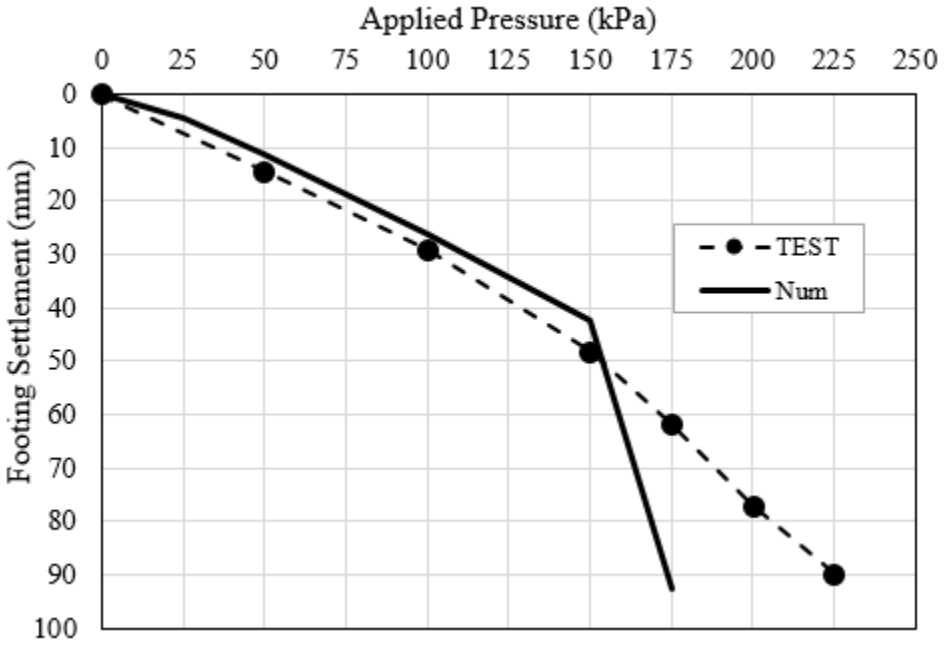

Figure 6.14 Pressure-settlement curve of the footing in the A2-I model

Figure 6.14 shows that footing settlement measured in the experimental test was less than that computed by the numerical analysis under the applied footing pressure higher than 150 kPa. For example, the footing settlement computed by the numerical analysis was about 92 mm under the applied footing pressure of 175 kPa, while the footing settlement measured in the experimental test was about 62 mm under the same applied load.

Vertical earth pressure distribution

Figure 6.15(a) presents the vertical earth pressures below the centerline of the footing along the depth under various footing loading computed by the numerical simulation and measured in the experimental test. In addition, Figure 6.15(b) compares the numerical results with those of the 2:1 distribution method using Equation (5.1). This figure shows that the vertical earth pressures computed by the numerical analysis and measured in the test increased with the increase of the applied footing pressure and decreased with the depth.

Figure 6.15(a) shows that the distribution of the vertical earth pressures computed by the numerical analysis agreed well with those obtained in the experimental tests under various applied footing pressures. A similar trend for the vertical pressure distribution was also found in the calculated results by the 2:1 distribution method. However, the vertical earth pressures calculated based on the 2:1 distribution method were slightly higher than those computed by the numerical analysis at the depth close to the bottom of the wall (i.e., at the depth of 0.7 m and deeper).

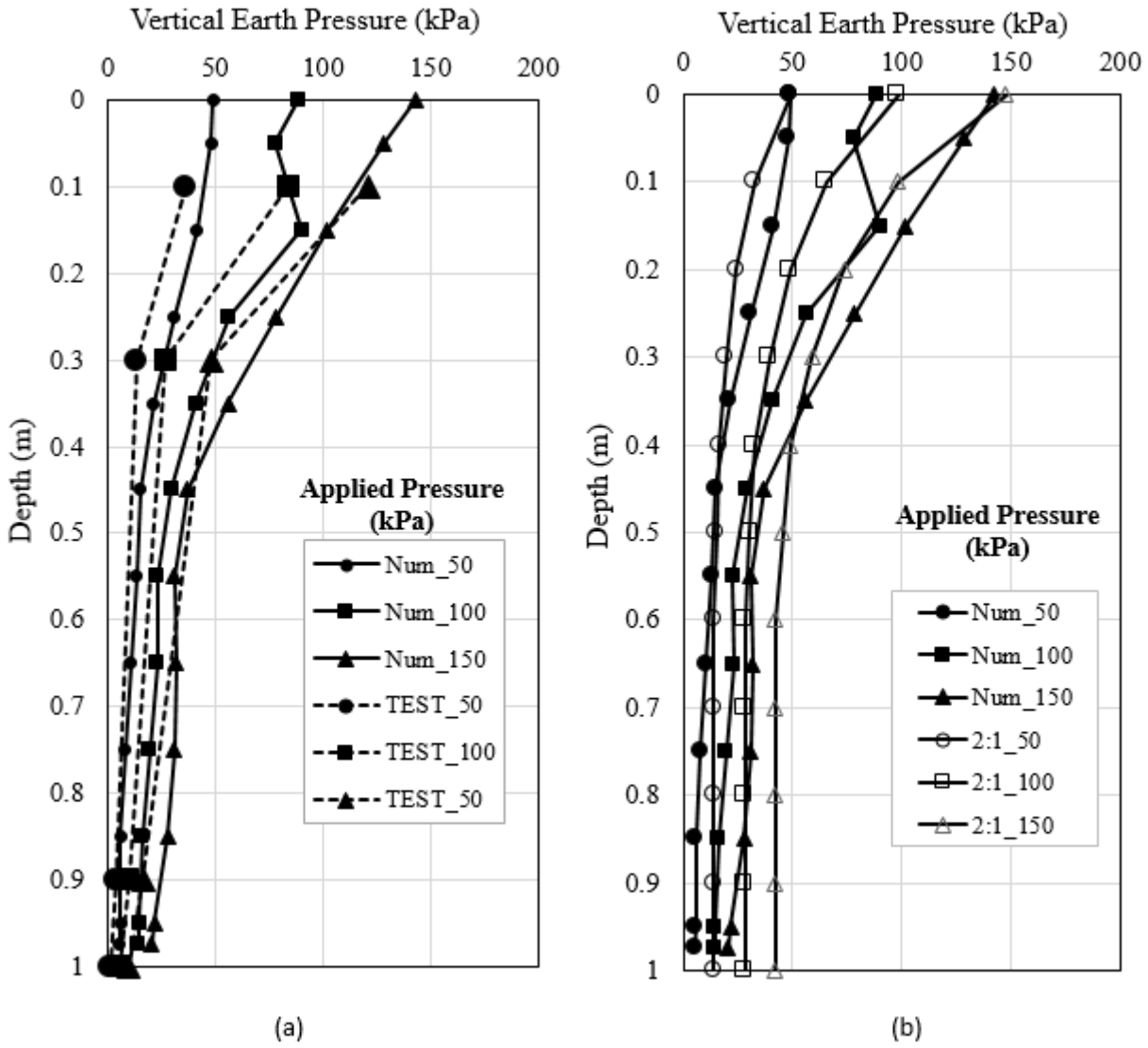

Figure 6.15 Vertical earth pressure distribution with depth for the A2-I model test: (a) Numerical versus test results and (b) Numerical versus calculated results by the 2:1 distribution method

The distribution of the vertical earth pressure along the wall width at the wall height of 0.9 m was also computed by the numerical analysis under various footing loadings. Figure 6.16 compares the vertical earth pressures computed by the numerical analysis with those measured in the experimental test. Even though the maximum vertical earth pressures computed by the

numerical analysis below the center of the footing were higher than those measured in the experimental test at the same location, their results are generally in agreement.

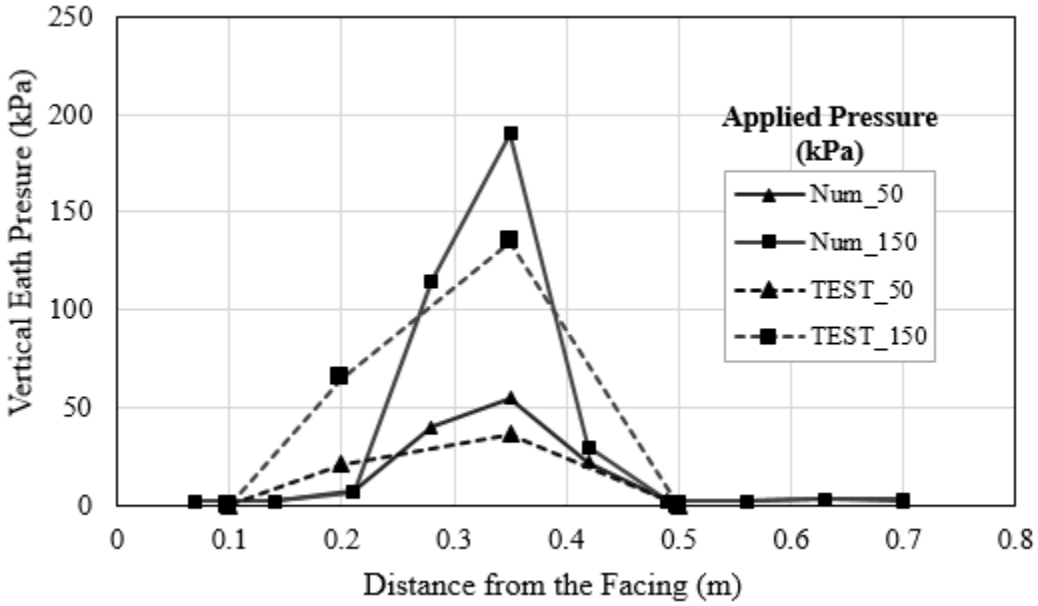

Figure 6.16 Vertical earth pressure distribution versus wall width at the wall height of 0.9 m for the A2-I model test

Lateral earth pressure distribution

Figure 6.17(a) compares the lateral earth pressures computed by the numerical analysis with those measured in the experimental test. Figure 6.17(b) shows the lateral earth pressures on the wall facing computed by the numerical analysis compared to those calculated based on the Rankine lateral earth pressure theory and the vertical pressure using the 2:1 distribution method.

Figure 6.17 shows that the lateral earth pressures computed by the numerical analysis approximately linearly decreased with depth starting at the depth of 0.25 m from the top of the wall. The lateral earth pressures computed by the numerical analysis were close to the measured lateral earth pressures from the experimental test at the depth of 0.4 m and higher as shown in Figure 6.17(a). However, the measured lateral earth pressures were lower than those computed

by the numerical analysis at the deeper depth (i.e., the depth below the mid-height of the wall). The calculated lateral earth pressures based on the Rankine earth pressure theory using Equation (5.3) are almost the same as those computed by the numerical analysis.

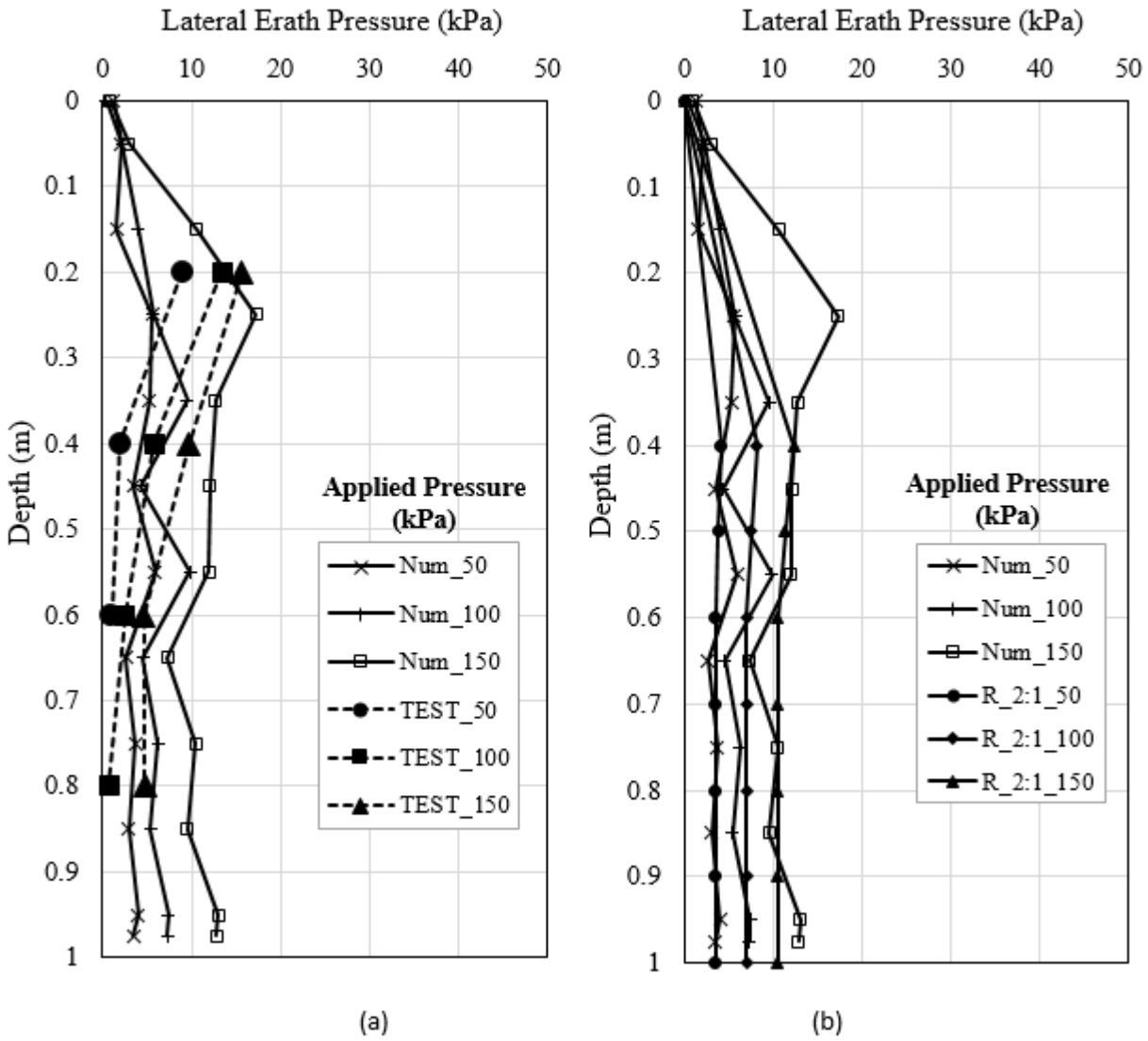

Figure 6.17 Lateral earth pressure distribution versus wall width for the A2-I model test: (a) Numerical versus test results and (b) numerical versus calculated results by the Rankine theory

6.5.2 A2-II wall model test

Wall facing displacement

Figure 6.18 shows the lateral displacements of the wall facing with the wall height computed by the numerical analysis and measured in the experimental test. This figure shows that the wall facing displacements increased with the increase of the applied footing pressure in both the experimental test and the numerical analysis. In addition, most of the displacements occurred above the mid-height of the wall and approached to the maximum value at approximately 4/5 of the wall height or at the depth equal to the width of the footing (i.e., at depth of 0.2 m). Figure 6.18 shows that the lateral displacements of the wall facing computed by the numerical analysis agreed well with those measured in the experimental test under all applied footing pressures.

Pressure-settlement curve

Figure 6.19 compares the pressure-settlement curve of the footing computed by the numerical analysis with that measured in the experimental test. This figure shows that the footing settlement computed by the numerical analysis increased approximately linearly with the increase of the applied footing pressure up to 150 kPa, and then increased suddenly after the footing pressure of 150 kPa and higher was applied. This figure also shows that the footing settlement computed by the numerical analysis matched well that measured in the experimental test under all the applied footing pressures.

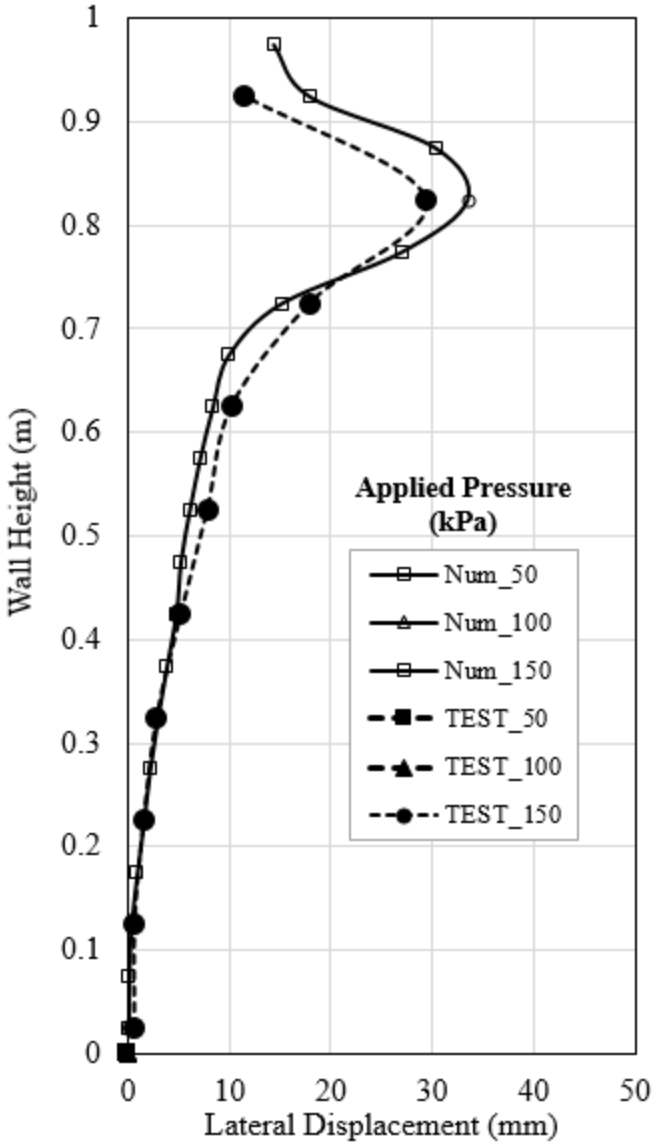

Figure 6.18 Lateral wall facing displacement versus wall height for the A2-II model

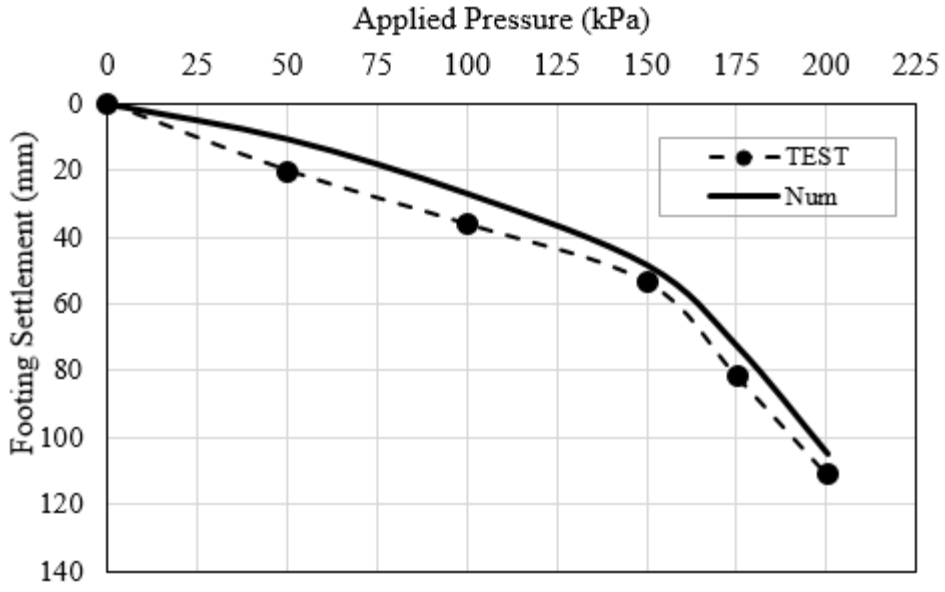

Figure 6.19 Pressure-settlement curve of the footing in the A2-II model

Vertical earth pressure distribution

Figure 6.20(a) compares the vertical earth pressures computed by the numerical analysis below the centerline of the footing along the depth with those measured in the experimental test while Figure 6.20(b) compares the numerical results with those calculated using the 2:1 distribution method. Both figures show that the vertical earth pressures computed by the numerical analysis increased with the increase of the applied footing pressure and decreased with depth.

Figure 6.20(a) shows that the distribution of the vertical earth pressures computed by the numerical analysis agreed well with those obtained from the experimental tests under various applied footing pressures. However, there is a slight difference between the results of the numerical analysis and those in the experimental test at the bottom of the wall. The vertical earth pressures computed by the numerical analysis agreed well with those calculated using the 2:1 distribution method. However, the vertical earth pressures computed by the numerical analysis

were slightly higher than those calculated based on the 2:1 distribution method at the depth close to the top of the wall (i.e., at the depth of 0.3 m and higher).

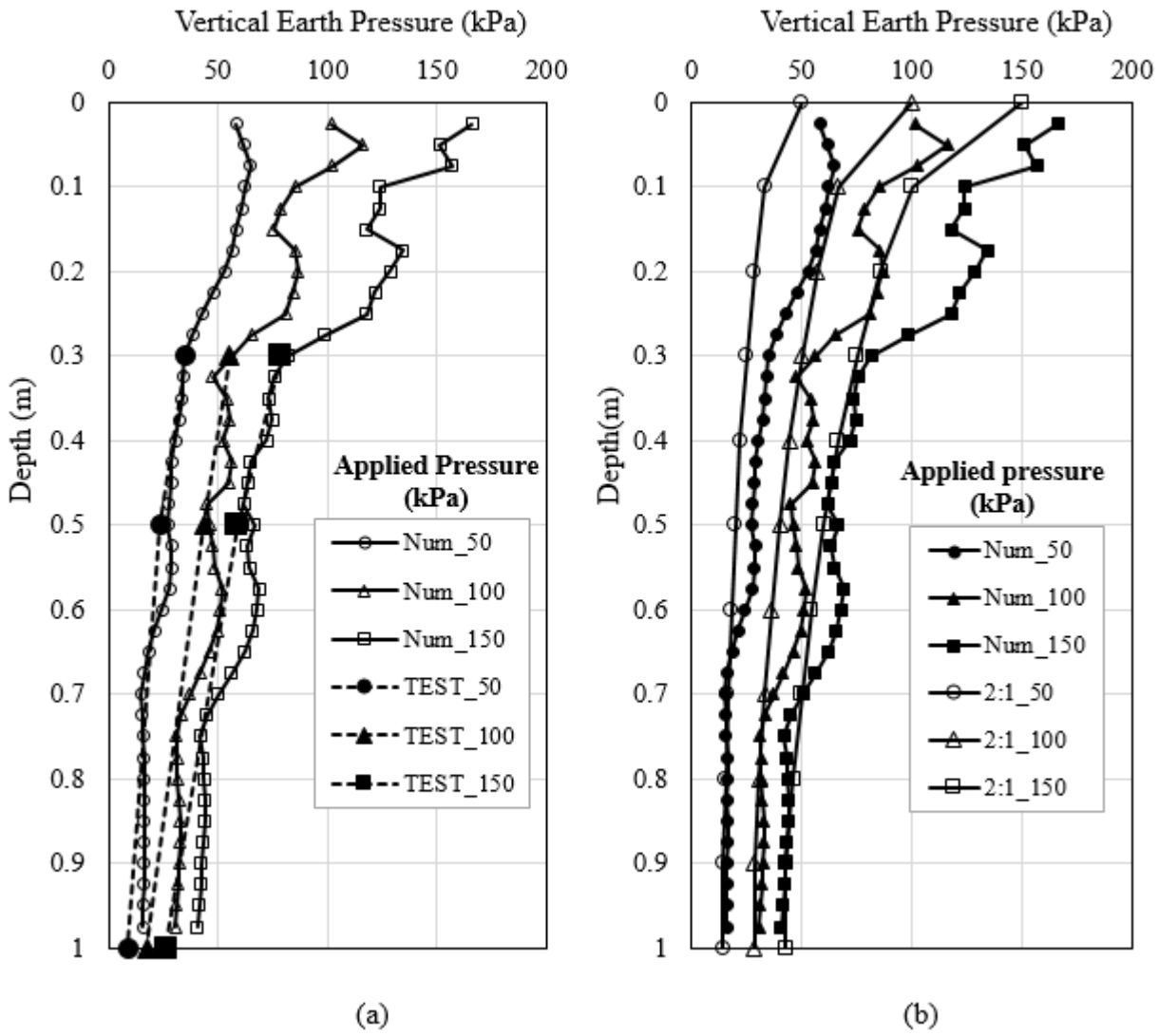

Figure 6.20 Vertical earth pressure distribution verse depth for the A2-II model test: (a) Numerical versus measured results and (b) Numerical versus calculated results using the 2:1 distribution method

Figure 6.21 compares the vertical earth pressures computed by the numerical analysis with those measured in the experimental test at the wall height of 0.7 m under various footing

loadings. This figure shows that the vertical earth pressures computed by the numerical analysis generally agreed with those measured in the experimental test. However, the vertical earth pressures computed by the numerical analysis under the applied footing pressure of 100 kPa and 150 kPa below the center of the footing were higher than those measured in the experimental test under the same applied load at the same location.

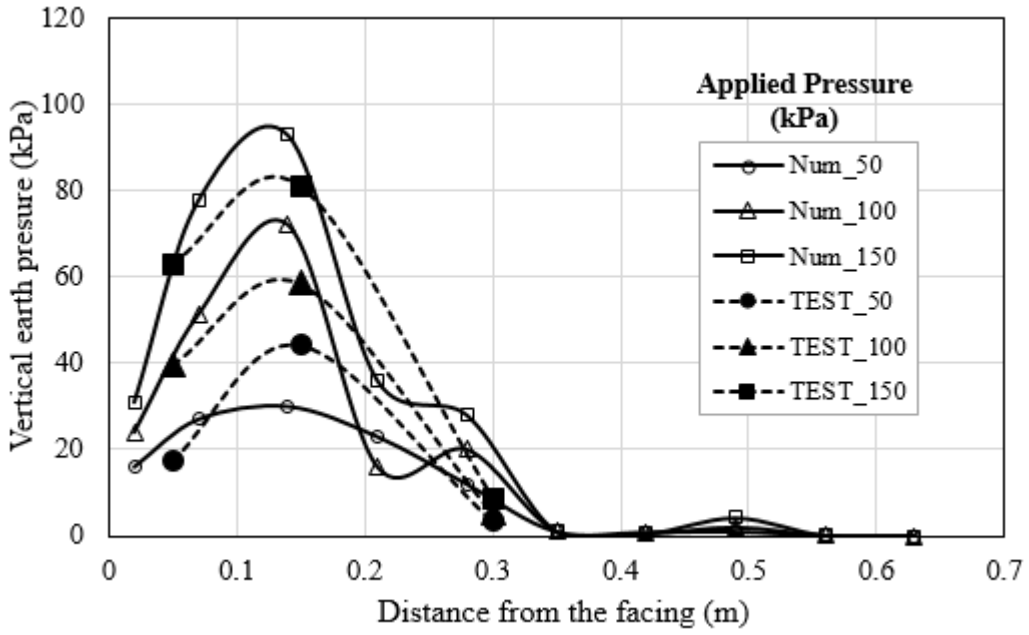

Figure 6.21 Vertical earth pressure distribution versus wall width at the wall height of 0.7H for the A2-II model test

Lateral earth pressure distribution

Figure 6.22(a) compares the lateral earth pressures computed by the numerical analysis with the lateral earth pressures measured in the experimental test while Figure 6.22(b) compares the lateral earth pressures on the wall facing computed by numerical analysis with those calculated based on the Rankine theory and the 2:1 distribution method.

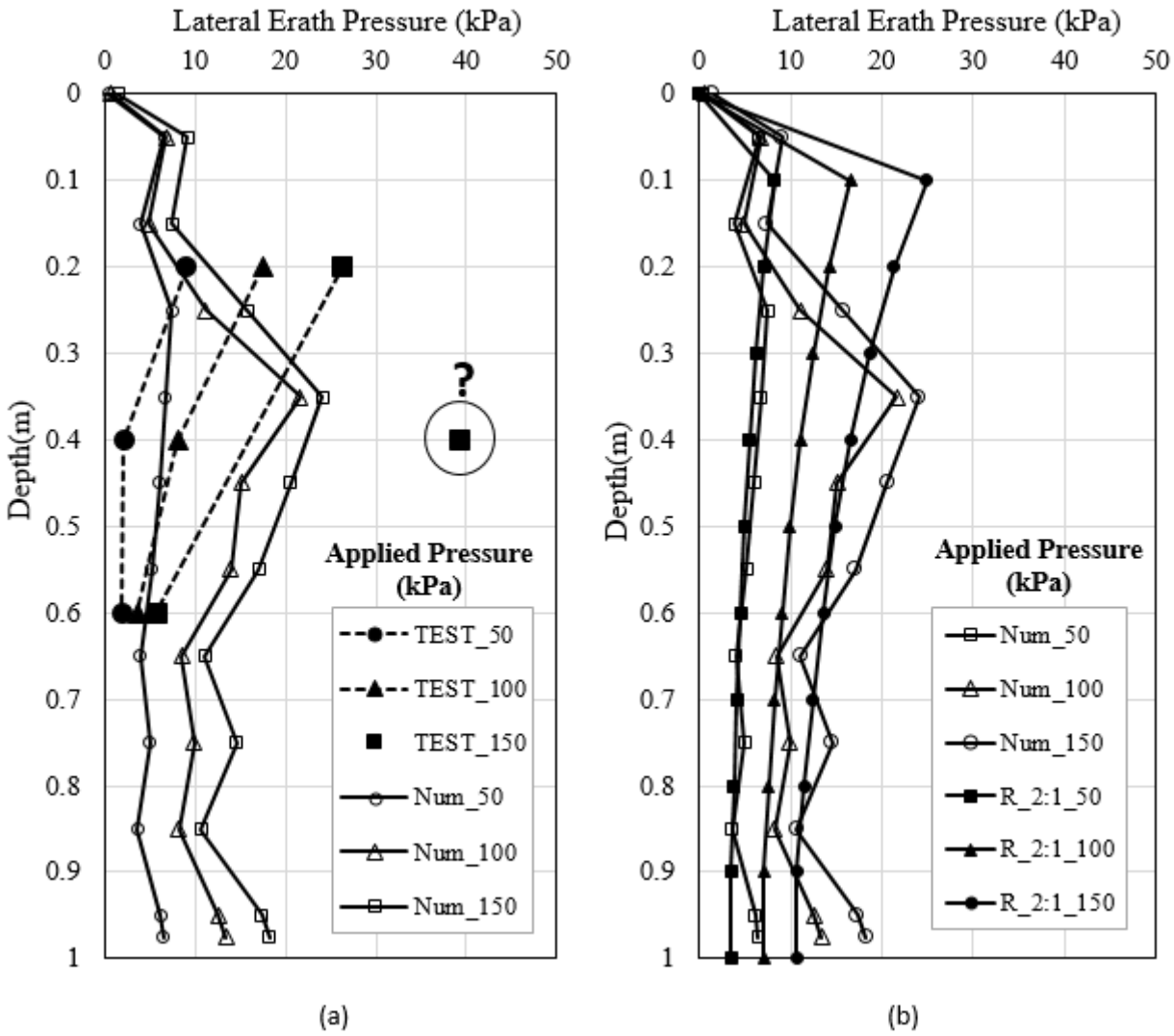

Figure 6.22 Lateral earth pressure distribution versus wall depth for the A2-II model test: (a) Numerical versus test results and (b) numerical versus calculated results based on the Rankine theory

Figure 6.22 shows that the lateral earth pressures computed by the numerical analysis generally decreased with depth with starting at the depth of 0.35 m from the top of the wall. In addition, the lateral earth pressures computed by the numerical analysis had similar trends for the all applied footing pressures. The lateral earth pressures computed by the numerical analysis were not in reasonable agreement with those measured in the experimental test at the depth of

0.4 m and deeper as shown in Figure 6.22(a). However, the measured lateral earth pressures were lower than those computed by the numerical analysis at the deeper depth (i.e., depth of 0.6 m). Figure 6.22(b) shows that the lateral earth pressures computed by the numerical analysis were almost the same as those calculated based on the Rankine theory.

6.5.3 A4 wall model test

Wall facing displacement

Figure 6.23 shows the lateral displacements of the wall facing computed by the numerical analysis and measured in the experimental test versus the wall height under various footing loadings. This figure shows a large increase in the displacements of the wall facing with the increase of the applied footing pressure from 35 kPa to 55 kPa in both the experimental test and the numerical analysis. In addition, most of the displacements occurred at the depth close to the mid-height of the wall and approached to the maximum value approximately at the depth of 0.6 m.

Figure 6.23 shows a good agreement between the lateral displacements of the wall facing computed by the numerical analysis and those measured in the experimental test under the applied footing pressure of 35 kPa. However, the lateral displacements of the wall facing computed by the numerical analysis under the applied footing pressure of 55 kPa were higher than those measured in the experimental test under the same applied pressure.

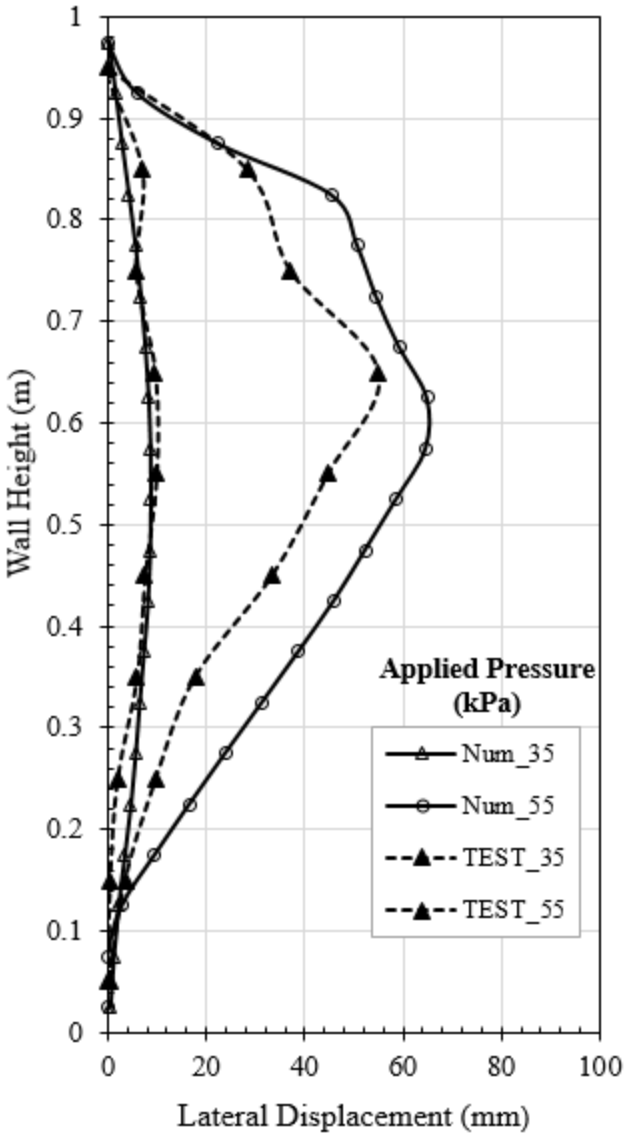

Figure 6.23 Lateral wall facing displacement versus wall height (H) for the A4 model test

Pressure-settlement curve

Figure 6.24 compares the pressure-settlement curve of the footing computed by the numerical analysis with that measured in the experimental test. The settlement of the footing increased approximately linearly with the increase of the applied footing pressure up to 40 kPa, and rapidly increased after a footing pressure higher than 40 kPa was applied.

Figure 6.24 shows that the footing settlement computed by the numerical analysis agreed well with that measured in the experimental test under the applied footing pressure of 40 kPa and lower. However, the applied pressure-settlement curve computed by the numerical analysis showed an abrupt increase in the footing settlement and the failure of the model after a footing pressure higher than 40 kPa was applied. In other words, the footing settlement measured in the experimental test was smaller than that computed by the numerical analysis under the applied footing pressure higher than 40 kPa.

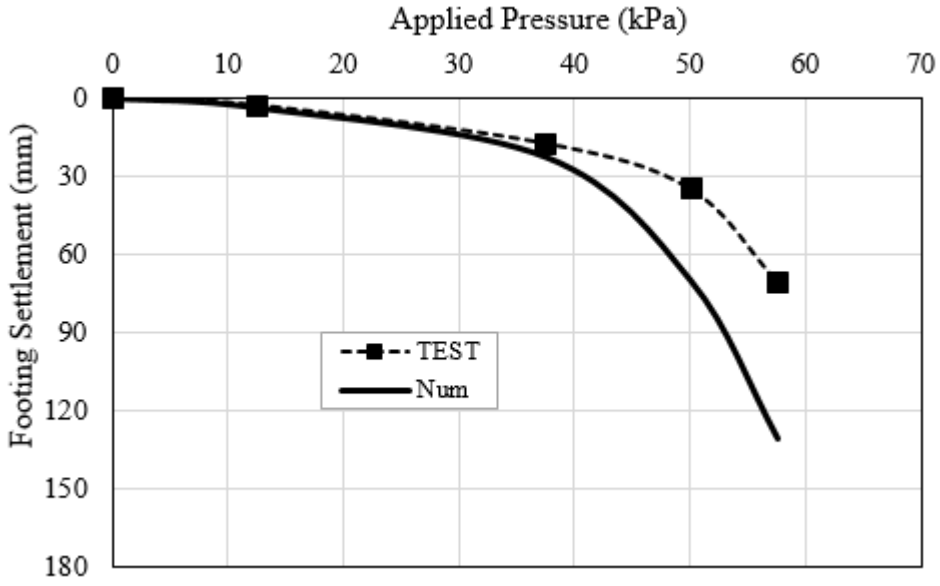

Figure 6.24 Pressure-settlement curve of the footing in the A4 model test

Vertical earth pressure distribution

Figure 6.25 shows the distributions of the vertical earth pressure versus depth computed by the numerical analysis, measured in the experimental test, and calculated using the 2:1 distribution method under various footing loadings.

This figure shows that the distribution of the vertical earth pressures computed by the numerical analysis agreed well with those obtained in the experimental test under different applied footing pressures. Figure 6.25 shows that at the low applied footing pressure (i.e., 12 kPa), the 2:1 method appears to provide a reasonable estimate of the vertical earth pressures along the depth of the model. However, at the higher applied pressure (i.e., 55 kPa), the 2:1 method appears to overestimate the vertical pressure in the model at the depth of 0.3 m and deeper.

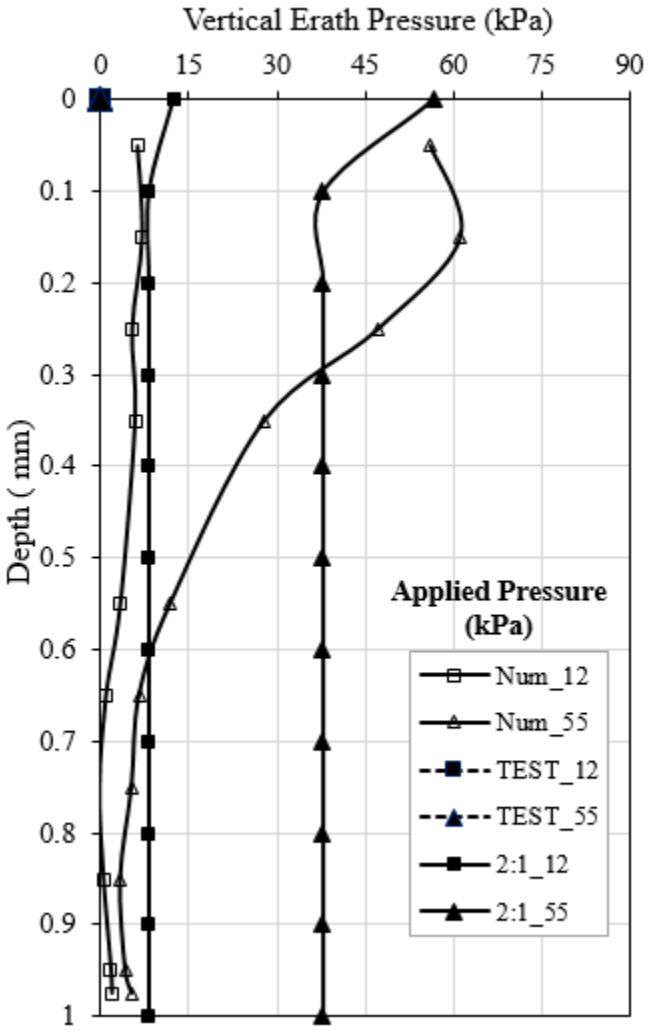

Figure 6.25 Vertical earth pressure distribution versus depth for the A4 model test

Lateral earth pressure distribution

Figure 6.26(a) compares the lateral earth pressures computed by the numerical analysis with those measured in the experimental. Figure 6.26(b) shows the lateral earth pressures on the wall facing computed by numerical analysis as compared with those calculated based on the Rankine theory and the 2:1 distribution method.

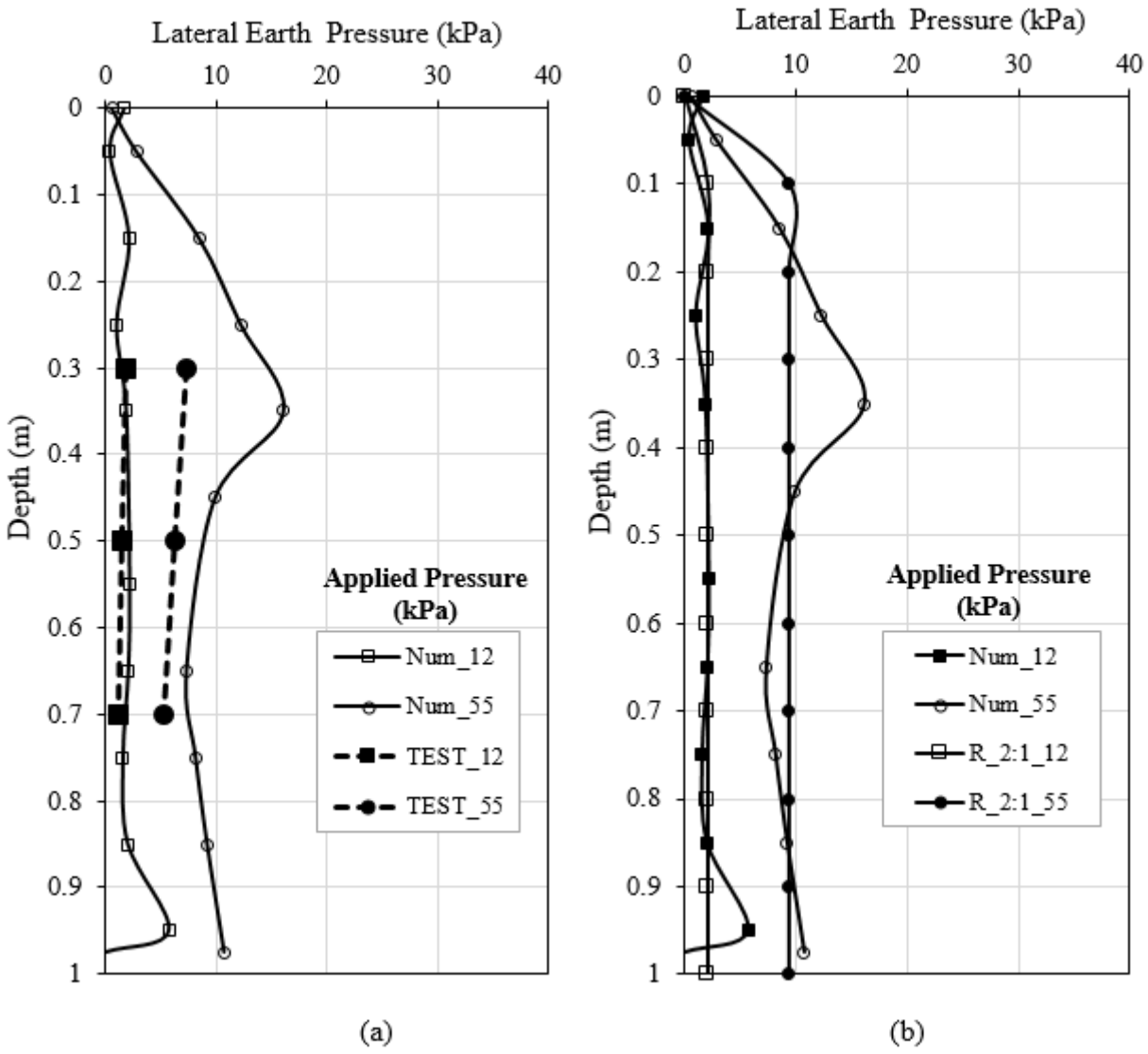

Figure 6.26 Lateral earth pressure distribution verse depth for the A4 model test: (a) Numerical versus test results and (b) numerical versus calculated results using the Rankine theory and Janssen's arching equation

Figure 6.26 shows that the lateral earth pressures computed by the numerical analysis increased approximately linearly with depth from the top of the wall to the depth of 0.35 m. The lateral earth pressures changed slightly from the depth of 0.4 m to the bottom of the wall. At the low applied footing pressure of 12 kPa, the lateral earth pressures computed by the numerical analysis matched the measured lateral earth pressures. At the higher applied pressure of 55 kPa, the measured lateral earth pressures are lower than those computed by the numerical analysis. In addition, the lateral earth pressures computed by the numerical analysis are in a fair agreement with those calculated based on the Rankine theory.

6.5.4 B1 wall model test

Wall facing displacement

Figure 6.27 shows the lateral displacements of the wall facing with the wall height (H) under various footing loading computed by the numerical analysis and measured in the experimental test.

This figure shows that the wall facing displacements increased with the increase of the applied footing pressure. In addition, the entire height of the wall facing displaced under the applied footing pressures with the maximum displacement occurring in the area around the mid-height of the wall height. Figure 6.27 also shows a good agreement between the lateral displacements of the wall facing computed by the numerical analysis and those measured in the experimental test under all applied footing pressures.

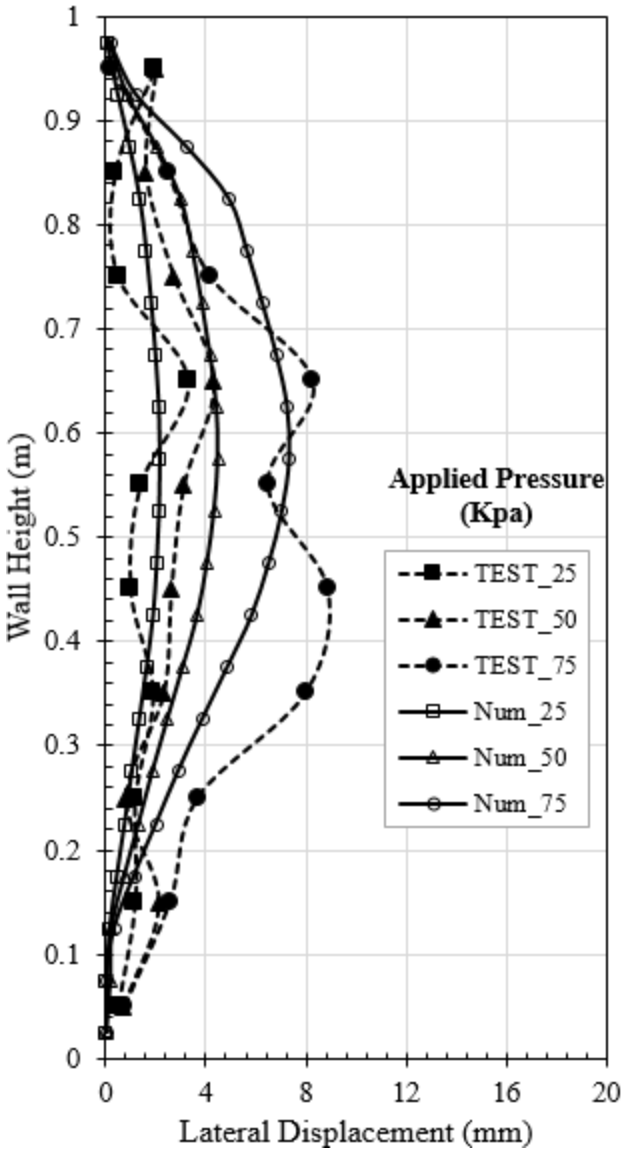

Figure 6.27 Lateral wall facing displacement versus wall height for the B1 model test

Pressure-settlement curve

Figure 6.28 compares the pressure-settlement curve of the footing computed by the numerical analysis with that measured in the experimental test. The settlement of the footing increased approximately linearly with the increase of the applied footing pressure.

Figure 6.28 indicates that the footing settlement computed by the numerical analysis matched that measured in the experimental test under all the applied footing pressures.

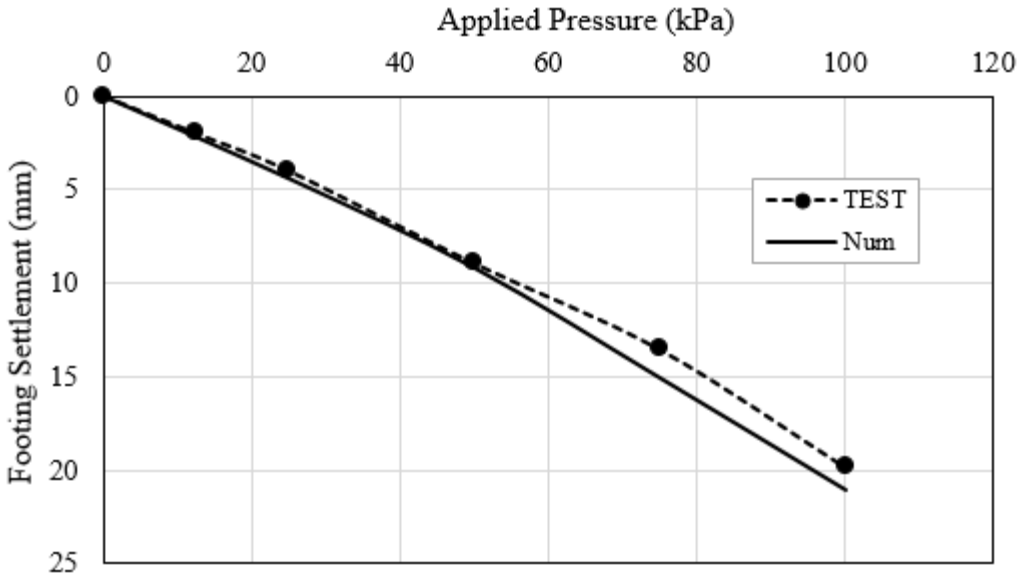

Figure 6.28 Pressure-settlement curve of the footing in the B1 model test

Vertical earth pressure distribution

Figure 6.29(a) compares the vertical earth pressures computed by the numerical analysis with those measured in the experimental test while Figure 6.29(b) compares the numerical results those calculated using the 2:1 distribution method. Figure 6.29(a) shows that the vertical earth pressures computed by the numerical analysis are higher than those obtained in the experimental test under the applied footing pressures except the vertical earth pressures computed by numerical analysis at the depth of 0.9 m were lower than those measured in the experimental test. Figure 6.29(b) shows that the vertical earth pressures calculated based on the 2:1 distribution method were higher than those computed by the numerical analysis at the depth close to the bottom of the wall (i.e., at the depth of 0.7 m and deeper).

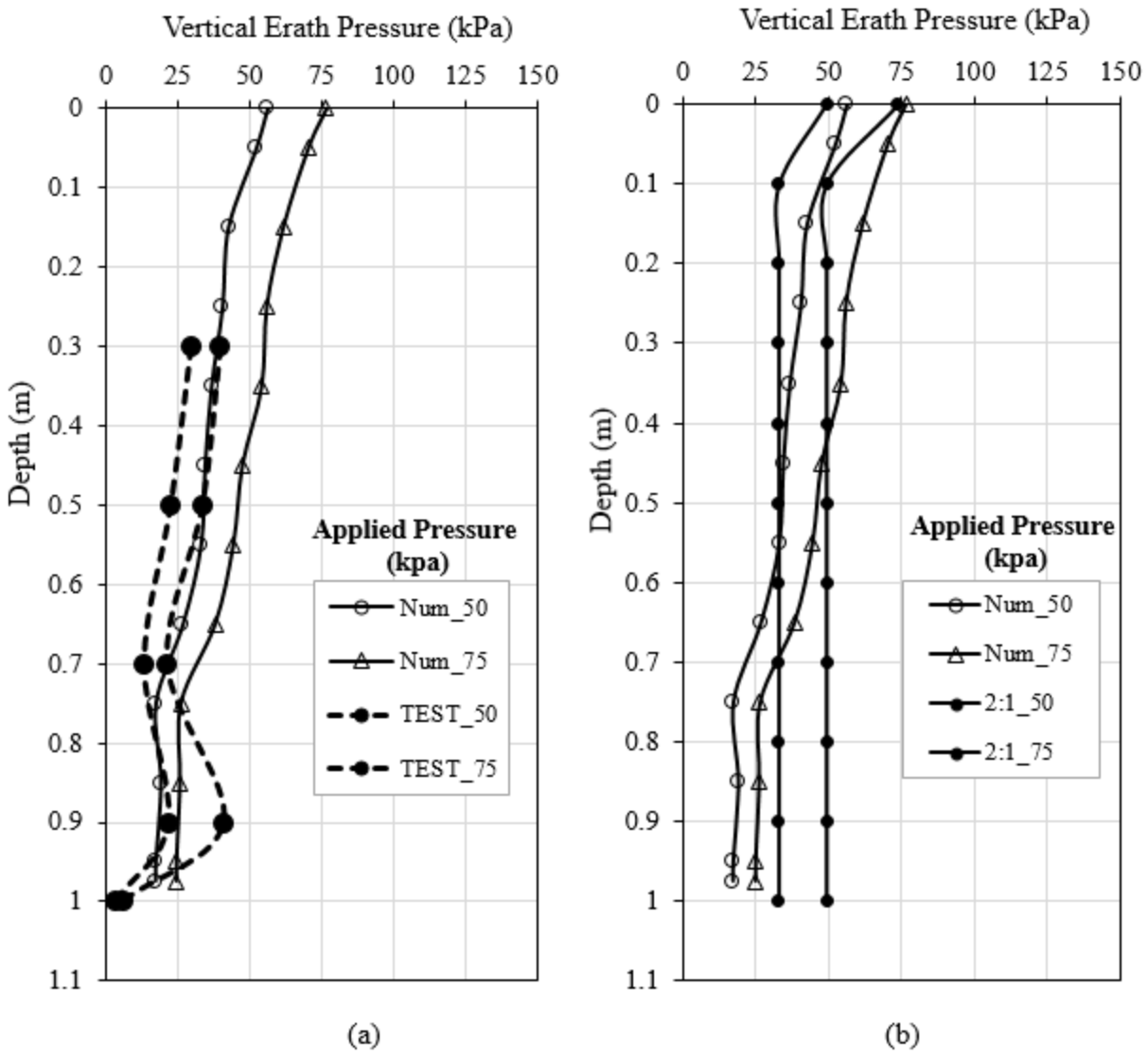

Figure 6.29 Vertical earth pressure distribution versus depth for the B1 model test: (a) Numerical versus test results and (b) numerical versus calculated results using the 2:1 distribution method

Lateral earth pressure distribution

Figure 6.30(a) compares the lateral earth pressures computed by the numerical analysis with that measured in the experimental test. Figure 6.30(b) shows the lateral earth pressures on the wall facing computed by numerical analysis compared with those calculated based on the Rankine theory with the 2:1 distribution method.

Figure 6.30 shows that the lateral earth pressures computed by the numerical analysis increased approximately linearly with the depth from the top of the wall to the depth of 0.25 m. There was no significant change in the lateral earth pressures from the depth of 0.25 m to the bottom of the wall. The lateral earth pressures computed by the numerical analysis agreed well with those measured in the experimental test. In addition, the numerical results were in a fair agreement with those calculated using the Rankine theory.

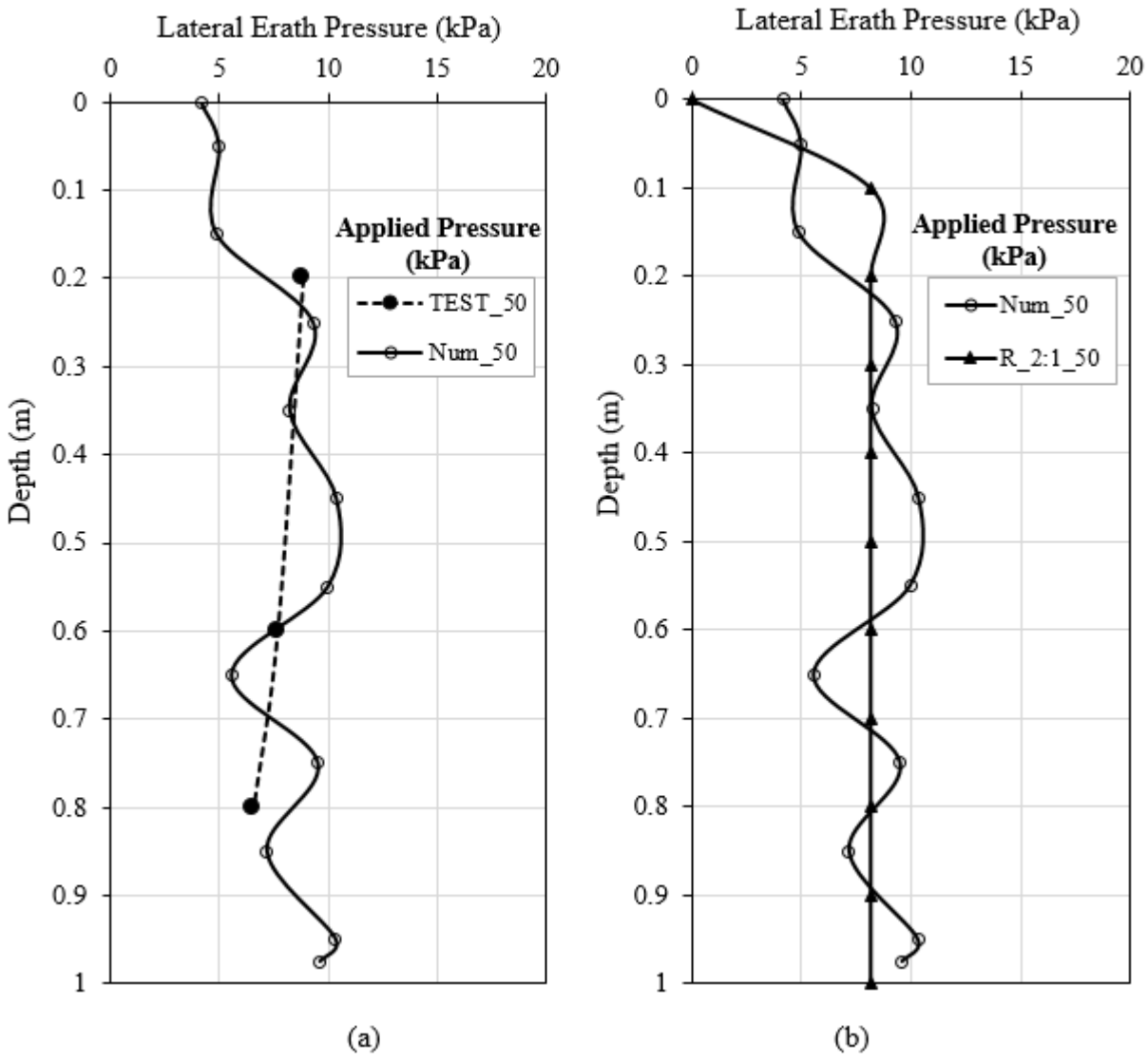

Figure 6.30 Lateral earth pressure distribution versus depth for the B1 model test: (a) Numerical versus test results and (b) numerical versus calculated results using the Rankine theory

6.5.5 C1 wall model test

Wall facing displacement

Figure 6.31 shows the lateral displacements of the wall facing with the wall height under various footing loadings computed by the numerical analysis compared with those measured in the experimental test.

Figure 6.31 shows that the displacements of the wall facing increased with the increase of the applied footing pressure with the similar trend in both the experimental test and the numerical analysis. In addition, most of the displacements occurred above the mid-height of the wall and approached to the maximum value at approximately 4/5 of the wall height or at the depth equal to the width of the footing (i.e., at depth of 0.2 m).

This figure shows the lateral displacements of the wall facing computed by the numerical analysis generally agreed with those measured in the experimental test under all applied footing pressures except that the lateral displacements computed by the numerical analysis had slightly larger maximum displacements than those measured in the experimental test under the high applied footing pressure of 150 kPa.

Pressure-settlement curve

Figure 6.32 compares the pressure-settlement curve of the footing computed by the numerical analysis with that measured in the experimental test. The settlement of the footing increased approximately linearly with the increase of the applied footing pressure. This figure shows that the footing settlement computed by the numerical analysis matched those measured in the experimental test under all the applied footing pressures.

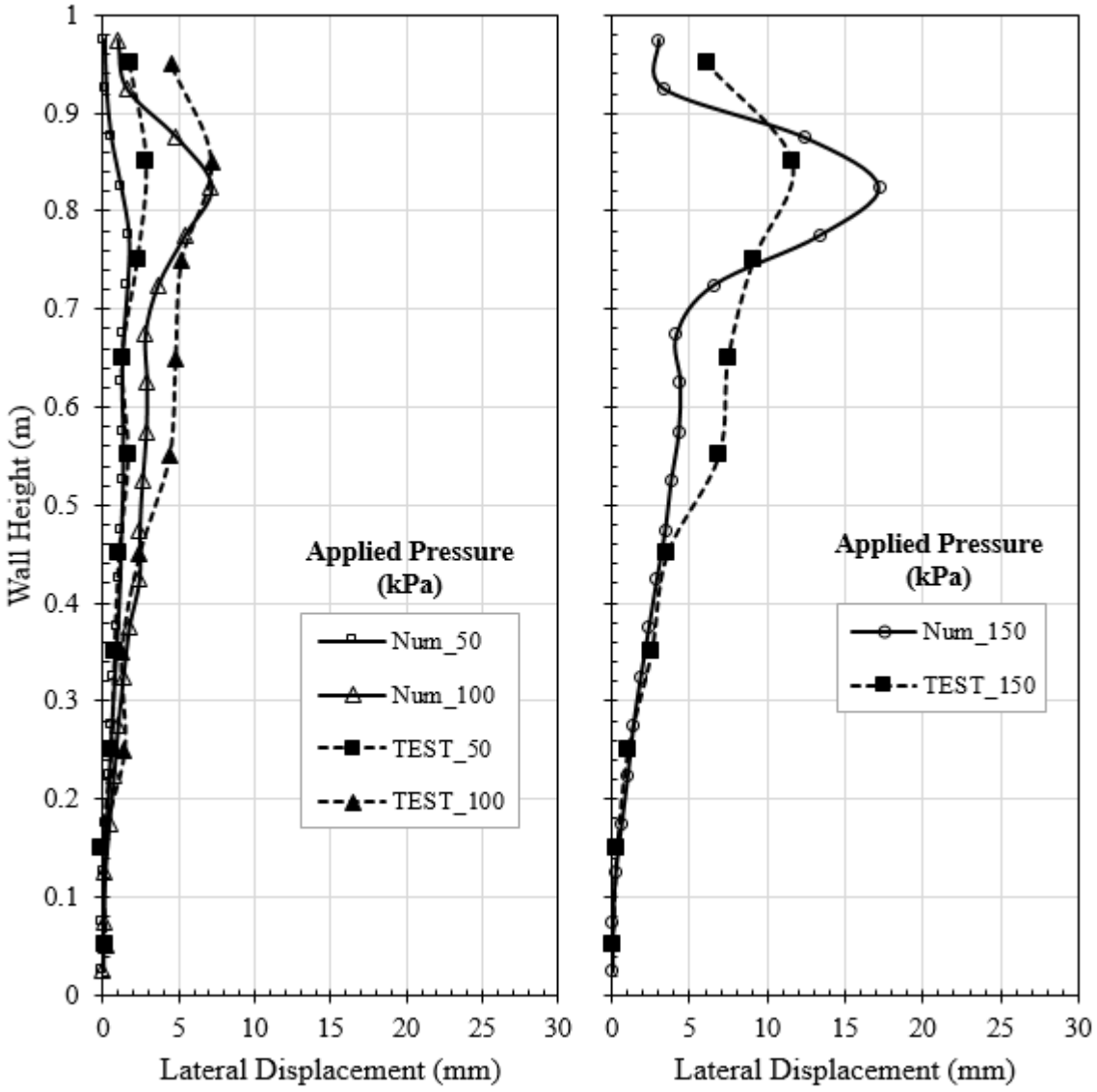

Figure 6.31 Lateral wall facing displacement versus wall height for the C1 model test

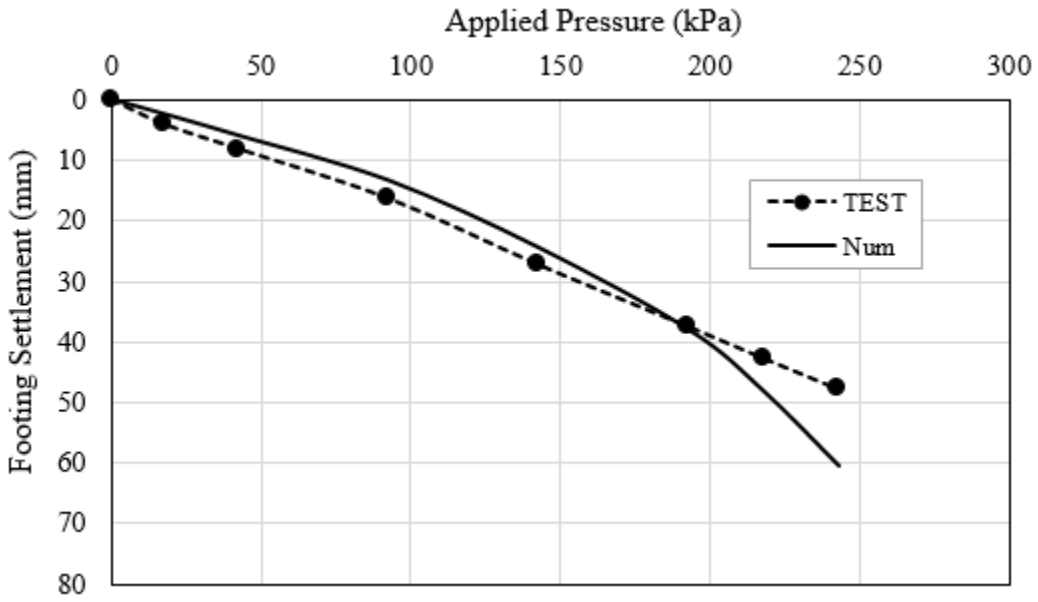

Figure 6.32 Pressure-settlement curve of the footing in the C1 model test

Vertical earth pressure distribution

Figure 6.33(a) compares the vertical earth pressures computed by the numerical analysis with those measured in the experimental test while Figure 6.33(b) compares the numerical results with those of the 2:1 distribution method. Figure 6.33 shows that the computed vertical earth pressures increased with the increase of the applied footing pressure. In addition, the vertical earth pressure computed by the numeric analysis decreased with the increase of the depth under all the applied footing pressures.

Figure 6.33(a) shows that the distribution of the vertical earth pressures computed by the numerical analysis agreed well with those obtained in the experimental test for all the applied footing pressures except that the vertical earth pressures computed at the bottom of the wall were higher than those measured in the experimental test at the same location.

The vertical earth pressures computed by the numerical analysis were lower than those calculated based on the 2:1 distribution method at the depth of 0.5 m and higher. However, the numerical results were higher than those calculated based on the 2:1 distribution method at the depth of 0.3 m and shallower.

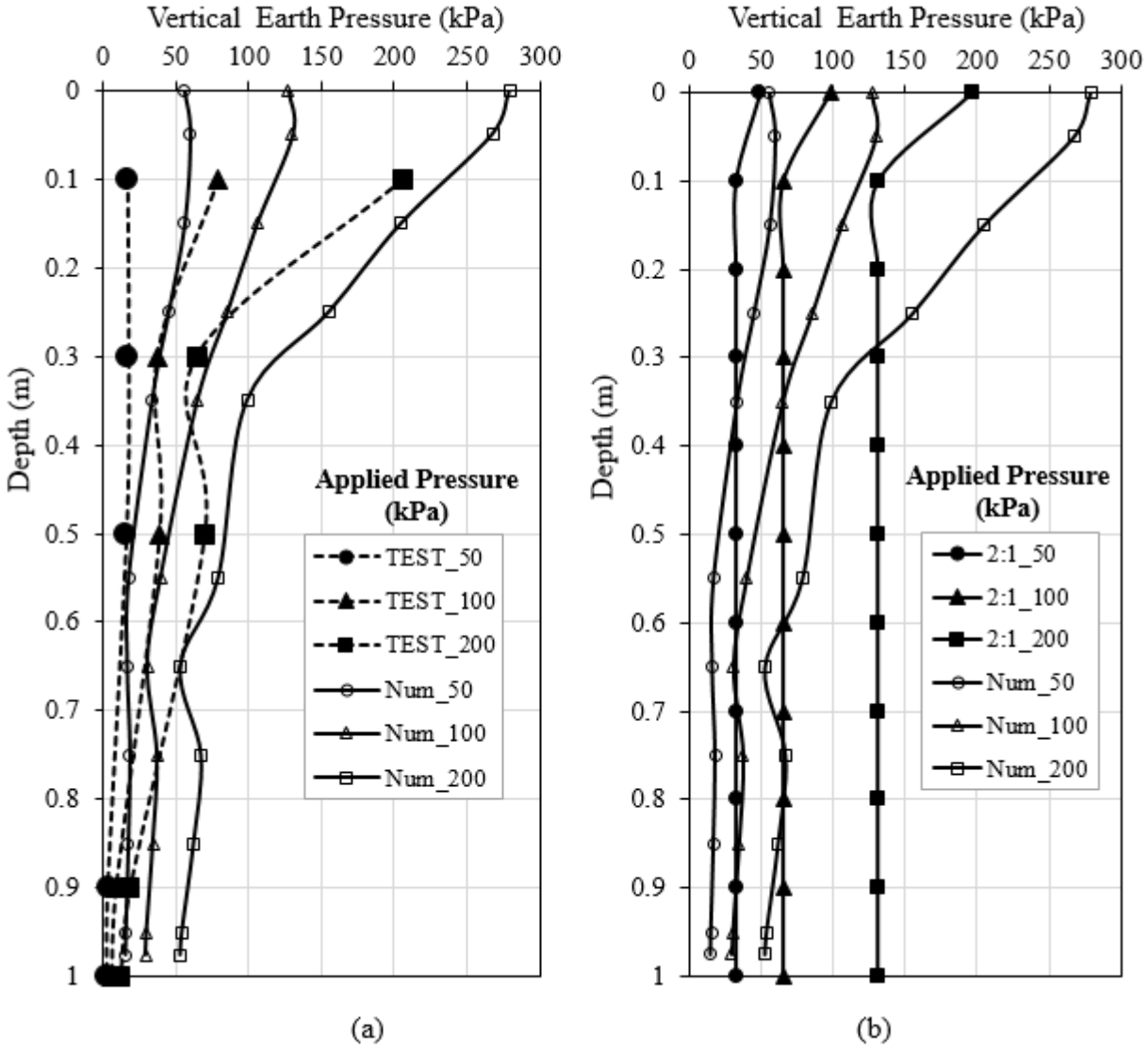

Figure 6.33 Vertical earth pressure distribution versus depth for the C1 model test: (a) Numerical versus test results and (b) numerical versus calculated results using the 2:1 distribution method

Lateral earth pressure distribution

Figure 6.34(a) compares the lateral earth pressures computed by the numerical analysis with those measured in the experimental test. Figure 6.34(b) shows that the lateral earth pressures on the wall facing computed by numerical analysis compared with those calculated based on the Rankine theory with the 2:1 distribution method.

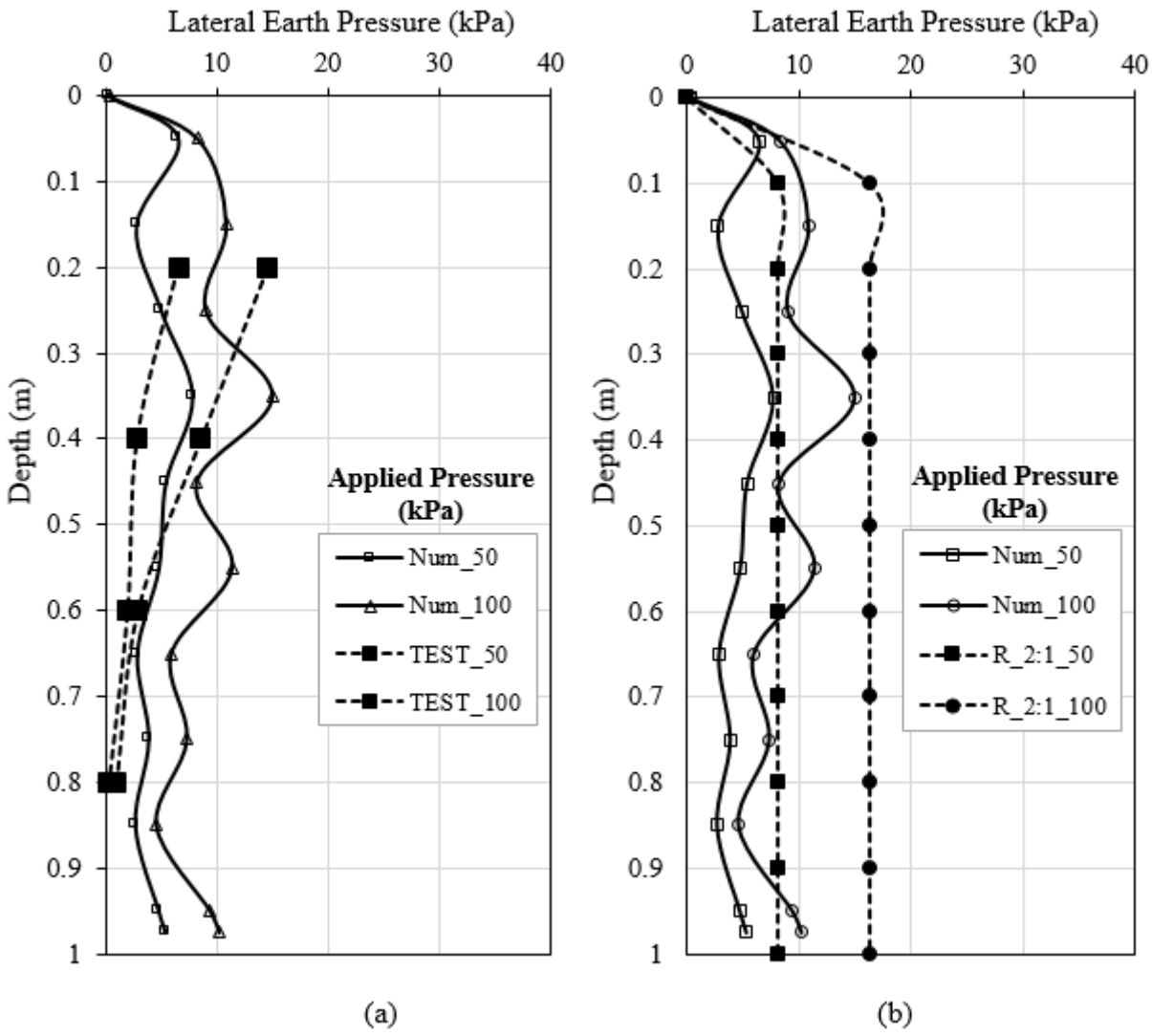

Figure 6.34 Lateral earth pressure distribution versus depth for the C1 model test: (a) Numerical versus test results and (b) numerical versus calculated results using the Rankine theory

Figure 6.34 shows that the lateral earth pressures computed by the numerical analysis increased with the increase of the applied footing load. In addition, there was no significant change in the lateral earth pressures from the depth of 0.2 m to the bottom of the wall. Figure 6.34(a) shows that the lateral earth pressures computed by the numerical analysis were in reasonable agreement with those measured in the experimental test at the depth of 0.2 and 0.4 m. However, the measured lateral earth pressures were lower than those computed by the numerical analysis at the deeper depth (i.e., at the depth of 0.6 m and 0.8 m). Compared to the calculated lateral earth pressures based on Equation (5.3) and (5.6), the lateral earth pressures computed by the numerical analysis were lower than those calculated using the Rankine theory but approximately parallel to the calculated lateral pressures.

Chapter 7 Parametric Study of Numerical Analysis

7.1 Introduction

Based on the numerical simulation of the experimental models presented in Chapter Six, a baseline case to simulate geosynthetic reinforced retaining (GRR) walls with limited fill space was developed. Figure 7.1 shows the geometry of the baseline case. The baseline case consisted of a foundation, a stable retained medium (stable wall), a reinforced fill (backfill soil and reinforcement), and wall facing. The reinforced fill width (also the reinforcement length, L) equal to 0.5H (H is the wall height) was chosen for the baseline case. The minimum required length of the reinforcement by FHWA (2009) is 0.7H). The wall height of the baseline case was chosen as 6.0 m, which is the common wall height used in the practice. The vertical spacing of reinforcement layers was 0.6 m, which is also typical in the design of GRR walls. The backfill soil was modeled as a linearly elastic perfectly plastic material with the Mohr Coulomb (MC) failure criterion. The behavior of the reinforcement was defined by a strip element, which was modeled as a linearly elastic perfectly plastic material. The wall facing, the stable retained medium, and the foundation soil were modeled as linearly elastic materials. The material properties, the interface properties, and the boundary conditions were the same as those presented in Chapter six and used in the numerical simulation of the GRR walls with limited fill space except for the stiffness of the reinforcement, which was 1000 kN/m in the baseline model.

Upon the completion of the numerical model for the baseline case, a parametric study was performed to study the influence of various parameters on the performance of GRR walls with limited fill space subjected to static footing loading. The influence parameters consisted of the reinforced fill width, the wall height, the reinforcement rear connection (e.g., connection of the reinforcement to the stable retained medium), the stiffness of reinforcement, the friction

angle of the backfill soil, the footing offset distance d (d is the distance from the edge of the footing to the back of the wall facing), and the footing size B_f. Table 7.1 shows the parameters used in the parametric study.

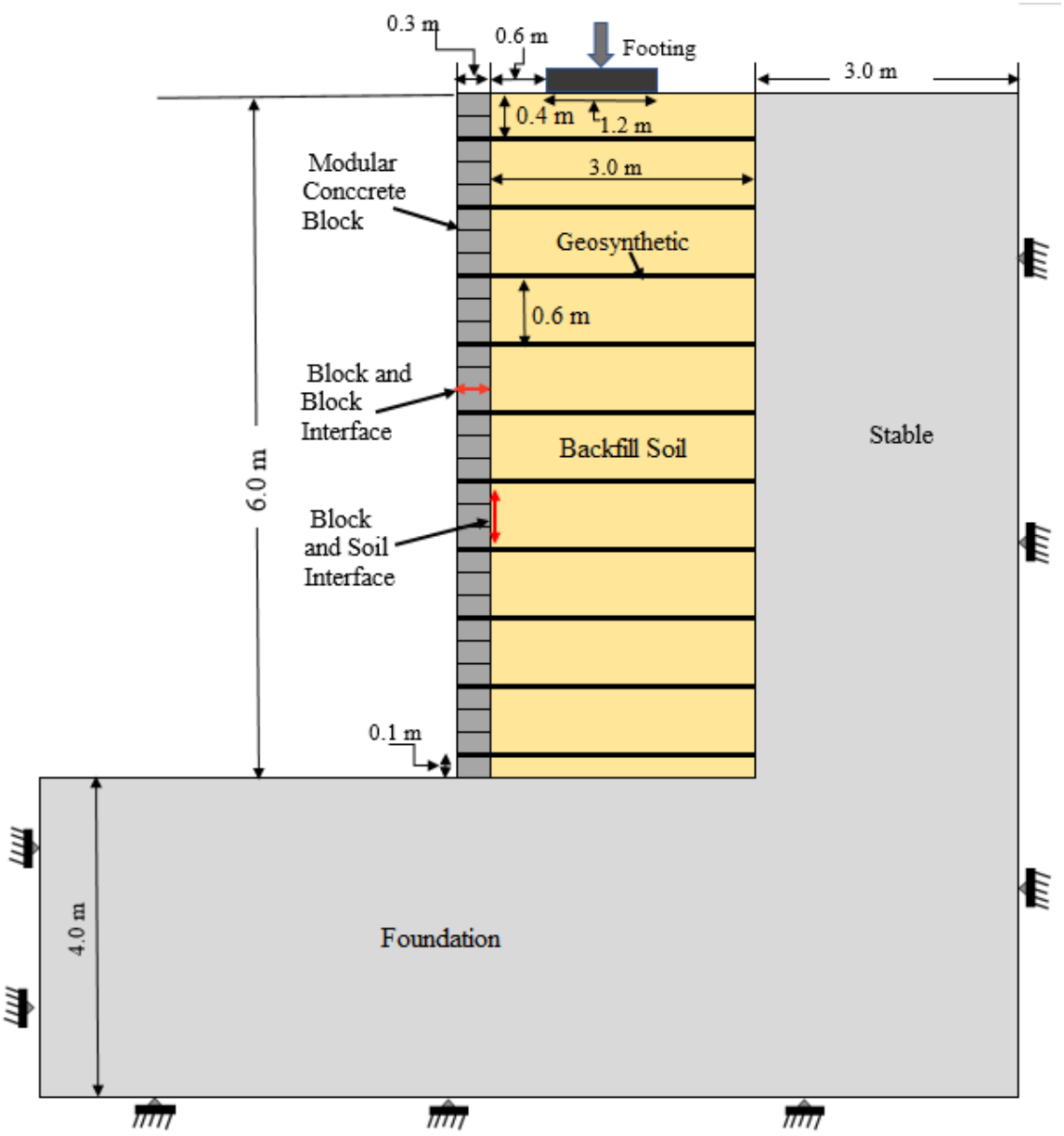

Figure 7.1 Cross section of the baseline case

Table 7.1 Parameters used in the parametric study

Parameters	Units	Range of Value
Wall height (H)	m	6.0*, 9.0
Reinforced fill width (L)	-	0.3H, 0.5H*, 0.7H
Reinforcement rear connection	-	Connected (fixed), free*, top layer connected, and overlapped
Soil friction angle (ϕ)	degrees	34, 38*
Geogrid stiffness (J)	kN/m	1000*, 2000
Footing offset (d)	-	0.05H, 0.H1, 0.15H
Footing size (B_f)	m	0.8, 1.2*, 1.6

*Parameters used in the base line case.

7.2 Numerical Results

7.2.1 Effect of reinforced fill width

The terms 0.7H, 0.5H and 0.3H used in texts and the legends of the figures shown in this chapter were referred to as the wall models with the reinforcement length of 0.7H, 0.5H, and 0.3H. Also, the numbers 50, 100 and 300 shown in the legends of the figures indicate the applied footing pressure of 50, 100, and 300 kPa.

Lateral wall facing displacement

Figure 7.2 shows the effect of the reinforced fill width on the lateral wall facing displacement under footing loading. This figure shows that the wall facing displacements in all three cases (i.e., 0.5H, 0.7H, and 0.3H) at the applied footing pressure of 100 kPa increased with the increase of the wall height until reaching the maximum value and then decreased with the height to the top of the wall. In the baseline case (i.e. 0.5H), the wall facing displacements reached the maximum values of 38 mm and 125 mm at the applied footing pressures of 100 kPa and 300 kPa, respectively. The maximum wall facing displacement occurred approximately at 3/4 of the wall height (i.e., at the wall height of 4.5 m) under the applied footing pressure of 100 kPa in the baseline case. In addition, the maximum wall facing displacement occurred at the higher elevation (i.e., at the wall height of 5.2 m) when a higher footing pressure was applied (i.e., under the applied footing pressure of 300 kPa). In other words, the increase of the footing pressure from 100 kPa to 300 kPa resulted in the change of the location of the maximum wall facing displacement in the baseline case.

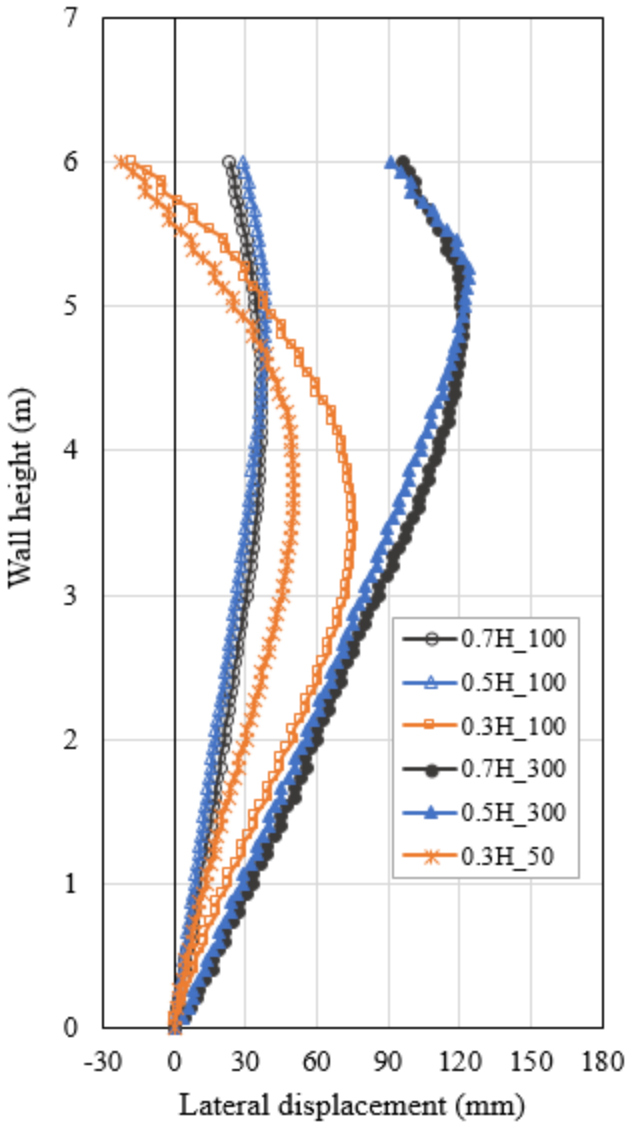

Figure 7.2 Effect of reinforced fill width on lateral wall facing displacement versus wall height

Figure 7.2 also shows that the profile of the wall facing displacements in the baseline case was similar to that in the case where the reinforced fill width was 0.7H, but different from that in which the reinforced fill width was 0.3H. In the 0.3H case, the maximum wall facing displacement occurred approximately in the middle of the wall. Subsequently, the displacements of the wall facing decreased with the wall height to approximately -25 mm at the top of the wall.

In other words, the facing wall displaced toward the wall at the top of the wall in case where the reinforced fill width was 0.3H.

In addition, Figure 7.2 shows that the increase of the length of the reinforcement from 0.5H to 0.7 H had an insignificant effect on the wall facing displacements. However, the reduction in the length of reinforcement from 0.5H to 0.3H resulted in a substantial increase in the displacement of the wall facing. For example, the maximum displacement of the wall facing was approximately 40 mm in the baseline case under the applied footing pressure of 100 kPa while the maximum displacement of the wall facing was approximately 75 mm in the 0.3H case under the same applied footing pressure.

Settlement of footing

Figure 7.3 shows the effect of the reinforced fill width on the settlement of the footing. The pressure-settlement curves of the baseline, 0.7H and 0.3H cases are shown in Figure 7.3, in which the settlement of footing increased with the increase of the applied footing pressure in all the three cases. This figure shows that the increase of the reinforced fill width from 0.5H to 0.7H had an insignificant effect on the settlement of the footing under all the applied footing pressures. However, the reduction in the reinforced fill width from 0.5H to 0.3H resulted in excessive settlement and large reduction in the bearing capacity of the footing. For example, in the 0.3H case, the footing settlement was approximately 240 mm under the applied footing pressure of 200 kPa, while the baseline case had only 150 mm settlement under the same applied pressure.

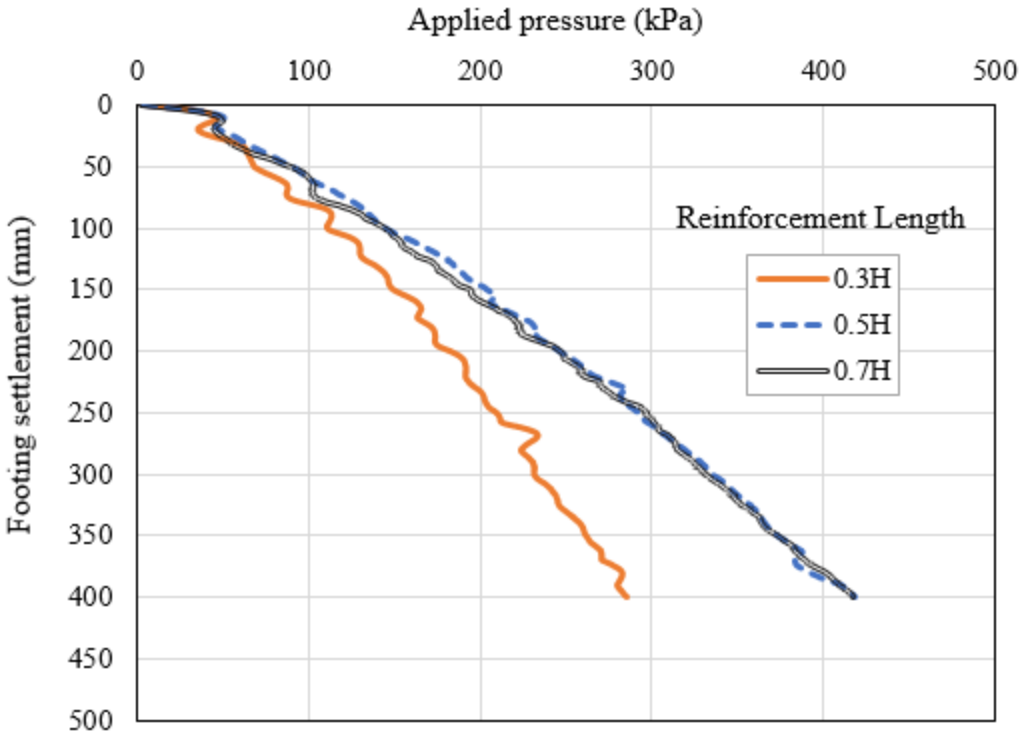

Figure 7.3 Effect of reinforced fill width on pressure-settlement curve of the footing

Vertical earth pressure distribution

Figure 7.4 shows the effect of the reinforcement length on the distribution of the vertical earth pressure due to the self-weight of the wall. Figure 7.4(a) shows the distribution of the vertical earth pressure on the wall facing and Figure 7.4(b) shows the distribution of the vertical earth pressure along the centerline of the footing. The phrase "the centerline of the footing" was referred to as a plane or line from the bottom to the top of the wall that goes through the center of the footing. The vertical earth pressure at the centerline of the footing was used to (1) demonstrate the difference between the distribution of the vertical earth pressures on the wall facing and on a plane away from the wall facing and (2) to examine the accuracy of the theoretical method used to predict the distribution of the vertical earth pressures under the applied footing load as presented later in this section.

For the comparison purpose, the vertical earth pressures calculated using Equation (7.1) were added in Figure 7.4 and designated as" γd" in the legends of the figures presented in this section.

$$\sigma_v = \gamma * d \ldots\ldots\ldots\ldots (7.1)$$

where:

σ_v is the overburden vertical earth pressure

γ is the unit weight of the backfill soil, and

d is the depth of the wall

Figure 7.4 shows that the vertical earth pressures in all three cases (i.e., 0.5H, 0.7H, and 0.3H) increased with the increase of the depth on the wall facing and along the centerline of the wall footing. In addition, the distributions of the vertical earth pressures had similar trends in all three cases. Figure 7.4(a) shows that the increase of the length of the reinforcement from 0.5H to 0.7H resulted in slightly less vertical earth pressures on the wall facing compared to those in the baseline case. On the other hand, the reduction in the length of the reinforcement from 0.5H to 0.3H resulted in a little higher vertical earth pressures than those in the baseline case, especially at the wall depths of approximately 2.5 m to 5.0. In addition, the vertical earth pressures along the centerline of the footing were almost the same in all three cases. In other words, the change of the reinforcement length had no considerable effect on the distribution of the vertical earth pressure along the centerline of the wall footing.

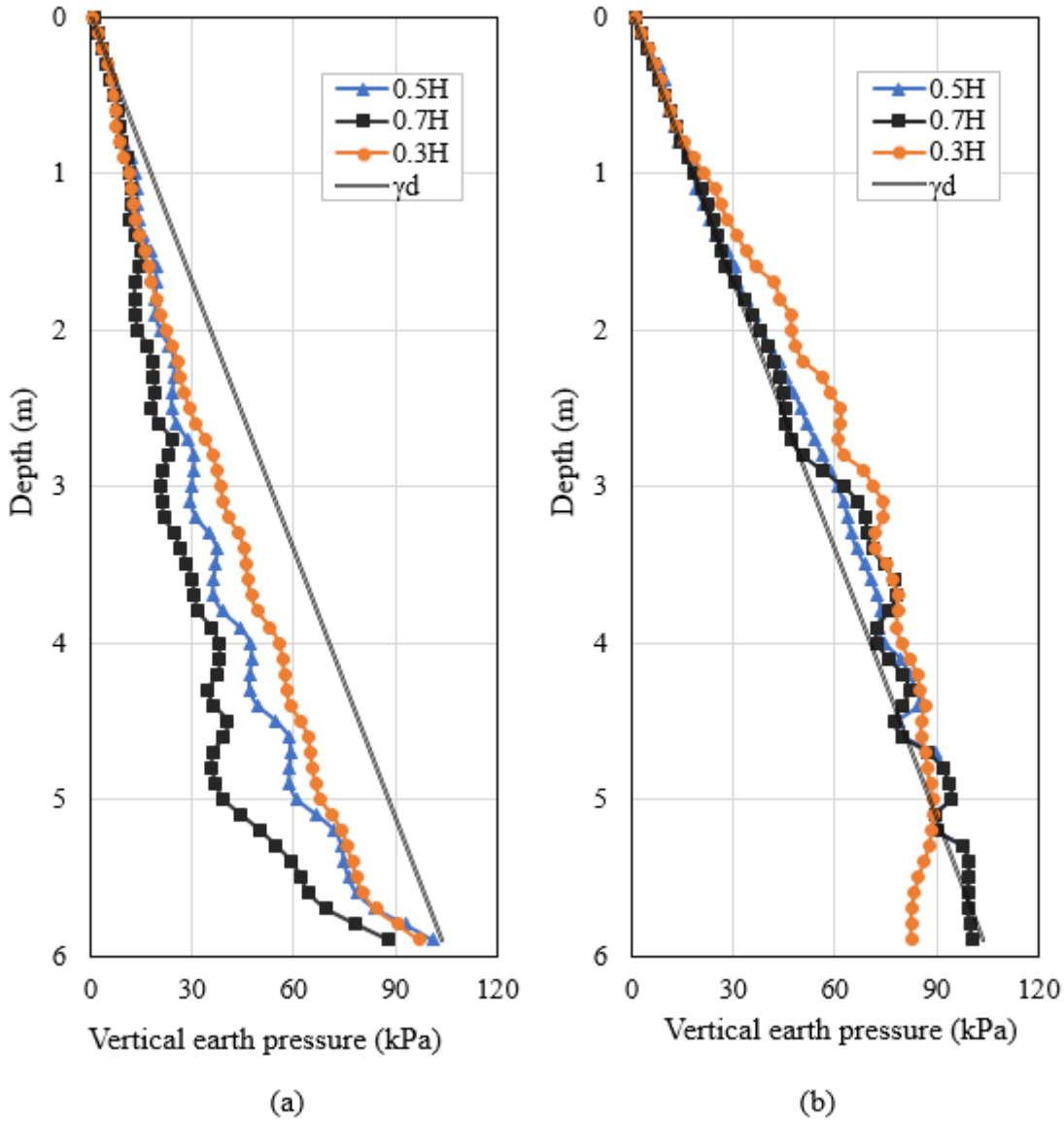

Figure 7.4 Effect of reinforced fill width on vertical earth pressure distribution due to self-weight of the wall: (a) along the wall facing and (b) along the centerline of the footing

Figure 7.4(a) also shows that the vertical earth pressures on the wall facing in all three cases were lower than those calculated using Equation (7.1). Moreover, the vertical earth pressures along the centerline of the footing in the 0.5H and 0.7H cases were almost the same as those calculated using Equation (7.1). However, the vertical earth pressures along the centerline

of the footing in the case where the length of the reinforcement was 0.3H were generally higher than those calculated using Equation (7.1).

Figures 7.5 and 7.6 show the effects of the reinforcement length on the distribution of the vertical earth pressures under footing loading. Figures 7.5 (a) and 7.6 (a) shows the distribution of the vertical earth pressures on the wall along the wall facing under the applied footing pressure of 100 and 300 kPa, respectively. Similarly, Figure 7.5 (b) and 7.6 (b) shows the distribution of the vertical earth pressures along the centerline of the footing under the applied footing pressure of 100 and 300 kPa, respectively. For the comparison purpose, the vertical earth pressures calculated using Equation (7.2) were added in Figures 7.6 and 7.7 and designated as Cal in the legends of the figures presented in this chapter.

$$\sigma_{vT} = \sigma_v + \Delta\sigma_v \ldots\ldots\ldots\ldots (7.2)$$

where:

σ_{vT} is the total vertical earth pressure due to the self-weight of the wall and the applied footing load

σ_v is the vertical earth pressure due to the self-weight of the wall using Equation (7.1)

$\Delta\sigma_v$ is the vertical earth pressure due to the footing load using the 2:1 distribution method (Equation (5.1))

Figures 7.5(a) and 7.6(a) also show that the vertical earth pressures on the wall facing in all three cases increased with the increase of the depth. Figure 7.5(b) shows that the vertical earth pressures along the centerline of the footing under the applied footing pressure of 100 kPa reached the maximum value near the top of the wall (i, e., close to the footing) and then slightly decreased with the depth to about 1/3 of the wall depth in all three cases. After that, the vertical earth pressures became relatively constant to the bottom of the wall. In addition, Figure 7.6(b)

shows that the vertical earth pressures along the centerline of the footing under the applied footing pressure of 300 kPa also reached the maximum value near the top of the wall and then linearly decreased with the depth down to the mid-depth of the wall, and became relatively constant from that depth (i.e., the wall depth of 3.0 m) to the bottom of the wall.

Furthermore, the increase in the length of the reinforcement from 0.5H to 0.7H resulted in less vertical earth pressures on the wall facing compared to those in the baseline case. However, the reduction in the reinforcement length from 0.5H to 0.3H generally resulted in higher vertical earth pressures on the wall facing than those in the baseline case, particularly from the mid-depth to the bottom of the wall. Regarding the vertical earth pressures along the centerline of the footing, the change of the reinforcement length showed no insignificant effect as demonstrated in Figures 7.5(b) and 7.6(b).

Figures 7.5 and 7.6 also show that the vertical earth pressures on the wall facing in all three cases were generally lower than those calculated using Equation (7.2). However, the vertical earth pressures along the centerline of the footing were generally higher than those calculated using Equation (7.2).

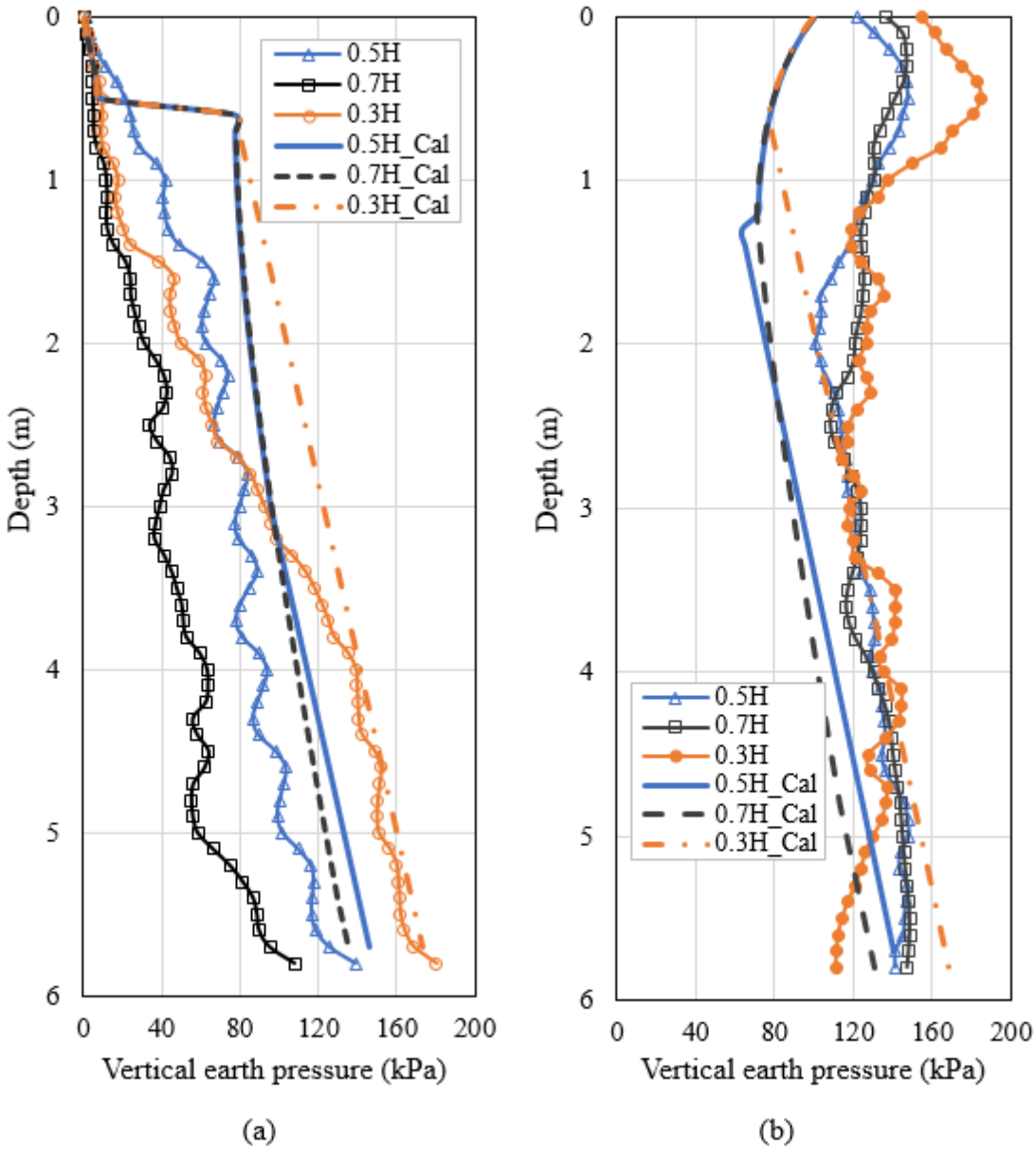

Figure 7.5 Effect of reinforced fill width on vertical earth pressure distribution on the wall facing under the applied footing pressure of 100 kPa: (a) on the wall facing and (b) along the centerline of the footing

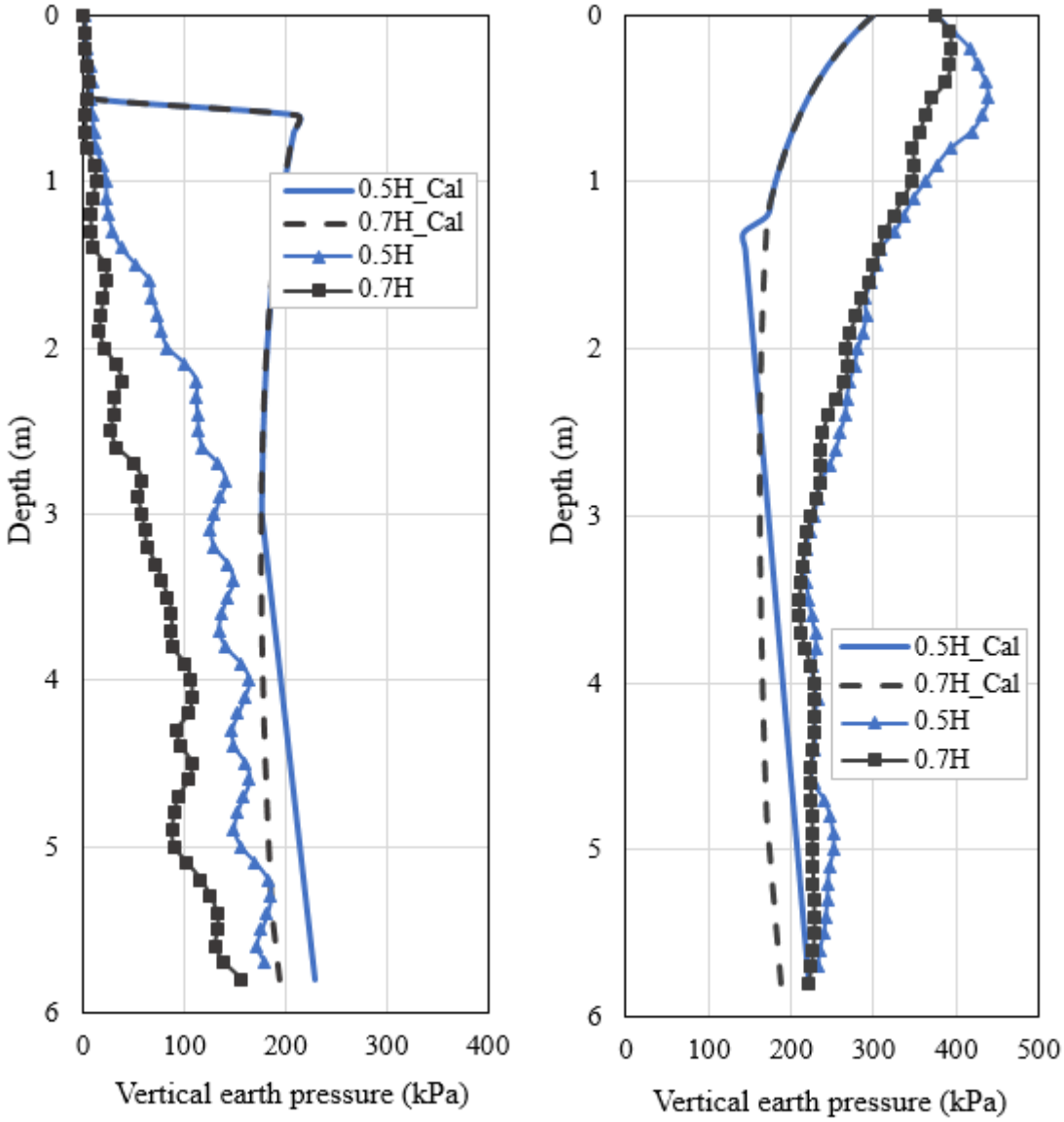

Figure 7.6 Effect of reinforced fill width on vertical earth pressure distribution under the applied footing pressure of 300 kPa: (a) on the wall facing and (b) along the centerline of the footing

Lateral earth pressure distribution

Figure 7.7 shows the effects of the reinforcement length on the distribution of the lateral earth pressure due to the self-weight of the wall. Figure 7.7 shows the distribution of the lateral earth pressure on the wall facing the depth of the wall in the 0.5H, 0.7H and 0.3H cases. For the comparison, the lateral earth pressures calculated using Rankine's active earth pressure theory and Janssen's equation (Equation (5.4)) were added in Figure 7.7 and designated as Rankine and Janssen in the legends of the figure.

Figure 7.7 shows that the lateral earth pressures increased with the increase of depth along the wall facing in all the three cases. In addition, the change of the reinforcement length had minor effect on the lateral earth pressures on the wall facing. Figure 7.7 shows that the lateral earth pressures on the wall facing in all three cases were lower than those calculated using Rankine's active earth pressure theory and Janssen's equation.

Figures 7.8 and 7.9 show the effects of the reinforcement length on the distribution of the lateral earth pressures under footing loading. Figures 7.8 show the distribution of the lateral earth pressures on the wall facing under the applied footing pressure of 100 and Figure 7.9 shows the distribution of the lateral earth pressure on the wall facing under the applied footing pressure 300 kPa.

For the comparison purpose, the lateral earth pressures calculated using Equations (7.3) and (7.4) were added in Figure 7.8 and 7.9 and designated as R and J in the legend of the figures shown in this section.

$$\sigma_{hT} = k_a(\sigma_v + \Delta\sigma_v) \dots\dots\dots\dots (7.3)$$

$$\sigma_{hT} = k_J(\sigma_v + \Delta\sigma_v) \dots\dots\dots\dots (7.4)$$

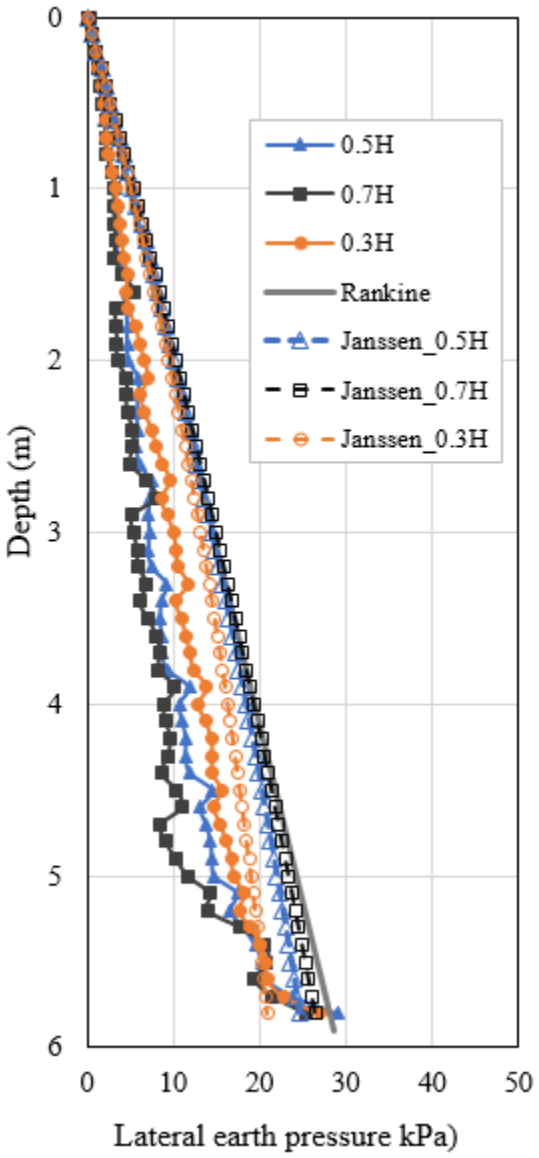

Figure 7.7 Effect of reinforced fill width on lateral earth pressure distribution on the wall facing due to the self-weight of the wall

where:

σ_{hT} is the total lateral earth pressure due to the self-weight of the wall and footing load

σ_v is the vertical earth pressure due to the self-weight of the wall

K_a is the Rankine's active lateral earth pressure coefficient using Equation (5.3)

K_{aJ} is the Janssen's lateral earth pressure coefficient using Equation (5.34)

$\Delta\sigma_v$ is the vertical earth pressure due to the footing load using the 2:1 distribution method (Equation (5.1)).

Figures 7.8(a) and 7.9(a) compare the lateral earth pressures computed by the numerical analysis with those calculated using equation (7.3) under the applied footing pressure of 100 and 300 kPa, respectively. Figures 7.8(b) and 7.9(b) compare the lateral earth pressures computed by the numerical analysis with those calculated using equation (7.4) under the applied footing pressure of 100 and 300 kPa, respectively.

Figures 7.8 and 7.9 show that the lateral earth pressures on the wall facing under the applied footing pressures increased with the increase of the depth in all three cases. Figures 7.8 and 7.9 also show that the increase of the length of the reinforcement from 0.5H to 0.7H resulted in less lateral earth pressures on the wall facing along the depth of the wall compared to those in the baseline case. In addition, the reduction of the length of the reinforcement from 0.5H to 0.3H resulted in higher lateral earth pressures on the wall facing compared to those in the baseline case as shown in Figures 7.8 and 7.9. In addition, the lateral earth pressures on the wall facing in all three cases were less than those calculated using Equation (7.3) and (7.4). In other words, Equation (7.3) and (7.4) overestimates the lateral earth pressures on the wall facing under the applied footing pressure. However, the lateral earth pressures calculated using Equation (7.4) were matched better to the lateral earth pressures computed by numerical simulation compared to those calculated using Equation (7.3). Consequently, Janssen's equation can estimates the lateral earth pressures on the wall facing under the applied footing loading more accurately than Rankine's active theory.

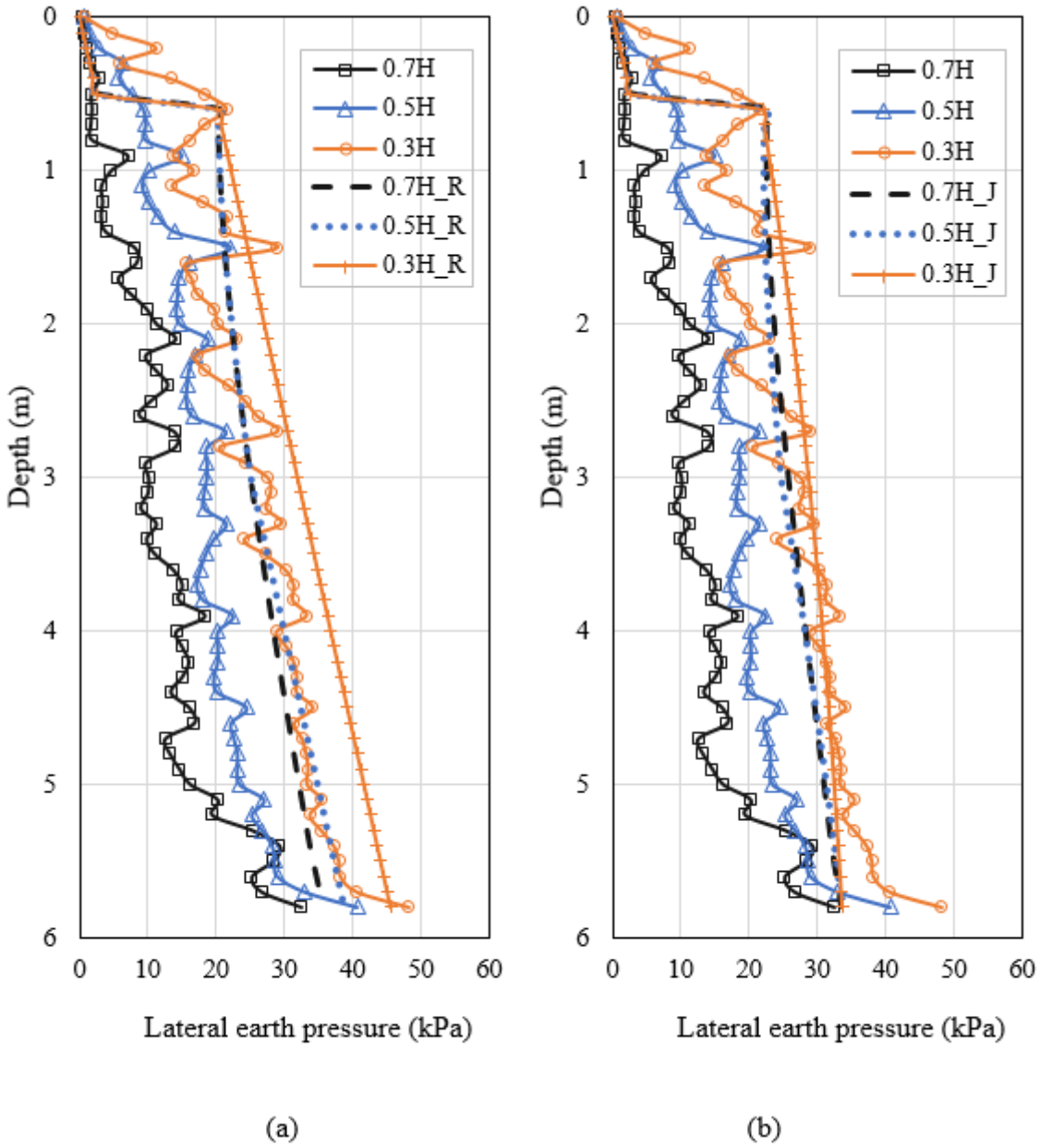

Figure 7.8 Effect of reinforced fill width on lateral earth pressure distribution on the wall facing under the applied footing pressure of 100 kPa: (a) Numerical versus calculated results using the Rankine theory and (b) numerical versus calculated results using Janssen's equation

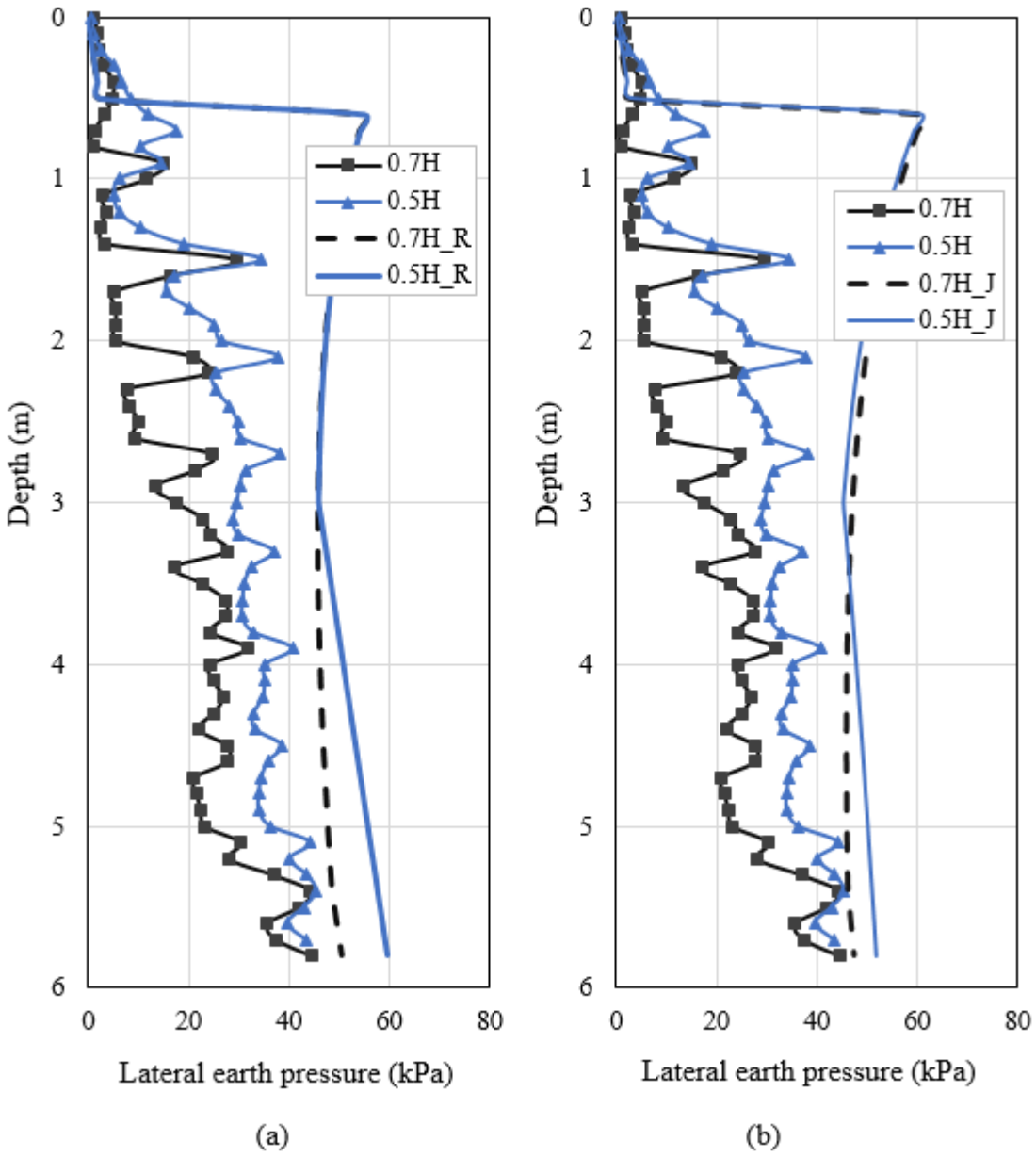

Figure 7.9 Effect of reinforced fill width on lateral earth pressure distribution on the wall facing under the applied footing pressure of 300 kPa: (a) Numerical versus calculated results using the Rankine theory and (b) numerical versus calculated results using Janssen's equation

Maximum strain of the reinforcement

Figure 7.10 shows the effect of the reinforcement length on the maximum strains of each reinforcement layer under the applied footing pressures of 100 kPa and 300 kPa. As shown in Figure 7.10, the maximum strain at each reinforcement layer increased with the increase of the applied footing pressure. The maximum strains were in the ranges of 0.06% to 1.4%, 0.13% to 1.2%, and 0.37% to 2.6%, under the applied footing pressure of 100 kPa for the 0.7H, 0.5H and 0.3H cases, respectively. Also, the maximum strains were in the ranged of 0.26% to 4.0% and 0.57% to 3.94% under the applied footing pressure of 300 kPa for the 0.7H and 0.5H cases, respectively.

The maximum strains of the reinforcement layers in both the baseline and 0.7H cases were almost the same under both the applied footing pressures of 100 kPa and 300 kPa. In other words, the increase of the length of the reinforcement form 0.5H to 0.7H had no considerable effect on the maximum strains of the reinforcement layers.

However, the reduction in the reinforcement length from 0.5H to 0.3H resulted in a large increase in the maximum strains of the reinforcement layers. For example, the maximum reinforcement strain at the wall height of 5 m in the 0.3H case was approximately 2.6% under the applied footing pressure of 100 kPa, while the maximum reinforcement strain in the baseline case was approximately 1.1% at the same wall height and applied footing pressure.

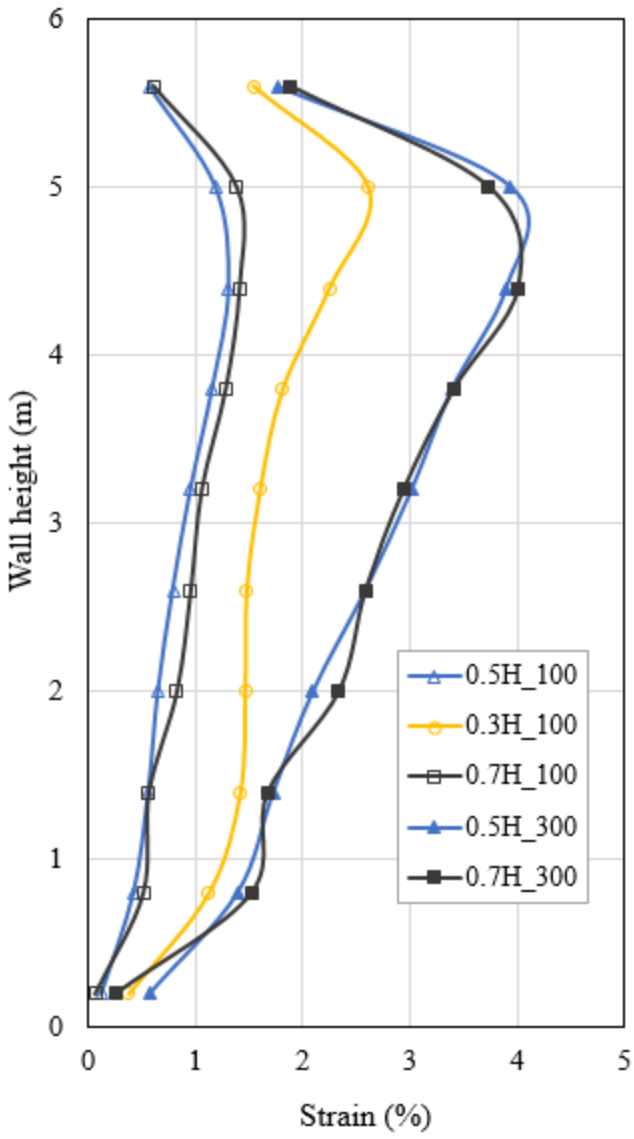

Figure 7.10 Effect of reinforced fill width on maximum strain of the reinforcement layers

7.2.2 Effect of reinforcement rear connection

This section presents the effect of the reinforcement rear connection on the displacement of the lateral wall facing, the settlement of the footing, the distribution of the vertical earth pressure, the distribution of lateral earth pressure, and the maximum strain of the reinforcement. To examine the effect of the reinforcement rear connection, three different models were simulated as follows and their results are compared with the results of the baseline case.

- Full connection (connected): this is the case where all the reinforcement layers were fixed to the stable medium. This connection condition is denoted as "connected" in the texts and legends of the figures.
- Top layers connected: this is the case in which only the two uppermost layers were connected to the stable medium. This condition is denoted as "top_connected" in the texts and the legends the figures.
- Overlapped: this is the case where a layer of reinforcement was added at each level of the primary reinforcement and they were connected to the stable medium and extended over the primary reinforcement (overlapped) up to 75% of the length of the primary reinforcement (i.e., 2.25 m from the stable medium). This condition is designated as "overlapped" in the texts and legends of the figures.

  Note: the baseline case is denoted as "unconnected" in the legends of the figures.

Lateral wall facing displacement

Figure 7.11 shows the effects of the reinforcement rear connection on the wall facing displacements along the wall height under footing loading. As shown in Figure 7.11, the wall facing displacements in all the cases increased with increase of the applied footing pressure. The

displacement of the wall facing in the cases where the reinforcement was connected to the stable medium at the rear (i.e., overlapped, connected, and top_connected cases) increased with the wall height and reached the maximum value at 3/4 of the wall height (i.e., 1.4 m from the bottom of the footing). Above this elevation the wall facing displacements decreased with the wall height to the top of the wall under the applied footing pressure of 100 kPa and 300 kPa.

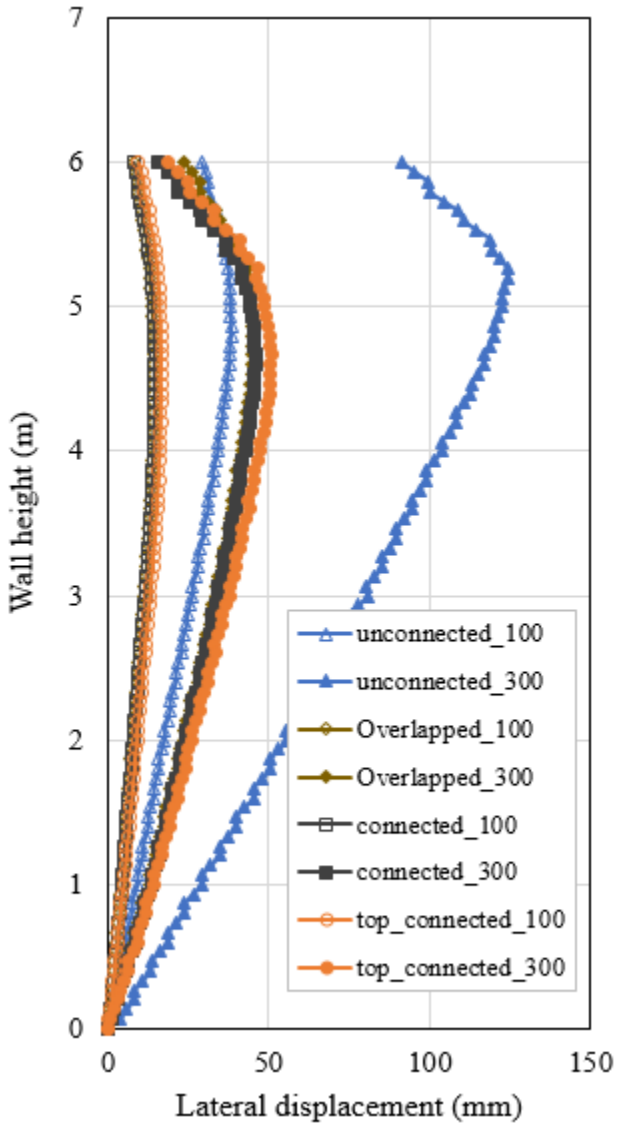

Figure 7.11 Effect of reinforcement rear connection on lateral wall facing displacement versus wall height

Figure 7.11also shows that the connection of the reinforcement layers to the stable medium ((i.e., the connection case) resulted in substantial reduction in the displacement of the wall facing as compared with that in the baseline (i.e., unconnected case) case under the same loading condition. For example, the maximum displacement was only about 45 mm in the connected case under the applied footing pressure of 300 kPa, while the maximum displacement was around 125 mm in the baseline case under the same applied footing pressure. In addition, overlapping the reinforcement layers (i.e., the overlapping case) also resulted in a large reduction in the displacement of the wall facing (i.e., the maximum displacement was about 45 mm under the applied footing pressure of the 300 kPa) as compared with that (i.e., 125 mm) in the baseline case under the same loading condition.

Moreover, Figure 7.11 indicates that even fixing the two uppermost layers of the reinforcement to the stable medium (i.e., the top_connected case) also resulted in a substantial reduction in the displacement of the wall facing as compared with that in the baseline case under the same loading condition. For example, the maximum wall facing displacement was only about 50 mm in the top_connected case under the applied footing pressure of 300 kPa, which is 2.5 times smaller than that of the baseline case under the same applied footing load.

Settlement of footing

Figure 7.12 shows the effects of reinforcement rear connection on the settlement of the footing. The figure demonstrates that the connection of the reinforcement layers to the stable medium resulted in a large reduction in the footing settlement as compared with the baseline case under the applied footing pressure. For example, the connected case had approximately 200 mm footing settlement under the applied footing pressure of 400 kPa, while the baseline case had 300

mm footing settlement under the same loading condition. In addition, overlapping of the reinforcement layers resulted in a large reduction in the footing settlement (e.g., 190 mm) as compared with the baseline case (e.g., 300 mm) at the same applied footing pressure (i.e., applied footing pressure of 400 kPa).

Additionally, connecting two uppermost layers of the reinforcement to the stable medium (i.e., as in the top_connected case) had also considerable effect on the reduction of the footing settlement and increase of the bearing capacity of the footing. The connection was as effective as the connected case. Consequently, the connection of the reinforcement to the stable medium significantly reduced the footing settlement and resulted in higher bearing capacity of the applied footing.

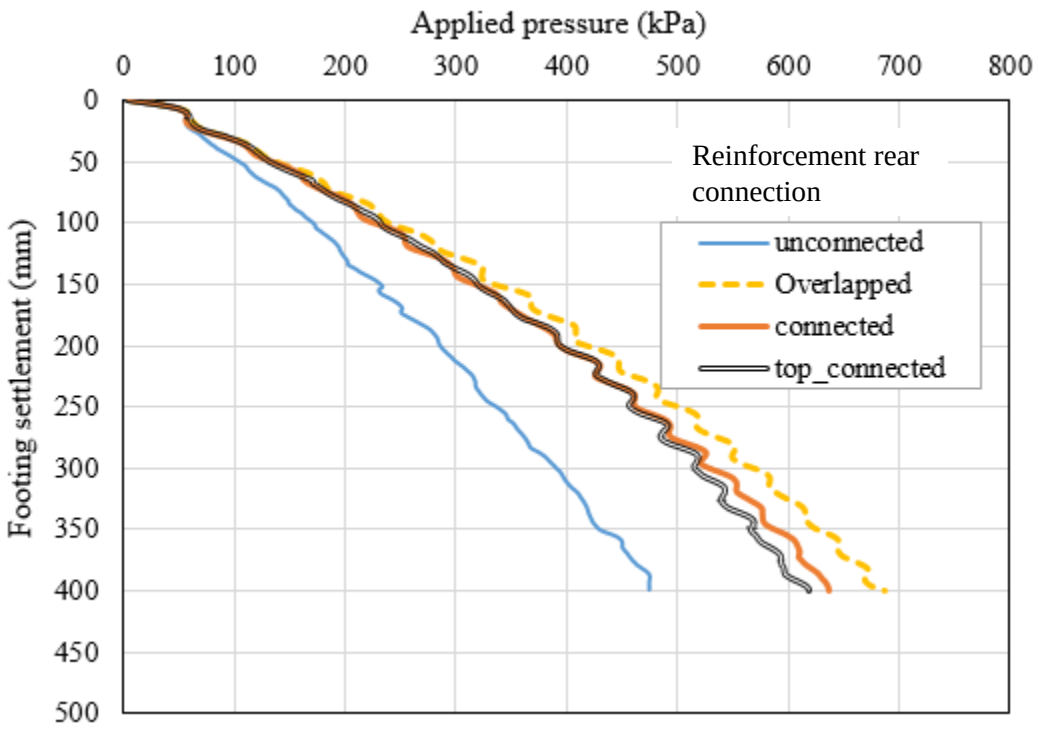

Figure 7.12 Effect of reinforcement rear connection on pressure-settlement curve of the footing

Vertical earth pressure distribution

Figure 7.13 shows the effects of the reinforcement rear connection on the distribution of the vertical earth pressure due to the self-weight of the wall. Figure 7.13(a) shows the distribution of the vertical earth pressure on the wall along the wall facing while Figure 7.13(b) shows the distribution of the vertical earth pressure along the centerline of the footing. For the comparison purpose, the vertical earth pressures calculated using Equation (7.1) were added in Figure 7.13.

Figure 7.13 shows that the vertical earth pressures on the wall facing and along the centerline of the footing increased with increase of the depth in all the cases. In addition, the vertical earth pressures along the centerline of the footing were higher than those on the wall facing but had the same trends in all the cases.

Additionally, as shown in Figure 7.13, the reinforcement rear connection had no considerable effect on distribution of the vertical earth pressures on the wall along the wall facing and below the centerline of the footing along the depth of the wall. Comparing to the vertical earth pressures calculated from Equation (7.1), the vertical earth pressures on the wall facing were lower. However, the vertical earth pressures below the centerline of the footing were almost the same as those calculated from Equation (7.1).

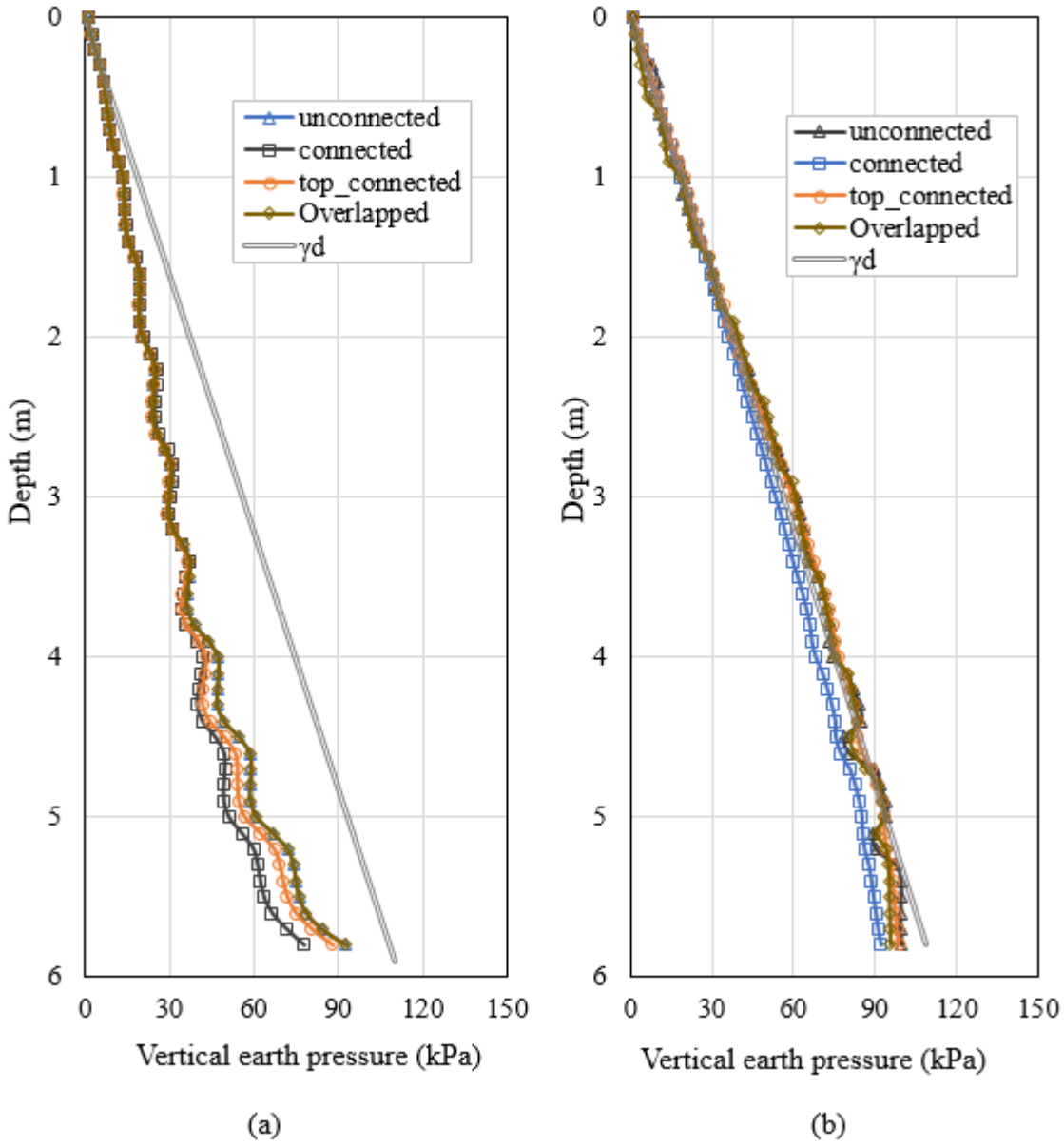

Figure 7.13 Effect of reinforcement rear connection on vertical earth pressure distribution due to self-weight of the wall: (a) on the wall facing and (b) along the centerline of the footing

Figures 7.14 and 7.15 show the effects of the reinforcement rear connection on the distribution of the vertical earth pressure under footing loading. Figure 7.14(a) and 7.15(a) shows the distribution of the vertical earth pressures on the wall along the wall facing under the applied

footing pressure of 100 and 300 kPa, respectively. Figure 7.14 (b) and 7.15 (b) shows the distribution of the vertical earth pressures along the centerline of the footing under the applied footing pressure of 100 and 300 kPa, respectively. For the comparison purpose, the vertical earth pressures calculated using Equation (7.2) were added in Figure 7.14 and 7.15.

Figures 7.14(a) and 7.15(a) show that the vertical earth pressures on the wall along the wall facing increased with the increase of the depth with similar trends in all the cases. In addition, Figures 7.14(b) and 7.15(b) show that the vertical earth pressures along the centerline of the footing reached the maximum values close to the top of the wall in all the cases and slightly decreased with the depth to a certain level (i.e., the wall depth of 2.0 m under the applied footing pressure of 100 kPa). After this point the vertical earth pressures became relatively constant to the bottom of the wall.

Figures 7.14 and 7.15 also show that the reinforcement rear connection had no considerable effect on the vertical earth pressures on either location. In addition, the vertical earth pressures on the wall along the wall facing in all the cases were generally lower than those calculated using Equation (7.2). However, the vertical earth pressures along the centerline of the footing were generally higher than those calculated using Equation (7.2).

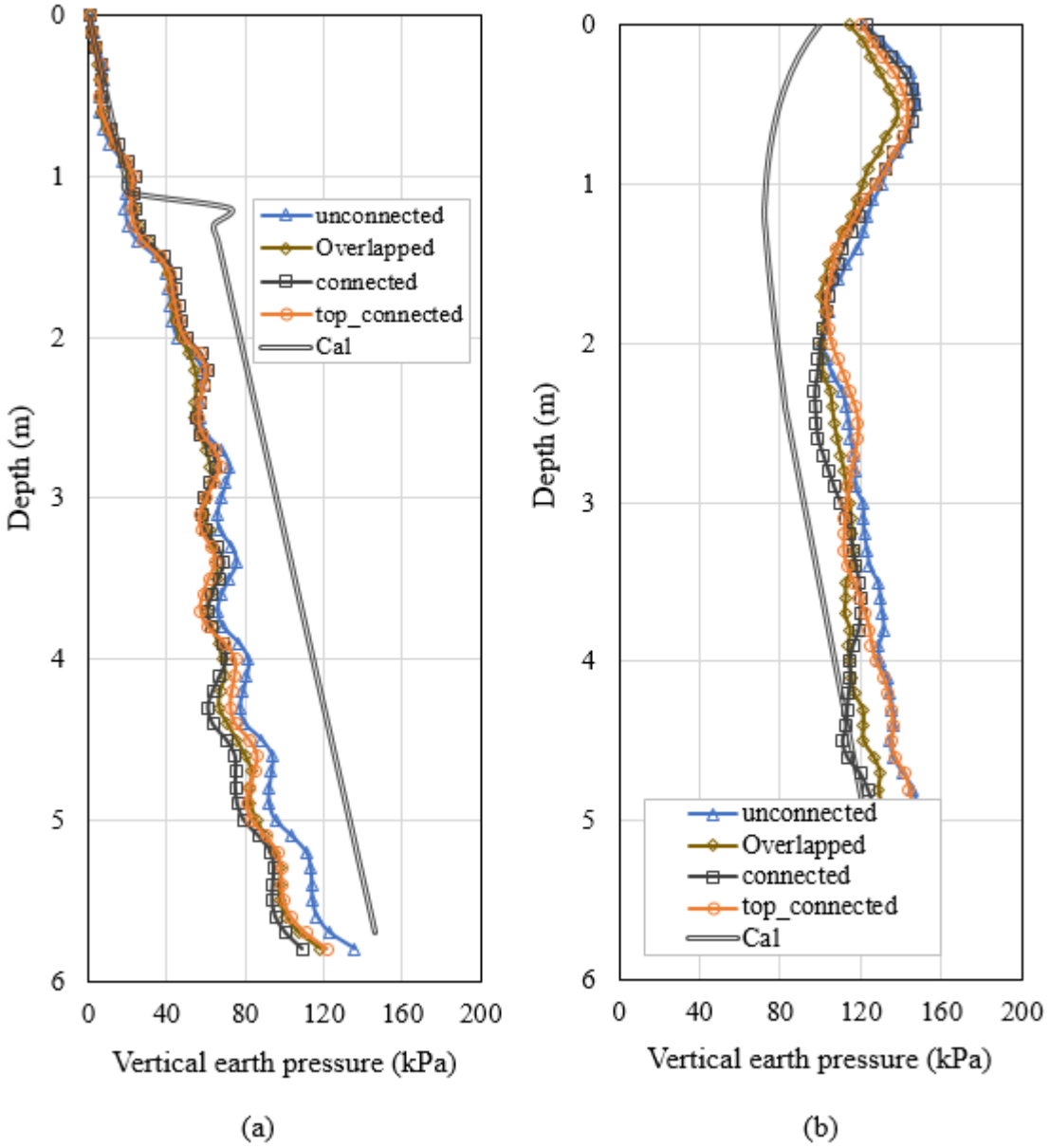

Figure 7.14 Effect of reinforcement rear connection on vertical earth pressure distribution under the applied footing pressure of 100 kPa: (a) on the wall facing and (b) along the centerline of the footing

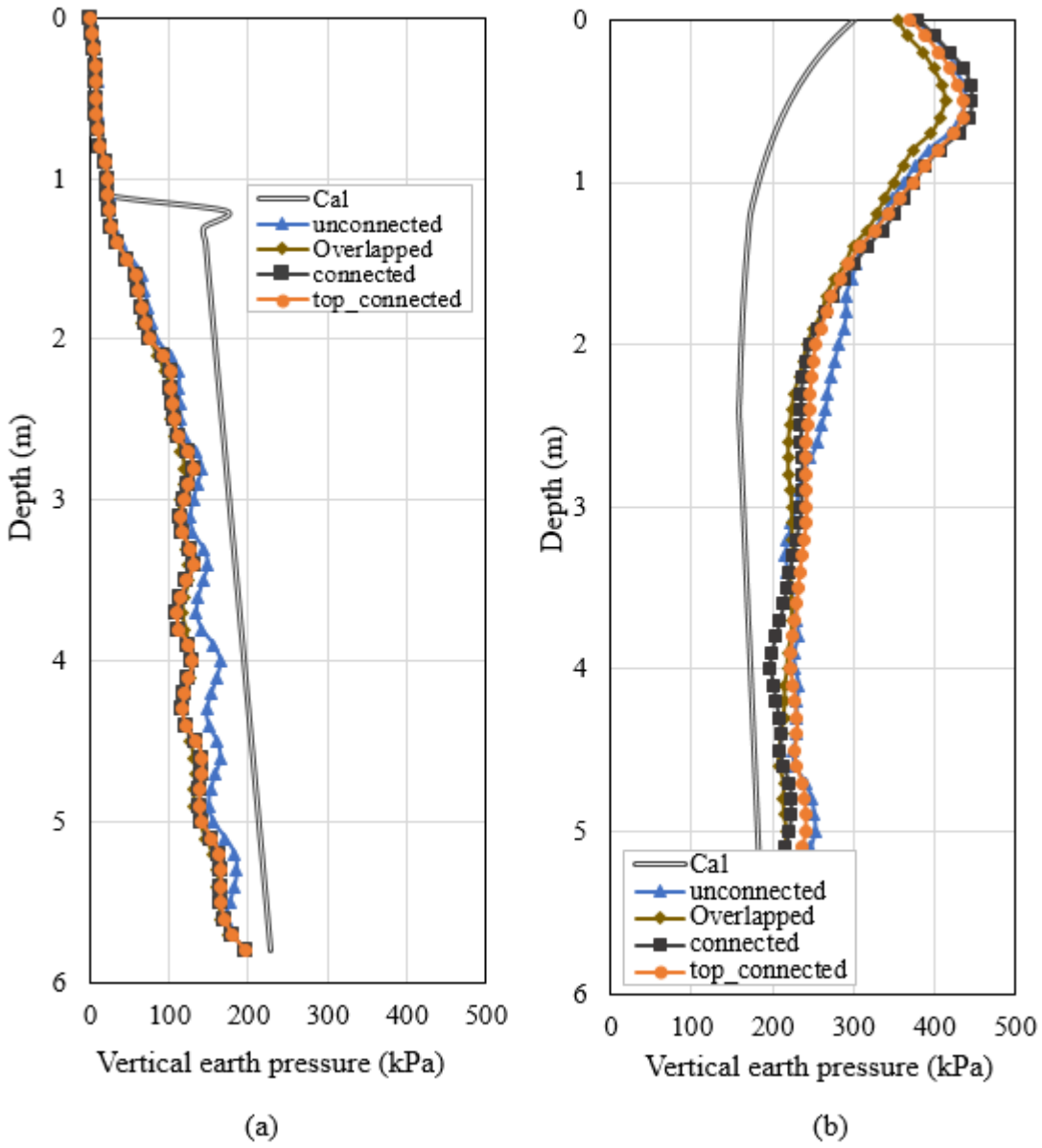

Figure 7.15 Effect of reinforcement rear connection on vertical earth pressure distribution under the applied footing pressure of 300 kPa: (a) on the wall facing and (b) along the centerline of the footing

Lateral earth pressure distribution

Figure 7.16 shows the effects of the reinforcement rear connection on the distribution of the lateral earth pressure on the wall facing due to the self-weight of the wall in the "unconnected", "connected", "top_connected", and "overlapped" cases. For the comparison purpose, the vertical earth pressures calculated using Rankine's active earth pressure theory and Janssen's equation were added in Figure 7.16 and designated as "Rankine" and "Janssen" in the legends of the figure.

Figure 7.16 shows that the lateral earth pressure on the wall facing increased with the increase of the depth in all the cases. In addition, the distribution of the lateral earth pressures had similar trends in all three cases. The figure also shows that the reinforcement rear connection had no considerable effect on the lateral earth pressures on the wall facing along the depth of the wall.

Furthermore, the lateral earth pressures on the wall facing were lower than those calculated using Rankine's active earth pressure theory and Janssen's equation in all the shown cases.

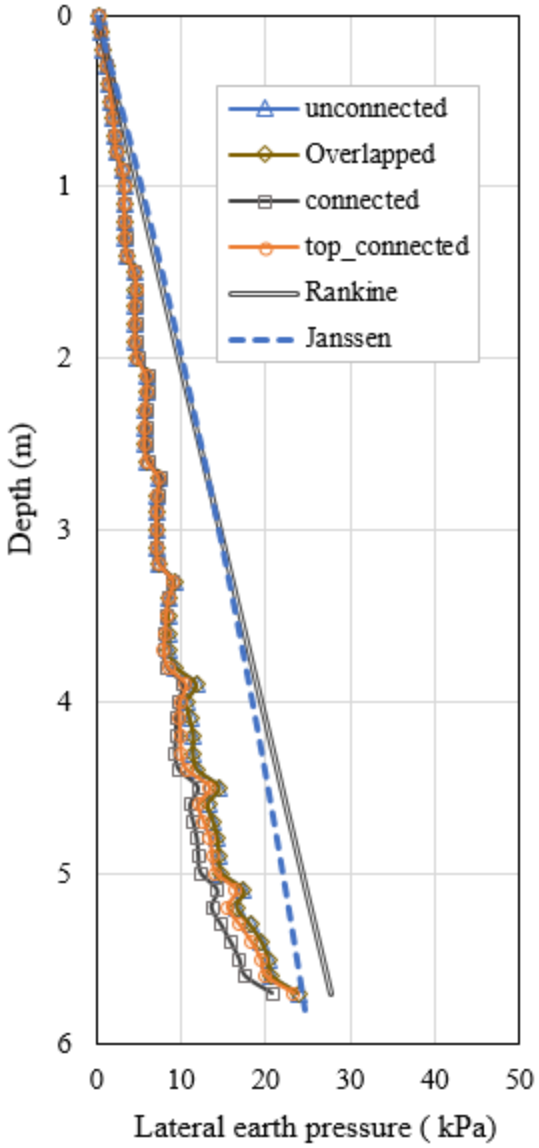

Figure 7.16 Effect of reinforcement rear connection on lateral earth pressure distribution on the wall facing due to the self-weight of the wall

Figures 7.17 and 7.18 show the effects of the reinforcement rear connection on the distribution of the lateral earth pressure on the wall facing under the applied footing pressure of 100 kPa and 300 kPa, respectively. For the comparison purpose, the lateral earth pressures calculated using Equations (7.3) and (7.4) were added in Figure 7.17 and 7.18 and are designated as “Rankine” and Janssen”, respectively.

Figures 7.17 and 7.18 show that the lateral earth pressures on the wall facing in all the cases increased with the increase of the depth under both the applied footing pressure. Figures 7.17 and 7.18 also show that the rear connection of the reinforcement had insignificant effect on the distribution of the lateral earth pressures on the wall facing.

In addition, the lateral earth pressures on the wall facing in all the cases were lower than those calculated using Equations (7.3) and (7.4) as well. However, the lateral earth pressures calculated using Equations (7.4) were lower than those calculated using Equation (7.3).

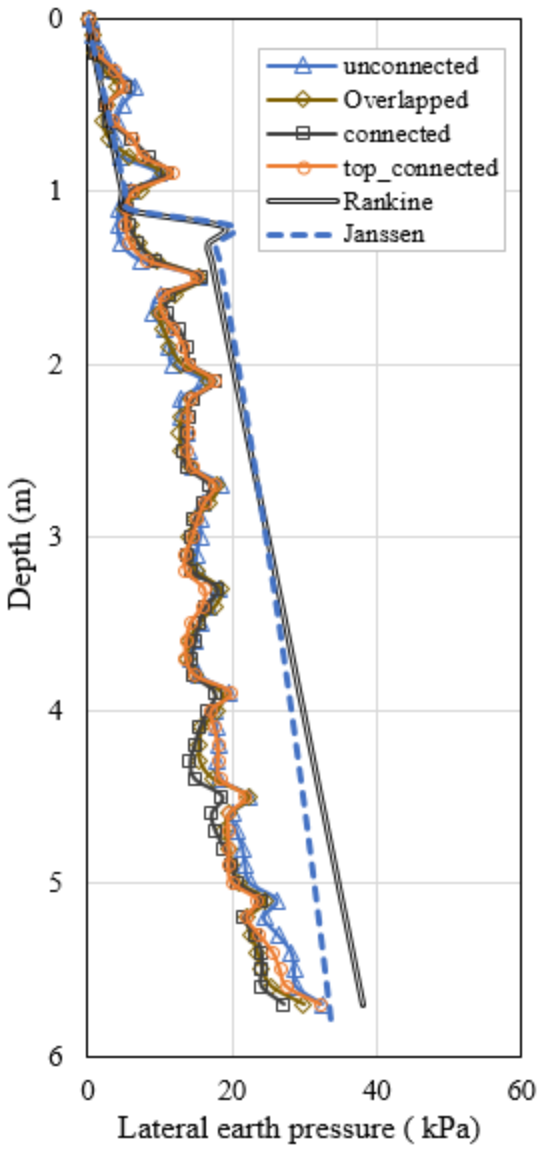

Figure 7.17 Effect of reinforcement rear connection on lateral earth pressure distribution on the wall facing under the applied footing pressure of 100 kPa

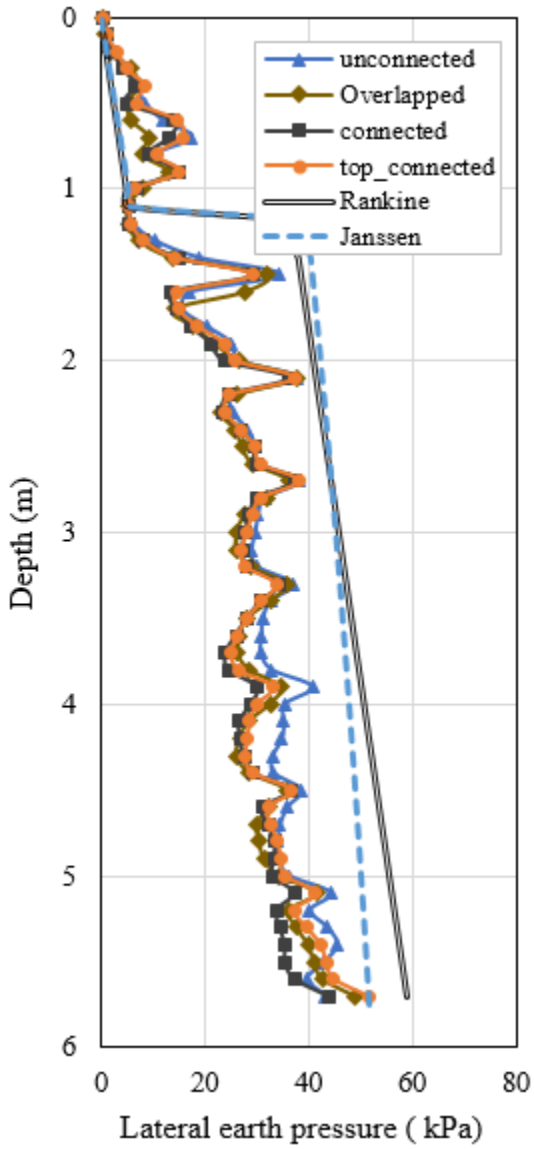

Figure 7.18 Effect of reinforcement rear connection on lateral earth pressure distribution on the wall facing under the applied footing pressure of 300 kPa

Maximum strain of reinforcement layers

Figure 7.19 shows the effect of reinforcement rear connection on the maximum strains of each reinforcement layer under the applied footing pressures of 100 kPa and 300 kPa. This figure shows that the maximum strain at each reinforcement layer increased with the increase of the applied footing pressure. The maximum strains in the reinforcement were in the range of 0.13% to 1.2%, 0.06% to 0.6 %, 0.06% to 0.7 %, and 0.06% to 0.7%, under the applied footing pressures of 100 kPa for the free, fixed, top-fixed, and overlapped cases, respectively. Similarly, the maximum strains in the reinforcement were in the range 0.2% to 3.9%, 0.2% to 1.95%, 0.15% to 2.1 %, and 0.2% to1.95%, under the applied footing pressure of 300 kPa respectively for the unconnected, connected, top_connected, and overlapped cases. In addition, the maximum strains of the reinforcement layers in all the cases where had the reinforcement connected to the stable medium were almost the same under both the applied footing pressures of 100 and 300 kPa. In other words, connecting all of the reinforcement layers to the stable medium (i.e., the connected case) had an insignificant effect on the value of the maximum strain of the reinforcement layers compared to the case in which only the two uppermost layers of the reinforcement were connected to the stable medium (i.e., the top_connected case).

Figure 7.19 also shows that connection of the reinforcement layers to the stable medium resulted in a large decrease in the maximum strains in all the reinforcement layers. For example, the maximum reinforcement strain at the wall height of 5 m in the baseline case was approximately 1.2% under the applied footing pressure of 100 kPa, while the maximum strain of the reinforcement in the connected case was approximately 0.6% at the same wall height and applied footing pressure. The difference became larger under the applied footing pressure of 300 kPa.

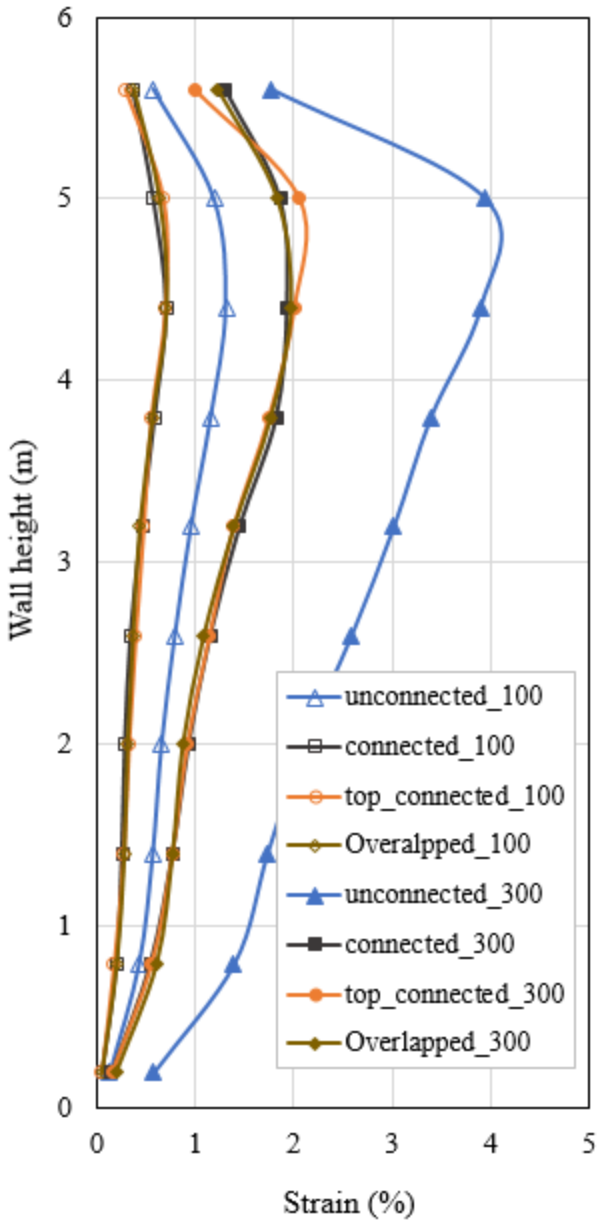

Figure 7.19 Effect of reinforcement rear connection on maximum strain of the reinforcement layers

7.2.3 Effect of footing size

This section presents the effect of the footing size on the performance of GRR walls with limited fill space subjected to footing loading. Three different footing sizes of 1.2 (i.e., the baseline case), 1.6, and 0.8 m were investigated. The terms “1.2m”, “1.6m” and “0.8m” used in the texts and legends of the figures are referred to as the baseline case and the cases where the footing sizes were 1.6, and 0.8 m, respectively.

Lateral wall facing displacement

Figure 7.20 shows the effect of the footing size (footing width) on the lateral wall facing displacement along the wall height under footing loading. As shown in Figure 7.20, the wall facing displacements in all the cases increased with the increase of the applied footing pressure. The displacements of the wall facing also increased with the wall height until reaching the maximum values and then decreased with the wall height to the top of the wall in all the cases. In the case where the footing size was 1.6 m (i.e., the “1.6m” case) the maximum wall facing displacement occurred approximately at the wall heights of 4.5 m and 4.8 m under the applied footing pressures of 100 and 300 kPa, respectively. Similarly, in the case where the footing size was of 0.8 m (i.e., the “0.8m” case), the maximum wall facing displacements occurred approximately at the wall heights of 5.0 and 5.5 m, respectively under the applied footing pressures of 100 and 300 kPa. In other words, the increase of the applied footing pressure from 100 to 300 kPa resulted in the change of the location of the maximum wall facing displacement in the both cases (i.e., the “1.6m” case and the “0.8m” case).

Figure 7.20 also shows that the increase of the footing size from 1.2 to 1.6 m had no significant effect on the displacements of the wall facing under the applied footing pressure of

100 kPa. However, the increase of the footing size from 1.2 to 1.6 m resulted in slightly larger wall facing displacement than that in the baseline case when the applied footing pressure of 300 kPa was applied. For example, the maximum displacement of the wall facing was approximately 136 mm in the "1.6m" case under the applied footing pressure of 300 kPa compared to that of the baseline case (i.e., 125 mm) under the same applied footing pressure.

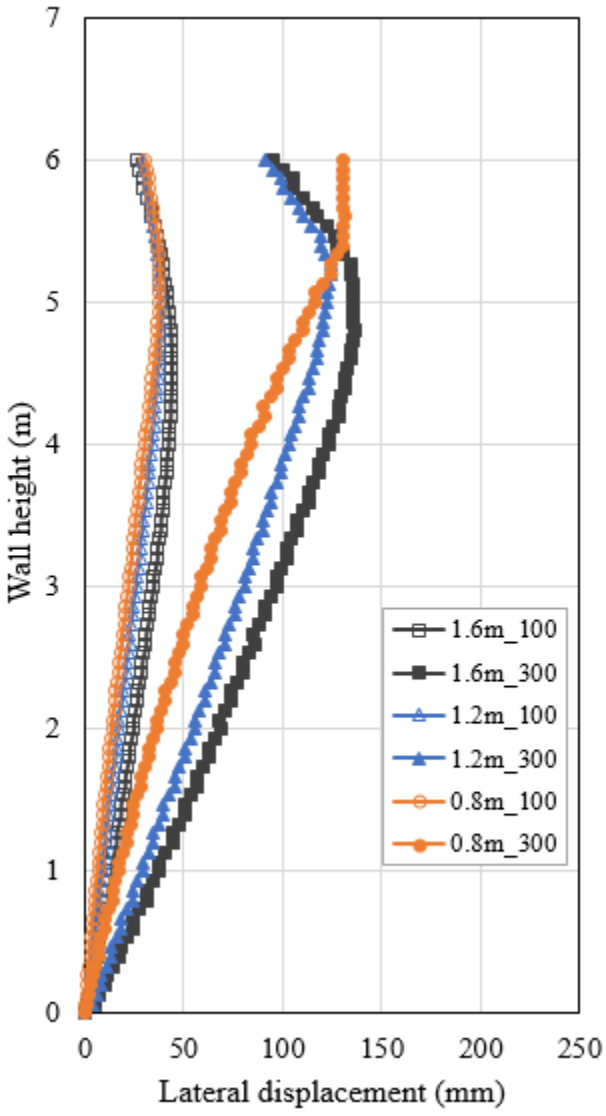

Figure 7.20 Effect of footing size on lateral wall facing displacement versus wall height

Similarly, the reduction of the footing size from 1.2 to 0.8 m had no significant effect on the wall facing displacements under the applied footing pressure of 100 kPa. However, the reduction of the footing size from 1.2 to 0.8 m generally resulted in smaller wall facing displacements than those of the baseline case when the applied footing pressure of 300 kPa was applied. In addition, the reduction of the footing size from 1.2 to 0.8 m resulted in the change of the profile of the wall facing displacement. In the "0.8m" case, the wall facing displacement did not decrease with the wall height after reaching the maximum value as occurred in the two other cases.

Settlement of footing

Figure 7.21 shows the effect of the footing size on the settlement of the footing. This figure shows that the increase of the footing size from 1.2 to 1.6 m had a significant effect on the settlement of the footing under all the applied loads. For example, the case that had the footing size of 1.6 m had approximately 160 mm footing settlement at the applied footing pressure of 300 kPa, while the baseline case had 215 mm footing settlement at the same applied footing pressure. Similarly, the reduction in the footing size from 1.2 to 0.8 m had a considerable effect on the settlement of the footing under all the applied loads and resulted in excessive footing settlement when the footing pressure was higher than 200 kPa compared to that of the baseline case. For example, the baseline case had approximately 130 mm footing settlement at the applied footing pressure of 200 kPa, while the footing settlement was 190 mm in the case where the footing size was 0.8 m at the same applied pressure. Consequently, the footing size has an significant effect on the settlement and bearing capacity of the applied footing.

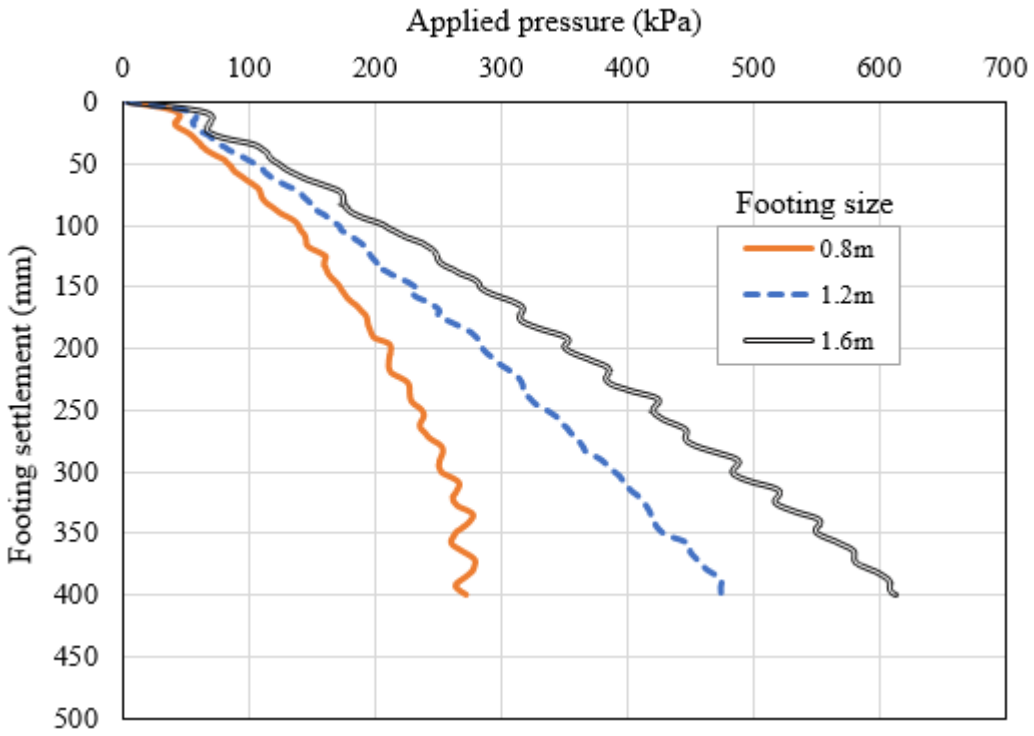

Figure 7.21 Effect of footing size on pressure-settlement curve of the footing

Vertical earth pressure distribution

Figures 7.22 and 7.23 show the effect of the footing size on the distribution of the vertical earth pressure under footing loading. Figures 7.22(a) and 7.23(a) show the distribution of the vertical earth pressure on the wall facing while Figures 7.22(b) and 7.23(b) show the distribution of the vertical earth pressures on the centerline of the wall footing under the applied footing pressures of 100 and 300 kPa, respectively. For the comparison purpose, the vertical earth pressures calculated using Equation (7.2) were added in Figures 7.22 and 7.23.

Figures 7.22(a) and 7.23(a) show that the vertical earth pressures on the wall facing in all the three cases increased with the increase of the depth under the applied footing pressure, and

the distribution of the vertical earth pressures had similar trends in all the three cases. In addition, Figures 7.22(b) and 7.23(b) show that the vertical earth pressures along the centerline of the wall footing in all the three cases reached the maximum values near the top of the wall and then slightly decreased with the depth to a certain depth where the vertical earth pressures became relatively constant to the bottom of the wall.

In addition, Figures 7.22(a) and 7.23(a) show that the footing size had no considerable effect on the vertical earth pressures on the wall facing under the applied footing pressures of 100 kPa and 300 kPa. However, Figures 7.26(b) and 7.27(b) show that the increase of the footing size from 1.2 to 1.6 m resulted in higher vertical earth pressures on the center of the footing wall compared to those of the baseline case under the applied footing pressures of 100 kPa and 300 KPa. Similarly, the reduction of the footing size from 1.2 to 0.8 m resulted in lower vertical earth pressure along the centerline of the wall footing than that of the baseline case under the applied footing pressures of 100 and 300 KPa.

Figures 7.22 and 7.23 also show that the vertical earth pressures on the wall facing in all the cases were generally lower than those calculated using Equation (7.2). However, the vertical earth pressures along the centerline of the wall footing were generally higher than those calculated using Equation (7.2).

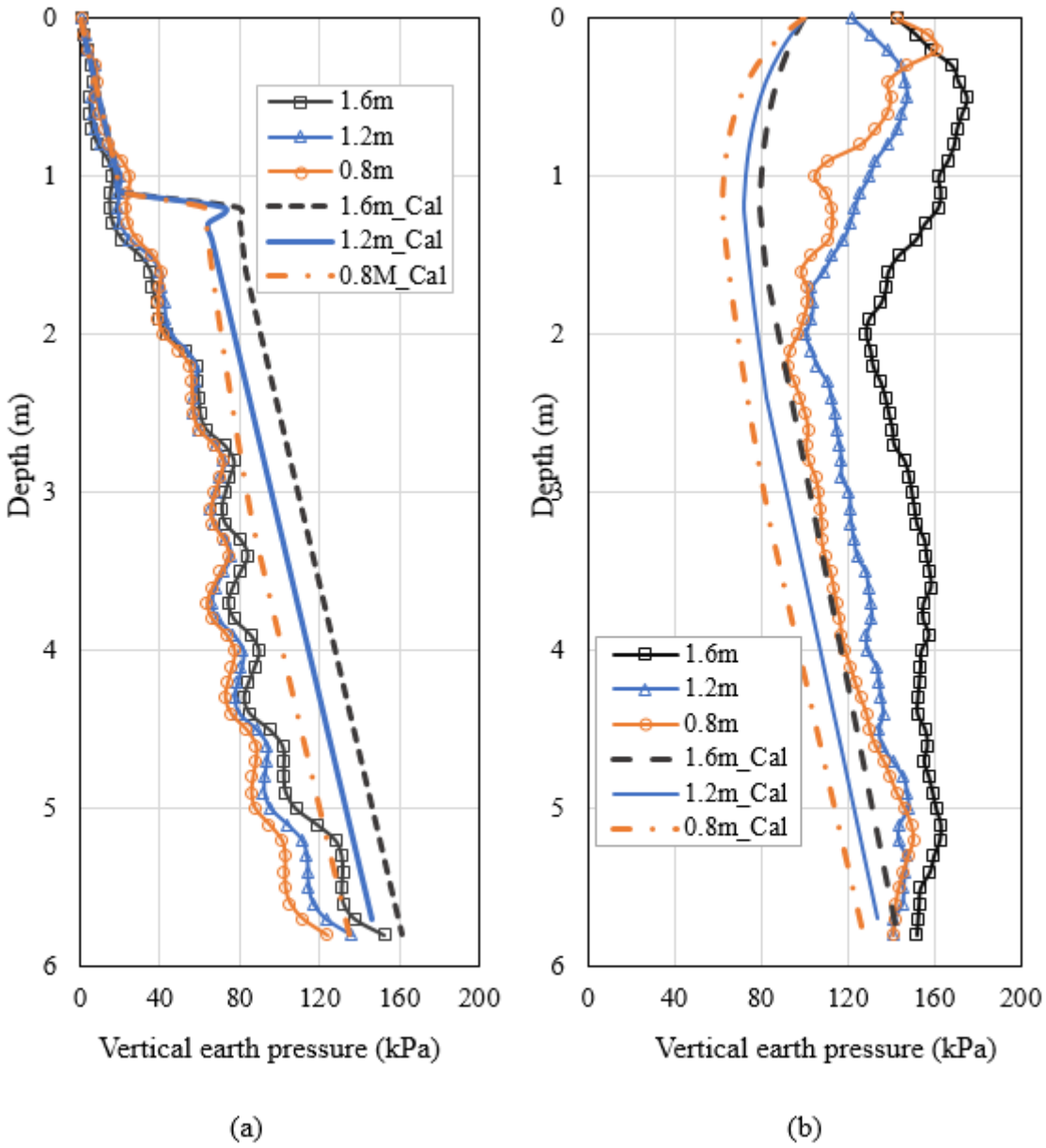

Figure 7.22 Effect of footing size on vertical earth pressure distribution under the applied footing pressure of 100 kPa: (a) on the wall facing and (b) along the centerline of the wall footing

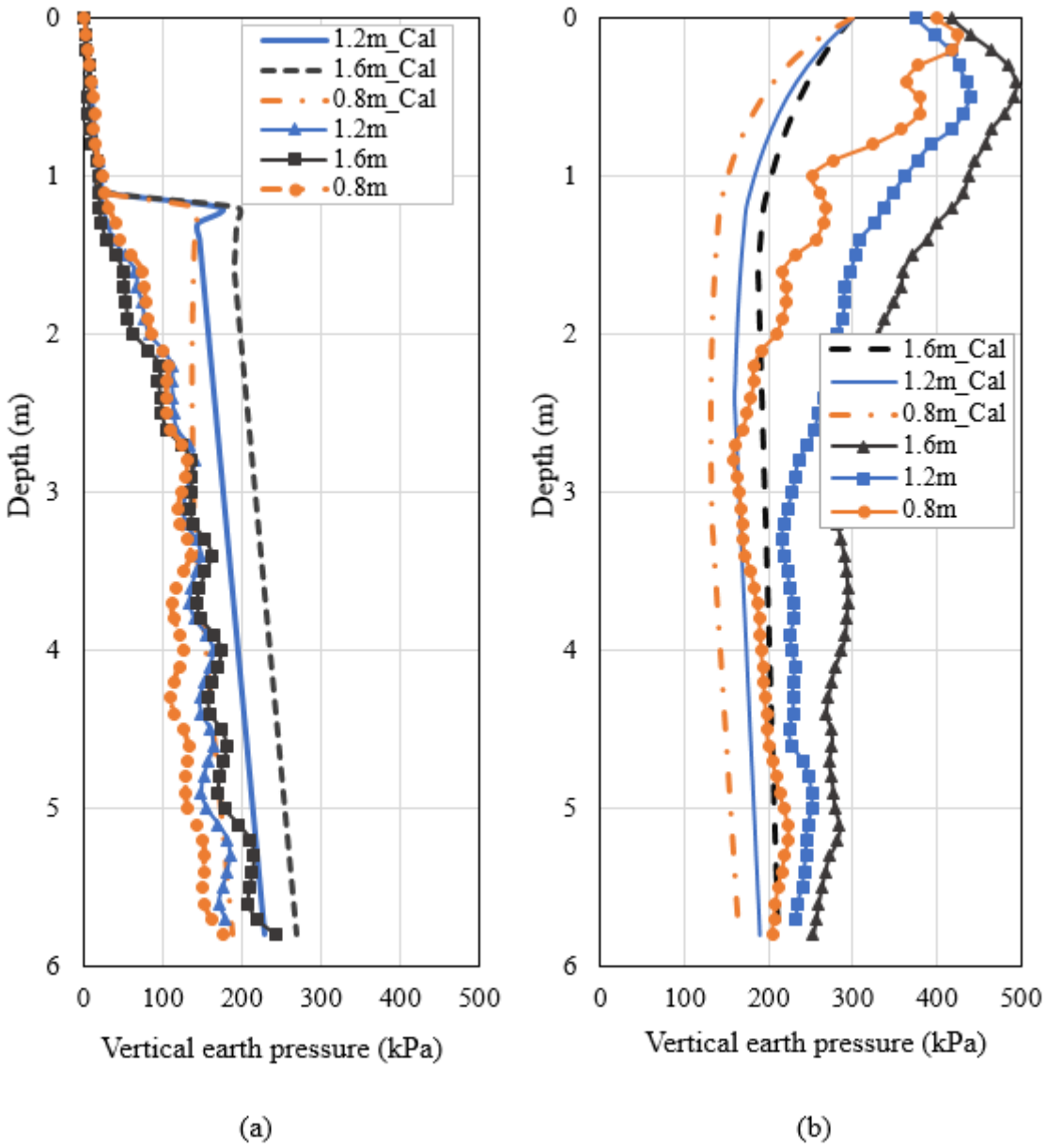

Figure 7.23 Effect of footing size on vertical earth pressure distribution under the applied footing pressure of 300 kPa: (a) on the wall facing and (b) along the centerline of the wall footing

Lateral earth pressure distribution

Figures 7.24 and 7.25 show the effect of the footing size on the distribution of the lateral earth on the wall facing under footing loading. For the comparison purpose, the lateral earth pressures calculated using Equations (7.3) and (7.4) were added in Figures 7.24 and 7.25. Figures 7.24(a) and 7.25(a) compares the lateral earth pressures computed by numerical analysis with those calculated using Equation (7.3) under the applied footing load of 100 kPa and 300 kPa, respectively. Figures 7.24(b) and 7.25(b) compares the lateral earth pressures computed by numerical analysis with those calculated using Equation (7.4) under the applied footing load of 100 kPa and 300 kPa, respectively.

Figures 7.24(a) and 7.25(a) show that the lateral earth pressures on the wall facing in all the cases increased with the increase of the depth and had similar trends under both the applied footing pressure. Figures 7.24 and 7.25 also show that the footing size had insignificant effect on the distribution of the lateral earth pressures on the wall facing under the applied footing pressure of 100 kPa. However, the footing size showed some effect on the distribution of the lateral earth pressures on the wall facing under higher applied footing load (i.e., at the applied footing pressure of 300 kPa).

In addition, the lateral earth pressures on the wall facing in all the three cases were lower than those calculated using Equations (7.3) and (7.4). However, the lateral earth pressures calculated using Equation (7.4) were lower than those calculated using Equation (7.3).

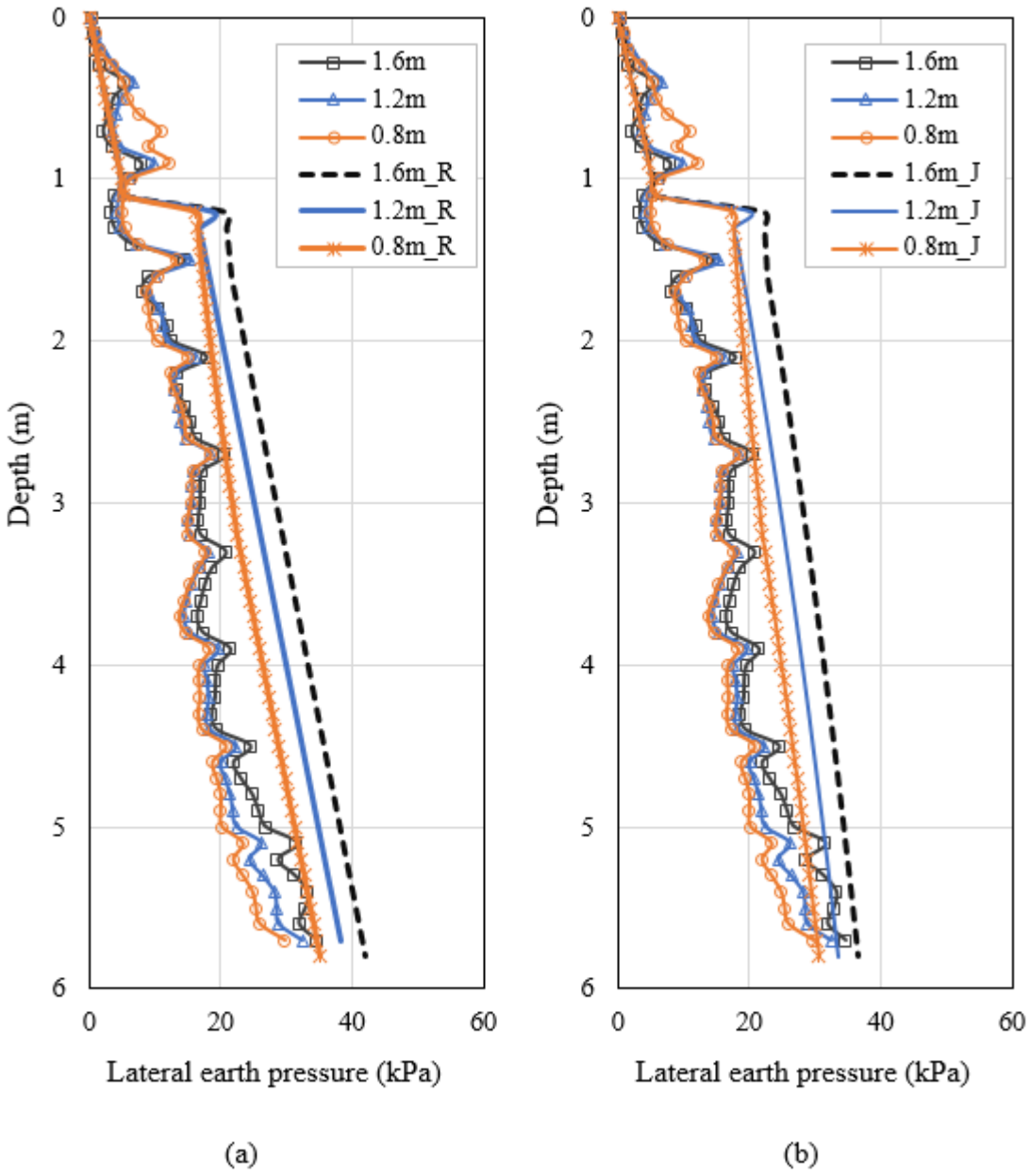

Figure 7.24 Effect of footing size on lateral earth pressure distribution on the wall facing under the applied footing pressure of 100 kPa: (a) Numerical versus calculated results using the Rankine theory and (b) numerical versus calculated results using Janssen's equation

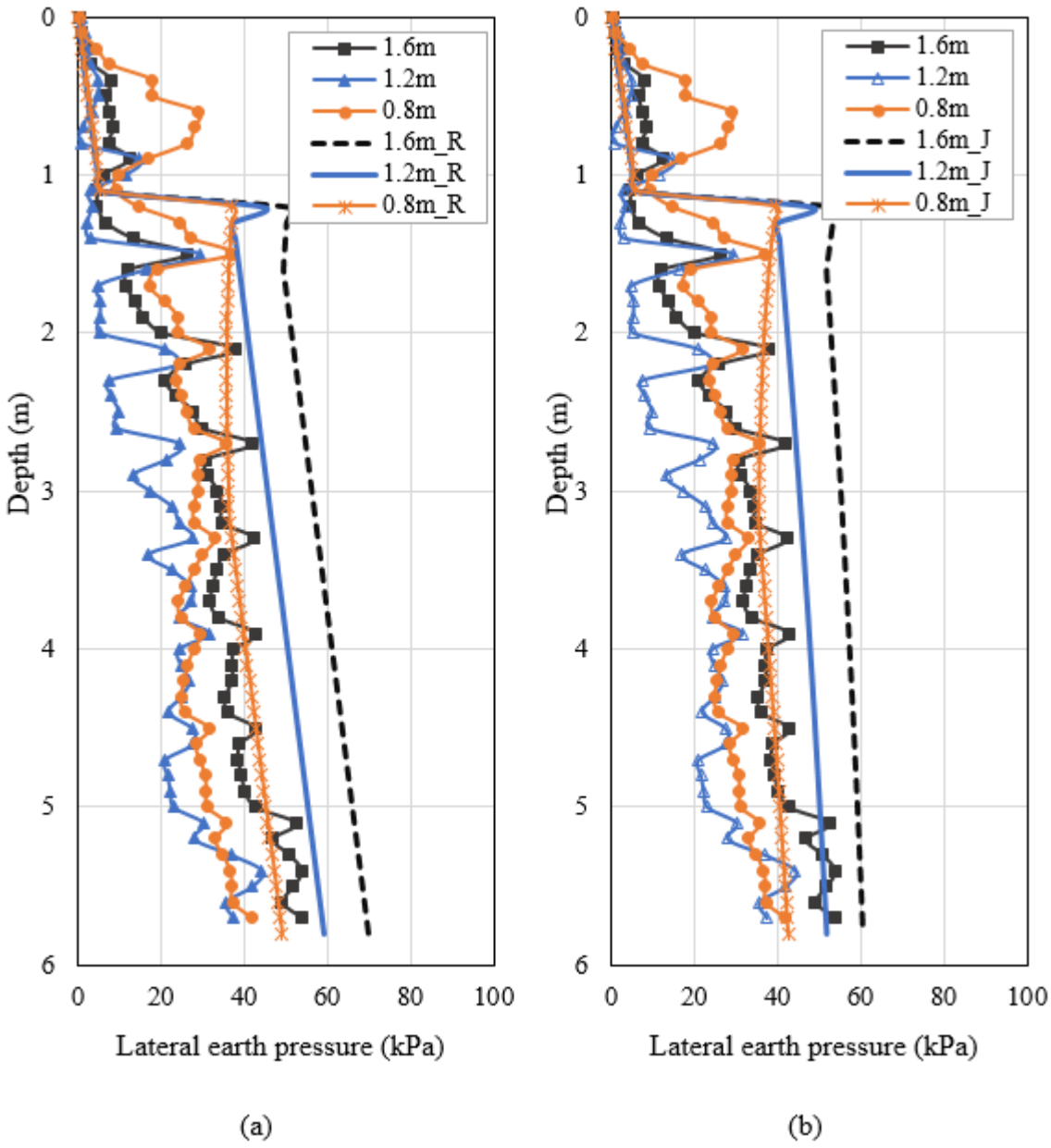

Figure 7.25 Effect of footing size on lateral earth pressure distribution on the wall facing under the applied footing pressure of 300 kPa: (a) Numerical versus calculated results using the Rankine theory and (b) numerical versus calculated results using Janssen's equation

Maximum strain of reinforcement layers

Figure 7.26 shows the effect of the footing size on the maximum strains of each reinforcement layer under the applied footing pressures of 100 kPa and 300 kPa. This figure shows that the profiles of the maximum strains of the reinforcement layers in all the cases were almost the same. In addition, the value of the maximum strain increased with the increase of the wall height until reaching the largest values and then decreased with the wall height to the top of the wall.

Figure 7.26 shows that the increase of the footing size from 1.2 to 1.6 m resulted in an increase in the maximum strains in all the reinforcement layers under the applied footing pressure of 100 kPa. For example, the maximum reinforcement strain at the wall height of 4.4 m in the baseline case was approximately 1.3 % when the footing pressure of 100 kPa was applied, while the maximum reinforcement strain in the case where the footing size was 1.6 m was approximately 1.65% at the same wall height and applied footing pressure. However, the increase of the footing size from 1.2 to 1.6 m resulted in a decrease in the maximum strains in all the reinforcement layers when the applied footing pressure of 300 kPa was used. For example, the maximum reinforcement strain at the wall height of 4.4 m in the case where the footing size was 1.6 m was about 2.8% at the applied footing pressure of 300 kPa. However, the maximum reinforcement strain in the baseline case was about 3.9 % under at the same height and loading condition.

In addition, the reduction of the footing size from 1.2 to 0.8 m had no considerable effect on the maximum strains in all the reinforcement layers at the applied footing pressure of 100 kPa. However, the decrease of the footing size from 1.2 to 0.8 m resulted in a considerable decrease in the maximum strains in almost all the reinforcement layers when the footing pressure

of 300 kPa was applied. For example, the maximum reinforcement strain at the wall height of 4.4 m in the case where the footing size was 0.8 m was about 3.0% at the applied footing pressure of 300 kPa.

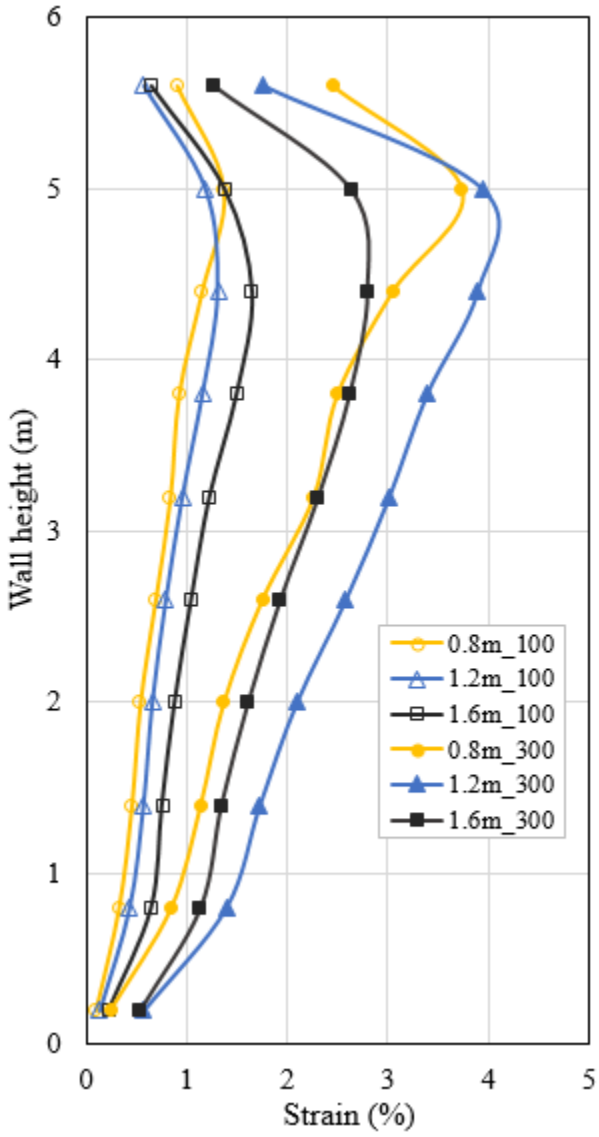

Figure 7.26 Effect of footing size on maximum strain of the reinforcement layers

7.2.4 Effect of footing offset distance

This section presents the effect of the footing offset distance (i.e., the distance from the edge of the footing to the back of the wall facing) on the performance of GRR walls with limited fill space subjected to footing loading. Three different footing offset distances, 0.6 (baseline case), 0.9, and 0.3 m were investigated. The terms “0.1H”, “0.15H” and “0.05H” used in the texts and legends of the figures are referred to as the baseline case and the cases in which the footing offset distances were 0.9 and 0.3 m, respectively.

Lateral wall facing displacement

Figure 7.27 shows the effect of the footing offset distance on the displacement of the lateral wall facing along the wall height under footing loading. This figure shows that the wall facing displacements in all the cases increased with the increase of the applied footing pressure. The displacements of the wall facing also increased with the wall height until reaching the maximum values and then decreased with the wall height to the top of the walls. In the “0.15H” case the maximum wall facing displacement occurred approximately at the wall height of 4.4 m under the applied footing pressures of 100 and 300 kPa as well. Similarly, in the “0.05H” case the maximum wall facing displacement occurred approximately at the wall heights of 5.2 and 5.4 m under the applied footing pressures of 100 and 300 kPa, respectively. In other words, the increase of the applied footing pressure from 100 to 300 kPa resulted in the change of the location of the maximum wall facing displacement in the case where the footing offset distance was 0.3 m.

Figure 7.27 also shows that the increase of the footing offset distance from 0.6 to 0.9 m resulted in smaller wall facing displacement in the portion higher than the mid-height of the wall

compared to that of the baseline case under the applied footing pressure of 100 kPa. In addition, the increase of the footing offset distance from 0.6 to 0.9 m had more effect on the wall facing displacement when the applied footing pressure was 300 kPa. For example, the maximum displacement of the wall facing was approximately 125 mm in the baseline case under the applied footing pressure of 300 kPa, while the maximum displacement of the wall facing was approximately 84 mm in the "0.15H" case under the same applied footing pressure.

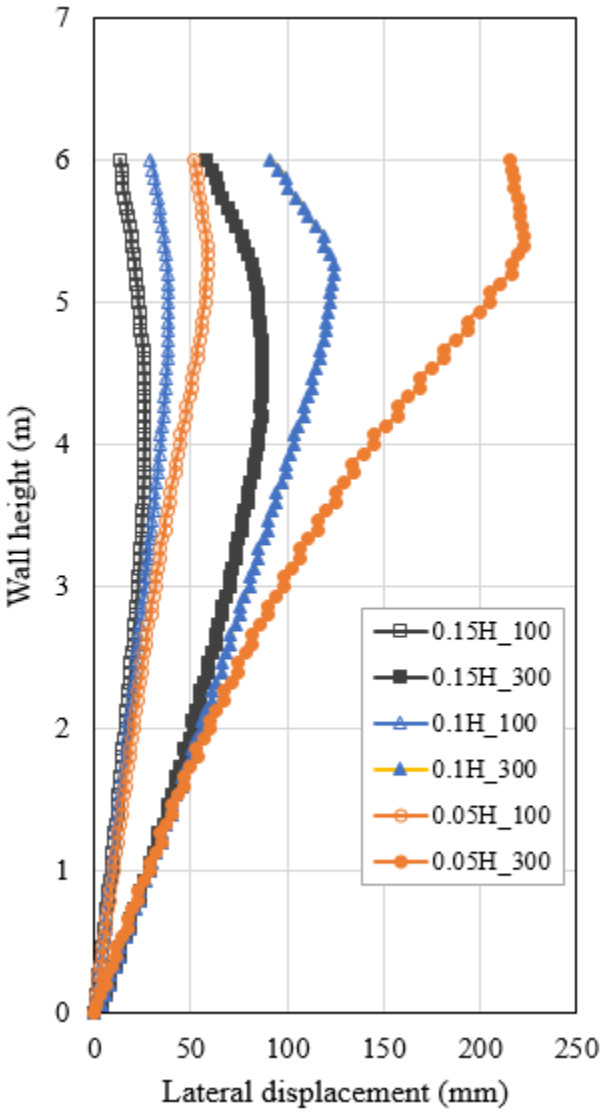

Figure 7.27 Effect of footing offset distance on lateral wall facing displacement versus wall height

Similarly, Figure 7.27 shows that the reduction in the footing offset distance from 0.6 to 0.3 m resulted in larger wall facing displacement in the portion higher than the mid-height of the wall compared to that of the baseline case under the applied footing pressure of 100 kPa. In addition, the reduction of the footing offset distance from 0.6 to 0.3 m resulted in a substantial increase in the displacement of the wall facing when the applied footing pressure was 300 kPa. The reduction of the footing size from 1.2 to 0.8 m also resulted in the change in the profile of the displacement.

Settlement of footing

Figure 7.28 shows the effect of the footing offset distance on the settlement of the footing. This figure shows the pressure-settlement curves of the footing for the baseline and the cases where the footing offset distances were 0.9 and 0.3 m.

Figure 7.28 indicates that the increase of the footing offset distance from 0.6 (i.e., the "0.1H" case) to 0.9 m (i.e., the "0.15H" case) slightly reduced the settlement of the footing. However, the reduction in the footing offset distance from 0.6 to 0.3 m (i.e., the "0.05H" case) resulted in larger settlement of the footing compared to that of the baseline case under all the applied footing pressures. For example, the baseline case had approximately 310 mm footing settlement under the applied footing pressure of 400 kPa, while the "0.05H" case had 390 mm footing settlement at the same applied footing pressure.

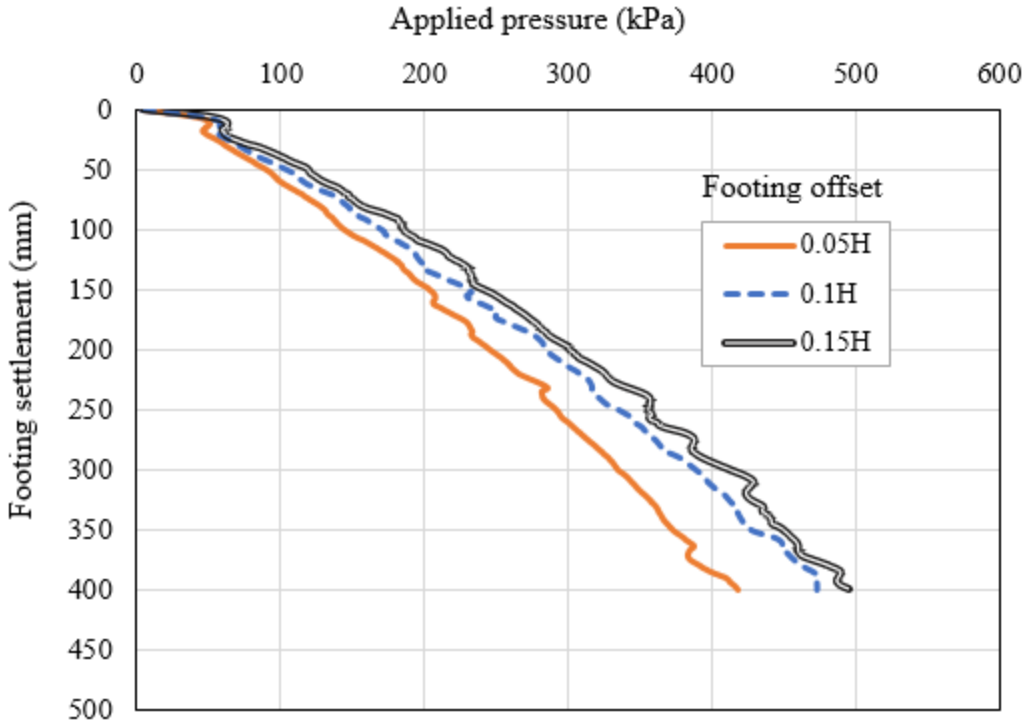

Figure 7.28 Effect of footing offset distance on pressure-settlement curve of the footing

Vertical earth pressure distribution

Figures 7.29 and 7.30 show the effect of the footing offset distance on the distribution of the vertical earth pressure under footing loading. Figures 7.29(a) and 7.30 (a) show the distributions of the vertical earth pressures on the wall facing under the applied footing pressures of 100 and 300 kPa, respectively. Also, Figures 7.29(b) and 7.30(b) show the distributions of the vertical earth pressures along the centerline of the wall footing, respectively under the applied footing pressures of 100 and 300 kPa. For the comparison purpose, the vertical earth pressures calculated using Equation (7.2) were added in Figures 7.29 and 30.

Figures 7.29(a) and 7.30 (a) show that the vertical earth pressures on the wall facing under the applied footing pressures in all the cases increased with the increase of the depth. In addition, Figures 7.29(b) and 7.30(b) show that the vertical earth pressures along the centerline

of the wall footing under the applied footing pressures of 100 and 300 kPa in all the cases reached the maximum values near the top of the wall and then slightly decreased with the depth to a certain depth. After that point, the vertical earth pressures became relatively constant to the bottom of the wall.

Figures 7.20(a) and 7.30(a) also show that the reduction of the footing offset distance from 0.6 to 0.3 m resulted in a slightly higher vertical earth pressures on the wall facing under both the applied footing pressure compared to that of the baseline case under the same loading condition. Furthermore, the increase of the footing offset distance from 0.6 to 0.9 m resulted in lower vertical earth pressures on the wall facing under the applied footing pressure of 100 kPa. However, the increase of the applied footing pressure form 100 to 300 kPa in the "0.15H" case resulted in a higher vertical earth pressure than that of the baseline case as shown in Figure 7.30 (a). Figures 7.29(b) and 7.30(b) also show that the footing offset distance had no considerable effect on the distribution of the vertical earth pressure along the centerline of the wall footing.

In addition, the vertical earth pressures on the wall facing in all the cases were generally lower than those calculated using Equation (7.2). However, the vertical earth pressures along the centerline of the wall footing were generally higher than those calculated using Equation (7.2).

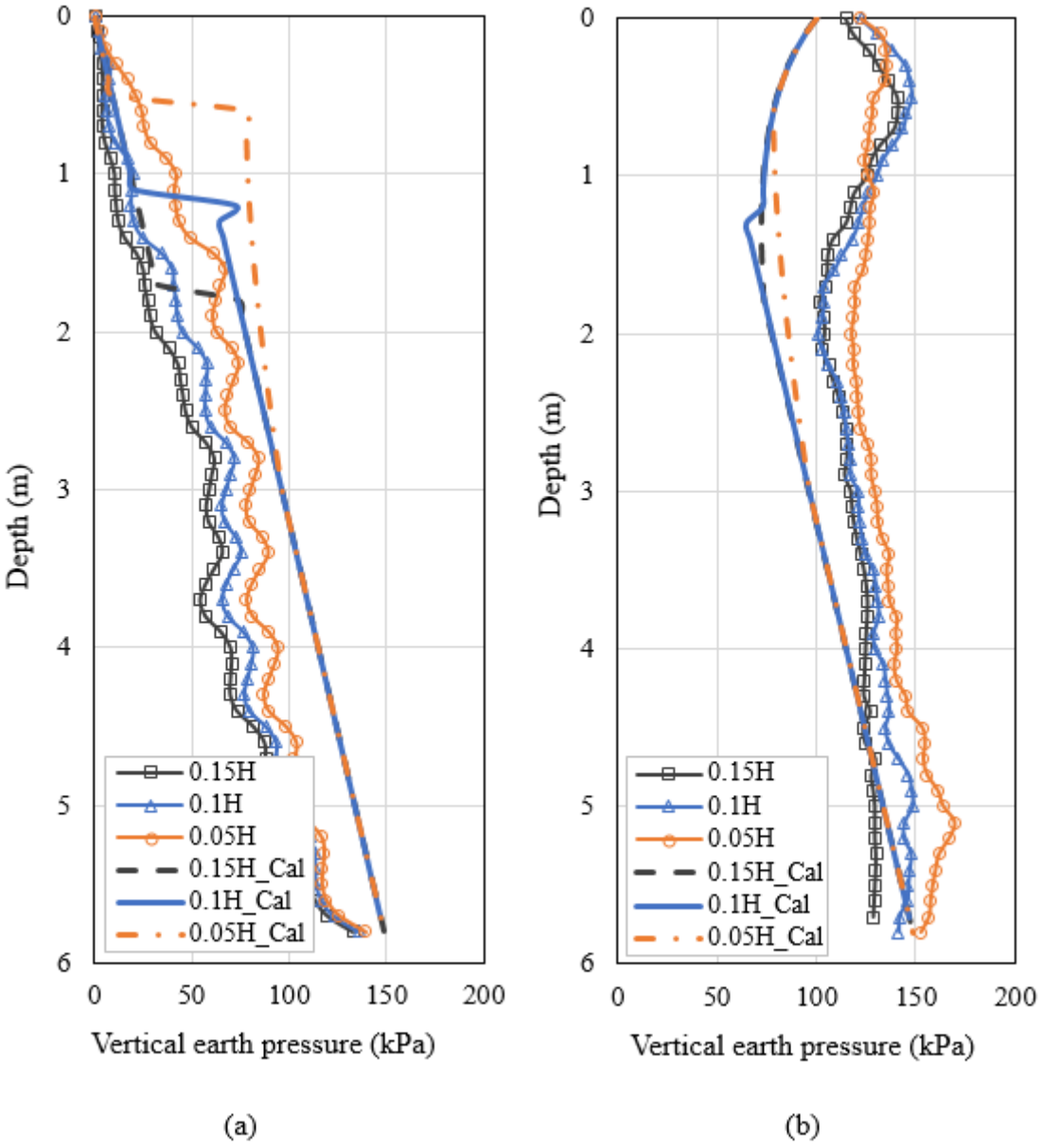

Figure 7.29 Effect of footing offset distance on vertical earth pressure distribution under the applied footing pressure of 100 kPa: (a) on the wall facing and (b) along the centerline of the footing

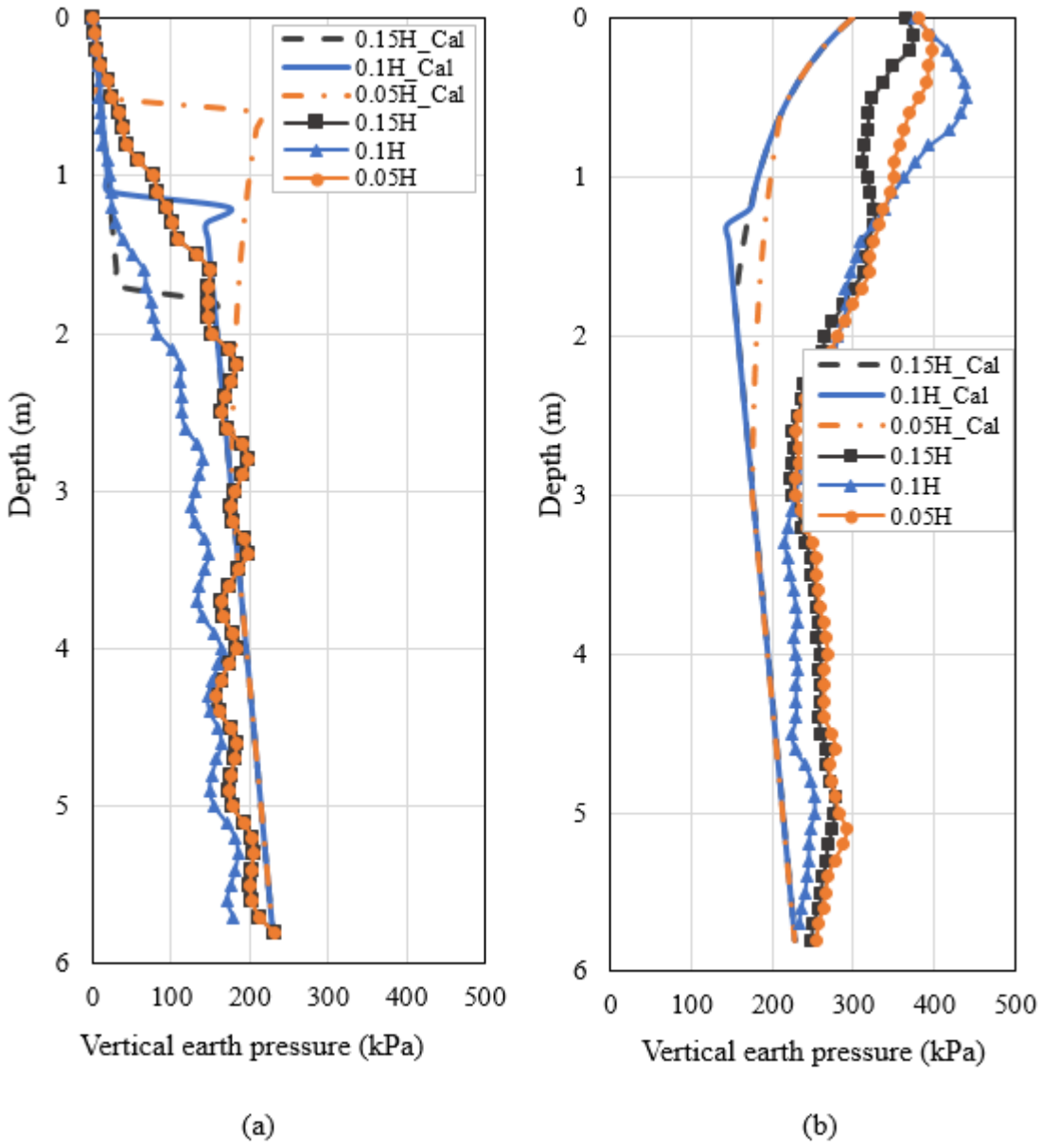

Figure 7.30 Effect of footing offset distance on vertical earth pressure distribution under the applied footing pressure of 300 kPa: (a) on the wall facing and (b) along the centerline of the footing

Lateral earth pressure distribution

Figures 7.31 and 7.32 show the effect of the footing offset distance on the distribution of the lateral earth pressure on the wall facing under the applied footing pressure of 100 kPa and 300 kPa, respectively. For the comparison purpose, the lateral earth pressures calculated using Equations (7.3) and (7.4) were added in Figures 7.31 and 7.32. Figures 7.31(a) and 7.32(a) compares the lateral earth pressures computed by numerical analysis with those calculated using Equation (7.3) under the applied footing load of 100 kPa and 300 kPa, respectively. Figures 7.31(b) and 7.32(b) compares the lateral earth pressures computed by numerical analysis with those calculated using Equation (7.4) under the applied footing load of 100 kPa and 300 kPa, respectively.

Figures 7.31 and 7.32 show that the lateral earth pressures on the wall facing in all the cases increased with the increase of the depth under both the applied footing pressure. These figures indicates that the footing offset distance had a slight effect on the lateral earth pressures on the wall facing under both the applied footing pressure.

In addition, the lateral earth pressures on the wall facing in all the three cases were lower than those calculated using Equation (7.3) and (7.4) as well. However, the lateral earth pressures calculated using Equation (7.4) were agreed better (i.e., closer) with the computed lateral earth pressures by numerical analysis as compared to those calculated using Equation (7.3).

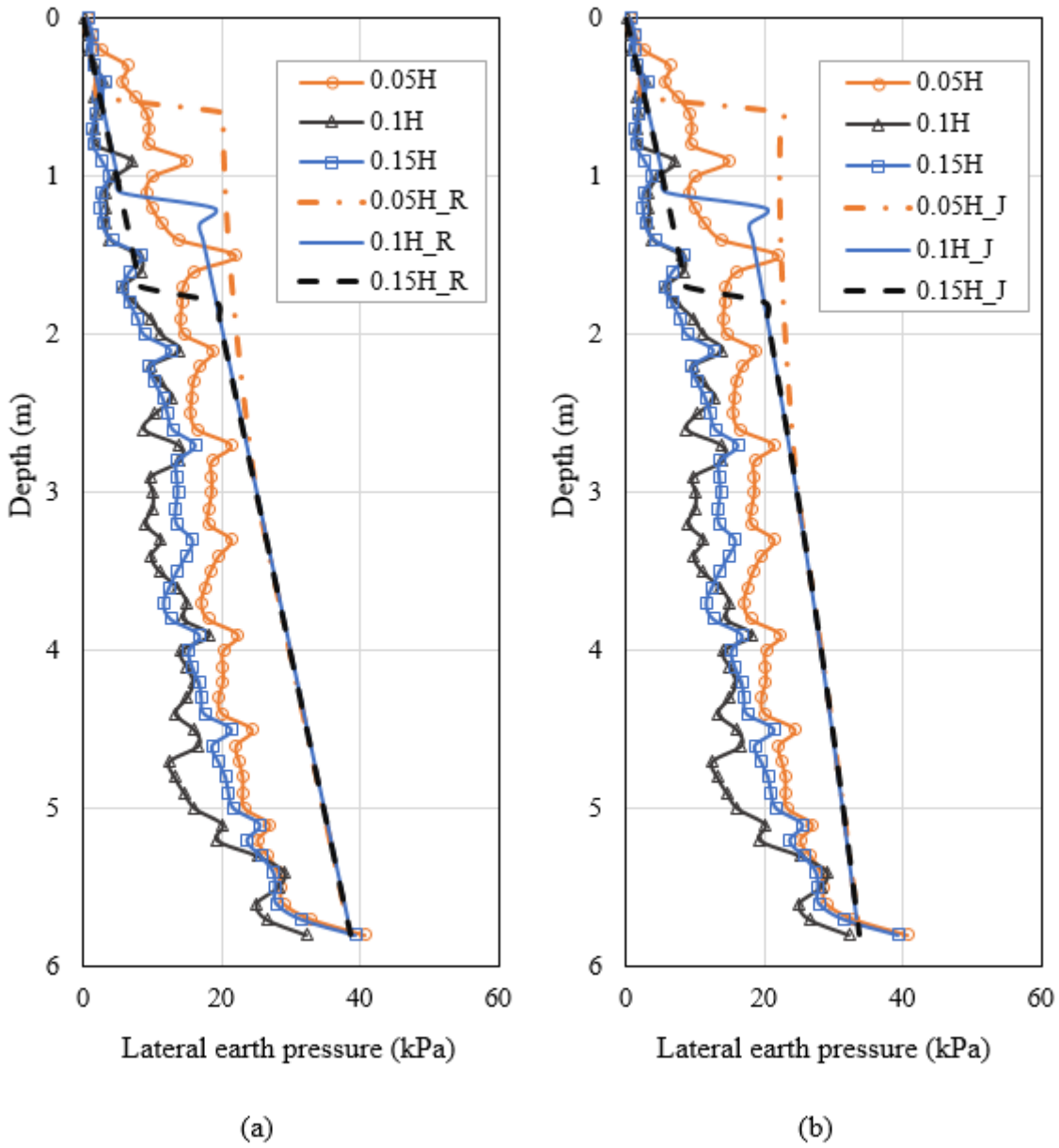

Figure 7.31 Effect of footing offset distance on lateral earth pressure distribution on the wall facing under the applied footing pressure of 100 kPa: (a) Numerical versus calculated results using the Rankine theory and (b) numerical versus calculated results using Janssen's equation

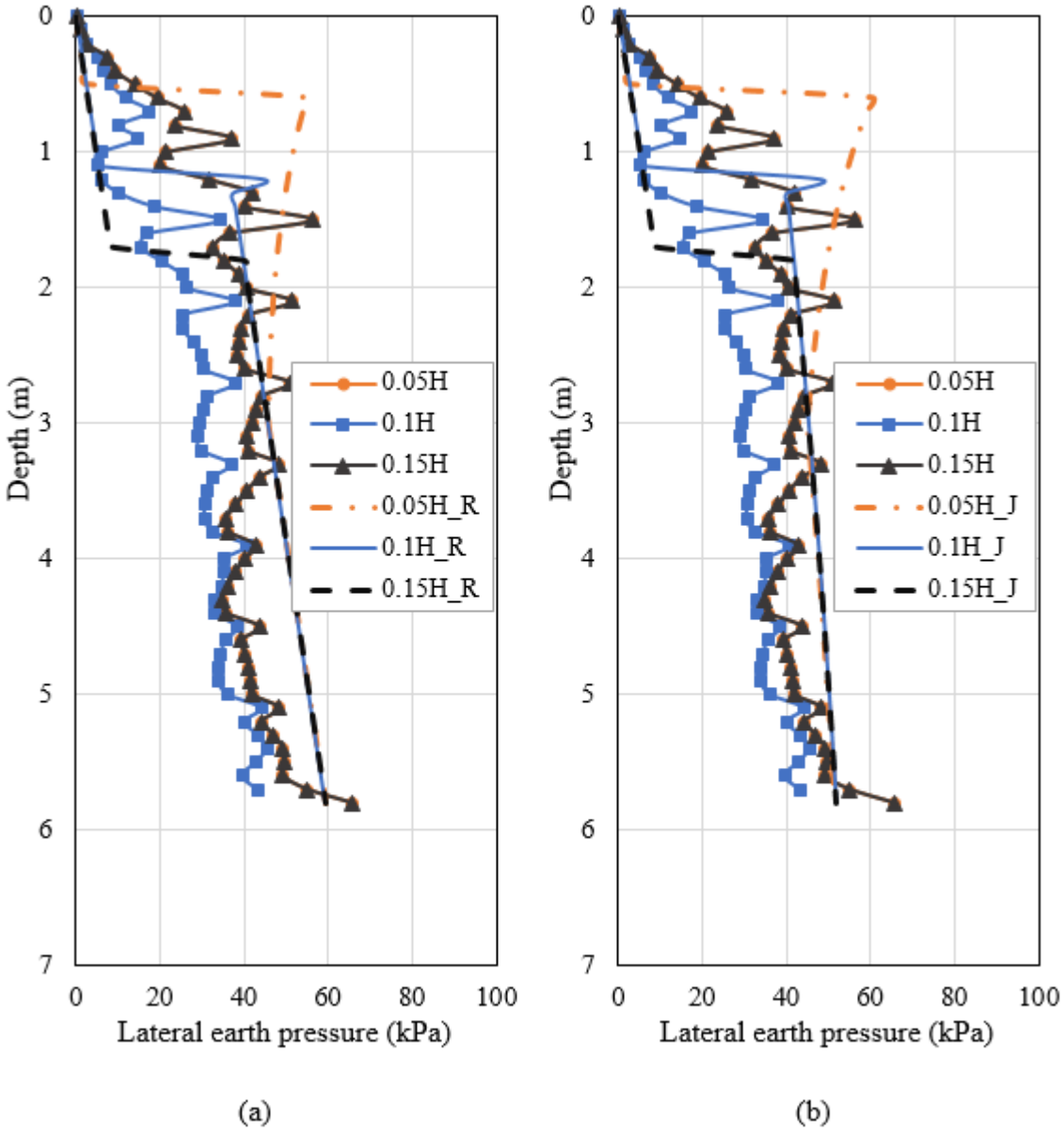

Figure 7.32 Effect of footing offset distance on lateral earth pressure distribution on the wall facing under the applied footing pressure of 300 kPa: (a) Numerical versus calculated results using the Rankine theory and (b) numerical versus calculated results using Janssen's equation

Maximum strain of reinforcement layers

Figure 7.33 shows the effect of the footing offset distance on the maximum strains of each reinforcement layer under the applied footing pressures of 100 and 300 kPa. Figure 7.32 shows that the increase of the footing offset distance from 0.6 to 0.9 m resulted in smaller maximum strains in all the reinforcement layers compared to those in the baseline case at the applied footing pressures of 100 and 300 kPa.

Similarly, the reduction of the footing offset distance from 0.6 to 0.3 m resulted in an increase in the maximum strains in all the reinforcement layers under the applied footing pressures of 100 and 300 kPa. For example, the maximum reinforcement strain in the case where the footing offset distance was 0.3 m (i.e., the "0.05H" case) was approximately 4.3% at the wall height of 4.4 m and the applied footing pressure of 300 kPa while the maximum strain of the reinforcement was 3.9% in the baseline case under the same conditions.

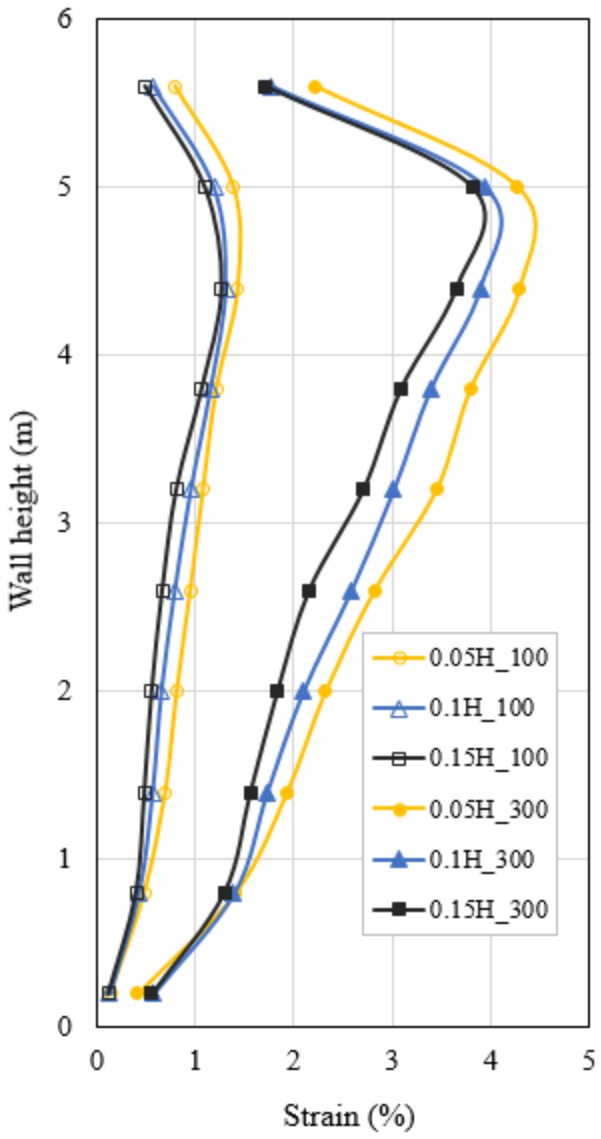

Figure 7.33 Effect of footing offset distance on maximum strain of the reinforcement layers

7.2.5 Effect of friction angle of backfill soil

This section presents the effect of the friction angle of the backfill soil on the performance of GRR walls with limited fill space. Two different friction angles $\phi = 38^o$ (baseline case) and $\phi = 34^o$ were investigated. The term "38" used in legends of the figures is referred to as the friction angle of the backfill soil in the baseline case while the term "34" is referred to as the case in which the friction angle of its backfill soil was 34^o.

Lateral wall facing displacement

Figure 7.34 shows the effect of the friction angle of the backfill soil on the displacement of the lateral wall facing under the applied footing loading. This figure shows that the reduction of the friction angle of the backfill soil from 38^o to 34^o resulted in a slightly larger wall facing displacement than that of the baseline case. For example, the maximum displacements of the wall facing were about 38 mm and 125 mm under the applied footing pressures of 100 and 300 kPa, respectively in the baseline case while in the case with the backfill soil friction angle of 34^o the maximum displacements of the wall facing were approximately 50 mm and 130 mm at the same loading conditions.

Settlement of footing

Figure 7.35 shows the effect of the friction angle of the backfill on the settlement of the footing. This figure shows the pressure-settlement curves of the load for the baseline case and the case where the friction angle of the backfill soil was 34^o. Figure 7.35 indicates that the reduction of the friction angle of the backfill soil from 38^o to 34^o resulted in larger settlement and lower bearing capacity of the footing compared to those of the baseline case. For example, the baseline

case had approximately 215 mm footing settlement at the applied footing pressure of 300 kPa, while the case with the soil friction angle of 34º had 305 mm footing settlement at the same applied pressure. Hence, the friction angle of the backfill soil had a considerable effect on the footing settlement and bearing capacity of the footing.

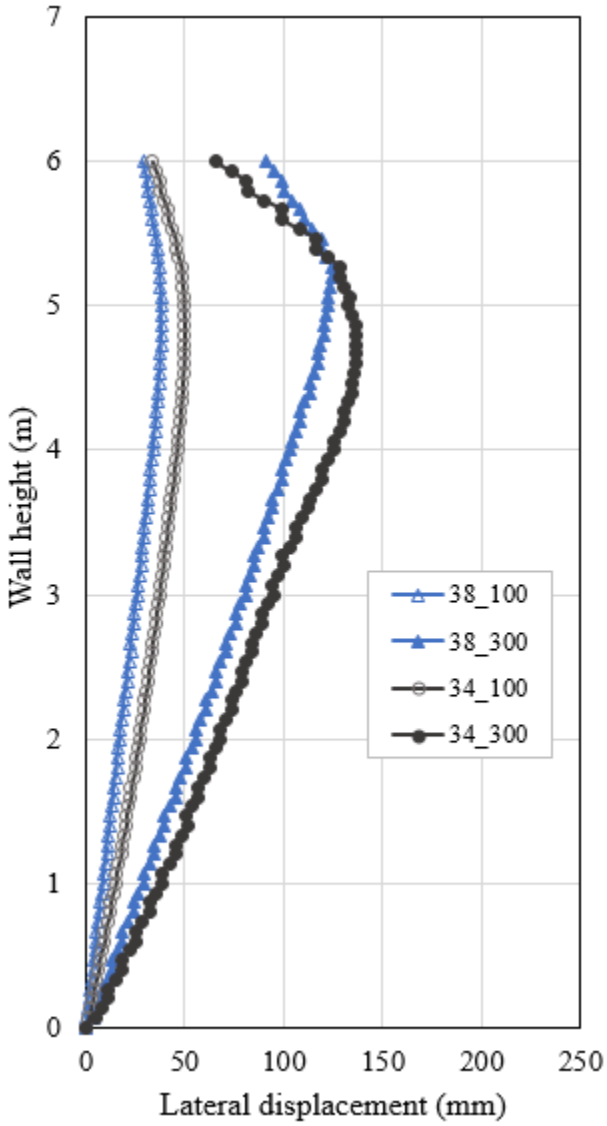

Figure 7.34 Effect of friction angle of backfill soil on lateral wall facing displacement versus wall height

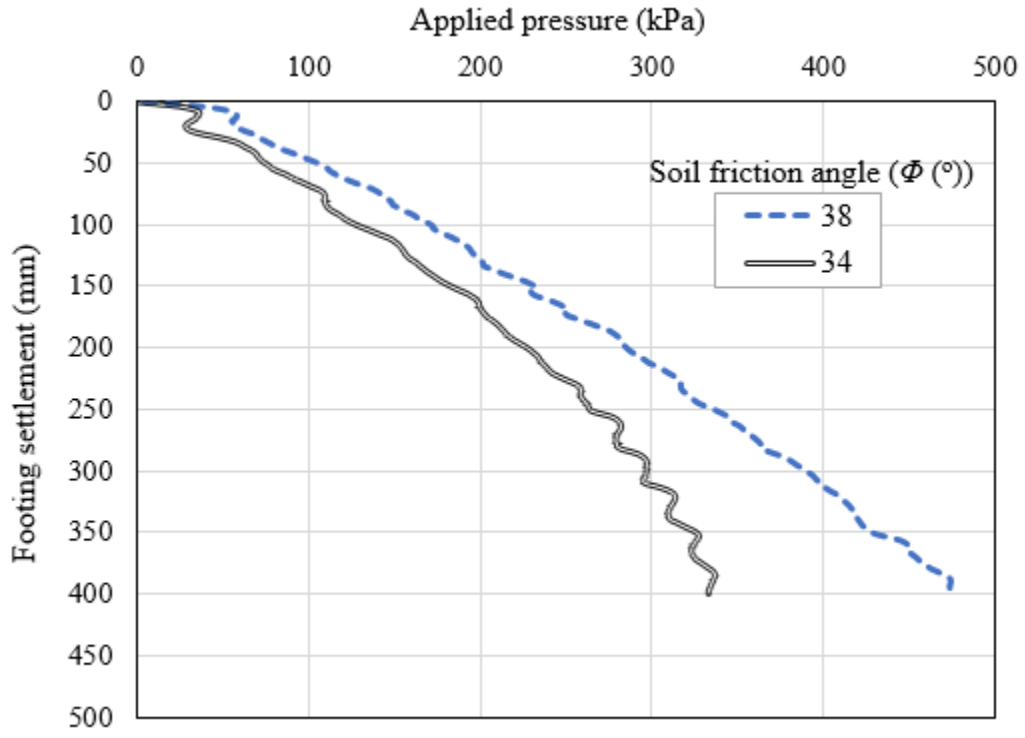

Figure 7.35 Effect of friction angle of backfill soil on pressure-settlement curve of the footing

Vertical earth pressure distribution

Figures 7.36 and 7.37 show the effect of the friction angle of the backfill soil on the distribution of the vertical earth pressure. Figure 7.36 shows the distributions of the vertical earth pressures on the wall facing and along the centerline of the wall footing under the applied footing pressure of 100 kPa. In addition, Figure 7.37 shows the distributions of the vertical earth pressures on the wall facing and along the centerline of the wall footing under the applied footing pressure of 300 kPa. For the comparison purpose, the vertical earth pressures calculated using Equation (7.2) were added in Figures 7.36 and 7.36. Both figures show that the reduction of the

friction angle of the backfill soil from 38^{o} to 34^{o} had an insignificant effect on the distributions of the vertical earth pressures under the applied footing pressures of 100 kPa and 300 kPa.

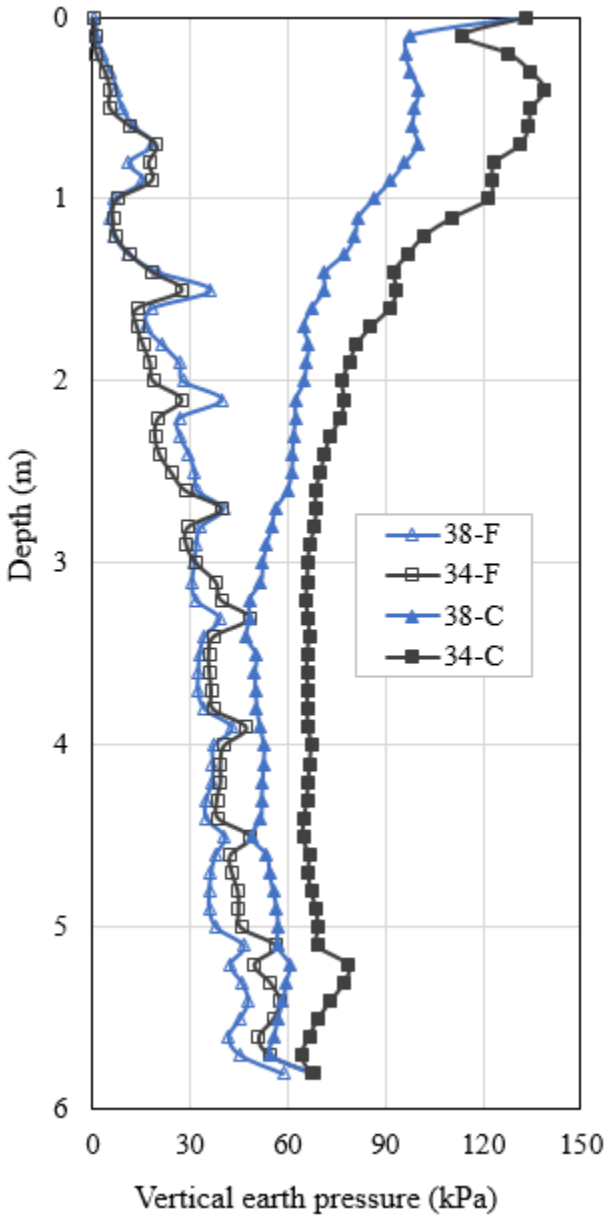

Figure 7.36 Effect of friction angle of backfill soil on vertical earth pressure distribution under the applied footing pressure of 100 kPa

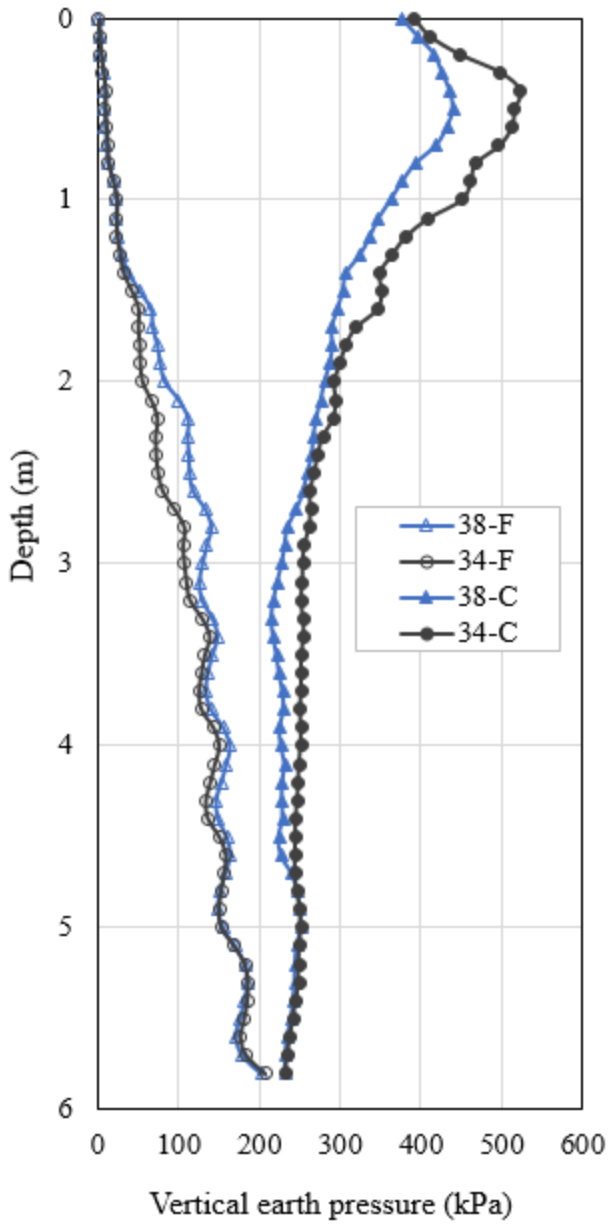

Figure 7.37 Effect of friction angle of backfill soil on vertical earth pressure distribution under the applied footing pressure of 300 kPa

Lateral earth pressure distribution

Figure 7.38 shows the effect of the friction angle of the backfill soil on the distribution of the lateral earth pressures. Figure 7.38(a) shows the distribution of the lateral earth pressure on the wall facing along the depth of the wall under the applied footing pressure of 100 while Figure 7.38(b) shows the distribution of the lateral earth pressure on the wall facing along the depth of the wall footing under the applied footing pressure of 300 kPa.

Figures 7.38 shows that the reduction of the friction angle of the backfill soil from 38^{o} to 34^{o} had insignificant effect on the distribution of the lateral earth pressures on the wall facing under the applied footing pressure of 100 kPa and 300 kPa.

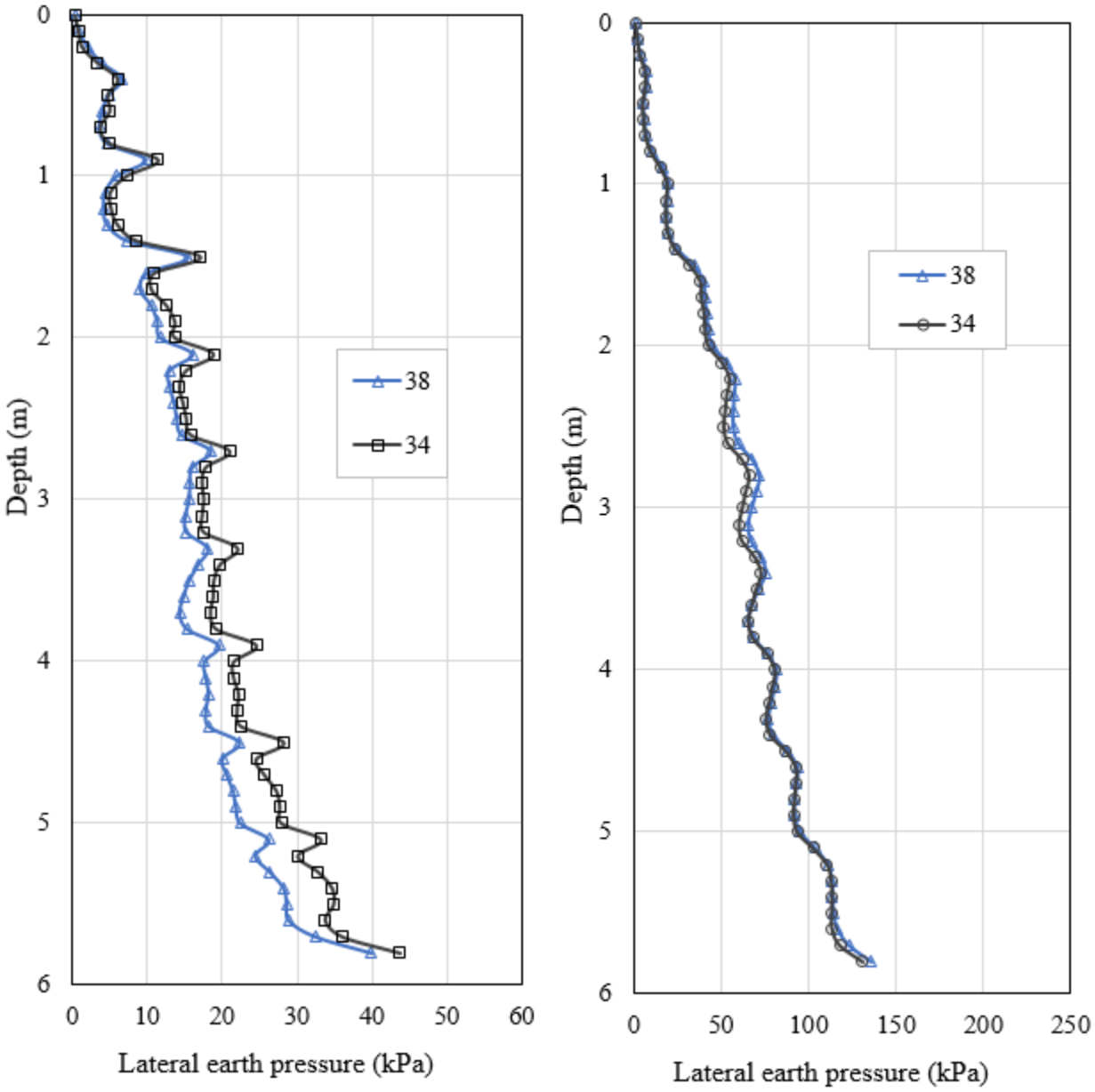

(a) (b)

Figure 7.38 Effect of friction angle of backfill soil on lateral earth pressure distribution on the wall facing: (a) under the footing pressure of 100 kPa and (b) under the footing pressure of 300 kPa

Maximum strain of reinforcement layers

Figure 7.39 shows the effect of the friction angle of the backfill soil on the maximum strains of each reinforcement layer under the applied footing pressures of 100 and 300 kPa. This figure shows that the decrease of the friction angle of the backfill soil from 38^{o} to 34^{o} resulted in an increase in the maximum strains in all the reinforcement layers at the applied footing pressures of 100 and 300 kPa. For example, the maximum reinforcement strains at the wall height of 4.4 m in the baseline case were approximately 1.3% and 3.9% at the applied footing pressures of 100 and 300 kPa, respectively, while the maximum strains of the reinforcement in the case where the friction angle of the backfill soil was 34^{o} were approximately 1.7% and 4.9%, respectively at the same wall height and applied footing pressure.

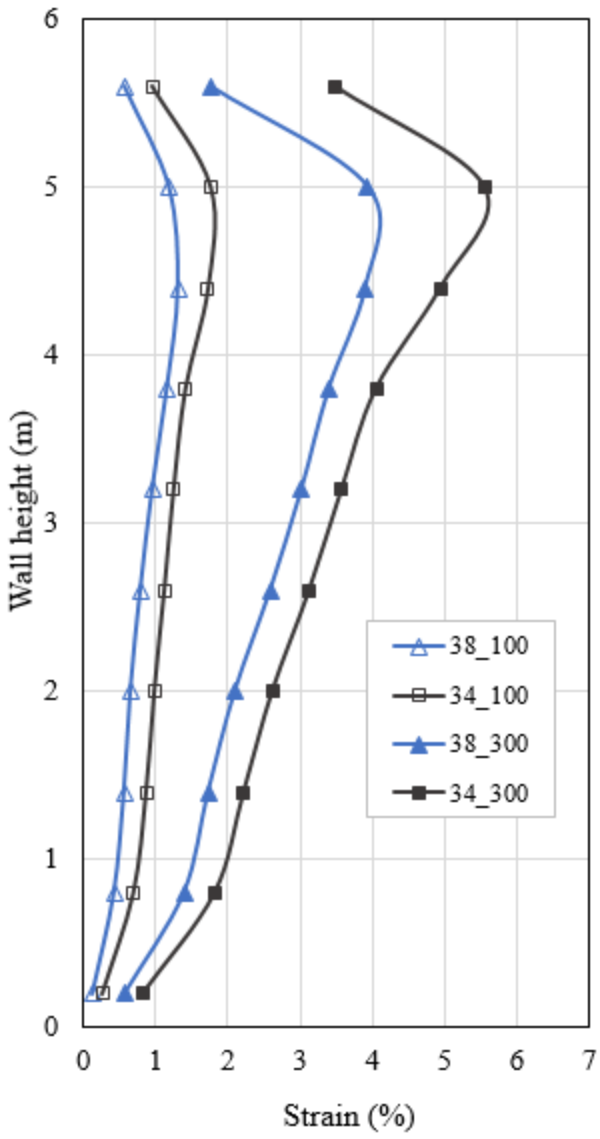

Figure 7.39 Effect of friction angle of backfill soil on maximum strain of the reinforcement layers

7.2.6 Effect of reinforcement stiffness

This section presents the effect of stiffness of the reinforcement on the performance of GRR walls with limited fill space. Two different stiffness values, J = 1000 kN/m (baseline case) and J = 2000 kN/m were investigated. The terms “1000”, and “2000” used in the legends of the figures represent the baseline case and the case in which the stiffness of the reinforcement was 2000 kN/m.

Lateral wall facing displacement

Figure 7.40 shows the effect of reinforcement stiffness on the displacement of the lateral wall facing under footing loading. This figure shows that the increase of the stiffness of the reinforcement from 1000 to 2000 kN/m resulted in smaller lateral displacement of the wall facing compared to that of the baseline case. For example, the maximum lateral displacement of the wall facing was approximately 38 mm in the baseline case at the applied footing pressure of 100 kPa while the maximum lateral displacement of the wall facing was approximately 22 mm in the case where the stiffness of the reinforcement was 2000 kN/m at the same applied footing pressure.

In addition, the effect of the reinforcement stiffness became more important when the applied footing pressure was 300 kPa. For example, the maximum lateral displacement of the wall facing was approximately 66 mm in the case where the stiffness of the reinforcement was 2000 kN/m compared to 125 mm maximum wall facing displacement in the baseline case.

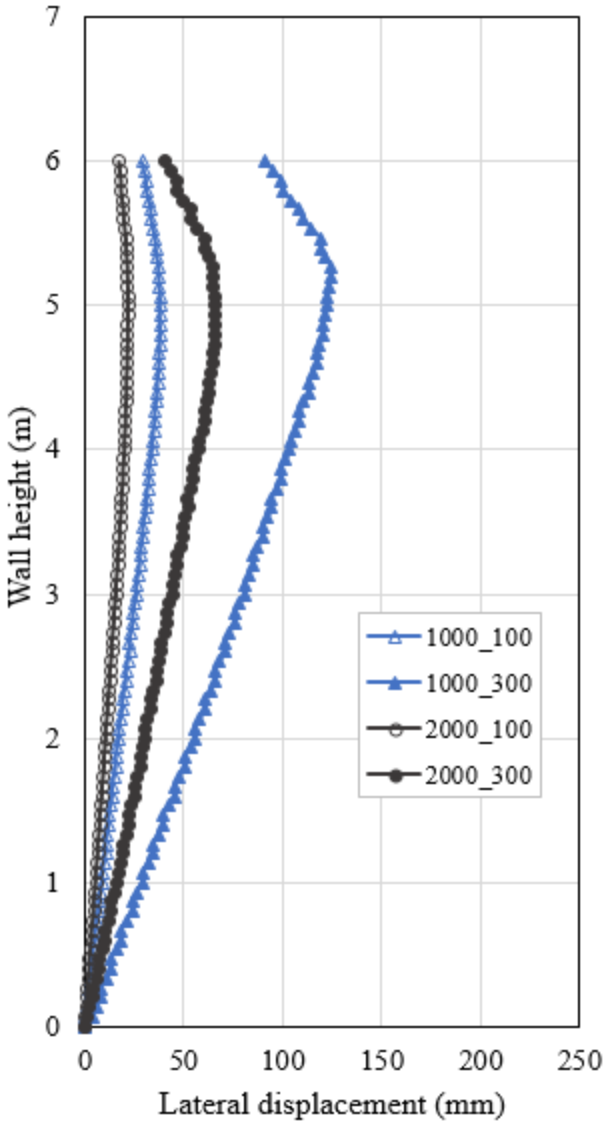

Figure 7.40 Effect of reinforcement stiffness on lateral wall facing displacement versus wall height

Settlement of footing

Figure 7.41 shows the effect of the reinforcement stiffness on the settlement of the footing. This figure indicates that the increase of the stiffness of the reinforcement from 1000 to 2000 kN/m resulted in large reduction in the settlement and large increase in the bearing capacity of the footing. For example, the baseline case had approximately 310 mm footing settlement at the

applied footing pressure of 400 kPa, while the case with higher reinforcement stiffness (i.e., the "2000" case) had 215 mm footing settlement under the same applied footing pressure. Consequently, the stiffness of the reinforcement had a considerable effect on the settlement and bearing capacity of the footing.

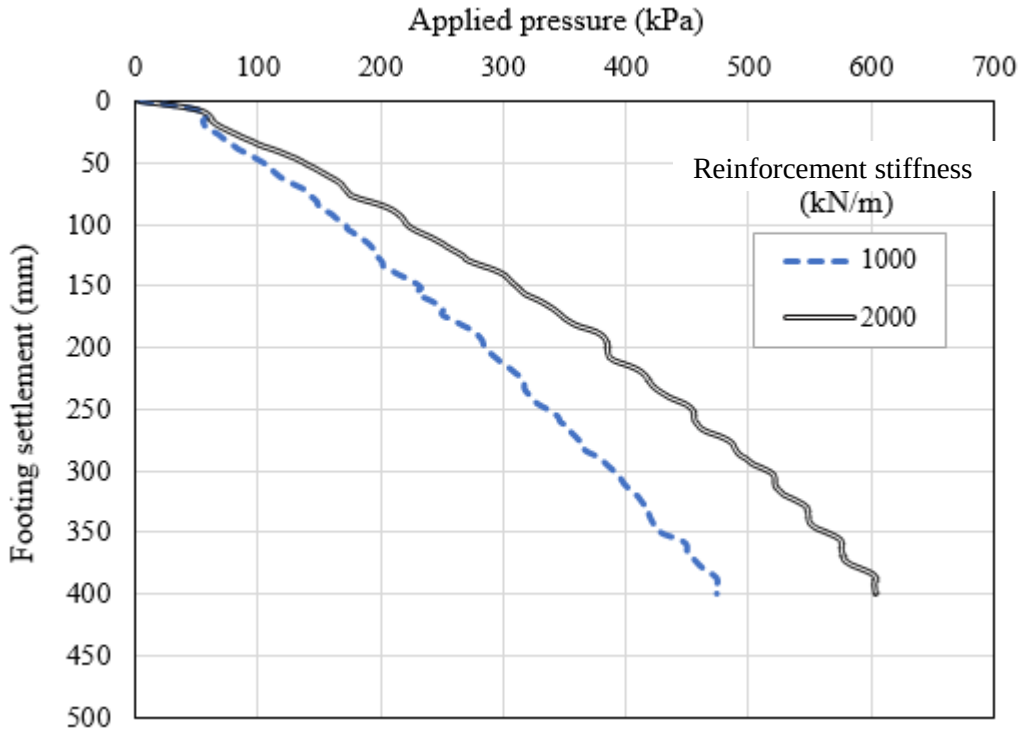

Figure 7.41 Effect of reinforcement stiffness on pressure-settlement curve of the footing

Vertical earth pressure distribution

Figures 7.42 and 7.43 show the effect of the stiffness of the reinforcement on the distribution of the vertical earth pressure. Figure 7.42 shows the distributions of the vertical earth pressures on the wall facing versus depth under the applied footing pressures of 100 and 300 kPa. Figure 7.43 also shows the distributions of the vertical earth pressures along the centerline of the footing versus depth under both the applied footing pressures.

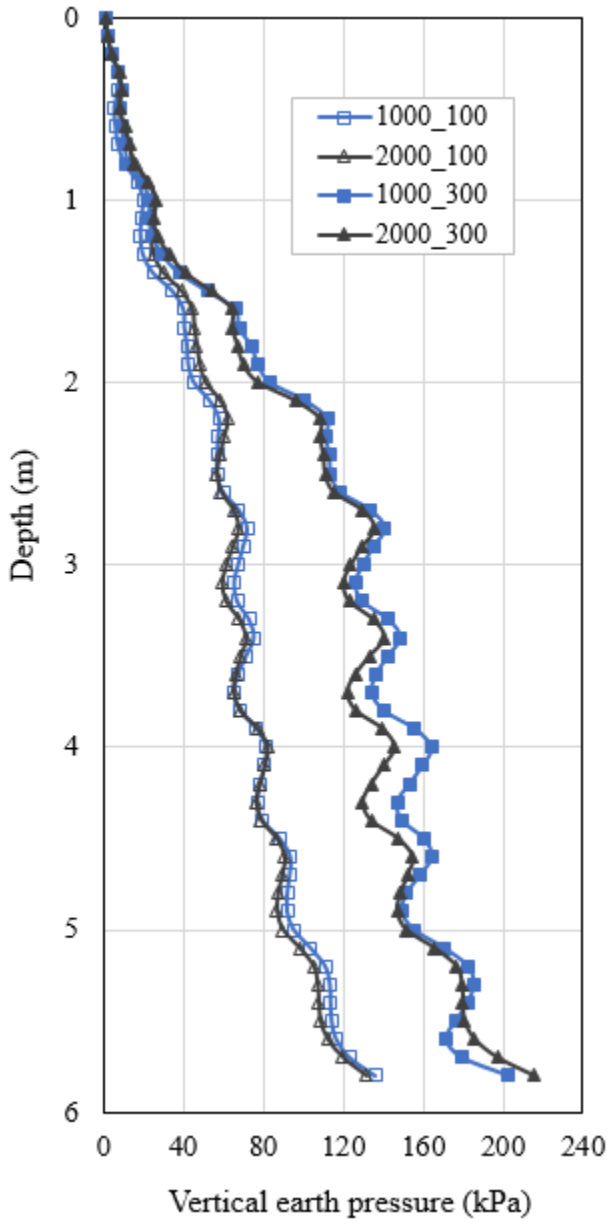

Figure 7.42 Effect of reinforcement stiffness on vertical earth pressure distribution on the wall facing under the applied footing pressure of 100 and 300 kPa

Figures 7.42 and 7.43 indicate that the vertical earth pressures increased with the increase of the applied footing pressure and the vertical earth pressures along the centerline of the wall footing were higher than those on the wall facing. In addition, the increase of the stiffness of the

reinforcement from 1000 to 2000 kN/m had an insignificant effect on the vertical earth pressures on the wall facing and along the centerline of the wall footing under the applied footing pressures of 100 and 300 kPa.

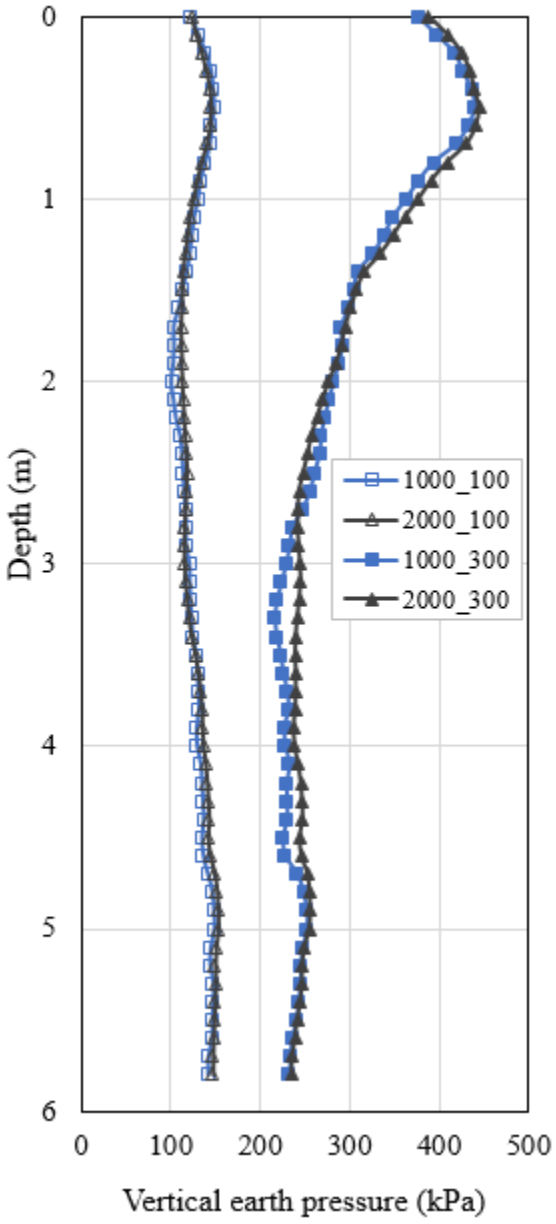

Figure 7.43 Effect of reinforcement stiffness on vertical earth pressure distribution on the centerline of the wall footing under the applied footing pressure of 100 and 300 kPa

Lateral earth pressure distribution

Figure 7.44 shows the effect of the stiffness of the reinforcement on the distribution of the lateral earth pressures on the wall facing under the applied footing pressure of 100 and 300 kPa as well.

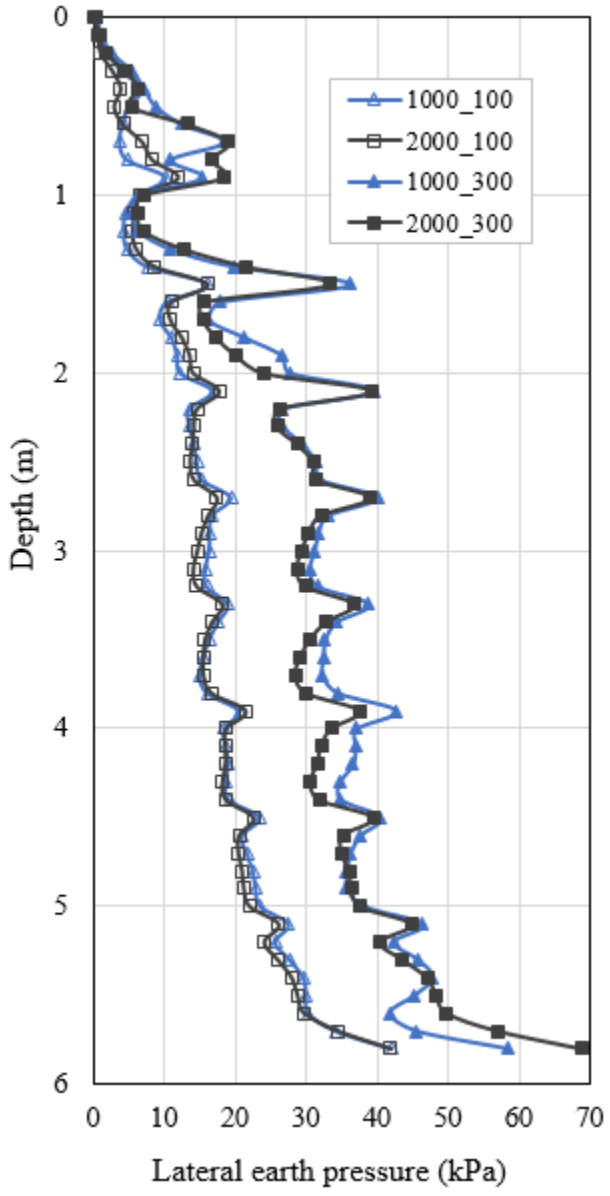

Figure 7.44 Effect of reinforcement stiffness on lateral earth pressure distribution on the wall facing under the footing pressure of 100 and 300 kPa

Figure 7.44 shows that the lateral earth pressures on the wall facing increased with the increase of the depth and the applied footing pressure. In addition, Figure 7.44 shows that the increase of the stiffness of the reinforcement from 1000 kN/m to 2000 kN/m had insignificant effect on the distribution of the lateral earth pressures on the wall facing under the applied footing pressure of 100 kPa and 300 kPa as well.

Maximum strain of reinforcement layers

Figure 7.45 shows the effect of the stiffness of the reinforcement on the maximum strains of reinforcement layers at the applied footing pressures of 100 kPa and 300 kPa. This figure shows that the increase of the stiffness of the reinforcement from 1000 to 2000 kN/m had a considerable effect on the maximum strains in all the reinforcement layers at the applied footing pressures of 100 and 300 kPa. For example, the maximum strain of the reinforcement at the wall height of 5.0 m was about 1.2% at the applied footing pressure of 100 kPa in the baseline case while in the case where the stiffness of the reinforcement was 2000 kN/m, the maximum strain of the reinforcement was approximately 0.6 % at the same wall height and applied footing pressure. The effect of the stiffness of the reinforcement became more significant when the applied footing pressure was 300 kPa.

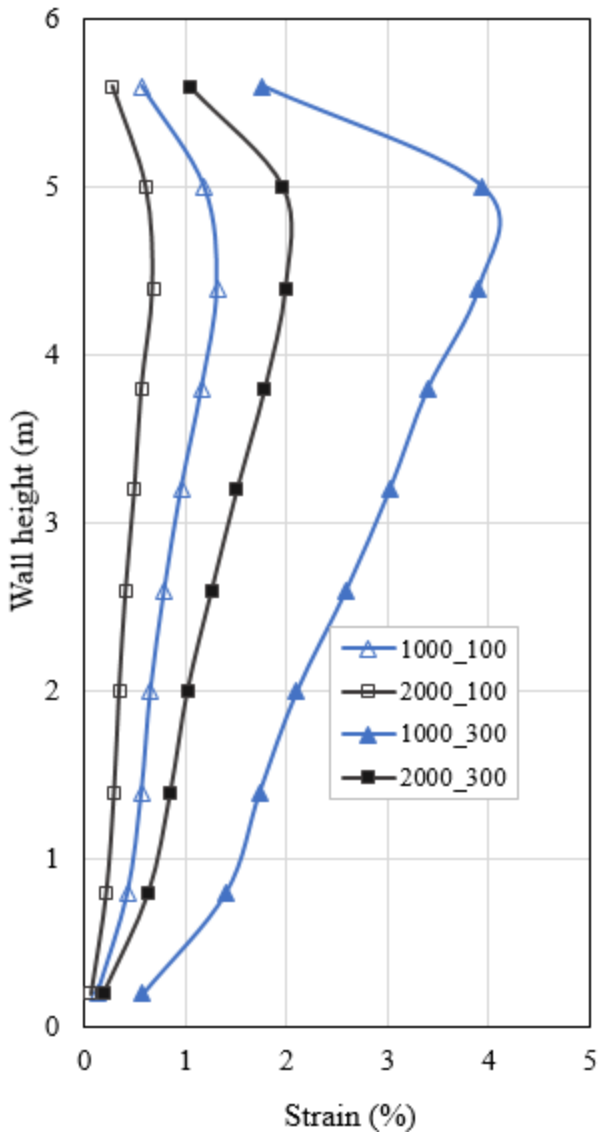

Figure 7.45 Effect of reinforcement stiffness on maximum strain of the reinforcement layers

7.2.7 Effect of wall height

This section presents the effect of the wall height on the performance of GRR wall with limited fill space. Two different wall height, H = 6.0 m (baseline case), and H= 9.0 m were investigated.

Lateral wall facing displacement

Figure 7.46 shows the effect of the wall height on the displacement of the lateral wall facing versus wall height under footing loading. As shown in Figure 7.46, the maximum wall facing displacements in the case where the wall height was 9.0 m occurred approximately at the 4/6 and 5/6 of the wall height under the applied footing pressures of 100 and 300 kPa, respectively, which are almost the same as those of the baseline case. For example, in the baseline case the maximum wall facing displacements occurred approximately at 5/6 of the wall height at the applied footing pressures of 100 and 300 kPa.

In addition, Figure 7.46 shows that the increase of the height of the wall from 6.0 to 9.0 m had an insignificant effect on the wall facing displacement at the applied footing pressure of 100 kPa. However, the increase of the height of the wall from 6.0 to 9.0 m resulted in smaller maximum wall facing displacement than that of the baseline case when the applied footing pressure was 300 kPa. For example, the maximum wall facing displacement in the baseline case was approximately 125 mm under the applied footing pressure of 300 kPa while the maximum wall facing displacement in the case with the wall height of 9.0 m was approximately 99 mm under the same applied footing pressure.

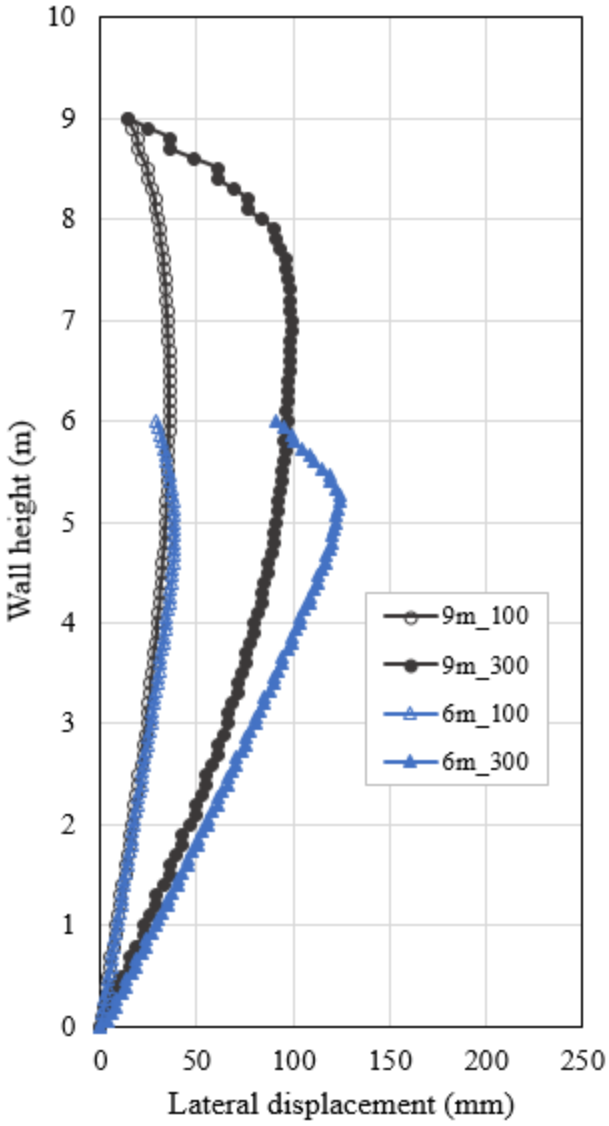

Figure 7.46 Effect of wall height on lateral wall facing displacement versus wall height

Settlement of footing

Figure 7.47 shows the effect of the height of the wall on the settlement of the footing. The figure shows that the footing settlement of the two cases linearly increased with the increase of the applied footing pressure. In addition, the increase of the height of the wall from 6.0 to 9.0 m resulted in larger settlement of the footing under all the applied footing pressures compared to

that of the baseline case. For example, the case with the wall height of 9.0 m had 380 mm footing settlement at the applied footing pressure of 400 kPa, while the case with wall height of 6.0 m (baseline case) had approximately 320 mm footing settlement at the same applied footing pressure. So, it can be concluded that the height of the wall had an effect on the settlement and bearing capacity of the footing.

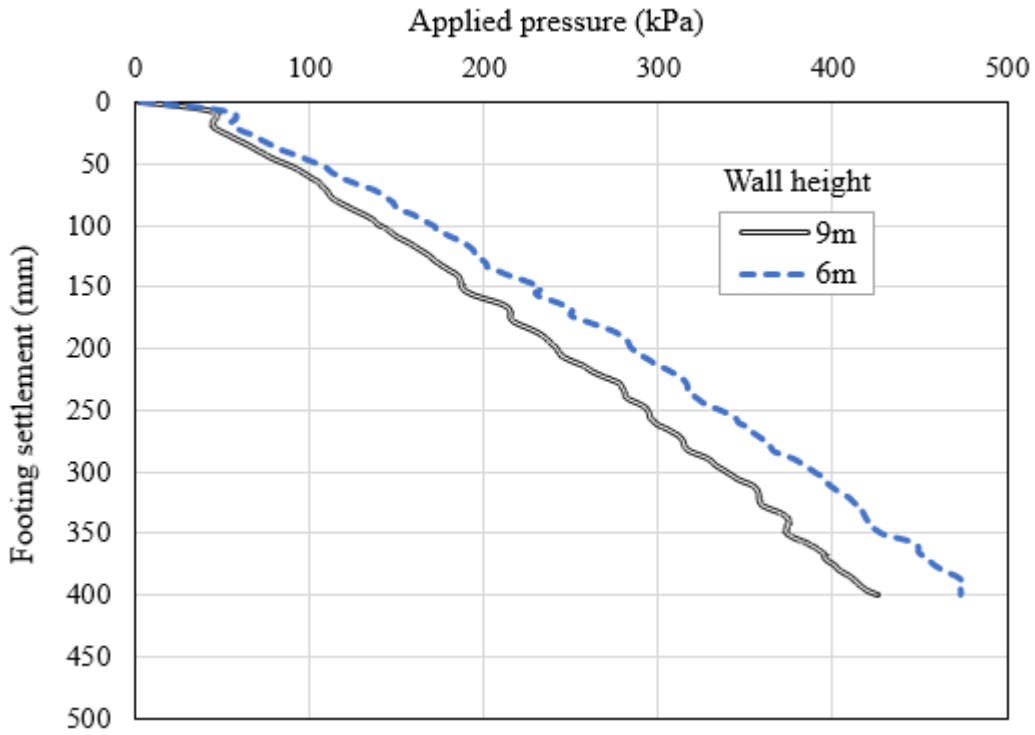

Figure 7.47 Effect of wall height on pressure-settlement curve of the footing

Maximum strain of reinforcement layers

Figure 7.48 shows the effect of the wall height on the maximum strains of reinforcement layers at the applied footing pressures of 100 and 300 kPa. This figure indicates that the maximum strains of the reinforcement layers in these two cases were almost the same at the

corresponding reinforcement levels. In other words, the increase of the height of the wall from 6.0 to 9.0 m had an insignificant effect on the profile of the maximum strains in all the reinforcement layers under the applied footing pressure.

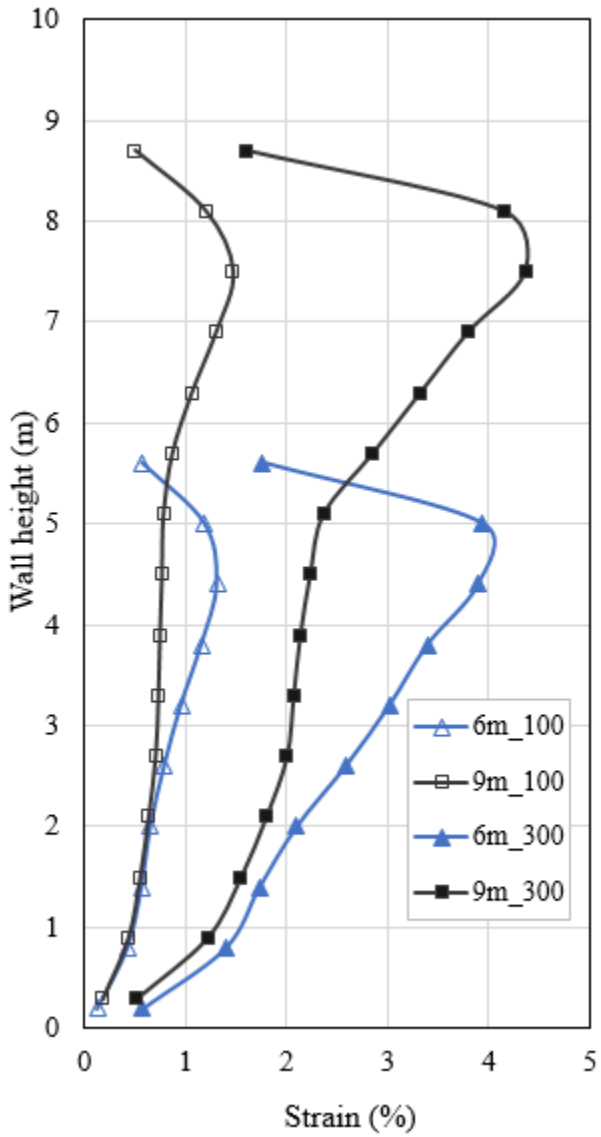

Figure 7.48 Effect of wall height on maximum strain of the reinforcement layers

7.2.8 Earth pressure ratio (K_r/K_a)

The earth pressure ratio, K_r/K_a is a very important parameter in design of GRR walls. K_r is the lateral earth pressure coefficient that is calculated based on the maximum tensile strength of reinforcement, vertical spacing of the reinforcement and applied vertical stress on the reinforcement (Equation (7.5)). K_a is the Rankine's active lateral earth pressure coefficient (Equation (5.2)).

$$K_r = \frac{T_{max}}{s_v * \sigma_v} \quad \text{..... (7.5)}$$

where:

T_{max} is the maximum tensile strength of reinforcement,

s_v is the vertical spacing of the reinforcement, and

σ_v is the total vertical stress on the reinforcement.

To investigate the influence of different parameters on K_r/K_a ratio, K_r/K_a was calculated for different cases using Equation (7.5), and the results were plotted and presented in Figures 7.49 and 7.50. Figure 7.49 shows the ratios of K_r/K_a calculated using Equation (7.5) and considering the applied vertical stress behind the wall facing while Figure 7.50 shows the ratios of Kr/Ka calculated using Equation (7.5) and considering the applied vertical stress along the centerline of the footing. AASHTO recommends a constant ratio of the K_r/K_a for GRR walls, which is one. For comparison purpose, the K_r/K_a ratio recommended by AASHTO is added to the Figures 7.49 and 7.50.

Figure 7.49 shows that the reduction in the reinforced fill width had minor effect on the ratio of K_r/K_a. However, the increase of the footing offset distance from 0.05H to 0.1H resulted in an increase in the ratio of K_r/K_a along the depth of the wall model. Similarly, the increase of

the footing size from 0.8m to 1.6m had considerable effect on the ratio of K_r/K_a along the depth of the wall model, particularly for the top portion of the wall.

In addition, Figure 7.50 shows that the reduction in the reinforced fill width from 0.7H to 0.5H had insignificant effect on the ratio of K_r/K_a along the depth of the wall model. However, the reduction in the reinforced fill width from 0.5H to 0.3H had considerable effect on the ratio of K_r/K_a along the depth of the wall model. Also, the change in the footing offset distance and footing size had little effect on the ratio of K_r/K_a along the depth of the wall model.

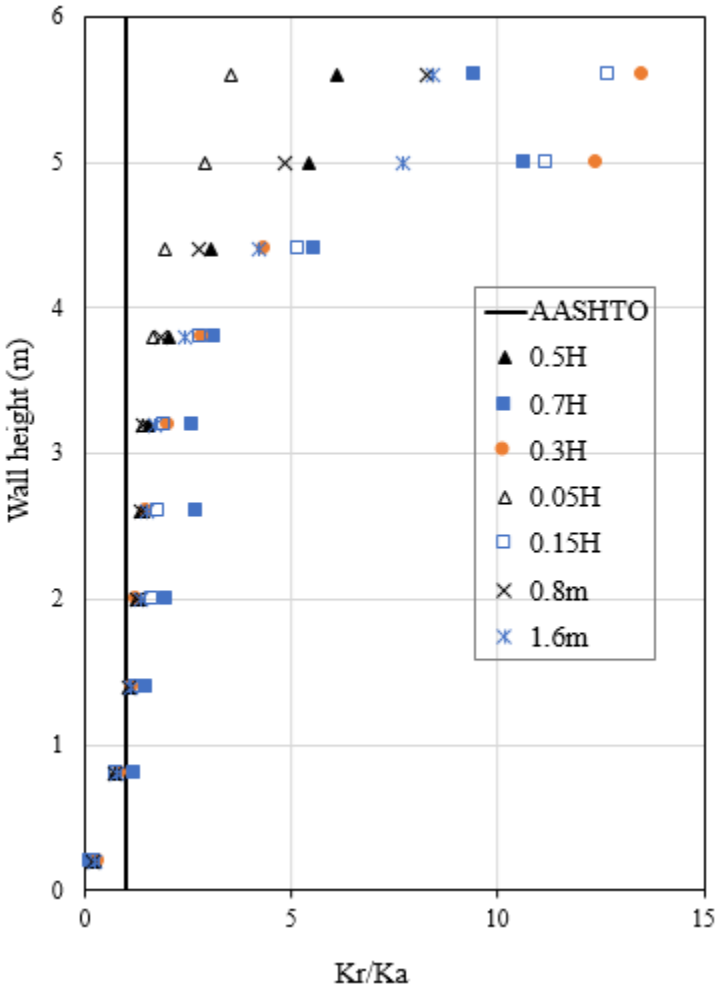

Figure 7.49 Effect of various parameters on the ratio of K_r/K_a based on the vertical stress behind wall facing

Furthermore, Figures 7.49 and 7.50 show that the calculated ratio of K_r/K_a using Equation (7.5) along the depth of the model was much higher than that recommended by AASHTO when the applied vertical stress behind the wall facing was considered. However, the calculated ratio of K_r/K_a using Equation (7.5) along the depth of the model was comparable with that recommended by AASHTO when the applied vertical stress along the centerline of footing was considered.

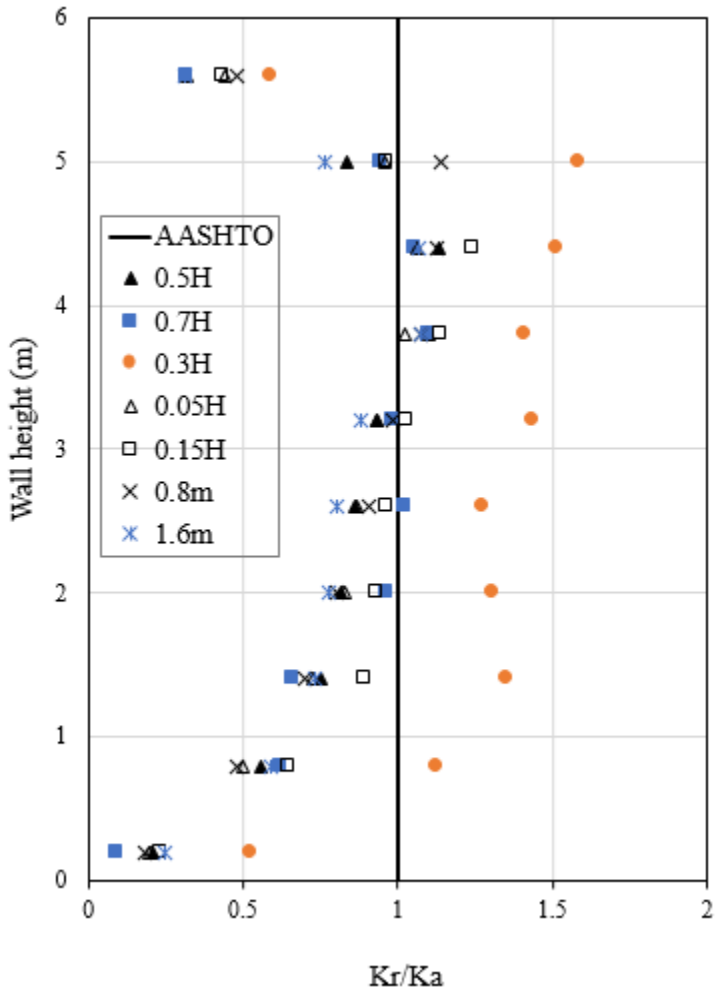

Figure 7.50 Effect of various parameters on the ratio of K_r/K_a based on the vertical stress along centerline of footing

Chapter 8 Conclusions and Recommendations

8.1 Conclusions

In this study, a series of laboratory reduced-scale model tests and numerical simulation were performed on geosynthetic-reinforced retaining (GRR) walls with limited space subjected to static footing loading. The models were designed based on the scale effect analysis conducted in this study, and tested under footing loading until failure. The lateral displacement of the wall facing, the vertical earth pressures, the lateral earth pressures, and the settlement of the footing in the experimental tests and the numerical simulation were analyzed and discussed. In addition, a parametric study was conducted to investigate the influence of various parameters on the performance of the GRR walls with limited fill space subjected to static footing loading. The following conclusions can be drawn from this study.

8.1.1 Scale effect analysis

1. Based on the scale effect analysis conducted in this study, the correct scale ratio must be N (N is the ratio of the dimension of the reduced-scale model to that of the full-scale prototype model) for the geometric similarity (i.e., the height and the width of the model), and N^2 for the reinforcement stiffness.
2. The scale-effect results obtained by three methods (i.e., the dimensional analysis, the FHWA equations for calculating tensile strength in the reinforcement, and the limit equilibrium method in ReSSA 3.0) were almost identical.

8.1.2 Experimental tests

1. The lateral displacement of the wall facing increased with the increase of footing load in all the model tests. In almost all the models, most of the wall facing displacements occurred above the mid-height of the wall, and the maximum wall facing displacements occurred at the depth approximately equal to the width of the footing from the top of the wall. In addition, the influence depth of the footing load ranged from1.5 to 2.5 times the footing width.
2. When the wall had a reinforced zone with L > 0.7H, limiting the width of the retained fill behind the reinforced fill had a minor effect on the wall facing displacement, the internal deformation of the wall, and the footing settlement when the reinforcement length was 0.7H (H is the wall height).
3. Reduction in the reinforced fill width from 0.7H to 0.5H had a minor effect on the overall wall facing displacement, the internal deformation of the wall, and the footing settlement. However, the reduction in the reinforced fill width from 0.7H to 0.5H resulted in an increase in the maximum wall facing displacement and the maximum footing settlement.
4. Reduction in the reinforced fill width from 0.5H to 0.3H resulted in excessive wall facing displacement, a significant increase in the footing settlement, a large decrease in the bearing capacity of the footing, and a sudden failure of the model wall. In addition, reduction in the reinforced fill width from 0.5H to 0.3H had a considerable effect on the vertical compression in the model and resulted in the increase of the influence depth of the footing load.
5. Reduction of the vertical spacing of the reinforcement from 0.2 m to 0.1 m resulted in the reduction of the maximum lateral displacement of the wall facing, the footing settlement,

and the substantial increase in the bearing capacity of the footing. However, the vertical spacing of the reinforcement had a minor effect on the influence depth of the footing in the model test.

6. The footing offset distance influenced the maximum wall facing displacement, the footing settlement, and the influence depth of the footing. Reduction in the footing offset distance from 0.2 to 0.05 m resulted in a considerable increase in the maximum lateral wall facing displacement, small vertical compression, and decrease in the influence depth of the footing in the model test. In addition, the reduction of the footing offset distance from 0.2 to 0.05m resulted in an increase in the settlement and a decrease in the bearing capacity of the footing.
7. Connection of the reinforcements to the stable medium in the wall models with the reinforced fill width of 0.3H resulted in a significant reduction in the wall facing displacement, the internal deformation of the wall, the footing settlement, and a large increase in the bearing capacity of the footing. Connection of only two of the uppermost reinforcement layers to the stable medium also substantially reduced the displacement of the wall facing and increased the bearing capacity of the footing.
8. Upward-bending of the reinforcement at the end of the reinforced fill provided sufficient internal stability that resulted in a huge reduction in the lateral displacement of the wall facing in the wall models with the reinforcement lengths of 0.3H and 0.5H. In addition, the upward-bending of the reinforcement substantially increased the bearing capacity of the footing and significantly reduced the footing settlement in the wall models with the reinforcement lengths of 0.3H and 0.5H.

9. The measured vertical earth pressures under the center of the footing along the depth of the wall models in all the model tests increased with an increase of the applied footing load. In the models with the reinforced fill width of 0.7H and 0.5H, the measured vertical earth pressures agreed well with the vertical pressures calculated based on the 2:1 method. In addition, the measured vertical earth pressures in the model tests with the reinforced fill width of 0.3H agreed reasonably with the vertical pressures calculated based on the 2:1 method at the low applied footing load. However, the 2:1 method appeared to overestimate the vertical pressure in the models at the high applied footing load. Therefore, the use of the 2:1 method is questionable for limited fill space walls, especially, when the reinforced fill width is less than 0.5H.
10. The measured lateral earth pressures on the wall facing in the models with the reinforced fill width of 0.7H and 0.5H matched fairly well the calculated lateral pressures based on Rankine's active earth pressure and Janssen's equation. However, in the wall models with the reinforced fill width of 0.3H, the measured lateral earth pressures on the wall facing did not match well the calculated earth pressures, especially in the wall models where the reinforcements had rear connection. In other word, The existing analytical methods (i.e., Rankine's active earth pressure and Janssen's equation) overestimates the lateral earth pressure induced by footing loading for the walls with the reinforced fill width less than 0.5H.
11. The lateral earth pressure coefficients calculated based on the measured data for the wall models with the reinforced fill width of 0.3H were lower than those calculated based on Rankine's active earth pressure and Janssen's equation under all the applied footing loads. In other words, the existing analytical methods (i.e. Rankine's theory and Janssen's

equation) may overestimate the lateral earth pressure induced by footing loading for the walls with the reinforced fill width less than 0.5H.

8.1.3 Numerical simulation of the experimental tests

1. The wall facing displacements computed by the numerical analysis increased with the wall height in all the simulated models until reaching the maximum value, and then decreased with the wall height. The wall facing displacements computed by the numerical analysis were slightly smaller than the measured wall facing displacements from the experimental tests at the low applied footing load, but were slightly higher than the measured wall facing displacements from the experimental tests at the high applied footing load. Overall, the wall facing displacements computed by the numerical analysis agreed well with those from the experimental tests.
2. The footing settlement computed by the numerical analysis increased with the applied footing load in all the simulated models and was in good agreement with that measured in the experimental tests.
3. The vertical earth pressures computed by the numerical analysis along the centerline of the footing increased with the depth of the wall models and the applied footing load. In addition, the distribution of the vertical earth pressures computed by the numerical analysis agreed reasonably with those obtained in the experimental tests under different applied footing loads. Additionally, the lateral earth pressures computed by the numerical analysis on the wall facing along the wall depth were generally in a good agreement with the measured lateral earth pressures in the experimental tests. In addition, the calculated lateral earth pressures based on the Rankine's earth pressure theory were similar to those

computed by the numerical analysis for the models with the reinforced fill widths of 0.5H and 0.7H.

8.1.4 Numerical parametric study

1. The lateral wall facing displacements computed by numerical analysis in the parametric study increased with the decrease in the reinforced fill width, the friction angle of the backfill soil, the footing offset distance and the increase in the footing size. On the other hand, the lateral wall facing displacements decreased with the increase in the stiffness of the reinforcement, the footing offset distance, and the decrease in the footing size. In addition, the lateral wall facing displacement decreased substantially with the rear connection of the reinforcement.
2. Reduction in the reinforced fill width, the footing offset distance, the friction angle of the backfill soil and the increase in the footing size resulted in a large increase in the footing settlement and decrease in the bearing capacity of the footing. The footing settlement decreased, and the bearing capacity of the footing increased with the increase in the stiffness of the reinforcement, the footing offset distance, and the decrease in the footing size, and with the rear connection of the reinforcement.
3. The maximum strain in the reinforcement increased with the decrease in the reinforced fill width, the friction angle of the backfill soil, the footing offset distance, and the increase in the footing size. In contrast, the maximum strain in the reinforcement decreased with the increase in the stiffness of the reinforcement, the footing offset distance, and the decrease in the footing size. In addition, connection of the

reinforcement to the stable medium at rear resulted in large decrease in the maximum strain in the reinforcement.

4. The reinforced fill width and the footing offset distance had an influence on the distributions of lateral earth pressures on the wall facing. However, the footing size and the friction angle of the backfill had an insignificant influence on the distributions of the lateral earth pressures on the wall facing. Also, the reinforcement rear connection and the reinforcement stiffness had an insignificant influence on the distribution of the vertical earth pressures and the distribution of the lateral earth pressures in the wall models.
5. The lateral earth pressure computed by the numerical analysis due to the self-weight of the wall on the wall facing was lower than the lateral earth pressure calculated based on both Rankine's active earth pressure theory and Janssen's equation. The vertical earth pressures on the wall along the wall facing computed by the numerical analysis under the applied footing load were lower than the vertical earth pressures calculated by the 2:1 distribution method. However, the vertical earth pressures along the centerline of the footing computed by the numerical analysis were higher than those calculated by the 2:1 distribution method.
6. The lateral earth pressures on the wall facing computed by the numerical analysis under the applied footing load were lower than the calculated lateral earth pressures. However, The lateral earth pressure calculated based on Janssen's equation were closer to the computed lateral pressure compared to those calculated based on Rankine's active earth pressure and 2:1 distribution method.

7. The calculated ratio of K_r/K_a along the depth of the model was much higher than that recommended by AASHTO when the applied vertical stress behind the wall facing was considered. However, the calculated ratio of K_r/K_a along the depth of the model was comparable with that recommended by AASHTO when the applied vertical stress along the centerline of footing was considered.
8. Base on the findings of this study, it is recommended that:
    a. The reinforcement rear connection, the bending upward, and overlapped techniques should be used for limited fill space GRR walls with the reinforced fill width smaller than 0.5H and subjected to static footing loading.
    b. Janssen's equation can be used to estimate lateral pressures on the wall facing, which showed better results than those of Rankine's theory.
    c. The boundary effects should be considered in the 2:1 stress distribution method, particularly for the walls with reinforced fill width less than 0.5H.

8.2 Recommendation for Future Work

1. This study has evaluated the performance of geosynthetic reinforced retaining (GRR) walls with limited fill space subjected to static footing loading. A study on the performance of GRR walls with limited fill space subjected to cyclic footing loading is recommended.
2. In addition, a study on the performance of GRR walls with limited fill space subjected to uniform loading or seismic loading as well is recommended.

3. The GRR walls with limited fill space subjected to vertical footing loading was evaluated in this study. A study on the performance of GRR walls with limited fill space under horizontal and vertical footing loading is recommended.
4. In this study, experimental work and numerical analyses were employed to evaluate the performance of GRR walls with limited fill space subjected to static footing loading. Development of a theoretical analysis to predict the behavior of GRR walls with limited fill space subjected to static footing loading is recommended.
5. In this study, the backfill soil was modeled as a linearly elastic perfectly plastic material with the Mohr-Coulomb failure criterion. Further studies are recommended to model the backfill soil using a stress-dependent model, such as the Cap Yield model or Duncan Chang model.
6. The models with wall facing of zero batter and vertical stable medium were investigated in this study. A study to investigate the effect of wall facing batter and the degree of inclination of the stable medium on the behavior of GRR walls with limited fill space subjected to static footing loading is recommended.
7. As part of this study a scale effect analysis using the limit equilibrium method was conducted. A study on the scale effect analysis using a comprehensive numerical analysis is recommended.

References

AASHTO. (2014). LRFD bridge design specifications. 7th ed., Washington, DC.

AASHTO. (2002). Standard specifications for highway bridges: AASHTO.

ADAMA Engineering, Inc. (2008). ReSSA version (3.0)., (www.Geoprograms.com), Newark, Del.

Adams, M.T., Nicks, J.E., Stabile, T., Wu, J.T.H., Schlatter, W., and Hartmann, J. (2011). "Geosynthetic Reinforced Soil Integrated Bridge System, Synthesis Report." Report No. FHWA-HRT-11-027, *Federal Highway Administration*, McLean, VA.

Anderson, P. L., Gladstone, R. A., and Sankey, J. E. (2012). State of the practice of MSE wall design for highway structures. *Proceedings of the Geocongress 2012*, state of the art and practice in geotechnical engineering, Oakland, March 25, 29.

Allen, T.M. and Bathurst, R.J. (2014a). "Performance of a 11 m High Block-Faced Geogrid Wall Designed Using The K-Stiffness Method." *Canadian Geotechnical Journal*, 51(1): 16-29 (http://dx.doi.org/10.1139/cgj-2013-0261).

Allen, T.M. and Bathurst, R.J. (2014b). "Design and Performance of a 6.3 m High Block-Faced Geogrid Wall Designed Using the K-Stiffness Method." *Journal of Geotechnical and Geoenvironmental Engineering*, 142(2): 1-12.

Berg, R., Christopher, B., and Samtani, N. (2009). November. NHI Courses No. 132042 and 132043. Design and construction of mechanically stabilized earth walls and reinforced soil slopes, vols. 1 & 2. Washington, DC: US Department of Transportation Federal Highway Administration. Publication No: FHWA-NHI-10–024.

Bilgin, Ö. (2009). Failure mechanisms governing reinforcement length of geogrid reinforced soil retaining walls. *Engineering Structures*, 31(9), 1967-1975.

Bloser, S., Shearer, D., Corradini, K., and Scheetz, B. (2012). "Geosynthetically Reinforced Soil-Integrated Bridge Systems (GRS-IBS) Specification Development for PennDOT Publication 447." Publication No. 447 (10-14), Pennsylvania Department of Transportation.

Chen, J.F., Liu, J.X., Xue, J.F., and Shi, Z.M. (2014). "Stability Analyses of a Reinforced Soil Wall on Soft Soils Using Strength Reduction Method." *Engineering Geology*, 177: 83-92.

Elias, V., Barry, P., and Christopher, R. (2001). Mechanically Stabilized Earth Walls and Reinforced Soil Slopes Design and Construction Guidelines: FHWA Report No. FHWA-NHI-00-043.

Ettema, R., Melville, B. W., and Barkdoll, B. (1998). Scale effect in pier-scour experiments. *Journal of Hydraulic Engineering*, 124(6), 639-642.

Fan, C.-C., and Fang, Y.-S. (2010). Numerical solution of active earth pressures on rigid retaining walls built near rock faces. *Computers and Geotechnics*, 37(7), 1023-1029.

Frydman, S., and Keissar, I. (1987). Earth pressure on retaining walls near rock faces. *Journal of Geotechnical Engineering*, 113(6), 586-599.

Greco, V. (2013). Active thrust on retaining walls of narrow backfill width. *Computers and Geotechnics*, 50, 66-78.

Han, J. (2015). “Principles and Practice of Ground Improvement.” John Wiley & Sons, Hoboken, New Jersey, USA, ISBN: 978-1-118-25991-7.

Han, J., and Leshchinsky, D. (2010). Analysis of back-to-back mechanically stabilized earth walls. *Geotextiles and Geomembranes*, 28(3), 262-267.

Han, J. and Leshchinsky, D. (2006). "General Analytical Framework for Design of Flexible Reinforced Earth Structures." *Journal of Geotechnical and Geoenvironmental Engineering*, 132(11): 1427-1435.

Holtz, R.D. and Lee, W.F. (2002). "Internal Stability Analyses of Geosynthetic Reinforced Retaining Walls." Report No. WA-RD 532.1, Washington State Department of Transportation, January, 379 p.

Huang, B.Q., Bathurst, R.J., and Hatami, K. (2009). "Numerical Study of Reinforced Soil Segmental Walls Using Three Different Constitutive Soil Models." *Journal of Geotechnical and Geoenvironmental Engineering*, 135(10): 1486-1498.

Huang, J., Parsons, R.L., Han, J., and Pierson, M.C. (2011). "Numerical Analysis of a Laterally Loaded Shaft Constructed Within an MSE Wall." *Geotextiles and Geomembranes*, 29: 233-241.

Huang, J., Han, J., Parsons, R.L., and Pierson, M.C. (2013). "Refined Numerical Modeling of a Laterally-Loaded Drilled Shaft in an MSE Wall." *Geotextiles and Geomembranes*, 37: 61-73.

Huang, J., Bin-Shafique, S., Han, J., and Rahman, M.S. (2014). "Modelling of Laterally Loaded Drilled Shaft Group in Mechanically Stabilized Earth Wall." *Proceedings of the ICE-Geotechnical Engineering*, 167(4): 402-414.

Itasca. (2015). Fast Lagrangian Analysis of Continua in 2 Dimensional (Flac2D) Software Manual.

ITASCA, FLAC. (2008). Itasca Consulting Group, Inc., FLAC/SLOPE User's Guide Version 8.0: License.

Kakrasul, J.I., Han, J., Rahmaninezhad, S.M., and Weldu, M. (2016). “Model tests of geosynthetic-reinforced earth walls with limited-space retained fill”. 3rd Pan-American Conference on Geosynthetics (GeoAmericas), pp. 1279-1286.

Karpurapu, R. and Bathurst, R.J. (1995). "Behaviour of Geosynthetic Reinforced Soil Retaining Walls Using the Finite Element Method." *Computers and Geotechnics*, 17: 279-299.

Kline, S. J. (1986). “Summary and Comparison of Methods Similitude and Approximation Theory.” Springer, Berlin, Heidelberg, ISBN: 978-3-642-61638-9

Kniss, K. T., Yang, K.-H., Wright, S. G., & Zornberg, J. G. (2007). Earth Pressures and Design Considerations of Narrow MSE Walls. Paper presented at the Proceedings of the Texas Section ASCE Spring Meeting.

Khurmi, R. (1987). “Textbook of Hydraulics, Fluid Mechanics and Hydraulic Machines.” S. Chand.

Lawson, C., and Yee, T. (2005). Reinforced soil retaining walls with constrained reinforced fill zones. Proceedings, *Geo-Frontiers 2005*, 2721-2734.

Lee YB, Ko HY, McCartney JS (2010) Deformation response of shored MSE walls under surcharge loading in the centrifuge. *Geosynthetics International*, 17(6):389–402

Leshchinsky, D., Hu, Y., and Han, J. (2004). Limited reinforced space in segmental retaining walls. *Geotextiles and Geomembranes*, 22(6), 543-553.

Ling, H., and Leshchinsky, D. (2003). Finite element parametric study of the behavior of segmental block reinforced-soil retaining walls. *Geosynthetics International*, 10(3), 77-94.

McKittrick, D.P. (1978). "Reinforced Earth: Application of theory and research to practice", keynote paper, Symposium on Soil reinforcing and Stabilizing Techniques, Sydney, Australia.

Mirmoradi, S.H., and Ehrlich, M. (2014). "Numerical Evaluation of the Behavior of GRS Walls with Segmental Block Facing under Working Stress Conditions." *Journal of Geotechnical and Geoenvironmental Engineering*, 141(3): 1-8.

Morrison, K. F., Harrison, F. E., Collin J. G., Dodds A., and Arndt B. (2006)."Shored Mechanically Stabilized Earth (SMSE) Wall Systems Design Guidelines." Report No. FHWA-CFL/TD-06-001, Federal Highway Administration.

NCMA. (2009). Design manual for segmental retaining walls. National Concrete Masonry Association, 3rd ed. (Edited by M. Bernardi).

Noche, R. E. (2013). "Scale model shake table testing of seismic earth pressures in soft clay." Master Thesis, *California Polytechnic State University*, San Luis Obispo.

Pinto, M., & Cousens, T. (2000). Modelling a geotextile-reinforced, brick-faced soil retaining wall (vol 5, pg 417, 1999). *Geosynthetics International*, 7(1), 75-76.

Reddy, D., Navarrete, F., Rosay, C., Cira, A., Ashmawy, A., & Gunaratne, M. (2003). Long-term behavior of geosynthetic reinforced mechanically stabilized earth (MSE) wall system-Numerical/Analytical studies, full-scale field testing, and design software development.

Rahmaninezhad S. M, Han, J., Weldu M, Kakrasul J. I., Razeghi H.R., (2016). "Effect of methods of applying normal stresses in pullout tests on pressure distribution and pullout resistance". In: *Proceedings of 3rd Pan-American Conference on Geosynthetics*. GeoAmericas 2016, Miami Beach April 10-14.

Rahmaninezhad, S.M., Han, J., Weldu, M., Kakrasul, J.I., and Razeghi, H.R. (2016). "Effects of methods of applying normal stresses in pullout tests on pressure distributions and pullout resistance." GeoAmericas 2016, 3rd Pan-American Conference on Geosynthetics, Miami Beach, FL, April 10-13.

Rahmaninezhad, S. M., Yasrobi, S.S., Eftekharzadeh, S.F. (2009). “Effects of compaction in the subgrade of the reinforced sand backfills with geotextile on bearing capacity.” *Int J Civil Eng.*

Skinner, G.D., and Rowe, R.K. (2005b). "Design and Behavior of a Geosynthetic Reinforced Retaining Wall and Bridge Abutment on a Yielding Foundation." *Geotextiles and Geomembranes,* Vol. 23, pp. 234-260.

Sperl, M. (2006). “Experiments on Corn Pressure in Silo Cells – Translation and Comment of Janssen’s Paper from 1895.” *Granular Matter,* 8: 59–65.

Take, W., and Valsangkar, A. (2001). Earth pressures on unyielding retaining walls of narrow backfill width. *Canadian Geotechnical Journal*, 38(6), 1220-1230.

Wang, Y.-H., Jiang, W.-G., & Wang, Y.-H. (2013). Scale effects in scour physical-model tests: cause and alleviation. J. Marine Sci. *Technology*, 21(5), 532-537.

Woodruff, R. (2003). Centrifuge modeling of MSE-shoring composite walls. (Master), the University of Colorado, Boulder, *the University of Colorado*, Boulder.

Xiao, C., Han, J., and Zhang, Z. (2016). “Experimental study on performance of geosynthetic-reinforced soil model walls subjected to static footing loading.” *Geotextiles and Geomembranes,* 44, 81-94.

Yang, K.-H., and Liu, C.-N. (2007). Finite element analysis of earth pressures for narrow retaining walls. Journal of GeoEngineering, 2(2), 43-52.

Yang, K.-H., Zornberg, J. G., Hung, W.-Y., and Lawson, C. R. (2011). Location of failure plane and design considerations for narrow geosynthetic reinforced soil wall systems. *Journal of GeoEngineering,* 6(1), 27-40.

Yasrobi, S.S., Rahmaninezhad, S.M., Eftekharzadeh, S.F. (2009). “Large physical modeling to optimize the geometrical condition of geotextile in reinforced loose sand.” In: *GeoHunan International Conference* 2009, pp. 53–59.

Yasrobi, S.S., Rahmaninezhad, S.M., Eftekharzadeh, S.F. (2009). “Characterization of shallow foundations on loose sand reinforced with geotextile. 2nd international Conference on New Development in Soil Mechanics and geotechnical engineering, 2009.

Yu, Y., Bathurst, R.J. and Allen, T.M. (2015). “Numerical modelling of the SR-18 geogrid reinforced modular block retaining walls.” *Journal of Geotechnical and Geoenvironmental Engineering*.

Zornberg, J. G., Mitchell, J. K., and Sitar, N. (1997). “Testing of Reinforced Slopes in a Geotechnical Centrifuge.” *Geotechnical Testing Journal*, ASTM 20(4): 470-480.